

**Design of an Air Gap Armature for the MIT  
Superconducting Generator**

by

**Maurice-Andre Recanati**  
B. S., Rensselaer Polytechnic Institute  
(1992)

SUBMITTED IN PARTIAL FULFILLMENT  
OF THE REQUIREMENTS FOR THE  
DEGREE OF

**MASTER OF SCIENCE IN  
MECHANICAL ENGINEERING**

at the

**MASSACHUSETTS INSTITUTE OF TECHNOLOGY**

May 1st, 1994

© 1994 Maurice-Andre Recanati  
All rights reserved

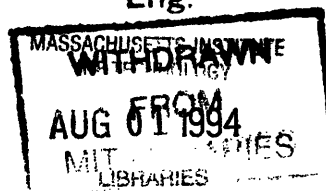
The author hereby grants to MIT permission to reproduce and to distribute publicly paper and electronic copies of this thesis document in whole or in part.

Signature of Author: \_\_\_\_\_  
Research Assistant, Department of Mechanical Engineering

Certified by: \_\_\_\_\_  
*Dr. Joseph L. Smith, Jr.*  
~~Thesis Supervisor~~

Accepted by: \_\_\_\_\_  
Dr. Ain Sonin  
Chairman, Department Committee

Eng.



## Notice

This thesis was prepared as a partial requirement for a Masters Degree in Mechanical Engineering at the Massachusetts Institute of Technology under the guidance and direct supervision of Professor Joseph L. Smith, Jr.

This report was prepared as an account of work originally sponsored by the United States Government. Neither the author, nor Professor Smith, nor M.I.T. nor its employees makes any warranties, express or implied, or assumes any legal liability or responsibility for the accuracy, completeness, or usefulness of any information, apparatus, product, or process disclosed, or represents that its use would not infringe privately owned rights. Reference herein to any specific commercial product, process or service by trade name, mark, manufacturer, or otherwise, does not necessarily constitute or imply its endorsement, recommendation, or favoring by the US Government.

All trademarks herein are the property of their respective owners.

Due to the high risk nature of the project, the writer of this thesis does not assume any financial or legal liability associated with this work.

# **Design of an Air Gap Armature for the MIT Superconducting Generator**

by Maurice-Andre Recanati  
Research Assistant

Submitted in May of 1994 in partial fulfillment of the requirements for the degree of Masters of Science in Mechanical Engineering.

## **ABSTRACT**

In the United States alone, increasing demand for electricity will create a 20% expansion of the current generating base in the next ten years. International markets will expand even faster, with most of the worldwide growth coming from natural gas fired combustion turbines and highly efficient combined-cycle plants.<sup>1</sup>

The MIT Superconducting Generator Program is a high risk, high payoff enterprise which makes use of advanced design concepts and materials in order to offer significant benefits to electrical utilities. Using a rotor which contains a superconducting field winding, a significantly higher magnetic field than that found in conventional generators is created. Due principally to Lens's Law, this intense magnetic field produces a large magnetomotive force (mmf) in the armature winding; hence special considerations must be taken while designing the stator assembly.<sup>2</sup>

In this thesis, we will begin by explaining in detail the motivations behind this project as well as review and compare the different types of airgap armature windings developed in industry before introducing the MIT design.

The core of the thesis is threefold. In the first part, the overall design is derived from basic design specifications and the general layout of the stator is produced. In the second part, various important components such as the conducting wire, the insulation, the end connectors and the spacers are analyzed and a selection is made based on experimental data. While the first two parts of the thesis have a strong emphasis on design, the third part consists of a basic electrical and thermodynamical analysis of the stator core assembly.

A brief section discussing manufacturing, assembly and testing is also included for possible industrial scale production of the generator before concluding on the feasibility of such a construction.

Thesis Supervisor: Professor Joseph L. Smith, Jr.  
Ford Professor of Mechanical Engineering



" Two of the most important duties of an engineer are the design of engineering systems and the analysis of the behavior or performance of these systems. [...] A good solution will provide the necessary engineering information about the situation within the time available for analysis and with an economy of effort. An analysis which is more complex than necessary is time consuming and wasteful. "

Joseph L. Smith,  
in Engineering Thermodynamics, 1981.

Inspired by Prof. Smith's philosophy, the author of this thesis has endeavored to accomplish the designing as well as the analysis of the superconducting generator armature.

Boston, Massachusetts, 1994

## **Acknowledgment**

This research thesis proved to be quite an interesting and complex endeavor. Despite the slow development of the investigation, mainly due to a lack of funding and of manpower, I have learned a lot about designing advanced technology machines. Since my undergraduate degree was in Physics, I had to teach myself in a very short time the basics of design, heat transfer, mechanical and electrical engineering causing an additional, but well spent, delay in the onset of the research.

There were many people who helped me in the course of the research at MIT and to whom I am deeply indebted. I would like to thank Bob Gertsen, who taught me all that I know about operating a machine shop; Lisa Langone, for her patience, and all the students of the Cryogenics Laboratory for their support. I would also like to thank Steve Umans and Wayne Hagman, who each proved to be invaluable assets in the development of the electrical aspect of the stator winding. Prof. James Kirtley, one of the finest professors at MIT, played a central role in my understanding and in my design of the generator. My deepest thanks are extended to Professor Joseph Smith, who patiently supervised my thesis, contributed encouragement and guidance, as well as many insightful ideas and comments.

Finally, I would like to thank the officers and staff of several corporations for their input and for the use of their facilities throughout my research. I am also grateful to my friends and especially to my family for their understanding and moral support.

Thank You

## **Foreword**<sup>3</sup>

The MIT Superconducting Generator Program, which is conducted jointly by the Mechanical and Electrical engineering departments, was established in 1967 by professor Joseph Smith. With the support of the Edison Electric Institute, a 45 kVA superconducting synchronous generator utilizing a rotating superconducting field winding was constructed. During the period between 1970 and 1975, EPRI supported the construction of a 3 MVA superconducting generator that was successfully tested as a synchronous condenser. Using DOE funding, the MIT group subsequently started developing a 10 MVA superconducting generator that would demonstrate advanced concepts not found in similar generators being designed elsewhere. The construction of the generator and the test facility (consisting of a General Electric LM 1500 turbine and an interconnection to the Cambridge Electric Company grid), were completed and operational in 1985 after a project stretch-out due to funding restrictions.

In late 1989, support from DOE ceased while EPRI and later DARPA continued to sustain the testing and modification phases of the generator. Using these DARPA funds, the rotor was modified in 1991 to operate at liquid helium temperature and at 3600 RPM with low vibrations. In the spring of 1992, EPRI funds were utilized to conduct a series of open circuit tests using a hydraulic spin motor which proved to have inadequate power.

Last summer, the generator was ready to be tested on the local power grid as a synchronous condenser operating at 13.8 kV at 3600 RPM. Unfortunately, due to an imperfection in manufacturing, the stator winding experienced a turn-to-turn flash over at 12.9 kV. However, because of an

excellent rotor design, the rotor remained superconducting during this sudden transient and no significant losses in the excitation current were detected. Both the rotor and stator structure withstood this transient without any damage or deformations. Further testing of the generator will require a new stator winding since this component is a total loss. This thesis, which is partially funded by EPRI, describes in detail how the new armature is to be constructed when sufficient funds will be appropriated.

## Table of Contents

	<u>Page</u>
<b>CHAPTER 1: INTRODUCTION</b>	
1.1 Motivation of Project	16
1.2 Description of the MIT Rotor	18
1.3 Benefits of Air Gap Armature Design	23
1.4 Types of Air Gap Armature Windings	27
1.5 Introduction to MIT Designs	43
<b>CHAPTER 2: ARMATURE DESIGN</b>	
2.1 Design Specifications	45
2.2 Layout Detail	51
2.3 Electrical Specifications	66
2.4 Design Calculations	78
<b>CHAPTER 3: COMPONENT DESIGN</b>	
3.1 Selection of the Conductor Bar	95
3.2 Selection of Bar Insulation	117
3.3 Design of the End Connector	129
3.4 Design of the Cooling Spacer	133
3.5 Torque Tube Selection	136
<b>CHAPTER 4: MANUFACTURING and TESTING</b>	
4.1 Production Sequence	137
4.2 Manufacturing and Testing of Bars	138
4.3 Assembly and Testing of the Armature	144
<b>CHAPTER 5: THERMODYNAMIC PROPERTIES</b>	
5.1 Cooling System Layout	150
5.2 Thermodynamic Analysis	152
5.3 Temperature Profiles	159
5.4 Generator Control	163
<b>CHAPTER 6: ELECTRICAL PROPERTIES</b>	
6.1 Circuit Modeling	168
6.2 Transient Behavior	177

	<b>Page</b>
<b>APPENDICES:</b>	
<b>APPENDIX LIST</b>	
Appendix A:	MIT 10 MVA Helical Armature Specifications 182
Appendix B:	Designing Bars with Smooth Transition Sections 195
Appendix C:	Quantum Mechanical Properties of Copper 199
Appendix D:	Electromagnetic Waves in Conducting Media 207
Appendix E:	Thermal Conduction and Convection in a Fin 209
<b>FOOTNOTES</b>	<b>214</b>

## List of Figures

	Page
<b><u>CHAPTER 1</u></b>	
Fig. 1.1	Schematic View of 10-MVA Generator Configuration 19
Fig. 1.2	Cross Section of the 10-MVA Rotor 19
Fig. 1.3	Schematic of Conventional Generator 24
Fig. 1.4	Schematic of Air-Core Synchronous Machine Geometry 24
Fig. 1.5	Topology of Wye and Delta Connected 3-Phase Winding 29
Fig. 1.6	Wye-Connected, Parallel Circuit Lap Winding 30
Fig. 1.7	Delta-Connected, Parallel Circuit Lap Winding 32
Fig. 1.8	Delta, Parallel Circuit, Limited-Voltage, Lap Winding 34
Fig. 1.9	Limited-Voltage-Gradient Winding by Kirtley 35
Fig. 1.10	Delta, Parallel Circuit Wave Winding 37
Fig. 1.11	Delta, Parallel Circuit Helical Winding 38
Fig. 1.12	Delta, Parallel Circuit, Limited Voltage, Helical Winding 39
Fig. 1.13	Modified Gramme-Ring Winding 41
Fig. 1.14	Spiral Pancake Winding 42
<b><u>CHAPTER 2</u></b>	
Fig. 2.1	Inner Bore Tube Dimensions as Built 46
Fig. 2.2	Circuit Topology of Wye Connected Armature Winding 47
Fig. 2.3	Delta-Wye Transformer Connection 49
Fig. 2.4	Conductor Used in Armature Bars 50
Fig. 2.5	Helical Winding Bar Layout 52
Fig. 2.6	End-Section of the Armature Bar 56
Fig. 2.7	Distribution of the Phase Belts at Lead Ends 57
Fig. 2.8	Layout of Phase Belts and End Connectors 61
Fig. 2.9	Circuit Layout for 10 MVA Generator Armature 63
Fig. 2.10	Insulation Systems Compatible with Air-Gap Armatures 65
Fig. 2.11	Rendering of MIT 10 MVA Wye Connected Armature 67
Fig. 2.12	Nominal Electrical Stress on Helically Winding Bar 77
Fig. 2.13	Allocation of Radial Space in the Armature 80
Fig. 2.14	Path of Helically Winding Bars Mounted on Armature 81
Fig. 2.15	End Tab Mounted at the Leads of the Bar 82
Fig. 2.16	Representation of Bar in Axial-Azimuthal Plane 84
Fig. 2.17	Iterative Calculation Flow Chart 87

### CHAPTER 3

Fig. 3.1	Hand Operated Lab-Bench Rolling Mill	101
Fig. 3.2	Magnetic Field Outside and Inside the Conductor	105
Fig. 3.3	Cut of Conducting Wire into Thin Concentric Shells	110
Fig. 3.4	Distribution of Induced Current within Wire	111
Fig. 3.5	Relationship Between Diameter and Dimensions of Litz	114
Fig. 3.6	Definition of Twist Pitch	116
Fig. 3.7	Fault Stresses on Armature Winding	121
Fig. 3.8	Torque Shear Stress on Center Section of Armature	125
Fig. 3.9	Sketch of the End Connector	131
Fig. 3.10	Top View of Compressed Bar	132
Fig. 3.11	Design of the End Connector	132
Fig. 3.12	Cooling Channel Design	135

### CHAPTER 4

Fig. 4.1	Assembly Process Flow Chart	139
----------	-----------------------------	-----

### CHAPTER 5

Fig. 5.1	Armature Cooling System	151
Fig. 5.2	Path of Cooling Channel	153
Fig. 5.3	Temperature Rise in Cooling Channel	158
Fig. 5.4	Temperature Profile in Armature Bar	164
Fig. 5.5	Generator Control Diagram	165

### CHAPTER 6

Fig. 6.1	Voltage-Current Phasors	174
Fig. 6.2	Current During Sudden Short Circuit	180

### APPENDIX

Fig. B1	Representation of Smooth Transition of Armature Bar	198
Fig. B2	Curvature for a Smooth Transition Bar	198
Fig. C1	Fermi Sphere in Momentum Space	204
Fig. C2	Shift of Fermi Sphere by an Electric Field	204
Fig. C3	Motion of Charged Carrier in Insulated Conductor	205
Fig. C4	Motion of a Charged Carrier in Electric Field	205
Fig. E1	Litz Cable Modeled as a Fin	212
Fig. E2	Heat Flow in Fin	213
Fig. E3	Temperature Distribution in Fin	213

The writer of this thesis gratefully acknowledges the contribution of other authors in some of the above figures and illustrations.



## List of Tables

	Page
<b><u>CHAPTER 1</u></b>	
Table 1.1	Comparison of Superconducting/Conventional Generators 17
Table 1.2	MIT Superconducting Generator Major Dimensions 22
Table 1.3	MIT 10 MVA High Voltage Armature Design Specs. 44
<b><u>CHAPTER 2</u></b>	
Table 2.1	MIT 10 MVA Wye Connected Armature Design Specs. 51
Table 2.2	Voltage Gradient Occurring at Phase Belt Interfaces 59
Table 2.3	Standard Nominal System Voltages and Ranges 68
Table 2.4	MIT 10 MVA Armature Electrical Design Specs. 78
Table 2.5	Design Calculation Equations and Results 93
<b><u>Chapter 3</u></b>	
Table 3.1	Comparison of Widely Used Conductor Materials 96
Table 3.2	Comparison of Film Insulation Materials 97
Table 3.3	Mechanical and Chemical Results of Tests 102
Table 3.4	Comparison of Bar Insulation Materials 128
<b><u>Chapter 4</u></b>	
Table 4.1	Part Requirement List 137
<b><u>Chapter 5</u></b>	
Table 5.1	Physical Properties of Armature Materials 152
<b><u>Chapter 6</u></b>	
Table 6.1	Electrical Characteristics of 10 MVA Generator 177

## List of Calculations

	Page	
<u>CHAPTER 2</u>		
Calculation 2.1	Relationship Between Line and Phase Voltages	69
Calculation 2.2	Calculating the Flux Linkage and the Number of Bars per Phase Belt	71
Calculation 2.3	Electric Power in Delta and Wye Connected Machines	73
<u>CHAPTER 3</u>		
Calculation 3.1	Power Dissipated by Eddy Current Losses in Cylindrical Wires	107
Calculation 3.2	Mechanical Shear Stress in the Armature	123
<u>CHAPTER 6</u>		
Equation 6.1	Flux-Current Relationships	170
Equation 6.2	The Park Transform	170
Equation 6.3	Transformed Flux-Current Relationships	171
Equation 6.4	Voltage-Current Relationship	171
Equation 6.5	Machine Inductance ( $L_a$ and $L_{ab}$ )	176
Equation 6.6	State-Space Synchronous Machine Model	178
Equation 6.7	Simplified Synchronous Machine Model	178
Equation 6.8	Current During a Symmetrical Fault	178

## **List of Pictures**

	<b>Page</b>
<b><u>CHAPTER 1</u></b>	
Picture 1.1 Generator Rotor in Bearings	20
Picture 1.2 Superconducting Field Winding	20
<b><u>CHAPTER 2</u></b>	
Picture 2.1 Close-up of the End of the 10-MVA Armature	54

# **CHAPTER I**

## **INTRODUCTION**

### **1.1 Motivation of Project**

The increasing demand for lower cost electricity has prompted worldwide innovations in generator design. MIT, as well as several other research labs, are currently investigating the applications of superconductors to electric machinery.

The advantages in using superconductors goes beyond simply eliminating field winding losses. Indeed, their ability to carry very large current densities helps improve machine efficiency by increasing the flux density and by reducing the ratio of armature loss to power produced. As a result, superconducting magnets are capable of making large magnetic fields over large volumes of space without dissipation and without needing iron magnetic circuits, thus offering significant benefits for use in turbo generators.<sup>4</sup>

The elimination of iron allows the armature to be located in a low permeance space, thus allowing it to carry large reaction currents with little reactive voltage drop. Consequentially, this technology permits a reduction in the overall size and weight of the generator as well as a reduction in core losses. When compared to conventional machines, the superconducting generator also offers an improvement in dynamic performance and machine transient stability.

These advantages do not, of course, come for free. It is necessary to cool the superconductor to cryogenic temperatures, a process which has both capital and energy cost consequences. Therefore, it is anticipated that commercial applications of superconductors will only be used in relatively

large (300 MVA) machines, in order to take advantages of economies of scale. However, the present generator's rating of only 10 MVA was selected because it is the highest rating which could be built using the facilities at MIT.

In an effort to quantify the substantial advantages of large superconducting generators over conventional machines, a comparison between three different types of 300 MW, 60 Hz, two pole generators, was compiled for EPRI, the Electric Power Research Institute. A brief summary of those results are contained in **Table 1.1**, below.<sup>5</sup>

Table 1.1: Comparison of Superconducting and Conventional Generators

	Cold	High	Conventional
Active Length (m)	1.91	1.91	4.70
Rotor Diameter (m)	.758	.758	1.04
Outside Diameter (m)	2.568	2.568	1.960
Refrigerator Power (kW)	37.4	16.2	0
Armature Conduction Loss (kW)	507	507	797
Field Winding Loss (kW)	0	0	1481
Synchronous Reactance	.529	.529	1.80
Generator Capital Cost	BASE	-	
Refrigerator Capital Cost	BASE	(\$ 86,000)	
Capitalized Losses	BASE	(\$ 42,000)	
Total	BASE	(\$128,000)	

In **Table 1.1**, the column labeled "cold" designates a machine similar in concept to the one developed at MIT. Namely, this generator is built with superconducting wires capable of operating at liquid helium temperature (4.2 K) and carrying  $1.6 \cdot 10^8 \text{ A/m}^2$  in a flux density of 6 T. The column labeled "high" refers to a hypothetical "high performance and high temperature" superconducting generator capable of achieving the same performance characteristics as the "cold" machine while operating at liquid nitrogen temperature (77 K). These two machines are compared to the "conventional" copper and iron design.

The data contained in **Table 1.1** unambiguously quantifies some of the advantages of the new technology. Thus, an energy investment into a refrigeration system returns an advantageous zero field winding conduction loss. Although the superconducting machine is more compact than conventional generators, it is slightly larger in diameter in order to operate near "tip speed". On the other hand, the larger flux produced permits a

shorter active length for the stator and thus lowers the armature losses. Hence, it is indisputable that, despite the assumptions made in the table, the application of superconductors to turbomachinery offers significant benefits to modern utility companies.

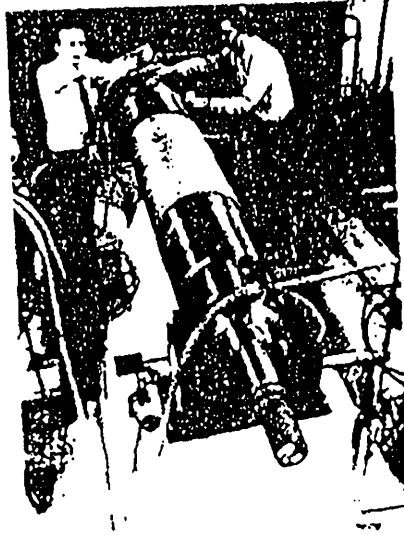
## **1.2 Description of the MIT Rotor**

At the heart of the 10 MVA Superconducting generator developed at MIT lays an "advanced concept" rotor. In this section we will briefly describe this rotor and highlight the advances in the design and shielding of the superconducting windings as well as its cryogenic cooling system.

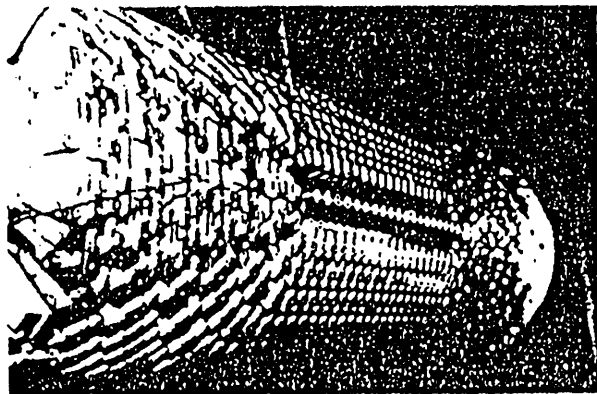
The generator rotor, which carries the superconducting field windings, the helium reservoirs and two electromagnetic shields, rotates in an insulating vacuum enclosure formed by the bore tube of the armature and the vacuum shaft seals at each end of the rotor. The rest of the generator, which consists of a stator winding and a magnetically shielded generator casing, is mounted radially outward from this stator bore tube, as shown in **Figure 1.1**. The rotor itself rotates on room temperature tilting pad bearings (see **Picture 1.1**) which are supported by two pedestals located on both sides of the machine.<sup>6</sup>

The MIT rotor, which is depicted in **Figure 1.2**, is a complex machine composed of several concentric "layers" of main components whose radial dimensions are tabulated at the end of this section. At the center, a helium inlet tube, connected to the helium reservoirs of the rotor cooling system, runs the length of the device. This system is in turn composed of two subsystems, one to cool the field winding and the other to cool the damper winding and can shield, which are connected in series under steady-state conditions.<sup>78</sup> Contrary to most rotors designed in industry, all of the rotating





Picture 1.1: Generator rotor in bearings



Picture 1.2: Superconducting field winding



elements in this machine (i. e. the winding and the two shields) operate at nearly liquid helium temperatures.<sup>9</sup> Radially outward of the helium inlet tube and axial reservoir, lays the inner support tube. This tube, as well as the outer support tube are both stainless steel forgings and thus serve as the torque carrying members of the rotor.

The principal component in the rotor assembly is the superconducting field winding which consists of a total of 1456 (=728x2) turns in saddle shaped modules, seven of which are mounted on each pole. Each individual module has 14 layers of wire in the radial direction and 4 to 10 layers, depending on its position on the pole, in the azimuthal direction. The wires, which are composed of 480 Nb-Ti strands, measure 63 microns in diameter and are embedded in a copper matrix. This field winding is retained between the aforementioned support tubes by a set of yokes capable of transmitting the steady-state torques acting on the winding to the main rotor body while at the same time insulating it from transient forces and torques. The MIT field winding shown in **Picture 1.2**, is capable of generating a magnetic dipole field of 4.8 T at a rated current of 939 Amperes.<sup>10</sup>

Two shields envelop the field winding. The single sheet of solid copper which forms the copper "can" shield, innermost of the two, serves to protect the superconductive windings from alternating magnetic fields. Like all metals, the copper can develop image eddy currents governed by Faraday's law<sup>11</sup> ( $V = \oint E \cdot ds = -\frac{d\Phi_m}{dt}$ ) which increase until the penetrating field is canceled. Hence, this rolled copper sheet must have a low and continuous resistance throughout the cylinder, while being strong enough to transmit very high levels of torque from the damper shield assembly to the support tubes during faults.

The wound damper shield, or main shield, is a two phase two circuit herringbone form winding operating at about 5 K. The winding, which is 60 turns per phase of a cable made up of 616 insulated and transposed strands, serves two main purposes. First, this component protects the field winding by dampening torques from 60 and 120 Hz electromechanical oscillations originating in the stator as a result of power system transients. Second, it is also the rotor's main source of shielding from transient magnetic fields. Since this energy dissipation is largely achieved by using a warm dampening resistor, a thermal isolation layer protects the field winding from transient temperature rises in the damper during faults.<sup>12</sup>

Finally, the rotor's outermost radial component is the filament wound prestressing tube. Made out of a stainless steel fiber embedded in an epoxy matrix, this element maintains a high radial compressive prestress on all rotor components mentioned above. This compressive force keeps the two shields in contact with the rotor even under centrifugal and magnetic loadings. The high compressive stresses produced by this force also permit the transmission of fault torques from the shields to the outer support tubes.<sup>13</sup>

**Table 1.2:** MIT-DOE Superconducting generator, Major Dimensions

	Inner Diameter (mm)	Outer Diameter (mm)
Field	207	287
Shield	332	342
Damper	365	416
Armature	468	650
Core	680	1040
Overall Length		1.060 (m)
Core Length		0.838 (m)
Field Turns (each)		204

Despite the advantages listed above, namely in the field winding support, the cryogenic system and the cold shielding system, the generator's armature winding must be able to take advantage of the rotor's exceptional capabilities.

### **1.3 Benefits of Air Gap Armature Designs**

We will begin this section by comparing conventional magnetic iron armatures to air gap ones before examining the advantages offered by this modern design.

In a conventional generator, the field winding, which usually carries a constant current density on the order of  $500 \text{ A/cm}^2$ , is just a hydrogen gas or water cooled electromagnet. The armature winding is located in slots within the stator core, a structure composed of thin sheets of magnetic steel, as shown in **Figure 1.3**. Because the steel is at ground potential, it is necessary to insulate every conductor, thus limiting the internal voltage to about 26 kV. Furthermore, the insulation thickness limits the slot current density to about  $300 \text{ A/cm}^2$ .<sup>14</sup>

When the generator operates under load, the rotor's rotating field is opposed by the magnetic flux created by the armature winding current. Under steady state conditions, this magnetic flux is principally a sinusoidal distribution, having the same angular frequency but lagging that of the rotor's rotation. The *reactive impedance* of the armature winding, which is a measure of the flux produced by the armature relative to that generated by the field winding, is inversely proportional to the "air gap" existing between the outside of the rotor and the inside of the stator assembly.

Since the *synchronous reactance* is the reactive impedance between the internal voltage and the armature's terminals, it is clear that too high a

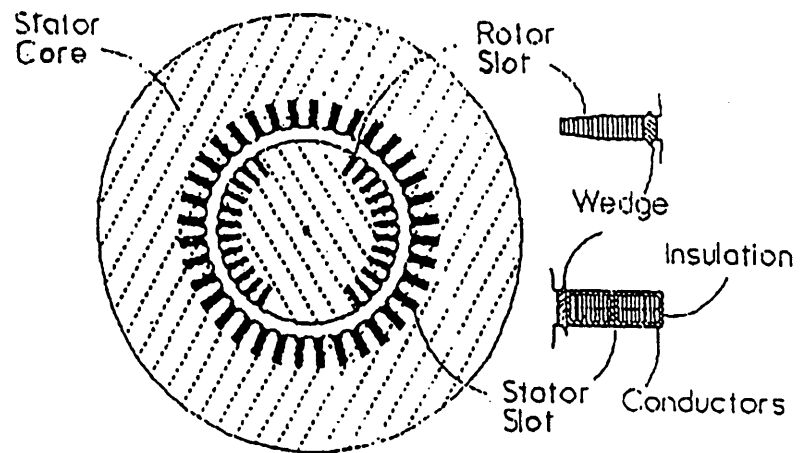


Figure 1.3: Schematic of Conventional Generator

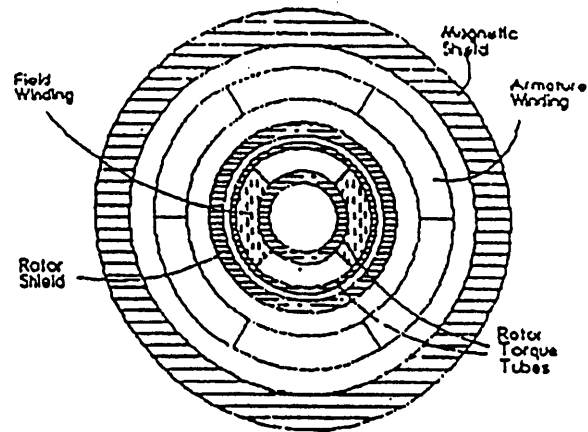


Figure 1.4: Schematic of Air-Core Synchronous Machine Geometry

value will result in inferior dynamic performance, low transient stability limits as well as more frequent adjustments of the excitation current for maintaining proper terminal voltage under varying loads. Hence, in order to built a satisfactory generator, the reactance must be reduced below a certain value. This is usually achieved by increasing the air-gap distance, which in turn requires an increase in the field current in order to maintain a comparable magnetic flux through the armature. Unfortunately, increasing the excitation current increases the  $I^2R$  losses within the rotor, thus decreasing efficiency and increasing the amount of heat that must be removed. Inevitably this leads to a design compromise: efficiency and refrigeration load are traded off in order to gain machine dynamic performance as well as voltage stability.<sup>15</sup>

The application of superconductors to generators has rendered the air-gap armature more feasible and appropriate for commercial application. Since superconductors can produce very large fields, as mentioned in section 1.1, it is possible to increase the air-gap to encompass the entire active region of the generator. Furthermore, superconductors are capable of producing higher flux densities than those of saturated iron, therefore magnetic iron would limit rather than enhance the magnetic flux within the machine. As a result, it is beneficial to eliminate the magnetic iron slots in both the rotor and the armature and replace them by composite (non-magnetic) "torque tubes" capable of providing torsional support and restraint from strains caused by the large magnetic stresses imposed by the field conductors. Such a generator design is portrayed in **Figure 1.4**.

The first advantage gained by eliminating the magnetic iron is the reduction in the reactance of the armature, which allows for higher currents as well as improves dynamic performance and voltage stability. Second, the

elimination of iron allows for more space for the armature itself thus increasing power density and efficiency. Third, since the "ground potential" iron is no longer present, the insulation required around the bars forming the armature winding could be reduced, resulting in an even larger conductor space factor and potentially higher terminal voltages. Finally, the replacement of iron by composite materials renders the machine significantly lighter and much simpler and cheaper to manufacture.<sup>16</sup>

In order to design an air-core machine and gain all of the aforementioned advantages, it is necessary to add two main components not found in conventional machines. The first is the rotor magnetic shields which, as described previously, prevent time-varying electro-magnetic fields from entering the rotor and inducing eddy currents capable of producing losses in the superconductor. Another component called the magnetic shield, which envelops the generator, must be built in order to confine the powerful dipole field within the machine by providing a "flux return path". It also slightly enhances the flux density in the active region.<sup>17</sup>

It should be pointed out that hybrid generators, which consist of a superconducting rotor and a conventional iron armature, could in principal be constructed. Except for the zero field winding losses, this machine would behave mostly like a conventional machine in size and performance and could not benefit from the many advantages, such as the reduction in reactance and the performance increase, offered by air-core geometry. Because of the iron's limiting effects, the flux densities within the machine would be comparable to those found in traditional generators, hence limiting the conductor current density to about 2,000 A/cm<sup>2</sup>.

In conclusion, it is clear that the air-core armature winding is superior to the magnetic iron slot design as it resolves the traditional design tradeoff

between machine efficiency and the advantages offered by a lower synchronous reactance. However, it is because of the superconductor's ability to produce extremely large flux densities that saturated iron is rendered obsolete and that an air-gap design is technologically feasible.

#### **1.4 Types of Air Gap Armature Windings**

Having seen the benefits inherent in air gap designs, we will now examine various types of winding schemes that are compatible with this technology before commenting on their advantages and disadvantages.

There are six major parameters that characterize an armature winding. The first three parameters, which are quantitative in nature, are: the number of phases, the number of circuits (or *phase belts*) within each of these phases and the number of turns within each individual circuit. Modern large scale electric machinery almost exclusively uses three phase (each 120 degrees out of phase) voltage, thus we will concentrate our discussion only on such machines. The fourth parameter distinguishes the manner in which the phase belts are mounted. Usually, for ease of manufacturing and for design simplicity, generator as well as motor armatures are constructed with two phase belts which could be mounted either in series or in parallel.

The fifth characteristic of an armature winding is the topology of the entire circuit. There are two common methods for connecting each of the three phases together: Wye and Delta. In a Wye connected machine, all three phases are grounded together at one point and thus four wires exit the generator. A Delta connected machine, however, has no ground since all three phases are strung one after the other in a closed loop. Certain design innovations, particularly with delta connected machines, are capable of taking advantage of the cylindrical geometry by limiting the difference of

potential which exists between adjacent conductors. The modifier "limited voltage gradient" is therefore added to the fifth parameter for machines thus constructed. **Figure 1.5** illustrates the preceding explanations graphically.<sup>18</sup>

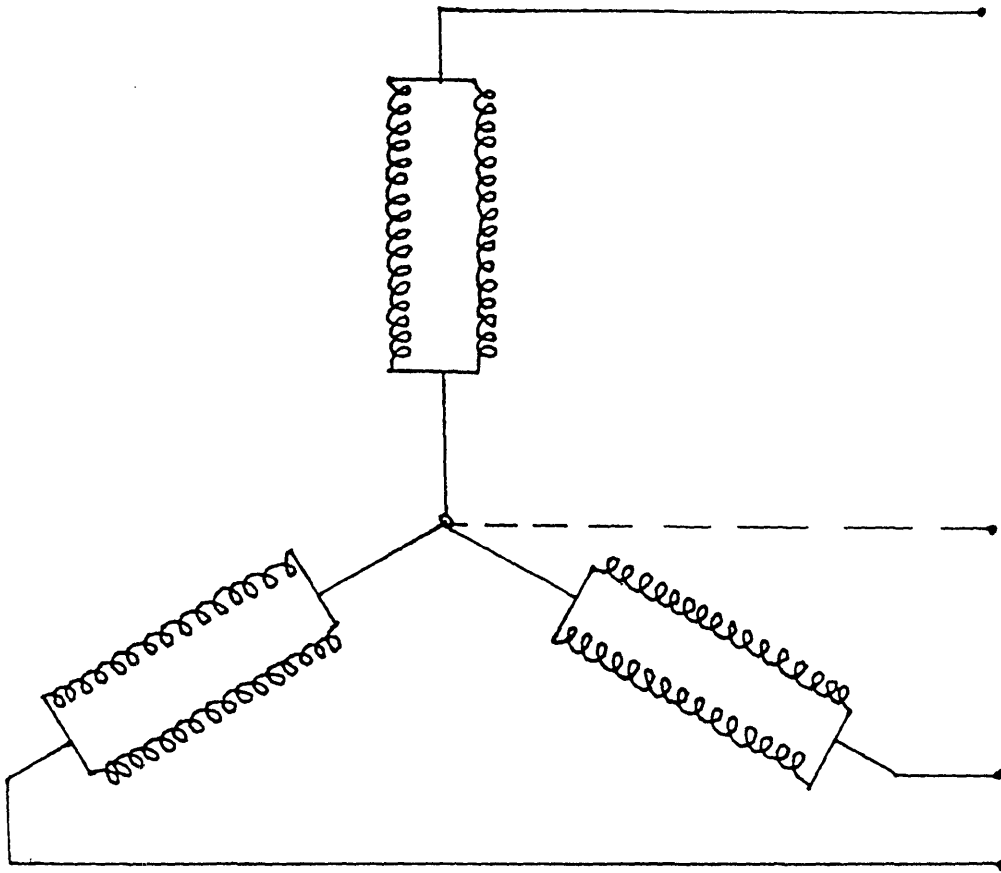
Finally, the sixth parameter refers to the method by which the winding, located in the active length of the armature, is made. In a lap winding, conductors first run positive in the theta direction, then run straight before turning in the opposite direction (negative in theta) when traveling axially on the cylinder's surface. When the straight part is removed, the conductors have a "kink" half way across the armature and the assembly appears like a chevron. The wave winding is similar to the lap winding, with the exception that, after passing through the straight section, the conductor continues in the same direction as it had begun. It can be shown that in both layouts, the conductors travel through the same "slots" and "capture" the same amount of flux. A helical winding is essentially, a wave winding who's straight section has been eliminated.

The most common arrangement found in conventional iron core generators is the Wye connected lap winding design with multiple parallel paths, each comprised of several dozen turns.<sup>19</sup> **Figure 1.6** illustrates an armature of this type, drawn with two phase belts and only six turns per phase. This type of design is well suited for a conventional generator for two reasons. First, the use of the common lap type winding allows for simple modular construction thus reducing manufacturing costs. Second, the use of a Wye connection allows for the minimization of circulating currents, particularly those due to third harmonics, by providing a common ground to all three phases. By following the conductors through the active region represented in **Figure 1.6**, it becomes apparent that there are large voltage differences between both radially and azimuthally adjacent conductors.

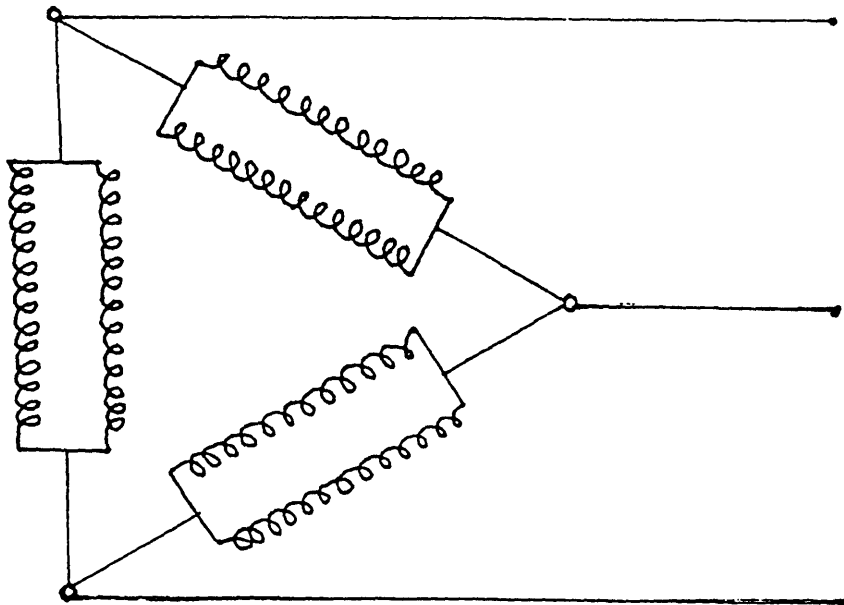


Figure 1.5: Topology of Wye and Delta Connected Three-Phase Winding

a) Wye Connected Parallel Circuit



b) Delta Connected Parallel Circuit



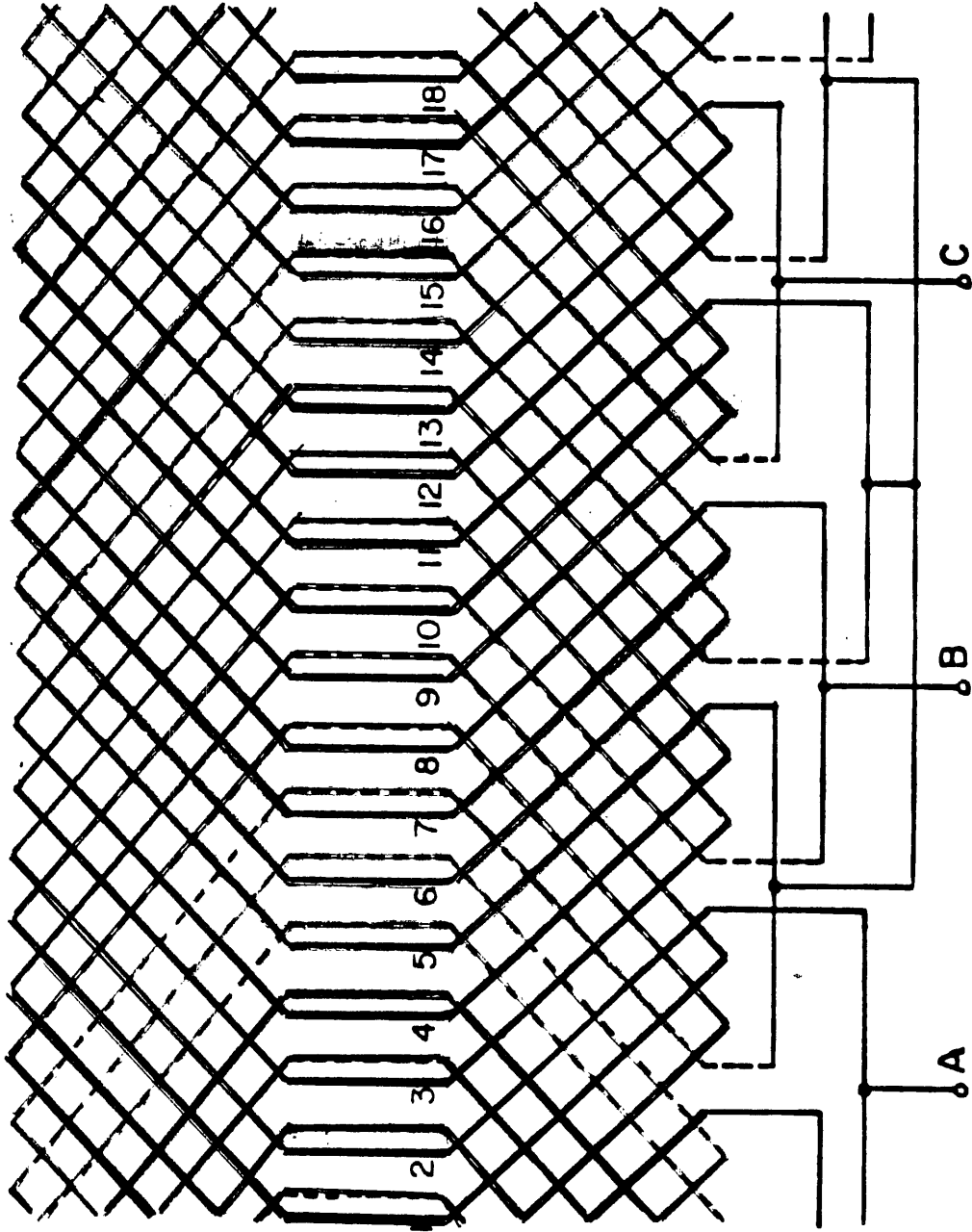


Figure 1.6: Wye-Connected, Parallel Circuit Lap Winding

Furthermore, as conductors carrying nearly the full machine voltage will inevitably cross conductors of another phase, even larger voltage differences exist in the end turn region. In a conventional machine, where each bar is insulated from the core and where the rated voltage is comparatively small, this design is justified. However, in the case of an air gap winding, which does not have a core, the conductors must each be heavily insulated to endure the rated voltage.<sup>20</sup>

In order to reduce the need for turn to ground insulation, the Wye topology must be abandoned and the Delta connection scheme, which has no "common ground", must be adopted. By modifying only the end connections of the previously depicted winding, we arrive at the delta connected design illustrated in Figure 1.7.

Unavoidably, this design suffers from several large voltage gradients within the machine. Large potential differences are especially prevalent in the end connections of phase belts, where a conductor of one phase belt shares a "slot" with that of another. Furthermore, within the active section, there are six regions where adjacent slots will carry conductors belonging to different phase belts. These azimuthally separated conductors, will be at greatly different potentials since one would be starting its journey through the machine while the other would be finishing it. Finally, a third type of voltage gradient exists, for a similar reason, between the radially separated conductors within a "slot" that belong to different phase belts of the same phase. All three of these problems are manifestations of a single cause: all of the phase belts are wound in the same sense. Figure 1.7 represents a left handed winding since entering the left end of the belt causes a rightward progression through the armature.<sup>21</sup>

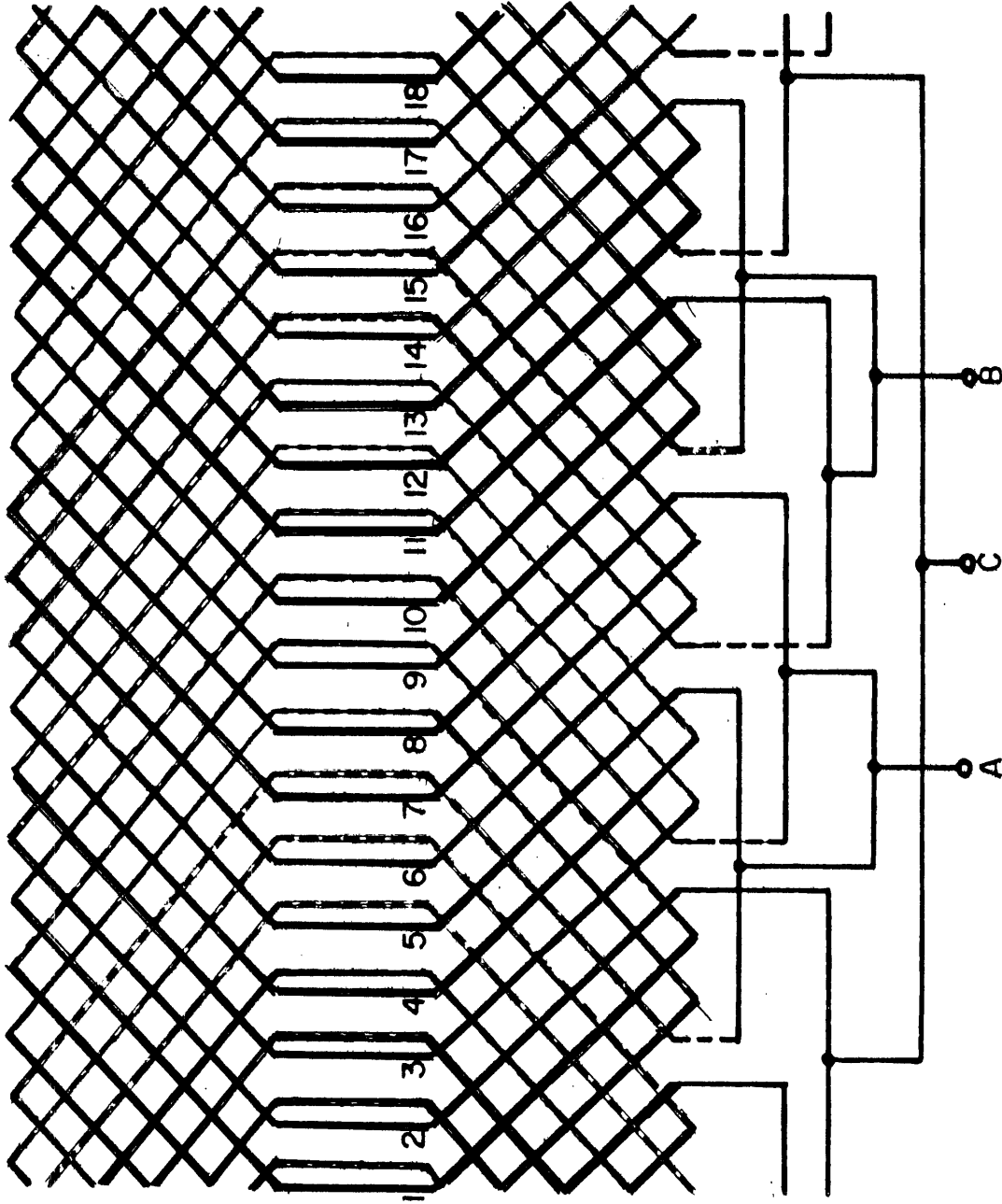


Figure 1.7: Delta-Connected, Parallel Circuit Lap Winding

The use of alternated sense phase belts was first suggested by Bratoljic<sup>22</sup> in the late 1970's as a solution to minimizing the voltage differences occurring at phase junctions and in the active region. **Figure 1.8** displays the Bratoljic "limited voltage" armature winding scheme. The insulation requirements of such a winding are reduced substantially compared to regular designs. since bars need only be insulated for bar-to-bar voltages. However, an insulating cylindrical shell must be inserted in order to radially insulate the end connections of one layer from those in the next. Two more shells must also be placed at the inner and outer radii of the armature to act as ground wall insulation. Westinghouse Corporation used this type of design in a 5 MVA superconducting generator.<sup>23,24</sup>

Despite its seemingly ideal design, the Bratoljic winding suffers from a geometrical problem. Bars that are closely packed together in the straight section will not fit in the end turns. This problem can be solved in either of two ways. The simplest solution, which Bratoljic recognized, involves leaving space between bars in the active section, just as in conventional armatures. A more complex solution, which was integrated in the Kirtley design advocates an increase in the radius of the bars located in the end turn region, in order to gain additional azimuthal space. In the Kirtley<sup>25</sup> winding, a dumb-bell frog leg configuration represented in **Figure 1.9**, the two layers of bars in the active section split into four "sub-layers" in the end turns. Since the difference in potential between radially adjacent bars is one turn voltage and that between azimuthally adjacent bars is two turn voltages, this design is subject to the same insulation requirements than the Bratoljic winding. A 3 MVA demonstration winding has successfully validated this design.<sup>26</sup>

Since Wave-wound armatures operate more satisfactorily than do those with lap windings without equalizers, they may replace lap designs

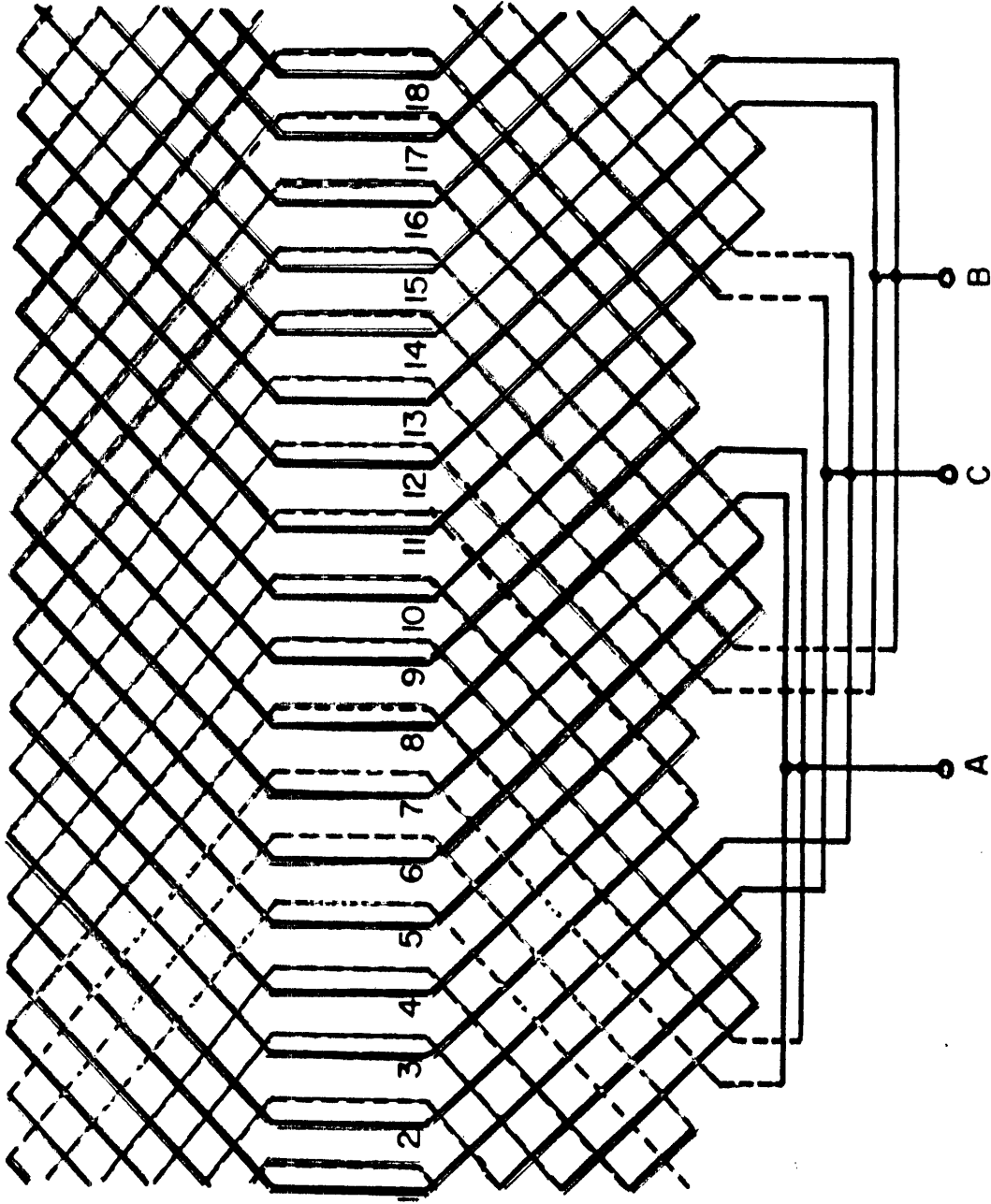


Figure 1.8: Delta-Connected, Parallel Circuit, Limited-Voltage-Gradient Lap Winding

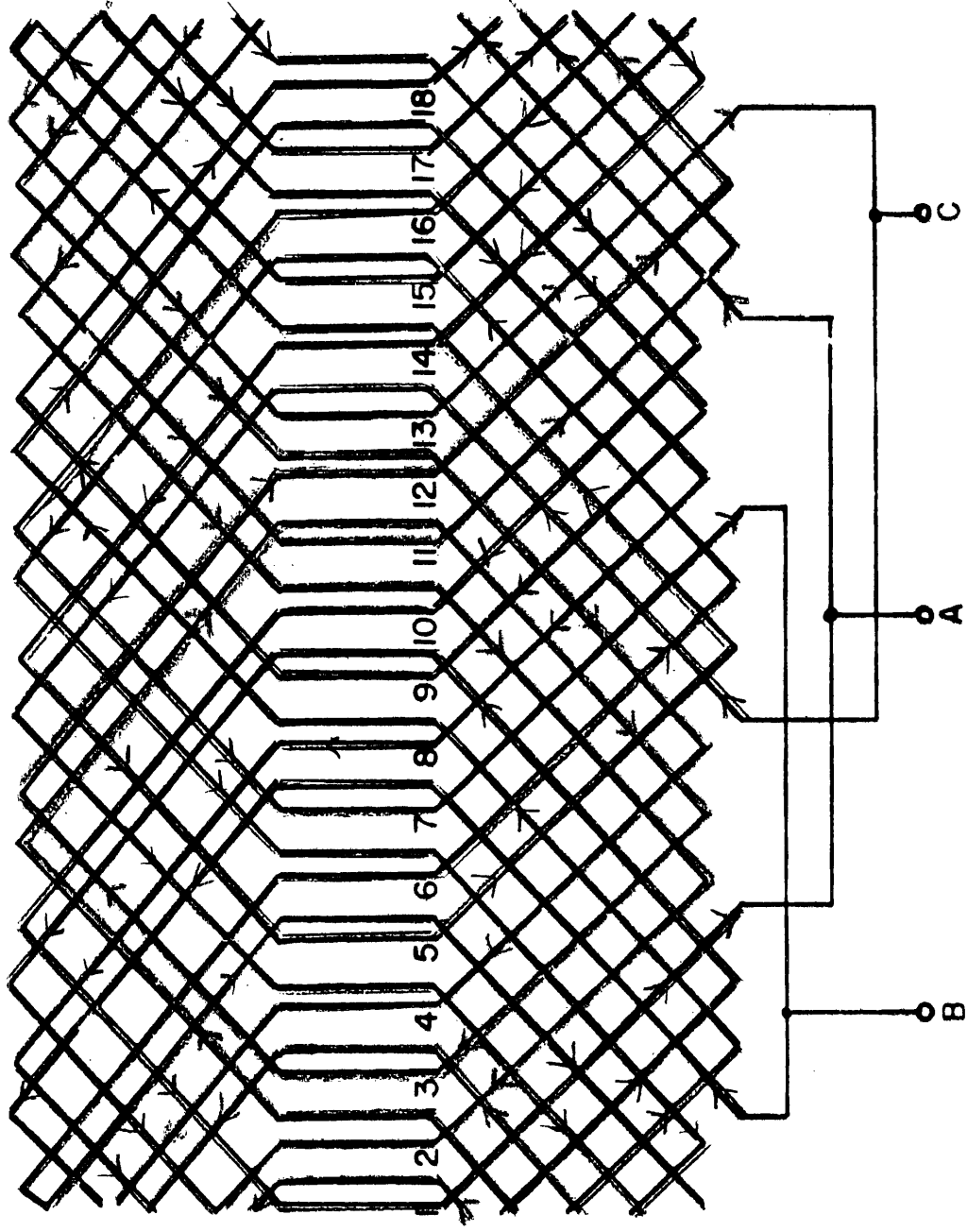


Figure 1.9: Limited-Voltage-Gradient Winding developed by Kirtley

provided that the current per circuit does not exceed 300 Amperes. A delta connected wave winding is illustrated in **Figure 1.10**. The manufacturing disadvantage characteristic in such type of winding can be mitigated, or even eliminated by using discrete bars rather than continuous conductors. It is apparent, however, that the wave winding suffers from the same problem (of end connections taking more azimuthal space than the straight section) than the lap winding.<sup>27</sup>

To make maximum use of the advantages offered by the superconducting rotor, the armature must have as much copper as possible in the active region. A helical winding, which is essentially a wave winding without the straight section, eliminates helically spiraling end turns altogether, thus liquidating the aforementioned problem. In such a design, the line-to-line crossings are located in the active region rather than in the end turns. Furthermore, the electro-mechanical stress inside is distributed sinusoidally along the machine, with zero stress at the center and ends.<sup>28</sup>

While the wave winding displayed in **Figure 1.11** is not of a "limited voltage" design, for the same reasons as given for the second winding, it is possible to modify the end connections so that the armature produced in **Figure 1.12** represents such a winding. The MIT 10 MVA Superconducting generator armature, which was built two years ago, was constructed in this fashion.

Like the Bratoljic scheme, the insulation requirements in this winding call for turn-to-turn voltages for the bars, for cylindrical shells capable of line-to-line insulation and for two line-to-ground insulating shells placed at the inner and outer radii of the armature. The helical winding offers, however, a much more efficient use of the armature's internal volume since



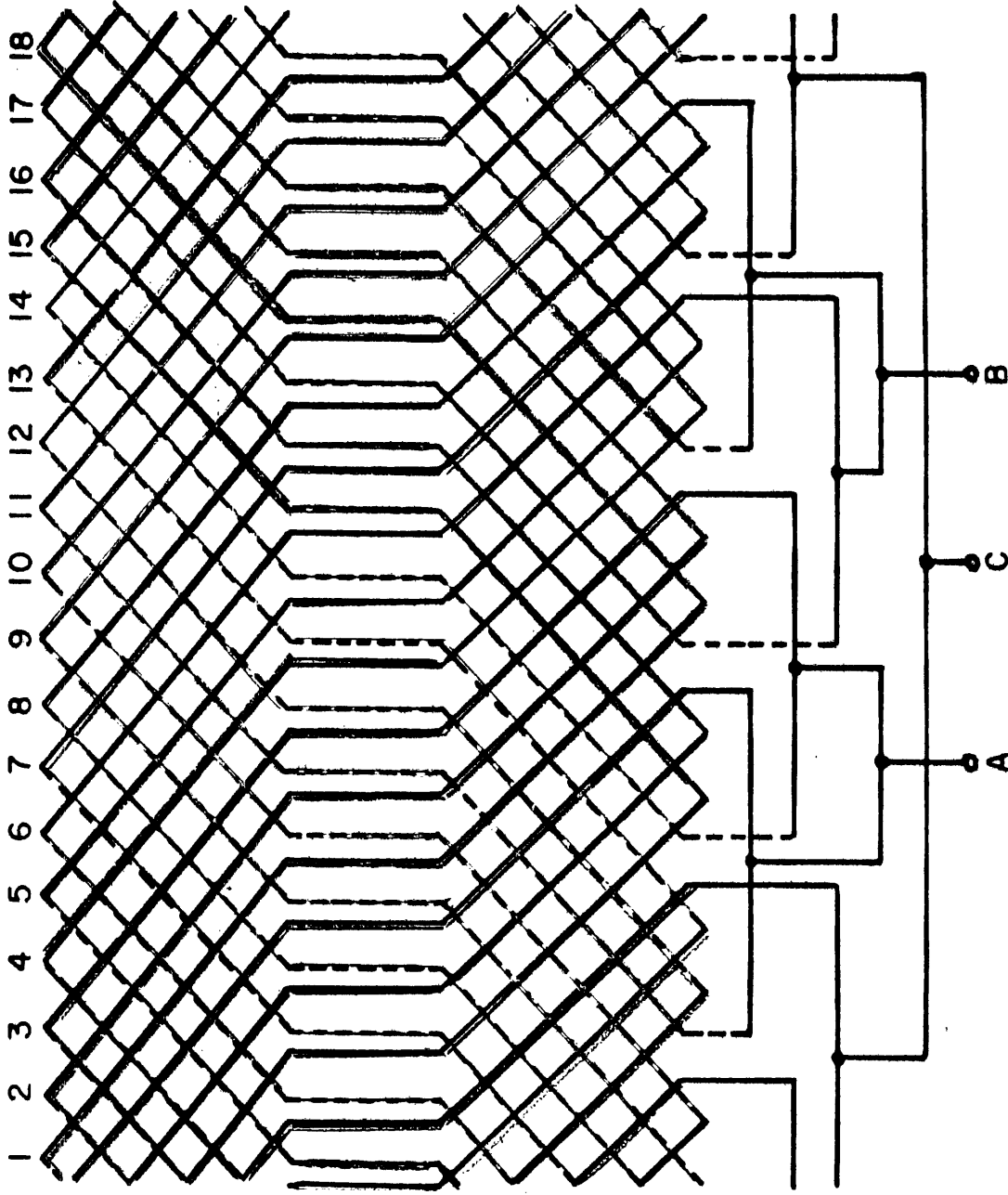


Figure 1.10: Delta-Connected, Parallel Circuit Wave Winding

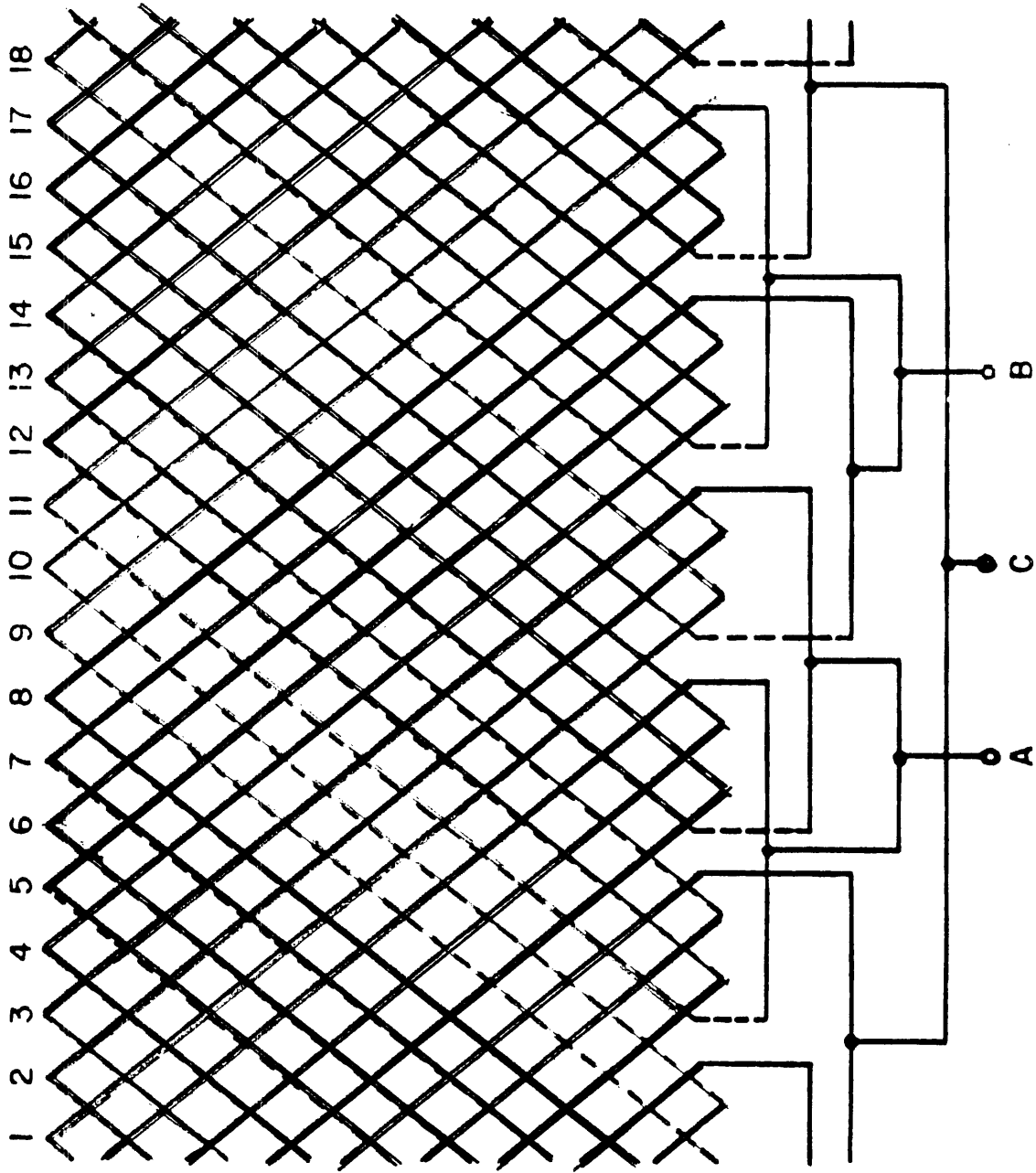


Figure 1.11: Delta-Connected, Parallel Circuit Helical Winding  
 ( Wave Winding With Straight Section Removed)

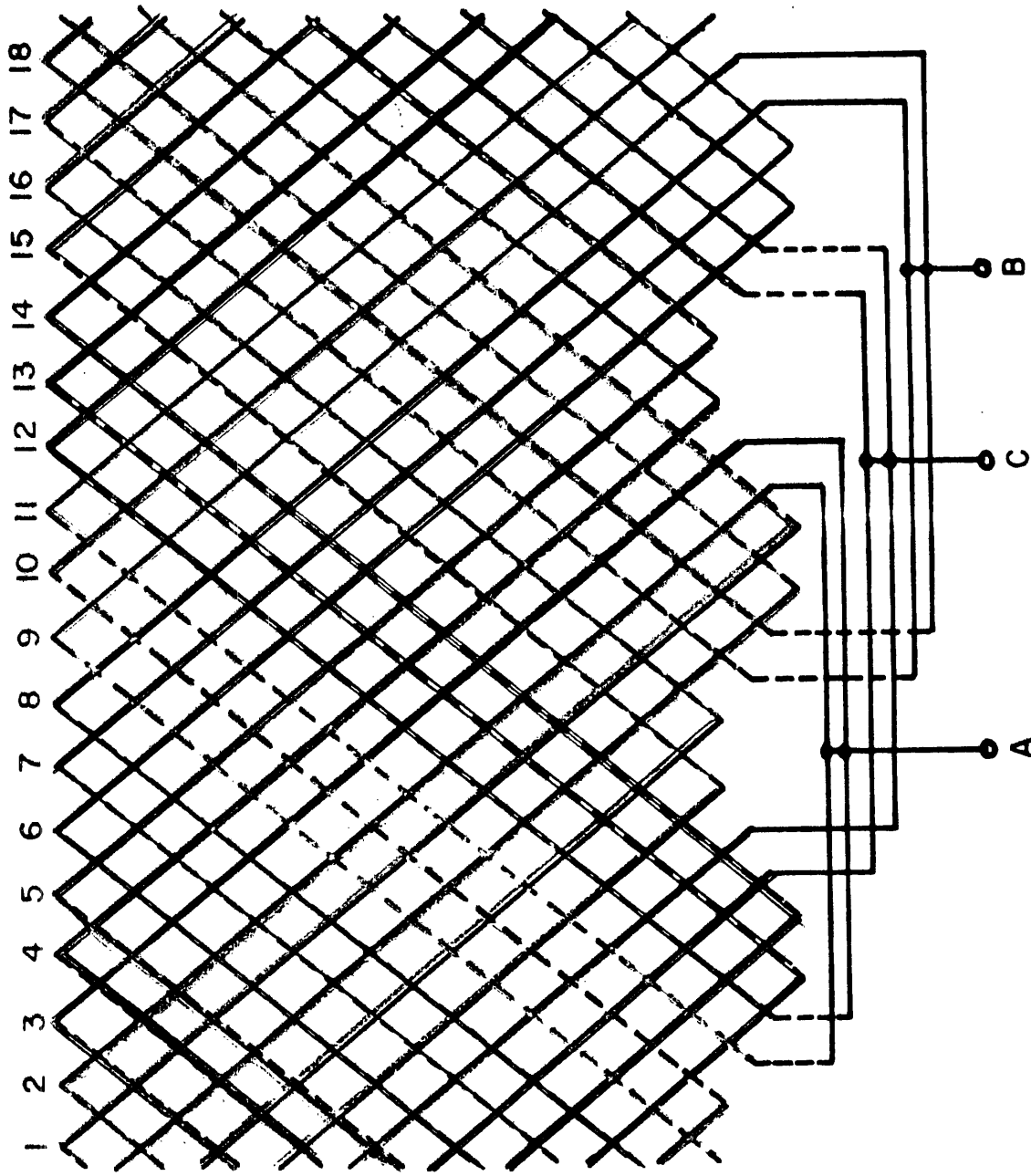


Figure 1.12: Delta-Connected, Parallel Circuit, Limited-Voltage-Gradient Helical Winding

the active region is not filled with unnecessary insulation while the end turns are cramped together.

Having followed the evolution of monolithic windings, we will now describe three completely different types of winding patterns. The first winding design is the modified Gramme-Ring<sup>29</sup> design which was proposed by Kirtley and Steeves. As illustrated in **Figure 1.13**, the nature of this winding is toroidal, with conductors wrapped around a ferromagnetic core. Since this winding is composed of alternated sense phase belts, it is also a limited voltage gradient design.<sup>30</sup> Since conductors do not cross each other in this winding, the insulation requirements are reduced to core insulation and to insulating cylinders at the inner and outer radii. This armature winding, unfortunately, suffers from unacceptably large electromagnetic losses and large reactances.<sup>31</sup>

**Figure 1.14** depicts another scheme, called the "Spiral Pancake" winding, which was first proposed by Aicholzer<sup>32</sup> and later adopted by Westinghouse<sup>33</sup> for a 300 MVA machine. This three phase design is composed of six spirally shaped pancake-coil phase belts, two of which form each phase, interleaved around a central cylinder. Each phase belt is comprised of two pancake coils, one spiraling into and the other one spiraling away from the center of the machine. The pancake coil is, in turn, composed of two circuits, each occupying different radial positions. The phase voltage is developed through a complicated set of series and parallel connections within and between phase belts. An advantage of this winding is its ability to be Wye connected, without causing adjacent bars to be at great potential differences. Since the maximum difference in potential at the inner bore tube is half the phase to neutral voltage, the insulation requirements call for one turn voltage bar-to-bar insulation within pancake coils and for line-to-line voltage

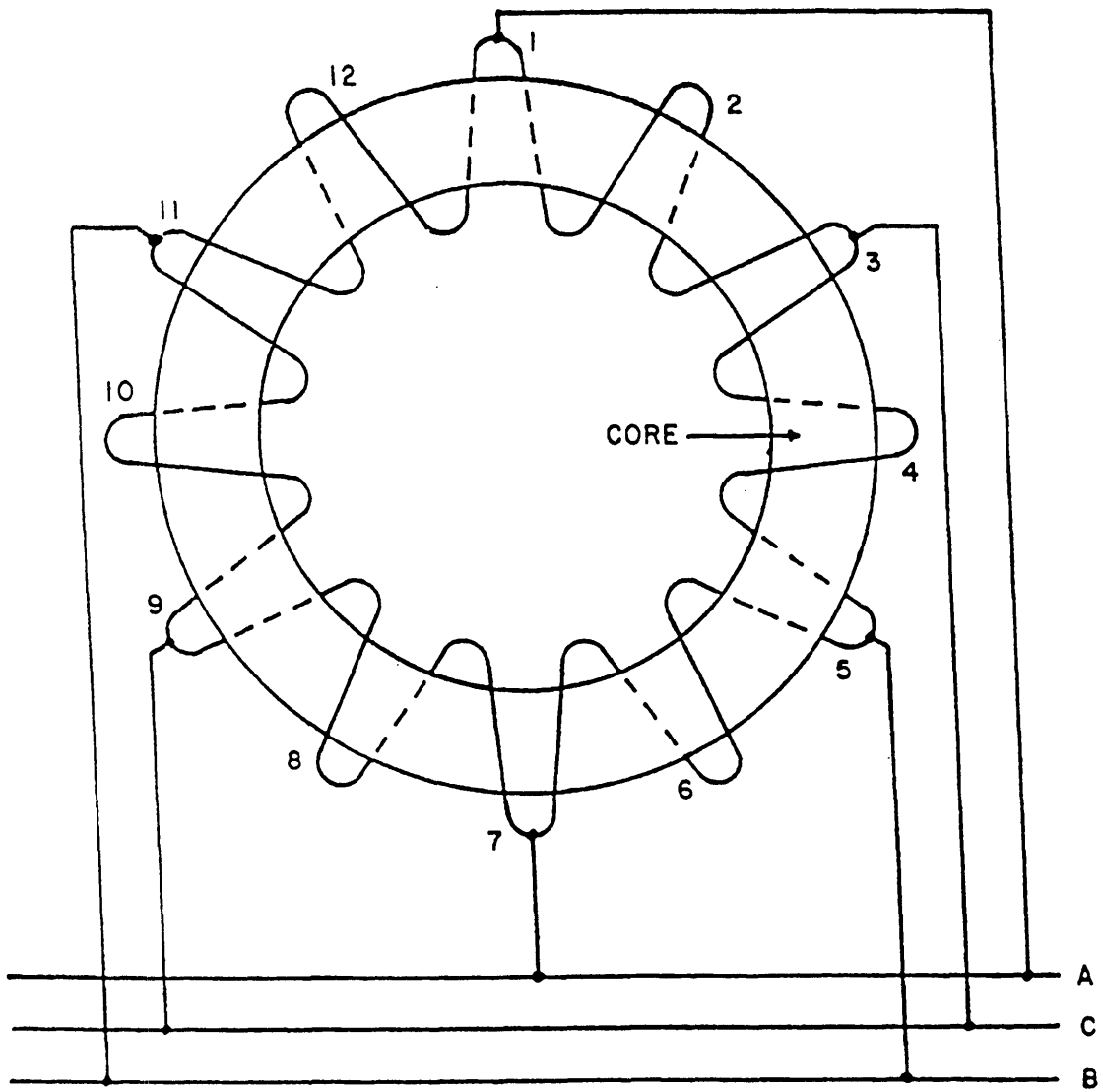
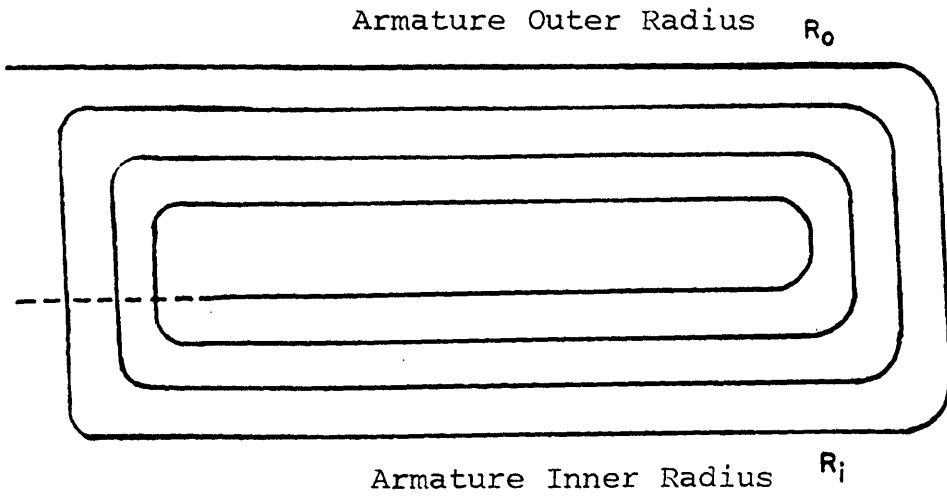
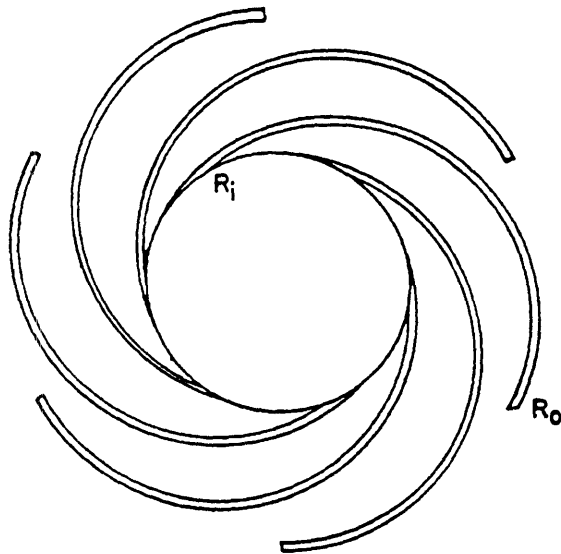


Figure 1.13: Modified Gramme-Ring Winding



a) Half Pancake



b) Axial View of Pancake Layout

Figure 1.14: Spiral Pancake Winding

between pancake coils. Unfortunately, cooling through four layers of high voltage insulation, especially in this geometry, is an inefficient process.<sup>34</sup>

The last design, called the "Coaxial Turn" winding, was also invented by Aicholzer<sup>35</sup>. The radical design consists of six concentric tubes, connected in series by specially design end connectors. This Wye-like connected machine requires much less insulation since the machine terminals are brought out at the inner and outer radii. Since this revolutionary design is impractical to manufacture on a commercial scale, we will not detail it further.

### **1.5 Introduction to MIT Designs**

Based on the various types of air-gap armature windings outlined in the previous section, the MIT group has constructed several different armature windings during the life of this project. A 60 kVA model, which was constructed in 1979, demonstrated the ability to design, construct and test an "advanced concept" armature. The design, which incorporated a helically wound delta connected limited voltage gradient armature, helped develop important construction techniques. For example, the thin Roebel transposed magnet wire used in the conductor bars had to be edge brazed to a flat plate and bar group moldings had to be made. In addition, the use of a silicone transformer fluid (Dow Corning #561) as an insulating and cooling medium was demonstrated. The theoretical values computed for inductances, synchronous reactance, armature resistance, temperature rise in the armature conductors and field current to achieve no-load voltage compared favorably to the experimental data. Unfortunately this apparatus was unsuitable to test the major insulation's performance and to test the structural integrity of the armature.<sup>36</sup>

A 10 MVA delta connected, helically wound limited voltage gradient armature winding, resembling the 60 kVA experiment, was subsequently constructed to the specifications listed in **Table 1.3**.

**Table 1.3:** MIT 10 MVA Superconducting Generator High Voltage Armature Design Specifications

Rating:	10 MVA
Phase Voltage:	13.8 kV
Phase Current:	245 A
Number of Phases:	3
Number of Circuits:	2
Arrangement:	Parallel
Turns per phase:	204
Connection:	Delta
Number of armature bars:	2448
Conductors in each bar:	24
Elementary conductors:	round copper magnet wire, AWG #21 Roebel transposed with pitch length of 2"

Unfortunately, this armature suffered from a turn-to-turn flashover before any significant tests could be conducted.

The goal of this thesis is to design a new armature for the 10 MVA machine while pioneering new concepts and techniques applicable in the construction of a commercially viable generator. Hence, the specifications and a detailed layout of this armature will be generated in the next chapter.

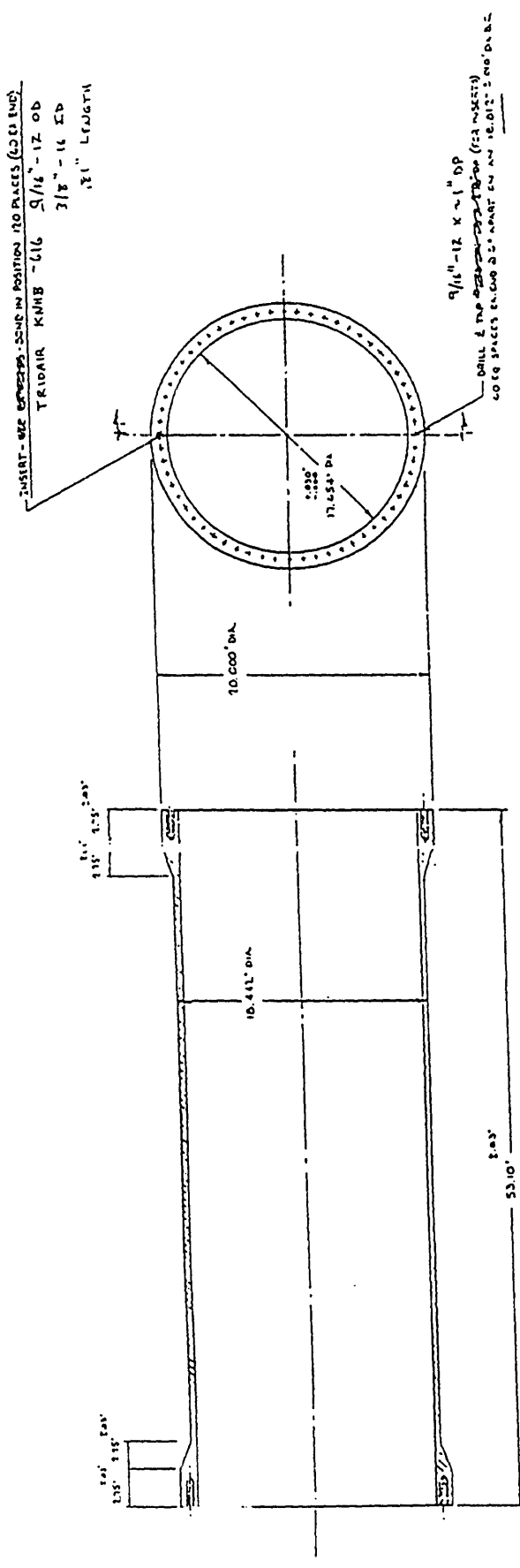


## CHAPTER 2 ARMATURE DESIGN

### 2.1 Design Specifications

The new 10 MVA armature winding, which will be designed to replace the damaged armature, must fit between the existing stator bore tube sketched in **Figure 2.1** and the magnetically shielded generator casing. The winding itself will consist of three helically wound Wye connected phases, each composed of two phase belts (circuits) mounted in series. By mounting the two phase belts in series, rather than in parallel, the generator can produce a higher terminal voltage so that lower ratio step-up transformers may be used. In addition, this arrangement eliminates circulating currents caused by uneven current flow through parallel circuits. A diagram of the circuit topology is depicted in **Figure 2.2**.

Despite the apparent disadvantage in replacing an advanced design limited voltage gradient armature with a simpler design, the Wye connected machine avoids some of the drawbacks and mitigates the risks involved in high voltage armatures. An obvious advantage inherent in Wye connected armature windings is the reduction in the machine internal and terminal voltages. A lower internal voltage not only reduces the chances of electrical flashovers but also reduces the need for the thick cylindrical insulation layer present in the high voltage delta connected armatures. Hence, it may be possible to increase the space factor of the armature and gain additional generating power. Furthermore, large conventional generators still use traditional Wye designs as they minimize circulating currents and reduce third harmonic losses. The two major drawbacks of this simpler design, when compared to the old 10 MVA described in the last section, are the need for



- NOTES:
1. MATERIAL - FIL WOUND GLASS/EPoxy.
  2. FOR MANDREL - SEE SET 31.5.
  3. FOR MFS SPEC. SEE MS-1011
  4. MACHINE FINISH ONLY, NO VARNISH.

CORRECTED COPY (A) B.117

PERMALL, INC.	
MT. PLEASANT, PENNSYLVANIA	
TUBE	
DATE	12-1-57
DESIGN	F-F-9357
REVISION	1

Figure 2.1: Inner Bore Tube Dimensions as Built

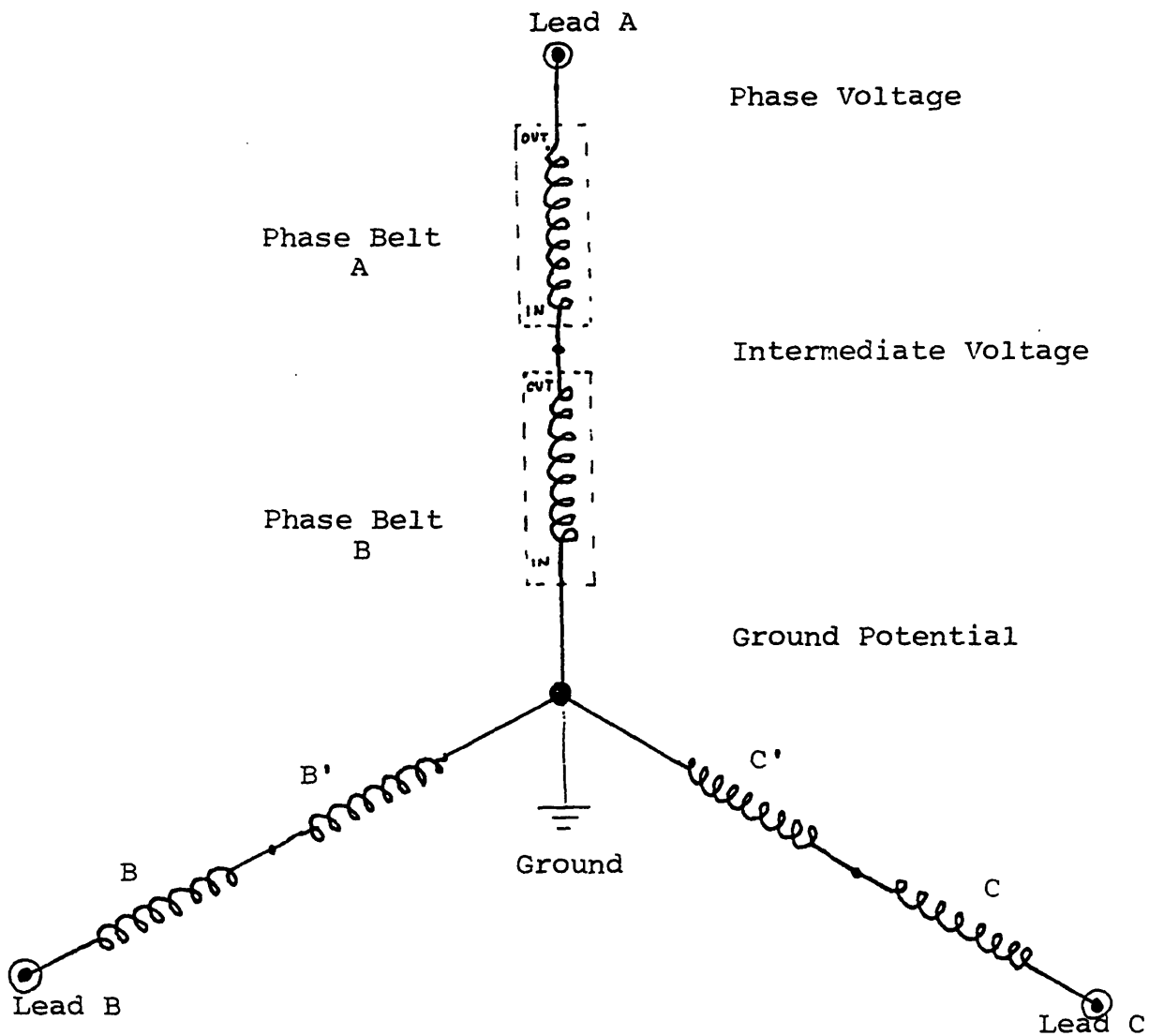


Figure 2.2: Circuit Topology of the Mit 10-MVA  
Wye Connected Armature Winding

Note: This generator design is based on a Wye connected, 2 serially mounted phase belts, 3 phase layout. Each phase belt is composed of 17 turns.

large step-up transformers and the much higher  $I^2R$  losses. An example of a typical connection to a transformer block is depicted in **Figure 2.3**. Typically, a generator of this type is connected to the delta side of the transformer and the transformer's Wye side is impedance grounded.

A qualitative selection of the conductor to be used in the bars forming the armature winding may be made next. The conductor will be comprised of a rectangular compacted Litz, which refers to a wire consisting of a number of separately insulated strands, or bundles of strands, which are bunched together such that each strand tends to occupy all possible positions throughout the cross section of the conductor. This Roebel transposition results in equalizing the flux linkages, and hence the reactances of the individual strands, thereby causing a uniform current distribution throughout the conductor. A sketch of a rectangular compacted (type 8) Litz wire, which has been developed and patented by New England Electric Wire Corporation, is given in **Figure 2.4**.

Since the primary benefit of a Litz conductor is the reduction of AC losses, the first consideration in any such design is the operating frequency. Since higher operating frequencies require a smaller diameter wire in order to maintain eddy current losses at a tolerable level, it is used to determine the maximum diameter of the individual magnet (film insulated) wires. These eddy currents tend to travel at the surface of conductors and thus reduce the effective current-carrying cross section. Therefore, the ratio of AC to DC resistance, which should ideally be near unity, and which is proportional to

$$x = 0.271 \times D \sqrt{F}$$
 Where  $D$  is the magnet wire diameter in mills,  $F$  is the operating frequency in Hz and  $x$  must be no larger than 0.25.

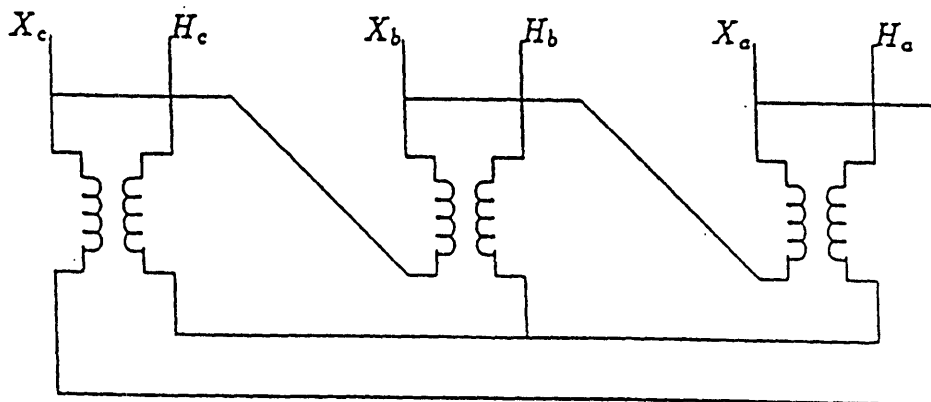
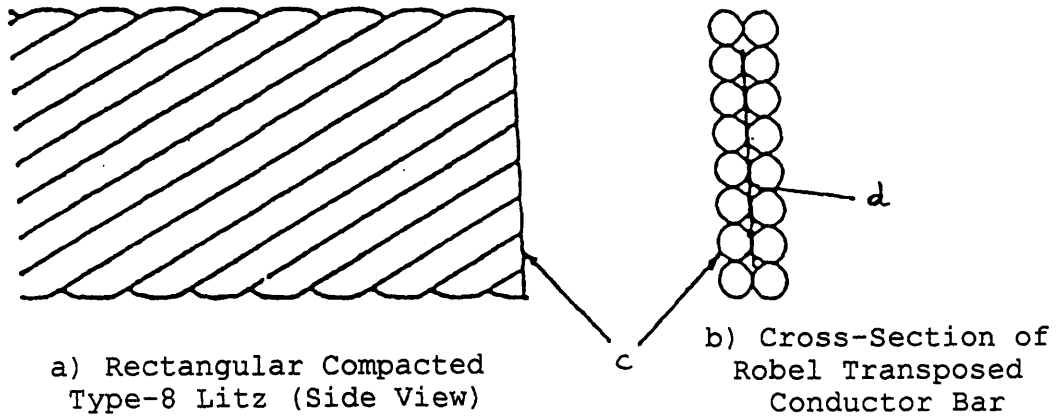


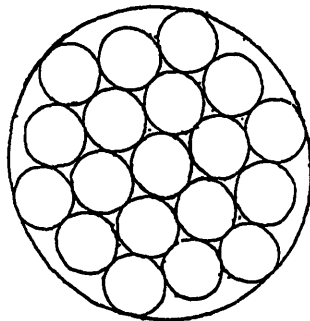
Figure 2.3: Delta-Wye Transformer Connection

Note: The Wye Connected Armature Winding is Typically Mounted to the Delta Side of the Transformer.

Figure 2.4: Conductor Used in Armature Bars



c) Bundle of 19 Conductors



d) Cross-Section of 19 Conductor Bundle

is a good indication of the effects of eddy currents. Operating at 60 Hz, the armature of the superconducting generator will be designed with AWG #20 or #21 copper magnet wire.<sup>37</sup> This wire must be film insulated with a material that has an excellent film flexibility and abrasion resistance, has good electrical properties, can operate at moderate to high temperatures and can be solderable.

**Table 2.1:** MIT 10 MVA Superconducting Generator Armature Design Specifications

Rating:	10 MVA
Number of Phases:	3
Number of Circuits:	2
Arrangement:	Serial
Connection:	Wye
Operating frequency:	60 Hz
Armature bore tube (in)	
Inner radius:	9.221
Outer radius:	13.372
Overall length:	53.1
Active length:	43.12
Finish tube thickness:	0.450 in
Elementary conductors:	round copper magnet wire, AWG #21 Roebel transposed, Type 8 rectangular compacted Litz.

Table 2.1 contains a recapitulation of our initial design specifications for this armature winding. In the following sections, the physical layout of the machine will be exposed in qualitative terms before a thorough quantitative design analysis.

## **2.2 Layout Detail**

A helical armature winding physically consists of layers of insulated conductor bars which twist 180° while traveling along the length of the cylindrical armature. Half of the layers of the armature are composed exclusively of right handed bars, while the other half is formed by left handed bars as shown in Figure 2.5. In order to link the rotor flux, a right handed





bar of one layer must be connected in series to a left handed bar of another layer so as to form a complete loop. Consequently, this type of winding must be composed of an even number of layers. The number of bar layers depends on the number of turns required to achieve the machine terminal voltage, the physical size of the insulated bar, the armature's circumferential length and the desired machine reactance. In order to maximize the present generator's space factor, only two layers of bars shall be used.

The helical winding, which resembles the traditional wave design, eliminates the need for circumferential end windings that occupy a lot of space at the ends of conventional armatures. Instead, the end connections in helical armatures consist of flat copper tabs, located at the ends of the machine, which connect the appropriate layers of bars. This design produces a cylindrically shaped monolithic armature with a constant radius, which could be encased in a non-metallic support tube.

However, unlike conventional iron core armatures that leave space between the bars in the active (straight) section, the helical armature must pack the bars together as closely as possible in the active region (where they are helically spiraling) in order to achieve the highest efficiency, terminal voltage and power density. Since the circumferential length available for the insulated bars is the same in the active section as in the end region, it is possible to gain some additional space for the end connections by straightening the ends of the bars. Hence, the bars used in this air-gap winding are composed of three sections: a central "helical portion" which is situated in the active section of the machine, a straight "end region" where the end connectors may be attached and an "end turn" region which serves as a transition between the two aforementioned sections. **Picture 2.1**, which



Picture 2.1: Close-up of the End of the 10 MVA Limited  
Voltage Gradient Armature

(Note the three sections of the bar)

represents a close-up of the ends of the 10 MVA limited voltage gradient armature, clearly illustrates these three conductor bar sections.

Being that the radius of the armature is large compared to the width,  $W$ , of the insulated bar, the circumferential distance,  $D$ , occupied by the bar is:

$$D_{\text{helical}} = \frac{W}{\cos\theta} \text{ in the helical section, and } D_{\text{end}} = W \text{ for the straight end section,}$$

as shown in **Figure 2.6**. Thus, the space gained by straightening the bars is proportional to the cosine of the helix angle. From the data supplied in Table 2.1,  $\theta$  is approximately:

$$\theta = \arctan\left(\frac{\text{circumference}}{\text{length}}\right) = \arctan\left(\frac{2\pi \times 9.221}{53.1}\right) = 47 \text{ degrees. Therefore, the space}$$

reduction factor is about 67%.

The armature itself is composed of a total of six individual phase belts (circuits) which are distributed at the "lead" end of the stator, as shown in **Figure 2.7**. Since each complete turn is composed of an upper and a lower bar, the upper bars of one phase belt complement the lower bars of the other phase belt of the same phase, at the end of the armature. In addition, in order for the two circuits to deliver the same induced voltage at the same phase angle, the two complementary phase belts must have the same number of turns and be located diametrically opposite to each other (with respect to the cylindrical stator's long axis) throughout the machine. For example, if the two phase belts comprising the first of the machine's three phases are labeled "A" and "A'", the bars of "A" pass above the bars of "A'" in a location half way across the armature, while the converse happens at the diametrically opposite location. Because of the requirement to complement upper and lower bars, helical armatures must be designed with an even number of phase belts within each phase. Furthermore, because of the need

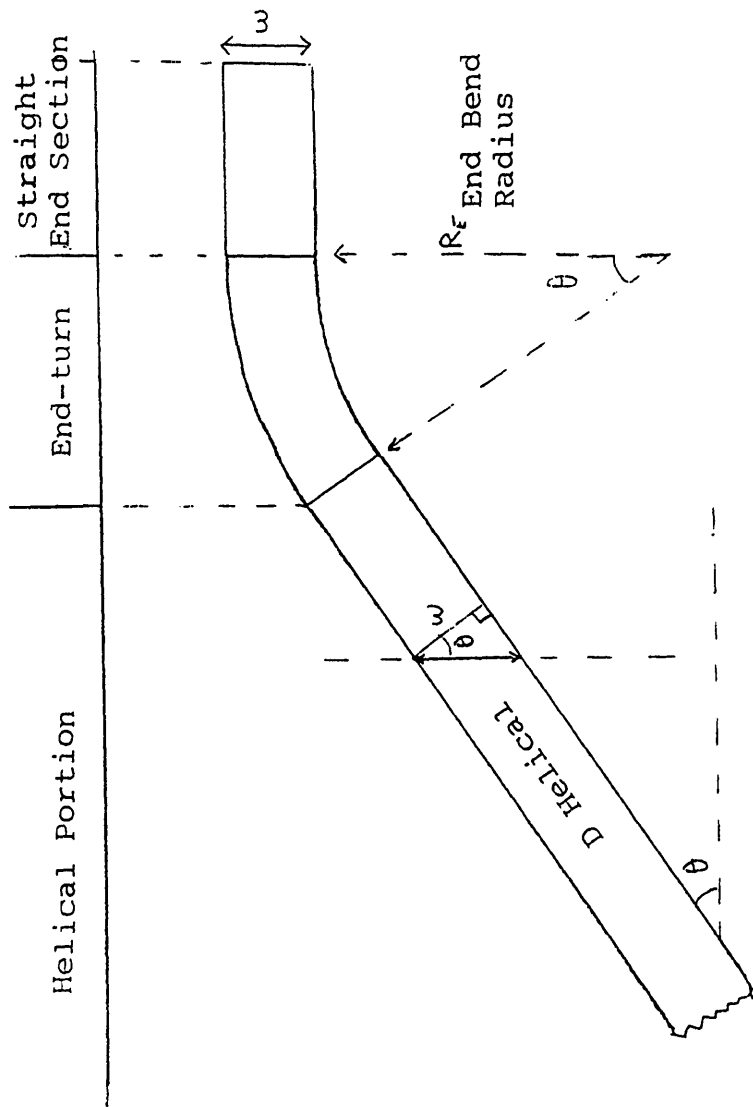


Figure 2.6: End-Section of the Armature Bar

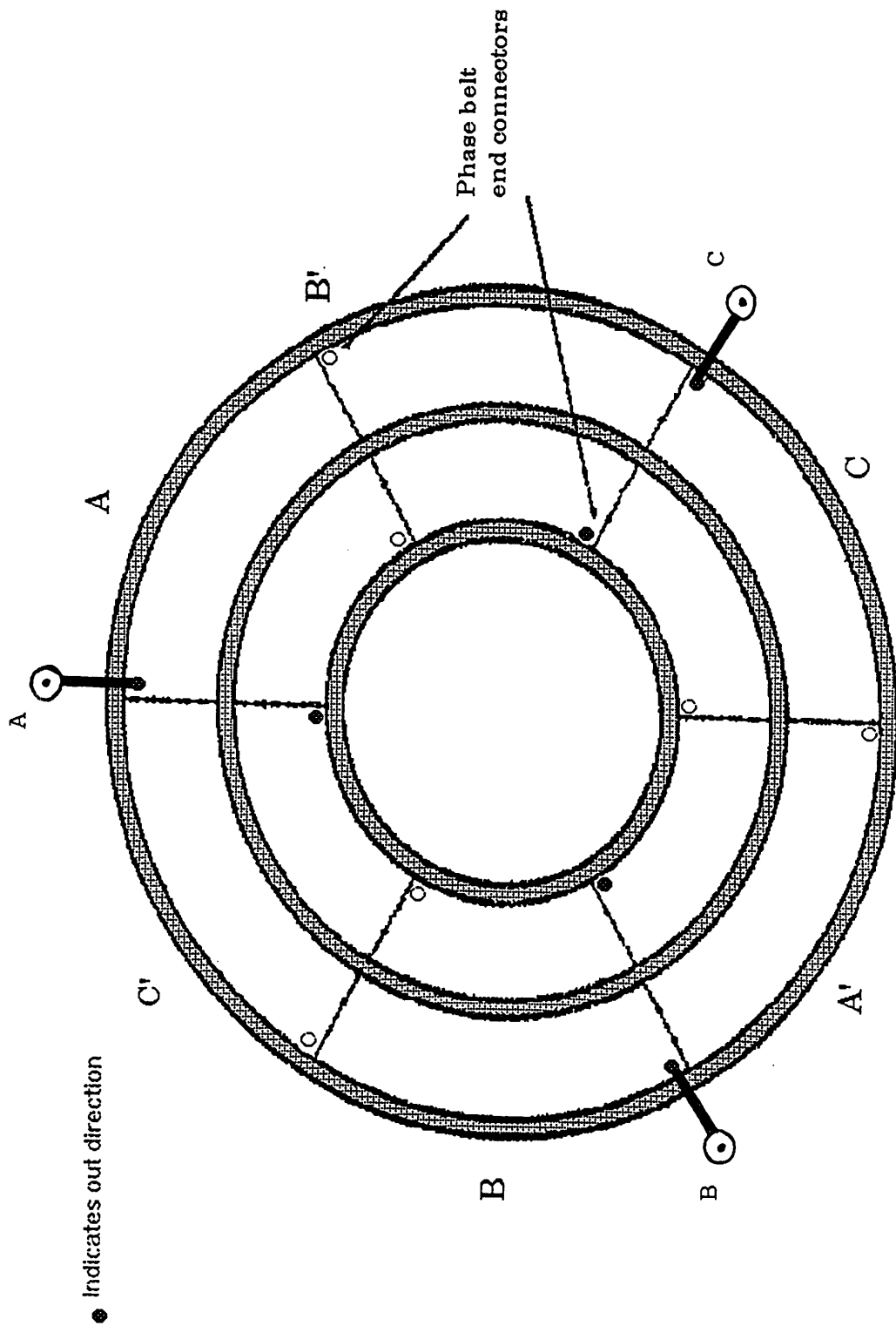


Figure 2.7: Distribution of the Phase Belts at the Lead Ends


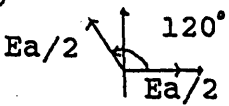

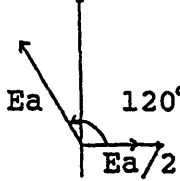
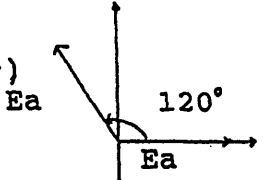
to electrically combine the two circuits, the two phase belts of a given phase are placed diametrically opposite to each other. Breaking down each phase of the generator into two individual phase belts offers yet another advantage. The current flowing in the alternating left-handed and right-handed helically spiraling bars in a phase belt possesses, in addition to the axial component, a small net azimuthal component due to the magnetic field's dependence on radial distance. This could create an axial magnetic moment, which would lead to an uneven loading of the rotor, if it were not balanced by the other phase belt that has been wound in the opposite direction and is situated on the other side of the armature.<sup>38</sup>

Having described the various geometrical aspects involved with helical windings in order to arrive at the armature's physical layout, we will now concentrate on the electrical and cryogenic issues. Since the present Wye connected generator must be designed with three diametrically opposed and serially mounted pairs of phase belts, only two possible phase belt arrangements may exist. As depicted in Figure 2.2, we have adopted a convention where primed phase belts are grounded at one end and connected to the non-primed belt of the same phase at the other end. The voltage differences that can exist at the interface between any one of five combinations two phase belts, taking account of phase differences, are reported in **Table 2.2**.

Hence, the optimum deployment for the phase belts is an alternating sequence of primed and non-primed belts, such as: A, B', C, A', B, C' and arranged as in **Figure 2.8**. The only other possible arrangement, which would consist of keeping the primed and non-primed belts contiguous to each other (i.e. A, B, C, A', B', C'), has been rejected because full line-to-line voltages would be incurred between the phase belt terminals. By combining

**TABLE 2.2A**

**VOLTAGE GRADIENTS OCCURRING AT PHASE BELT INTERFACES**

Type of Interface	Phasors	Calculations	Results in $E_a$
Medium to Ground (*)	$E_a/2$ 	$\vec{V}_1 = \begin{vmatrix} E_a/2 \\ 0 \end{vmatrix}$	0.5 (Best)
Medium to Medium		$\vec{V}_1 = \begin{vmatrix} E_a/2 \\ 0 \end{vmatrix}$ $\vec{V}_2 = \begin{vmatrix} -E_a/4 \\ E_a\sqrt{3}/4 \end{vmatrix}$ $\vec{V}_1 - \vec{V}_2 = \begin{vmatrix} 3E_a/4 \\ -E_a\sqrt{3}/4 \end{vmatrix}$ $\ \vec{V}_1 - \vec{V}_2\  = E_a\sqrt{3}/2$	0.866
High to Ground	$E_a$ 	$\vec{V}_1 = \begin{vmatrix} E_a \\ 0 \end{vmatrix}$	1.0
High to Medium (*)		$\vec{V}_1 = \begin{vmatrix} E_a/2 \\ 0 \end{vmatrix}$ $\vec{V}_2 = \begin{vmatrix} -E_a/2 \\ E_a\sqrt{3}/2 \end{vmatrix}$ $\vec{V}_1 - \vec{V}_2 = \begin{vmatrix} E_a \\ -\sqrt{3}/2 \end{vmatrix}$ $\ \vec{V}_1 - \vec{V}_2\  = E_a\sqrt{7}/2$	1.323
High to High (~)		$\vec{V}_1 = \begin{vmatrix} E_a \\ 0 \end{vmatrix}$ $\vec{V}_2 = \begin{vmatrix} -E_a/2 \\ E_a\sqrt{3}/2 \end{vmatrix}$ $\vec{V}_1 - \vec{V}_2 = \begin{vmatrix} 3E_a/2 \\ E_a\sqrt{3}/2 \end{vmatrix}$ $\ \vec{V}_1 - \vec{V}_2\  = E_a\sqrt{3}$	1.732 (Worst)

NOTE:  $E_a$  is the machine phase-voltage.  
 (\*) Indicates the types of interfaces that occur in our wye armature design  
 (~) the high-to-high interface, which results in full line to line voltage, does not appear in our design due to the alternation of primed and non-primed phase belts.

	Medium	High
To Ground	0.5	1
To Medium	0.866	1.323
To High		1.732

Table 2.2B: Voltage Gradients Occurring at Phase Belt Interfaces



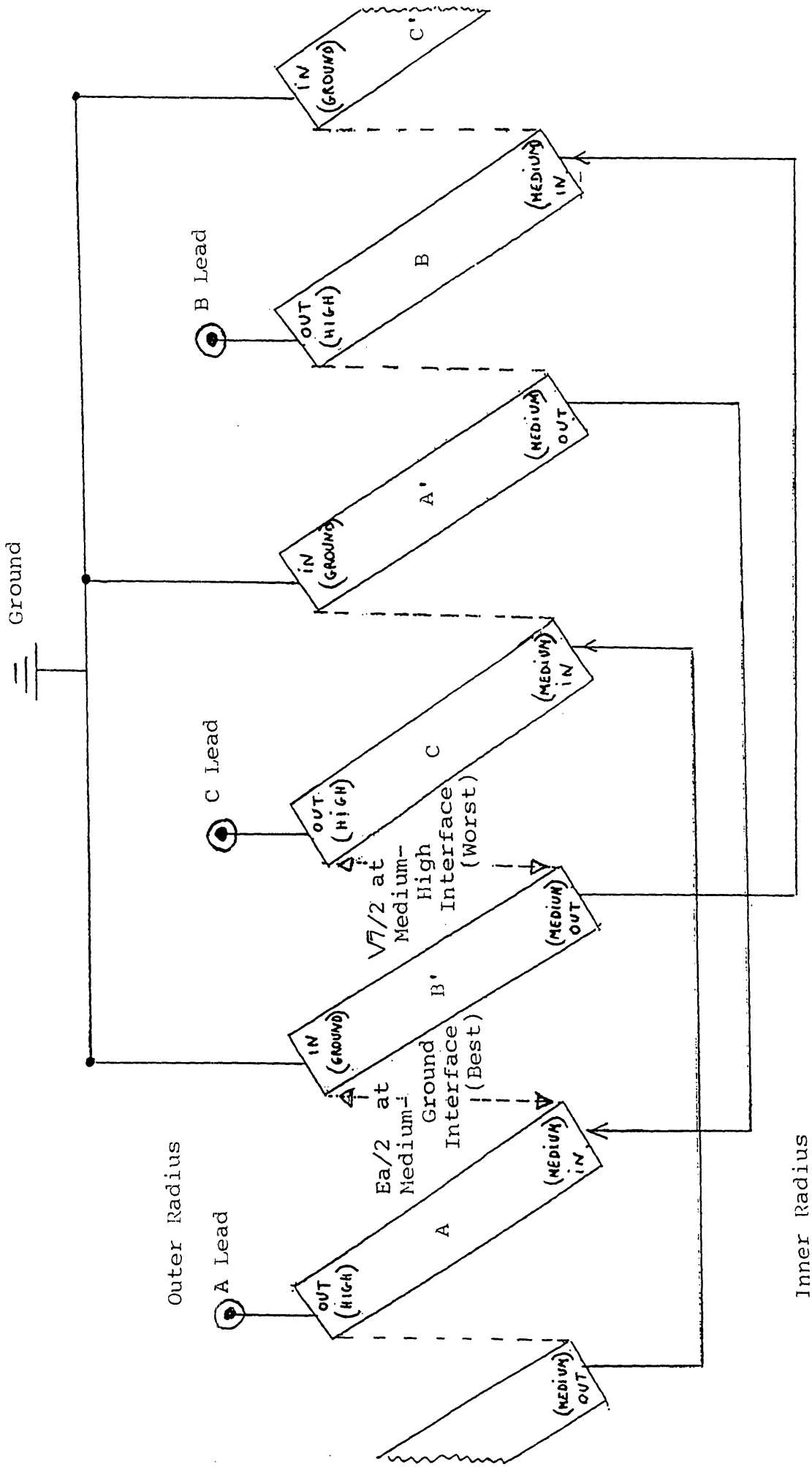


Figure 2.8: Layout of Phase Belts and End Connectors

Note: Direction convention as shown in Figure 2.2

the aforementioned design specifications, a model of the circuit layout is obtained and displayed in **Figure 2.9**.

The insulation requirements for helical armatures in general, can be separated into seven categories.<sup>39</sup> The first requirement involves insulating the basic conductors that compose the armature bars. Although these thin copper wires are roughly at the same potential at any given place, they must be individually insulated in order to prevent the formation of eddy currents. Physically, this insulation typically consists of a thin layer of film or of fiber. The second requirement consists of insulating the bars themselves from each other. Hence, at minimum, the bar insulation must be designed to withstand one turn voltage. However, as described above, azimuthally adjacent bars of two different phase belts or radially adjacent bars of opposite helix direction may be at vastly different electrical potentials, especially in non-limited voltage gradient designs.

Therefore, in complex high voltage multi-layer helical armatures, two more insulation requirements can exist: a set of thin minor insulating cylindrical shells and a single thick major insulating cylindrical shell. The minor layers, which are placed between layers of bars having the same helix direction, must be designed for slightly more than one turn voltage. On the other hand, the single major layer is located between the layers of bars of opposing helical winding direction and must be able to insulate the full line-to-line voltage.

The fifth type of insulation that is commonly used in helical armatures is called the *ground wall* insulation. Since, during normal operation, the generator and the stator's support tube can be assumed to be at ground potential it is apparent that the simple bar to bar insulation, designed for one turn voltage, is inadequate. The ground wall insulation layers consist of two

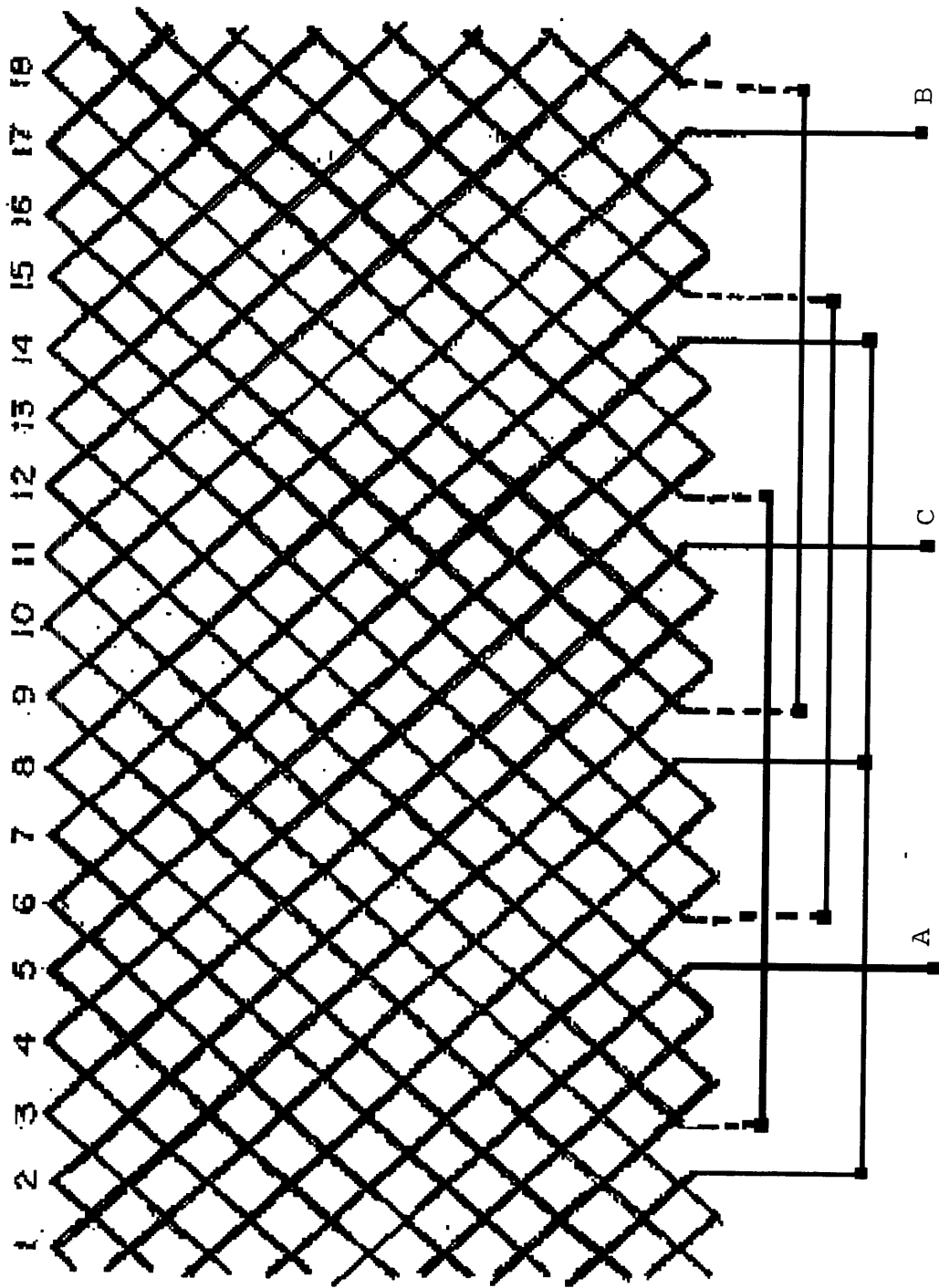


Figure 2.9: Circuit Layout for the 10 MVA Superconducting Generator Armature

cylindrical shells which envelop the conducting bars. Since both the inner and outer shells must only be rated line-to-ground, they are slightly thinner than the major insulating layer. **Figure 2.10** illustrates the aforementioned insulation components for the case of the high voltage (13.8 kV) 10 MVA armature winding developed at MIT.

After much consideration of the aforementioned insulating options, it has been determined that the optimal insulation scheme for the MIT 10 MVA armature will solely consist of a thick bar insulation rated for line-to-ground insulation. This simpler scheme offers a number of benefits. First, the need for ground wall insulation is eliminated as each individual bar is already insulated line-to-ground. Second, the thick major insulation layer is no longer necessary since the two layers of bars are mutually isolated by twice the line-to-ground voltage. This combination of insulation is slightly superior to line-to-line shielding. Thirdly, by designing the entire armature with only one pair of bar layers, the need for minor layers is also eliminated. Hence, this conservative design offers an armature with a simple layout, a higher space factor, an ease of manufacturing and a lower production cost.

The remaining two insulation requirements, which will be implemented in our design, concern the end connections and the coolant. The end connections, which must be insulated from each other, require only turn-to-turn insulation, when they are located within a phase belt. However, as discussed above, the end connections which are adjacent to end connections belonging to another phase belt must be insulated for phase-to-ground voltage. This "boundary" between adjacent phase belts is one of the areas of highest electrical stress in this armature design.

The heat generated within the conductors is mostly due to Joule effect losses and must be eliminated in an efficient manner. Although individual

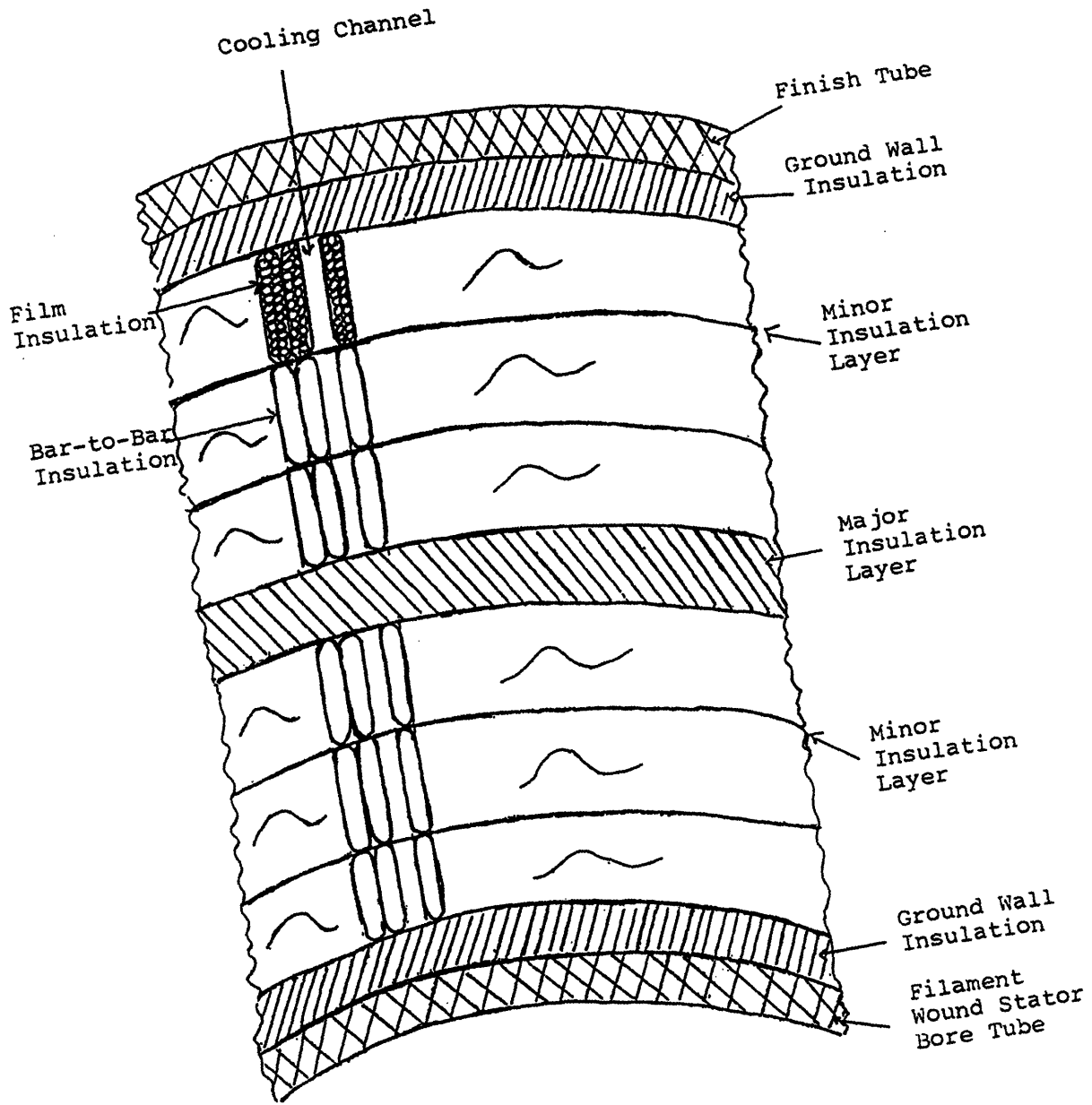


Figure 2.10: Insulation Systems Compatible with Air-Gap Armatures

conductor cooling, often provided by intra-bar conductive cooling channels, is possible in certain types of machines such as large conventional armatures, they are impractical for our generator. In our design, cooling channels will be placed directly above and below each insulated bar and will travel parallel to the axis of the armature. Since the two radially separated bars are each insulated line-to-ground, the electric field in the region between the two layers is negligible and, therefore, our cooling fluid need not be a good dielectric capable of withstanding significant electrical stresses.

Thus, in this chapter we have described qualitatively, yet thoroughly, the geometrical, electrical and cryogenic layout of the 10 MVA helical armature and have arrived at the stator layout displayed in **Figure 2.11**. In the next sections we shall build upon this "general description of the layout" and obtain, from design calculations, a detailed schematic of the stator unit.

### **2.3 Electrical Specifications**

In this section, we will supplement the armature's basic design specifications which were described in part 2.1, by adding the electrical design specifications. By using the layout data contained in the preceding section, we shall compile a design specification spreadsheet.

One of the most important specifications of the armature is the desired line-to-line voltage. Ideally, this voltage must be as high as possible, so as to minimize losses and reduce the size of the transformer, and must be one that is widely used commercially. On the basis of the data contained in **Table 2.3**, which lists the most widely used voltages in the United States, it was determined through a series of compromises that the most feasible armature design would deliver a rated line-to-line voltage of: 4,000 V rms. As demonstrated in **Calculation 2.1**, the line-to-ground voltage, otherwise

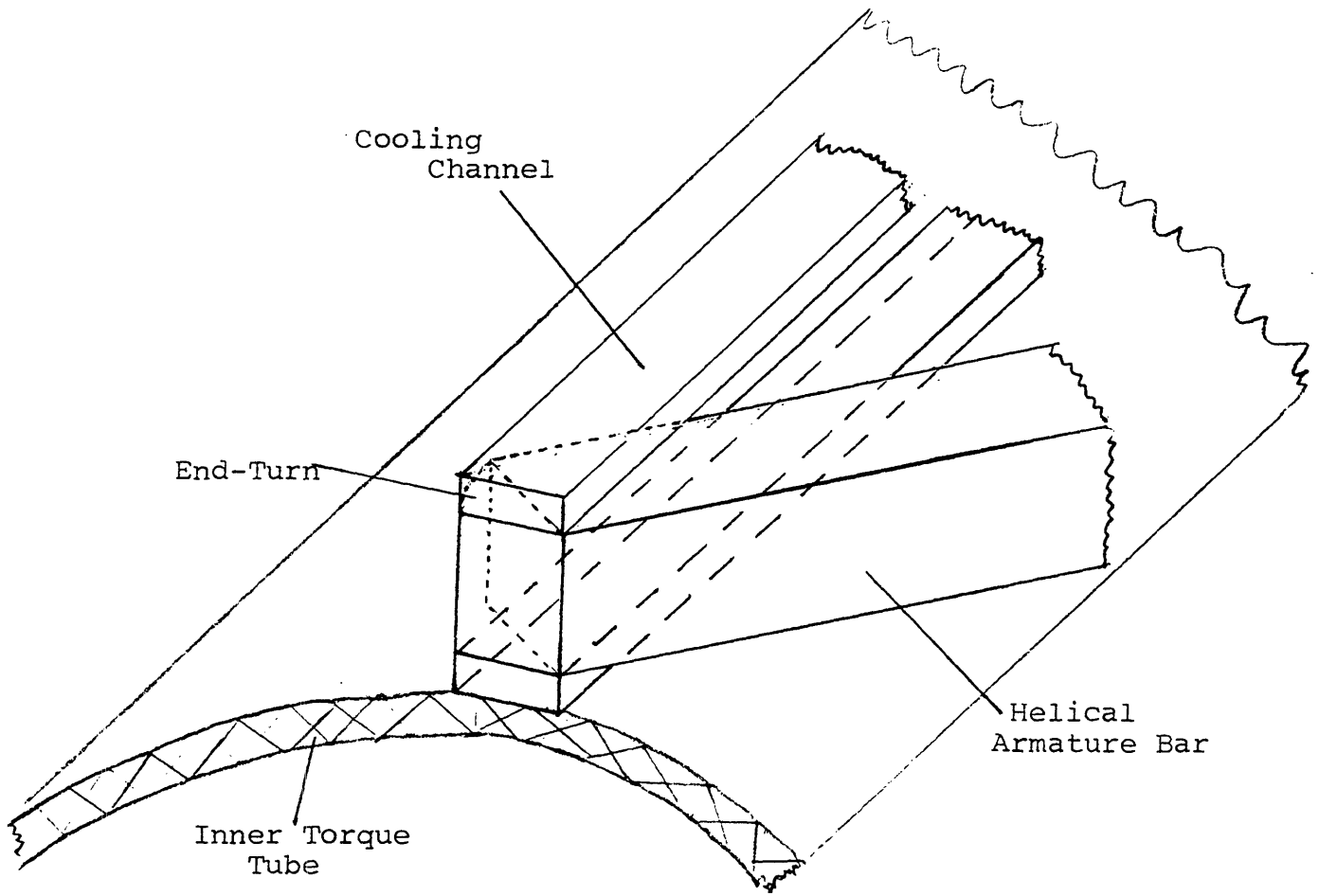


Figure 2.11: Rendering of the MIT 10-MVA  
Wye Connected Armature

Note: Not drawn to scale.

Table 2.3:

Standard Nominal System Voltages and Voltages Ranges

Voltage Class	Nominal System Voltage (Note a)			Voltage Range A (Note b)			Voltage Range B (Note b)		
	Two-wire	Three-wire	Four-wire	Utilization Voltage	Service Voltage	Utilization and Service Voltage (Note c)	Utilization Voltage	Service Voltage	Utilization and Service Voltage
Low Voltage (Note 1)	Single-Phase Systems								
	120	120/240		110 110/220	114 114/228	126 126/252	106 106/212	110 110/220	127 127/254
	Three-Phase Systems								
			208Y/120 (Note d) 240/120	191Y/110 220/110	197Y/114 228/114	218Y/126 252/126	184Y/106 (Note 2) 212/106	191Y/110 (Note 2) 220/110	220Y/127 254/127
		240	480Y/277	440Y/254 440	456Y/263 456	504Y/291 504	428Y/245 424	440Y/254 440	508Y/293 508
		480 600 (Note e)		550	570	630 (Note e)	530	550	635 (Note e)
	Medium Voltage	2400	4160Y/2400	2160 3740Y/2160	2340 4050Y/2340	2520 4370/2520	2080 3600/2080	2280 3950Y/2280	2540 4400Y/2540
		4160		3740	4050	4370	3600	3950	4400
		4800		4320	4680	5040	4160	4560	5080
		6900		6210	6730	7240	5940	6560	7260
		8320Y/4800 12 000Y/6930 12 470Y/7200 13 200Y/7620 13 800Y/7970		8110Y/4680 11 700Y/6760 (Note f) 12 160Y/7020 12 870Y/7430 13 460Y/7770	8730Y/5040 12 600Y/7270 (Note f) 13 090Y/7560 13 860Y/8000 14 490Y/8370		7900Y/4560 11 400Y/6580 (Note f) 11 850Y/6840 12 604Y/7240 13 110Y/7570	8800Y/5080 12 700Y/7330 (Note f) 13 200Y/7820 13 970Y/8070 14 520Y/8380	
13 800			12 420	13 460	14 490	11 880	13 110	14 520	
		20 780Y/12 000 22 860Y/13 200		20 260Y/11 700 22 290Y/12 870 (Note f) 22 430	21 820Y/12 600 24 000Y/13 860 (Note f) 24 150		19 740Y/11 400 21 720Y/12 540 (Note f) 21 850	22 000Y/12 700 24 200Y/13 970 (Note f) 24 340	
23 000			24 940Y/14 400 34 600Y/19 920	24 320Y/14 040 33 640Y/19 420	26 190Y/15 120 36 230Y/20 920		23 690Y/13 680 32 780Y/18 930	26 400Y/15 240 36 510Y/21 080	
34 600				33 640	36 230		32 780	36 510	
High Voltage		46 000 69 000		Maximum Voltage (Note g) 48 300 72 500		NOTES: (1) Minimum utilization voltages for 120-600 V circuits not supplying lighting loads are as follows:			
	115 000 138 000 161 000 230 000		121 000 145 000 169 000 242 000		Nominal System Voltage	Range A	Range B		
	(Note h) 345 000 500 000 765 000		362 000 550 000 800 000		120	108	104		
	1 100 000		1 200 000		120/240	108/216	104/208		
					(Note 2) 208Y/120	187Y/108	180Y/104		

NOTE: Notes (a) through (h) integrally apply to this table.

(a) Three-phase three-wire systems are systems in which only the three-phase conductors are carried out from the source for connection of loads. The source may be derived from any type of three-phase transformer connection, grounded or ungrounded. Three-phase four-wire systems are systems in which a grounded neutral conductor is also carried out from the source for connection of loads. Four-wire systems in Table 15 are designated by the phase-to-phase voltage, followed by the letter Y (except for the 240/120 V delta system), a slant line, and the phase-to-neutral voltage. Single-phase services and loads may be supplied from either single-phase or three-phase systems. The principal transformer connections that are used to supply single-phase and three-phase systems are illustrated in Fig 3.

(b) The voltage ranges in this table are illustrated in ANSI C84.1-1977 [2], Appendix B.

(c) For 120-600 V nominal systems, voltages in this column are maximum service voltages. Maximum utilization voltages would not be expected to exceed 125 V for the nominal system voltage of 120, nor

appropriate multiples thereof for other nominal system voltages through 600 V.

(d) A modification of this three-phase four-wire system is available as a 120/208Y V service for single-phase, three-wire, open-wye applications.

(e) Certain kinds of control and protective equipment presently available have a maximum voltage limit of 600 V; the manufacturer or power supplier or both should be consulted to assure proper application.

(f) Utilization equipment does not generally operate directly at these voltages. For equipment supplied through transformers, refer to limits for nominal systems voltage of transformer output.

(g) For these systems Range A and Range B limits are not shown because, where they are used as service voltages, the operating voltage level on the user's system is normally adjusted by means of voltage regulation to suit their requirements.

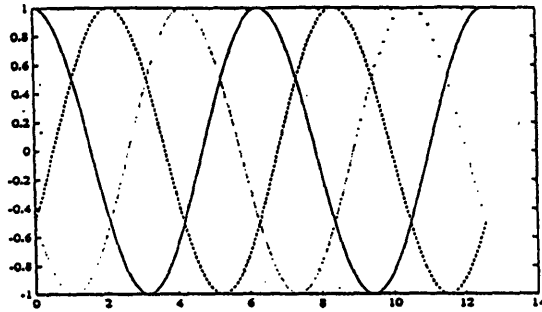
(h) Information from ANSI C92.2-1978 [3]. Nominal voltages above 230 000 V are not standardized. The nominal voltages listed are typically used with the associated preferred standard maximum voltages.



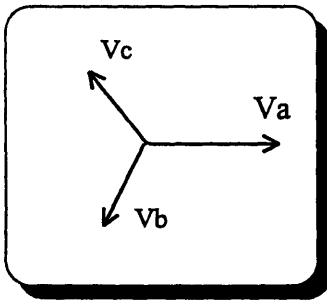
## CALCULATION 2.1

Relationship between line-to-line voltage and line-to-ground (or phase) voltage for a three phase machine.

A three phase machine delivers its voltage 120 degrees out of phase, as illustrated in the time domain below.



The instantaneous voltages may be visualized by taking the projections of the vectors in the phasor diagram, drawn below, onto the horizontal axis.



The three phase voltages are:

$$\begin{aligned} V_a &= V \cos(\omega t) = \text{Re}[V \cdot e^{j\omega t}] \\ V_b &= V \cos(\omega t - \frac{2\pi}{3}) = \text{Re}\left[V \cdot e^{j(\omega t - \frac{2\pi}{3})}\right] \\ V_c &= V \cos(\omega t + \frac{2\pi}{3}) = \text{Re}\left[V \cdot e^{j(\omega t + \frac{2\pi}{3})}\right] \end{aligned} \quad (1.1.1)$$

A balanced three-phase set of voltages has a well defined set of line-to-line voltages:

$$\begin{aligned} V_{ab} &= V_a - V_b = \text{Re}\left[V(1 - e^{-j\frac{2\pi}{3}})e^{j\omega t}\right] = \text{Re}\left[\sqrt{3} V e^{j\frac{\pi}{6}} e^{j\omega t}\right] \\ V_{bc} &= V_b - V_c = \text{Re}\left[V(e^{-j\frac{2\pi}{3}} - e^{j\frac{2\pi}{3}})e^{j\omega t}\right] = \text{Re}\left[\sqrt{3} V e^{-j\frac{\pi}{2}} e^{j\omega t}\right] \\ V_{ca} &= V_c - V_a = \text{Re}\left[V(e^{j\frac{2\pi}{3}} - 1)e^{j\omega t}\right] = \text{Re}\left[\sqrt{3} V e^{j\frac{5\pi}{6}} e^{j\omega t}\right] \end{aligned} \quad (1.1.2)$$

Hence, it is clear that the line-to-line voltage set has a magnitude that is larger than the line-to-ground (or phase) voltage by a factor of  $\sqrt{3}$ . Thus:

$$V_L = \sqrt{3} V_\phi \quad (1.2.1)$$

Furthermore, the line-to-line voltages are phase shifted by 30 degrees ahead of the line-to-neutral voltages. (1.2.2)

known as the *phase voltage*, is related to the line-to-line voltage by:

$V_{l-l} = \frac{V_{l-l}}{\sqrt{3}}$  for a three phase machine. Thus the phase voltage is: 2,300 V

rms, which corresponds to a voltage amplitude of:  $V_{\max} = V_{\text{rms}} \cdot \sqrt{2} = 3,253 \text{ V}$ .

Using the armature design specifications listed in Table 2.1, the flux linkage of a single turn is calculated and the induced electromotive force is determined in **Calculation 2.2**. Although this calculation oversimplifies reality by assuming that the average magnetic field within the stator is independent in the radial (r) and axial (z) components but depends only on the azimuthal ( $\theta$ ) coordinate, it is still correct for order of magnitude calculations. Since the path of the bars in this armature is exactly the same as that in the high voltage 10 MVA winding, the result of the full three dimensional analysis performed by Umans<sup>40</sup> may be used to scale  $B_0$ , the root-mean-square value of the magnetic field within the stator, in such a way as to find meaningful results. By incorporating the results of the Umans analysis, which has been validated by experiment, we find that the phase voltage per turn is 67.65 V/turn rms. Hence, each one of the three phases of the machine must be composed of  $n=2300/67.65 = \underline{34 \text{ turns}}$ . Since each phase is composed of two phase belts mounted in series, the belts themselves will consist of 17 turns and will be physically comprised of 34 half-turn bars. Hence, the present armature winding will be manufactured with a total of  $3 * 2 * 34 = \underline{204 \text{ half turn bars}}$ .

Using the formulas derived in **Calculation 2.3**, which relate the line and phase voltages and currents for delta and Wye connected machines, the terminal current, which is the same as the bar current since the two circuits are in series, may be calculated. As computed at the bottom of Calculation 2.3, the bar current is 1,445 Amperes at the rated power.

## CALCULATION 2.2

### I. Calculating the Flux Linkage

The magnetic flux linked by one turn,  $\lambda$ , is given by:

$$\lambda = \int_0^L \int_{-\theta}^{+\theta} B_o \cos(\theta) \cdot R \cdot d\theta \cdot dz \quad (2.1.1)$$

$$= \int_0^L \int_{-z\pi/L}^{+z\pi/L} B_o \cos(\theta) \cdot R \cdot d\theta \cdot dz$$

$$= \int_0^L B_o R \cdot 2 \cdot \sin\left(\frac{\pi z}{L}\right) \cdot dz$$

$$= \left[ -B_o R \cdot 2 \cdot \frac{L}{\pi} \cdot \cos\left(\frac{\pi z}{L}\right) \cdot dz \right]_0^L$$

$$= \frac{4}{\pi} B_o \cdot R \cdot L \quad (2.1.2)$$

Where  $B_o$  is the rms value of the magnetic field within the armature and  $R$  and  $L$  are the average radius of the armature and the active length respectively.

From the design specifications contained in Table 2.1, we note that:

$R=0.2577$  m and  $L=0.8$  m so:

$$\lambda = 0.2625 \cdot B_o \quad (2.1.3)$$

### II. Calculating the Induced Voltage Per Turn

The electromotive force, according to Lenz's law, is equal to minus the time rate of change of the magnetic flux. Hence, the amplitude of the induced voltage is given by:

$$V_{\max} = \omega \cdot \lambda \quad (2.2.1)$$

where  $\omega$ , the angular velocity of the rotor spinning at 3600 rpm is:

$$\omega = 2\pi f = 377 \text{ rad/s} \quad (2.2.2)$$

The rms value of the induced voltage per turn is:

$$V_{\text{rms}} = \frac{V_{\max}}{\sqrt{2}} = \frac{\omega \cdot \lambda}{\sqrt{2}} = 69.977 \cdot B_o \quad (2.2.3)$$

### III. Determining the value of $B_o$

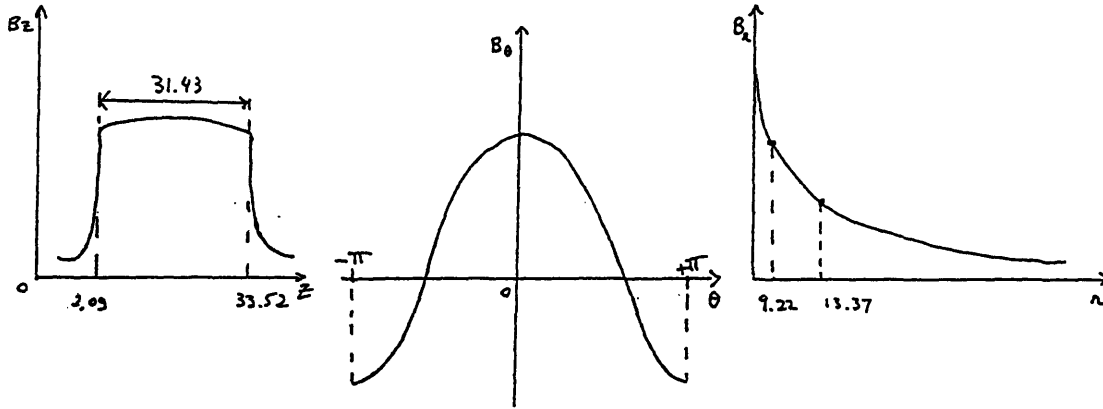
The Umans analysis and the experimental data obtained with the Delta connected high voltage (13.8 kV) armature winding which was built with 204 turns per phase indicate experimentally that:

$$V_{\text{rms}}/\text{turn} = \frac{13800}{204} = 67.647 \text{ V} \quad (2.3.1)$$

Hence,  $B_o$  is experimentally determined to be:

$$B_o = \frac{67.647}{69.977} = 0.967 \text{ T} \quad (2.3.2)$$

This value corresponds to an average magnetic field whose amplitude within the stator is:  $B_{max} = 1.37 \text{ T}$ . This value is much weaker than the actual intensity of the rotor's field because we assumed that it was independent in the axial and radial directions. The actual shape of the magnetic field,  $B(r, \theta, z)$ , has been plotted below.



#### IV. Determining the Number of Bars per Phase Belt

From the results obtained in the last two sections, we will calculate the number of turns per phase needed to obtain a phase voltage of 2300 V rms. As seen above, the line-to-ground voltage per turn is:

$$V_{rms/turn} = 69.977 \cdot B_o = 69.977 \times 0.967 = 67.66 \text{ V rms/turn} \tag{2.4.1}$$

In order to obtain a phase voltage of 2300 V rms we need:

$$n = \frac{2300}{67.66} \approx 34 \text{ turns per phase} \tag{2.4.2}$$

Since the two phase belts are mounted in series, they must each be composed of  $\frac{34}{2} = 17$  turns. But since each turn is physically comprised of a pair of armature bars, each phase belt is made up of 34 bars and the armature, as a whole, contains  $6 \times 34 = 204$  bars distributed equally between the two layers.

Note: This result could be reached directly from the experimental results contained in equation 2.3.1 without having to calculate the flux linkage and the empirical value of  $B_o$ . However, in so doing, some insight in the design of the armature would be lost.

## CALCULATION 2.3

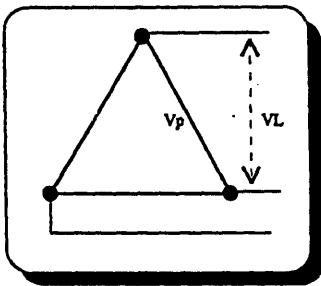
### I. Definition of Electric Power

For a single phase machine, the electric power is given by:  $P = V_\phi \cdot I_\phi$  where  $V_\phi$  is the phase voltage and  $I_\phi$  is the phase current. Similarly, the electric power of a three phase machine is three times that of the single phase machine.

$$P = 3 V_\phi \cdot I_\phi$$

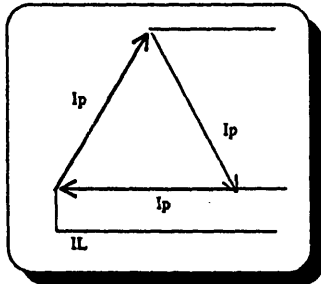
### II. The Delta Machine

#### 1) Voltage



As one can clearly see from the illustration, the phase voltage and the line voltages are equal:  $V_\phi = V_L$

#### 2) Current



The simplest way to determine the relationship between the line and phase currents is to draw a phasor diagram and to take the vector difference between two phase-current phasors. Taking the lower left corner of the triangle drawn here as the origin of our orthonormal frame and knowing that the inside angle of an equilateral triangle is 60 degrees, we may write vectorially:

$$I_L = \begin{bmatrix} \frac{1}{2} * I_\phi \\ \frac{\sqrt{3}}{2} * I_\phi \end{bmatrix} - \begin{bmatrix} -I_\phi \\ 0 \end{bmatrix} = \begin{bmatrix} 1.5 * I_\phi \\ \frac{\sqrt{3}}{2} * I_\phi \end{bmatrix}$$

$$\text{Thus } \|I_L\|^2 = \left[ (1.5)^2 + \left(\frac{\sqrt{3}}{2}\right)^2 \right] I_\phi^2 \quad \text{and} \quad I_L = \sqrt{3} I_\phi$$

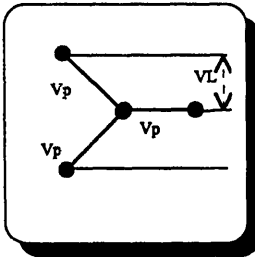
#### 3) Power

Substituting the two relationships determined in this section into the definition of electric power, shown above, we find that:

$$P = \sqrt{3} V_L \cdot I_L \quad \text{where } V_L \text{ and } I_L \text{ are the line voltage and current respectively.}$$

### III. The Wye Machine

#### 1) Voltage

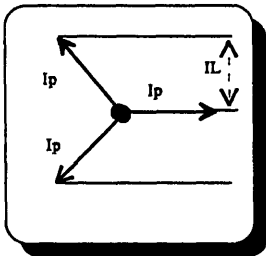


The most direct way of relating the line voltage to the phase voltage is to draw a phasor diagram and take the vector difference between two phase-voltage phasors. Making the center node of the Wye the origin of an orthonormal frame and knowing that the three phases are 120 degrees apart, we may write vectorially:

$$V_L = \begin{bmatrix} V_\phi \\ 0 \end{bmatrix} - \begin{bmatrix} -\frac{1}{2} * V_\phi \\ \frac{\sqrt{3}}{2} * V_\phi \end{bmatrix} = \begin{bmatrix} \frac{3}{2} * V_\phi \\ -\frac{\sqrt{3}}{2} * V_\phi \end{bmatrix}$$

$$\text{Thus, } \|V_L\|^2 = \left[ \left(\frac{3}{2}\right)^2 + \left(\frac{-\sqrt{3}}{2}\right)^2 \right] \cdot V_\phi^2 \quad \text{and} \quad V_L = \sqrt{3} V_\phi$$

#### 2) Current



It can be inferred from inspection of the figure at left that the line current is equal to the phase current in the case of a Wye connected machine:  $I_\phi = I_L$

#### 3) Power

Substituting the two expressions relating the line and phase voltages and currents into the definition of electric power, we find, as before, that:

$$P = \sqrt{3} V_L \cdot I_L \quad \text{where } V_L \text{ and } I_L \text{ are the line voltage and current respectively.}$$

#### 4) Application

The new Wye connected armature winding will be designed to deliver a rated power of  $P=10$  MVA at a terminal voltage of  $V_L=4$  kV (rms). The terminal current, at rated power, is:

$$I_L = \frac{P}{\sqrt{3} V_L} \approx 1,445 \text{ A (rms)}$$

Since this is a Wye connected circuit,  $I_\phi = I_L = 1,445$  (rms). Moreover, since the present armature is designed with two phase belts mounted in series, the current flowing through an armature bar has the same value as the phase current.

Therefore:

$$\text{Bar Current} = 1,445 \text{ A (rms).}$$

#### 4) Application

The old high voltage armature was designed to deliver a power of  $P=10$  MVA at a terminal voltage of  $V_L=13.8$  kV rms line. Using the equation for power derived in part three, we find that the terminal current, at rated power, is:

$$I_L = \frac{P}{\sqrt{3} V_L} \approx 420 \text{ A. (rms)}$$

The phase current, as explained previously, is:

$$I_\phi = \frac{I_L}{\sqrt{3}} \approx 242.5 \text{ A (rms) but since each phase is constructed of two parallel$$

phase belts, circuit theory tells us that the current within an individual bar is:

$$\text{Bar current} = \frac{I_\phi}{2} \approx 120 \text{ A (rms)}$$

As explained in the previous section, the only two insulation schemes employed in this armature winding are the basic conductor insulation and the thick bar insulation. Each of the individual wires which make up the litz conductor will be insulated from each other by Phelps Dodge ML, a film insulation, in order to prevent eddy currents. A heavy coating of about 2.2 mil will be more than adequate to withstand potential gradients of the order of one volt.

The bar insulation, which is a 60 mil thick frame around the rectangular litz, is designed for line-to-ground performance. Its maximum nominal stress, as shown in **Figure 2.12**, is:  $\frac{\Delta V}{\Delta L} = \frac{2,300}{60} = 38.3 \text{ V / mil}$ . The insulation will consist of a half lap wrapped layer of a glass fiber cloth containing mica flakes. This glass cloth, which is sold by General Electric under the name of MicaMat<sup>41</sup>, is very porous and can easily be impregnated with an epoxy resin. The combination of mica flakes, glass and epoxy permits the manufacture of monolithic bars with excellent electrical and mechanical properties.

The aforementioned cooling channels, which run the length of the cylindrical armature winding, are located above and below each layer of bars. Each channel has a height of 1/8 of an inch and a width comparable to the conductor bar width. As in the 60 kVA and the high voltage 10 MVA machines, the coolant will be Dow Corning 561 silicone transformer fluid. This dimethyl siloxane fluid<sup>42</sup> has good characteristics such as a viscosity of about 32.5 St and a dielectric strength of 18.8 kV/mm. It is anticipated that the maximum operating temperature of the armature will be at, or below, 145 °C.



Nominal  
Stress on Bar

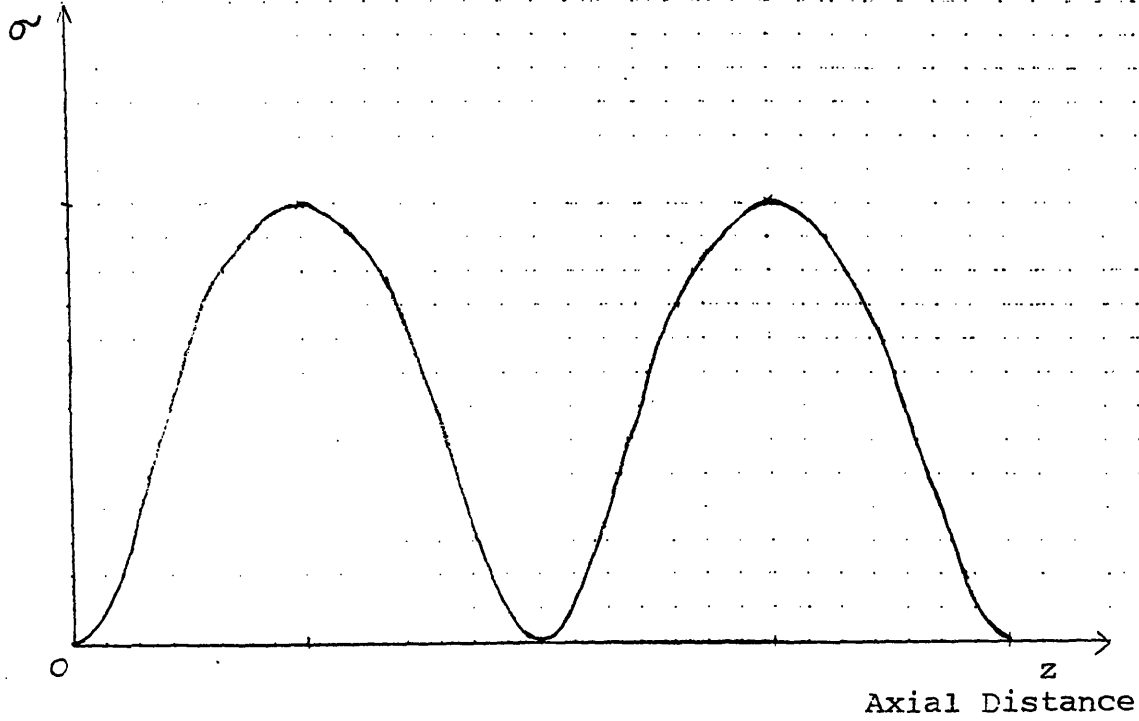


Figure 2.12: Nominal Electric Stress Acting on  
Helically Winding Bar

The aforementioned specifications have been summarized in **Table 2.4** below for easy reference.

**Table 2.4:** MIT 10 MVA Armature Electrical Design Specifications

Rated line-to-line voltage:	4,000 V rms
Corresponding phase voltage:	2,300 V rms
Phase voltage per turn:	67.65 V rms
Number of turns per phase:	34 turns
Number of turns per circuit:	17 turns
Number of bars per phase belt:	34
Total number of bars in armature:	204
Terminal current at rated power:	1,445 Amps
Bar current at rated power:	1,445 Amps
Conductor Insulator:	Heavy ML 2.2 mil
Bar Insulation	Glass and mica flake 60 mils
Nominal Stress	38.3 V/mil
Cooling channel height:	.125 inch
Coolant	Dow 561
Maximum operating temperature:	145 °C

## **2.4 Design Calculations**

Using the armature specification data that is summarized in Table 2.1 and the electrical design specifications tabulated above, we will proceed with the armature design calculations.

### **1) Height of Conductor Bar**

First, the height of the rectangular conductor bars must be determined. These bars must fit over the Permali bore tube of inner radius 9.221 inches and, in addition, the entire monolithic stator must fit inside the laminated iron magnetic shield of inner radius 13.390 inches. Leaving about an 18 mil clearance between the stator's outer finish tube and the magnetic shield, the monolithic armature's outer radius should be 13.372 inches. Hence, the disposable radial space within the stator is:  $13.372 - 9.221 = 4.151$  inches. This radial space between the stator's inner and outer radii is taken up by the .450 inch thick outer torque-carrying finish tube, the four .125 inch

cooling channels located above and below each of the two layers of bars, the four layers of .060 inch line to ground bar insulation (Ti) and the two conductor bar themselves. **Figure 2.13** clearly illustrates this allocation of radial space by displaying a cross section of the stator. Thus:

$$\text{Bar Height} = (\text{Outer Radius} - \text{Inner Radius} - \text{Finish tube thickness} - 4 * \text{Cooling channel thickness} - 4 * \text{Insulation}) * (1/2)$$

$$\text{Bar Height} \equiv H_b = (13.372 - 9.221 - .450 - (4 * .125) - (4 * .060)) * (1/2) = \underline{1.481 \text{ inches}}$$

### 2) The Length to Ends

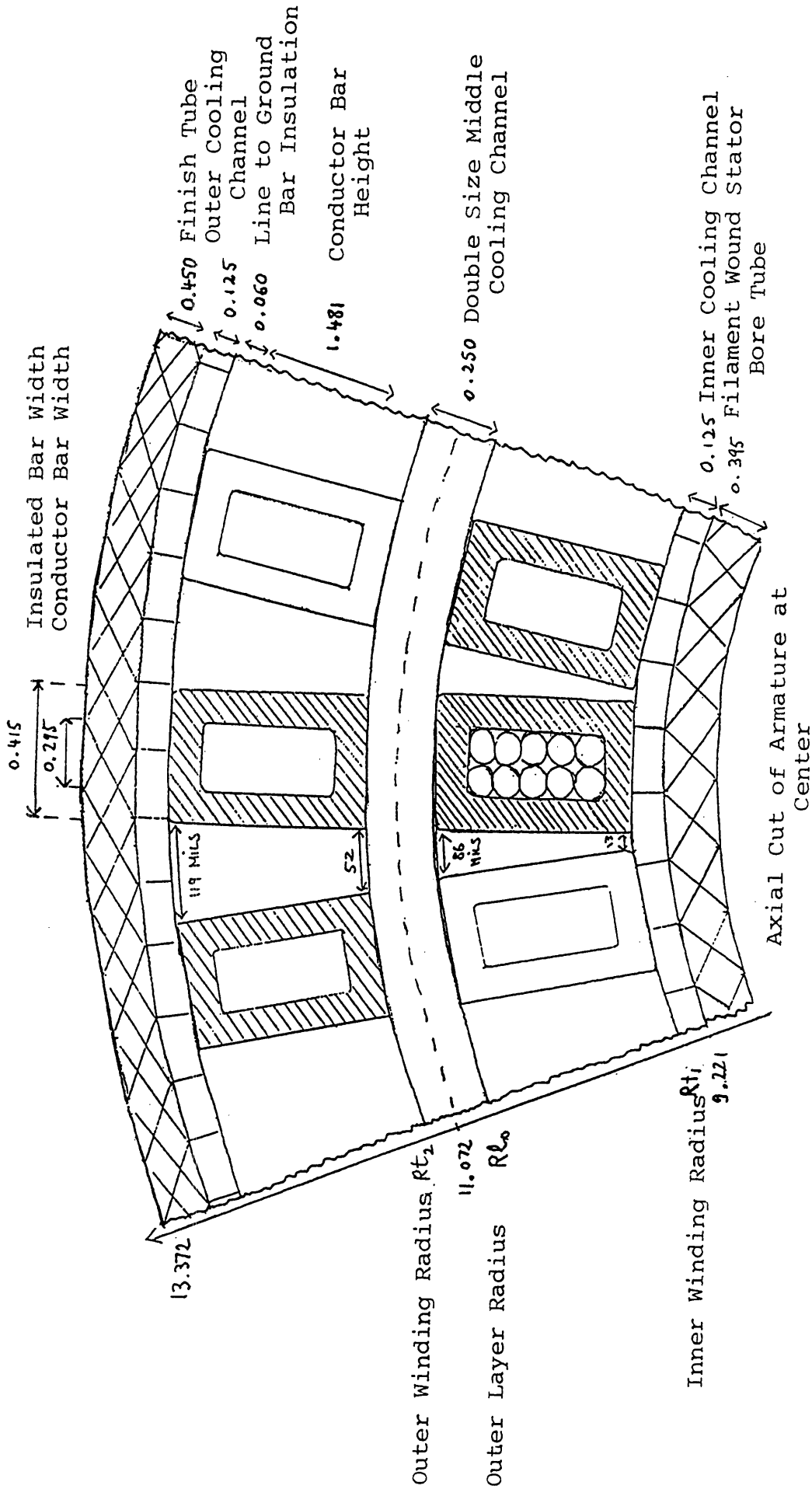
The next step in the design of the armature involves the determination of the axial length of the helical plus the transition portions of the bars, as shown in **Figure 2.14**. Since this measurement, known as the *length to ends*, includes neither the straight portion at the ends of the bar nor the end connectors and since the complete bar must fit in the active region of the armature, the length to ends can easily be determined. On both ends of the bar, the .75 inch long straight end section (Lst) depicted in **Figure 2.15** will be mated to an L shaped end connector measuring 3.75 inches in the axial direction. As reported in Table 2.1, the active length of the Permali bore tube measures 43.12 inches so it follows that:

$$\text{Length to ends} \equiv L = \text{Active length} - 2 * (\text{Straight end section} + \text{end connector axial length})$$

$$L = 43.12 - 2 * (.75 + 3.75) = \underline{34.12 \text{ inches.}}$$

### 3) The Transition Region

The nature of the bar's transition region, which exists between the helical and straight end section, should be quantitatively determined at this point. The transition region employed in the high voltage armature winding which was constructed in the early 1980's consisted of a smooth parabolic curve that matched the helical and straight sections. The main advantages of this design are twofold. First, all of the bars lie exactly on top of each other and, second, it can easily be programmed in an NC milling machine that



Note: Interbar spacing shown in bar frame.

Figure 2.13: Allocation of Radial Space in the Armature

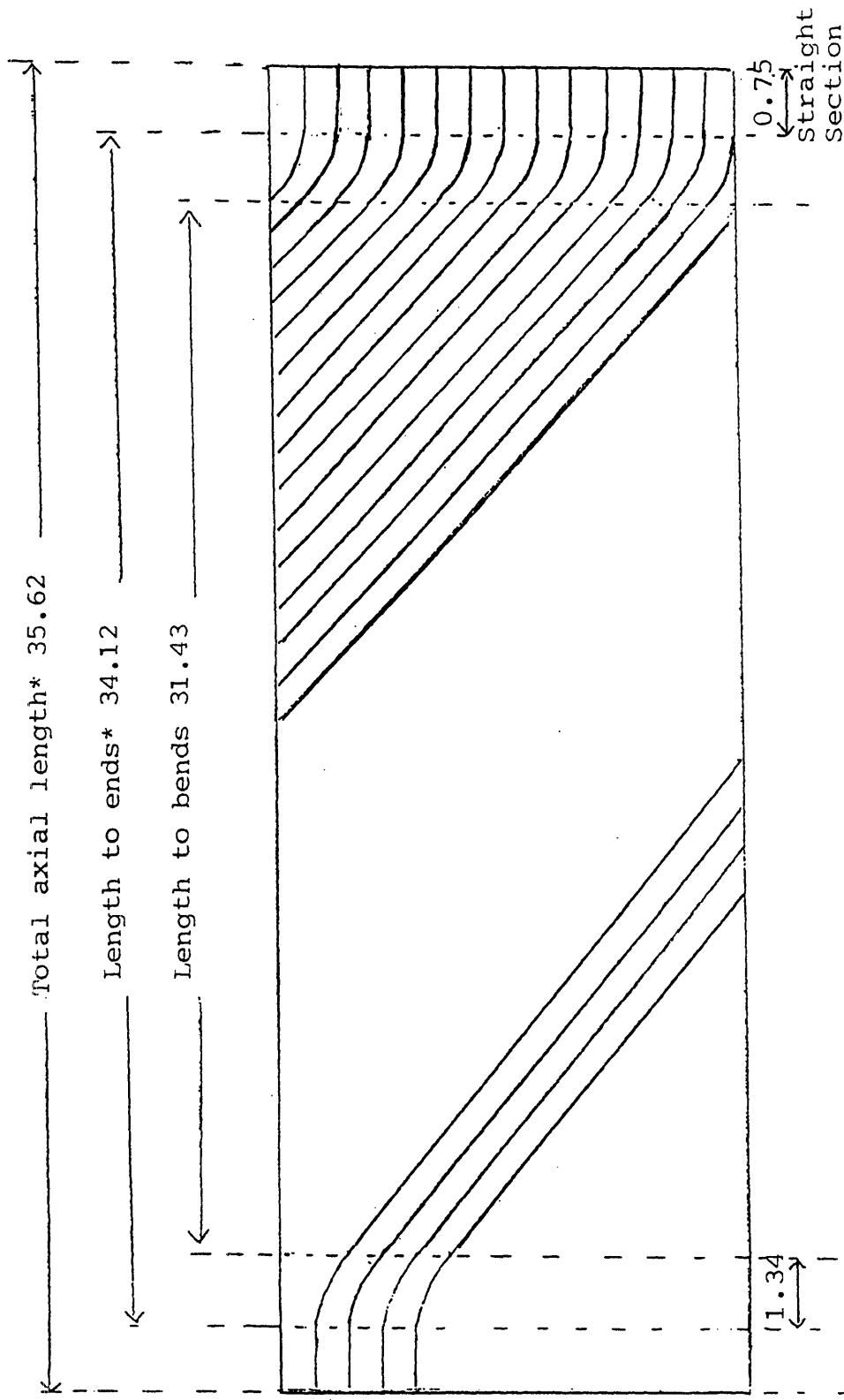


Figure 2.14: Path of Helically Winding Bars Mounted on Cylindrical Armature

\* Constant from layer to layer (length to bends calculated for the first layer.)

Note: End connectors are not displayed.

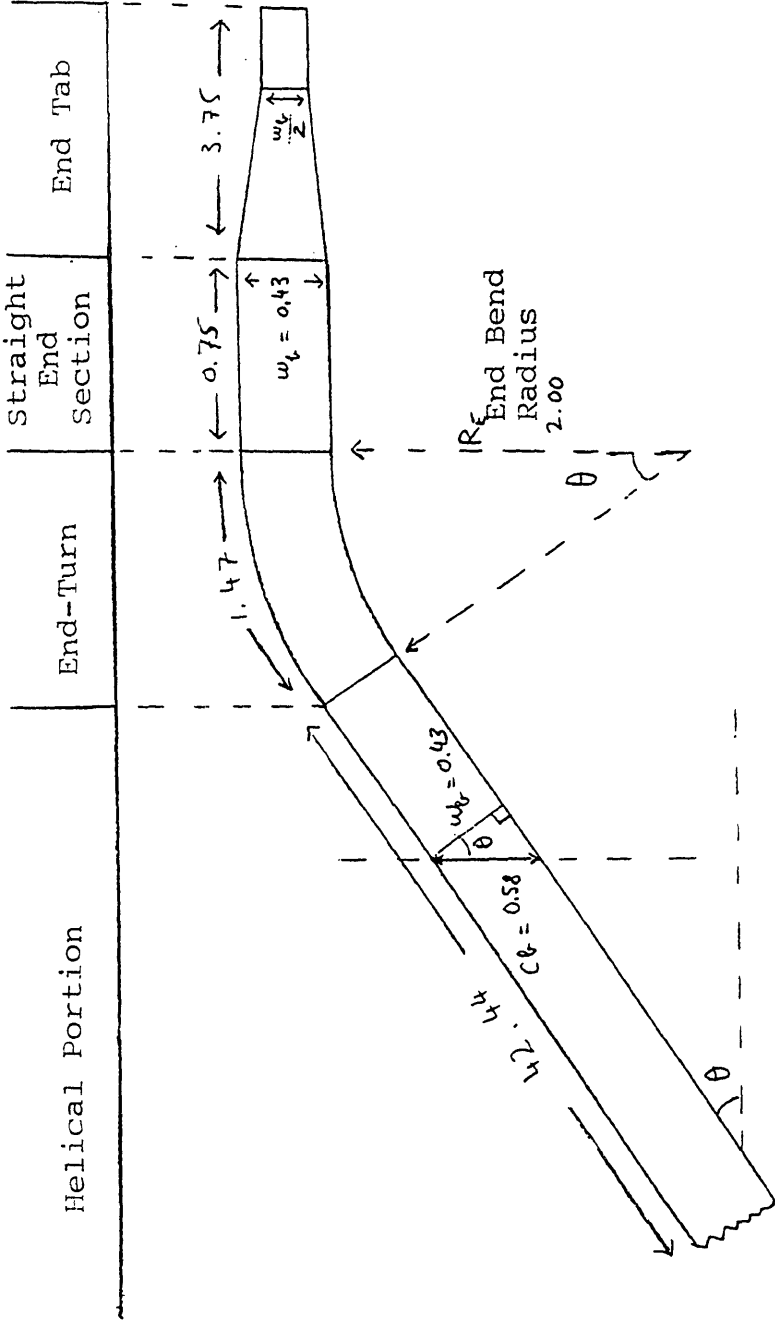


Figure 2.15: End Tab Mounted at the Leads of the Bar

operates exclusively in the Z-theta plane<sup>43</sup>. **Appendix B** details the armature bar design calculations for the old high voltage machine in great detail. Since most milling machines are now capable of performing circular arcs, and since matching the helical to the straight section is relatively simple to do with such curves, we will employ circular end turns. The radius of curvature which will be used in the transition region is proportional to the width of the armature bars. By winding samples of the insulated bars which are to be used in the present armature around cylindrical mandrels of various diameters, it was experimentally determined that a conservative value for the end-bend radius, Re, is 2.0 inches.

#### 4) Scaling the Axial-Azimuthal Plane

The length of the helical portion of the conducting bar must be determined next. Instead of performing the numerical integration method outlined in Appendix B, a series of "flowing" iterative equations can be set-up in order to obtain the helix angle of the bars relative to the axial direction. This calculation method, which is easy to solve using a personal computer, involves working in the axial-azimuthal plane obtained by "unfolding" a cylindrical shell. **Figure 2.16** is a planar representation of the path of a complete helical bar that turns half way around the cylindrical stator while traveling across it. The three dimensional path of the bar in space can be observed by taping the top and bottom of the paper together.

The total azimuthal length of the bar, which is measured along the vertical axis, can effortlessly be determined first. For this reason, the *winding radius*, which corresponds to the radius of the cylindrical shell on which the insulated bars are mounted, must be found. For the first layer of bars, the winding radius is:

$$Rt_1 = \text{Stator inner radius} + \text{Cooling channel thickness}$$

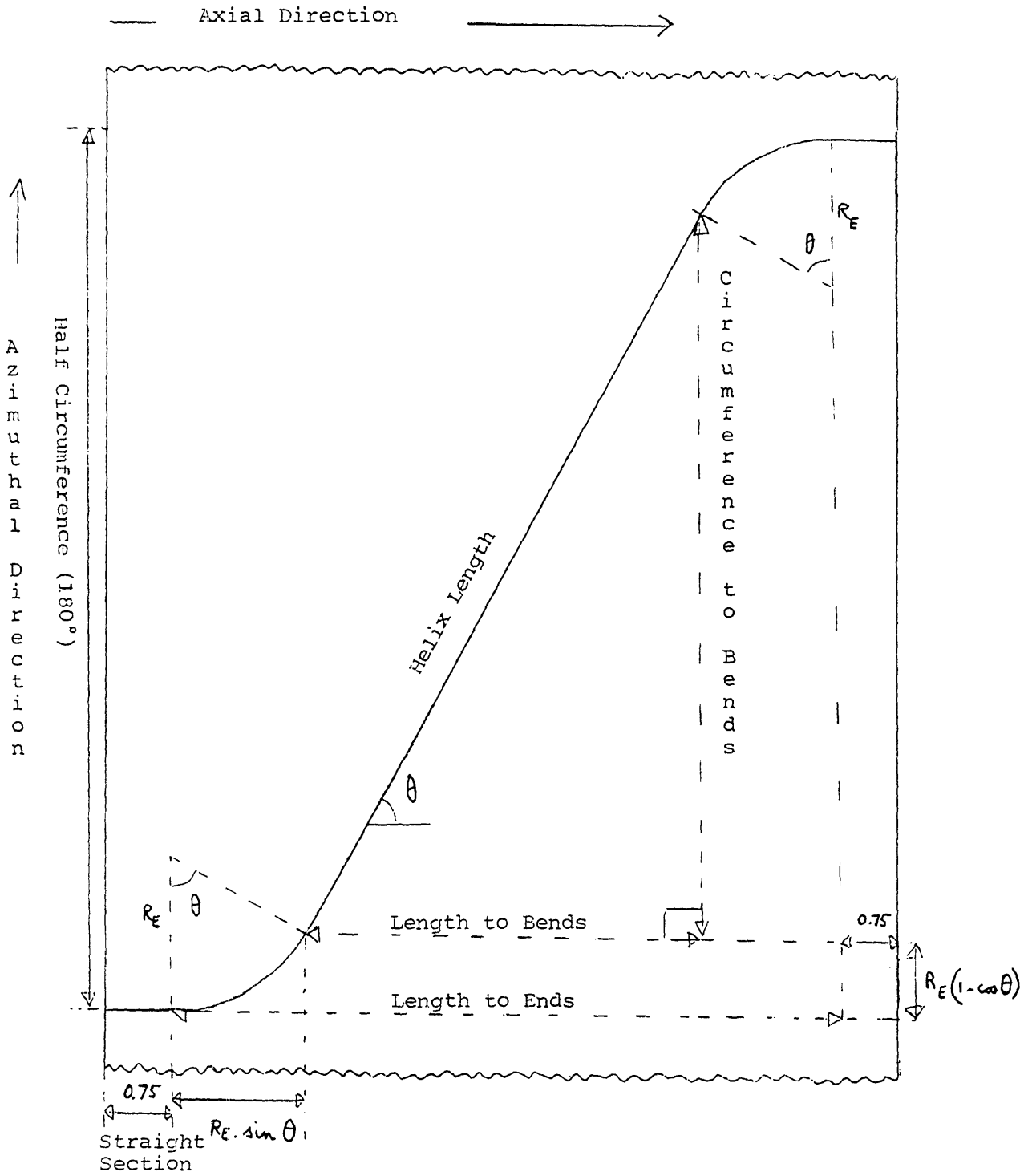


Figure 2.16: Representation of an Armature Bar in the Axial-Azimuthal Plane



$Rt_1 = 9.221 + .125 = \underline{9.346 \text{ inches}}$ , as shown in Figure 2.15. However, since the entire bar turns only half way around the armature, the azimuthal length of the bar is just one half of the circumference of the cylindrical shell. Hence:  $Ct_1 = 1/2 \ 2*\pi*Rt = \underline{29.361 \text{ inches}}$ .

The bar's total axial length, which is measured along the horizontal direction, has been previously defined as the length to ends and has been illustrated in Figure 2.14. We recall that the value of the length to ends, which is independent of the bar layer, was determined to be equal to 34.12 inches.

### 5) Helical Length and Angle Calculation

In this section we shall set aside the transition and straight sections located at the ends of the bar and concentrate exclusively on the helical portion. The *circumference to bends*, which is similar to the total azimuthal length, is defined as the measurement of the projection of the helical section of the bar onto the azimuthal axis. Thus, the circumference to bends can be determined by subtracting the azimuthal component of the two transitional sections from the total azimuthal length. If the helix angle  $\theta$  is known, and if both curves are properly matched, it can be seen from inspection of Figure 2.16 that:

Circumference to bends  $\equiv Ca = \text{Total azimuthal length} - 2* \text{azimuthal component of transitional section}$

$$Ca = Ct - 2*(Re - Re*\cos(\theta)) = Ct - 2*Re(1-\cos(\theta))$$

Similarly, the *Length to bends* is the measurement of the axial component of the helical part of the bar, as illustrated in Figure 2.14. This quantity can be related to the length to ends, defined as the axial length of the helical plus the transitional portions, and to the helix angle. Using the same process as above, it can be determined by inspection of Figure 2.16 that:

Length to bends  $\equiv La = \text{Length to ends} - 2* \text{axial component of transitional section}$

$$L_a = L - 2 \cdot (R_e \cdot \sin(\theta))$$

The helix angle and the length of the helical portion of the bar can finally be determined from the last two quantities. Since the axial-azimuthal frame is an orthogonal frame, it is apparent from elementary trigonometry that:

$$\theta = \text{Tan}^{-1} (C_a/L_a) \text{ and}$$

$$\text{Helix Length} \equiv L_h = \sqrt{C_a^2 + L_a^2}.$$

In order to use this iterative method, one must input into the computer a crude approximation for  $\theta$  as a starting point. A value of .785 rad (=45°) was selected based on the stator's geometry. After several repetitions of the process depicted in **Figure 2.17**, the helix angle can be determined with great precision. Contrary to the technique outlined in Appendix B, when using circular arcs as matching elements the value of the helix angle changes from layer to layer.

### 6) Total Bar Length

After determining the helix angle, the length of the transition region for the inner bars can be subsequently calculated. Since the end turns are circular arcs, it can be observed in **Figure 2.16** that the circumferential length of each of the transition sections is given by:

$$L_{b1} = R_e \cdot \theta = 2.00 \cdot .733 = \underline{1.467 \text{ inches}}$$

The total length of an armature bar may be found by adding to the helical length twice the sum of the lengths of the transition and straight sections. Thus, for bars of the first layer:

$$L_{\text{total}} = L_h + 2 \cdot (L_b + L_{st}) = 42.438 + 2 \cdot (1.467 + .750) = \underline{46.758 \text{ inches}}.$$

### 7) Bar Width

The width of the conductor bar will be determined in this sub-section through a series of calculations. First, the maximum azimuthal

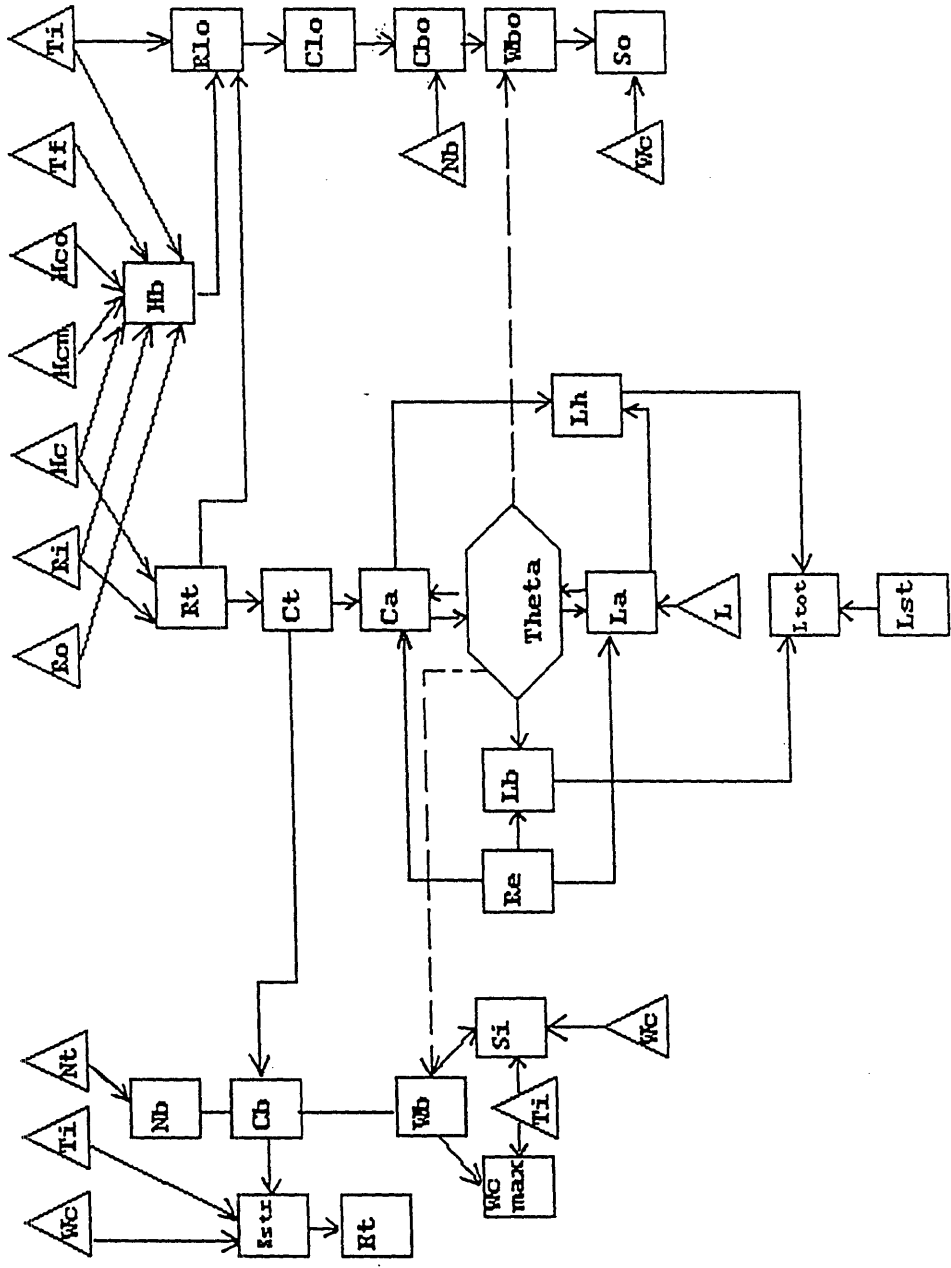


Figure 2.17: Iterative Calculation Flow Chart

(Note the interdependencies between each of the attributes of the armature)

(circumferential) space available to each bar of a given layer must be calculated. This circumferential space per bar is given by taking the ratio of the circumference at the winding radius to the number of bars per layer.

Recalling that  $C_t$  is one half of the appropriate circumference, we have:

$$C_{b1} = \frac{2 * C_{t1}}{\text{Bars per layer}} = (2 * 29.36) / 102 = \underline{.576 \text{ inches per insulated bar.}}$$

However, the maximum insulated bar width,  $W_b$ , is smaller than the maximum circumferential space available since the bars are inclined at the helix angle  $\theta$ . As Figure 2.6 suggests, the maximum width of the insulated bar is related to the above result by the following formula:

$$W_{b1} = C_{b1} * \cos(\theta) = \underline{0.428 \text{ inches per insulated bar.}}$$

The conductor bar's maximum thickness is found by subtracting the insulation thickness from the maximum insulated bar width computed above. Recalling that the bar insulation thickness is  $T_i = 0.060$ , the maximum width of the conductor bar becomes:

$$W_{cmax} = W_b - 2 * T_i = \underline{0.308 \text{ inches.}}$$

For ease of manufacturing and since the current density within each conductor bar must remain constant, only one size of conductor bar will be used in the design of the armature. As such, only the smallest value for the conductor bar's maximum thickness is relevant. Clearly  $W_{cmax}$  is smallest in the first layer so:  $W_{cmax} \equiv W_{cmax_1} = W_{cmax_2}$ .

Knowing the bar's maximum height (from part 1) and having determined the maximum width, we find the litzwire that best suits our design requirements. The nearest commercially available match is a litzwire composed of 19 bundles of 19 wires, each of size AWG #21. The finished height and width for this cable is:  $H_b = 1.481$ " and  $H_c = 0.295$ " respectively<sup>44</sup>.

### 8) Bar Width at Outer End

Since bars have rectangular cross sections and since the armature is cylindrical, the volume of space separating the bars in the helical section of the armature is shaped like a wedge. Thus the maximum allowable width of an insulated bar is greater at the outer end than at the root of the bar.

Conceivably a tapered bar could be manufactured in order to take advantage of the azimuthal space gained by increased radial distance, but the high costs of manufacture outweigh the benefits reaped by larger space factors. The first step in determining the maximum width of an insulated bar at its outer radius consists of finding the *outer layer radius* itself. This outer radius is found by adding to the winding radius the bar's height and the thickness of the insulation layers located above and below each bar. Thus:

$$\text{Outer Layer Radius} \equiv R_{lo} = R_t + H_b + 2 * T_i = 9.346 + 1.481 + 2 * (0.060) = \underline{10.947 \text{ in}}$$

for the first layer.

The maximum azimuthal space available at the outer end of the conductor bar can be found by taking the perimeter of a circle whose radius is the outer layer radius and dividing it by the number of bars per layer. Hence:

$$\text{Outer Circumference per bar} \equiv C_{bo} = \frac{2 * \pi * R_{lo}}{N_b} = \frac{2 * \pi * R_{lo}}{102} = \underline{34.389 \text{ in}}$$
 for the first layer.

As explained before, the maximum width of an insulated bar at the outer radius depends on the helix angle. A first order approximation for  $W_{bo}$  is given by:

$$\text{Outer Width per bar} \equiv W_{bo} = C_{bo} * \cos(\theta) = 34.39 * \cos(.73) = \underline{0.501"}$$
 for the first layer.

It should be noted that this model disregards the fact that, for the outer edge of the bar, the helix angle  $\theta$  is slightly larger. A more accurate calculation for  $W_{bo}$  would either use the helix angle at the mid-point of the bar or account for the bar's own "twist".

## 9) Bar Spacing

The size of the space that exists in between the bars traveling in the helical portion of the armature, can be determined next. As explained above, this wedge shaped space, represented in Figure 2.13, is due to the cylindrical nature of the stator. It is important at this point to select an appropriate frame of reference. Although it is possible to determine the azimuthal separation between the bars in an axial cut, this measurement would not yield the desired result as the bars are pitched. Since, by definition, the conductor spacing is measured in the direction transverse to the bars, we will simplify the task by working in the bar frame. Thus, for the first bar layer, we may write that the distance separating the innermost edges of two adjacent bars in the bar frame is:

$$\text{Bar Spacing}_{\text{Inner}} \equiv S_i = W_b - W_c - 2 \cdot T_i = \underline{0.013 \text{ in}}$$

Similarly, the distance separating the outermost edges of two adjacent bars is, in the bar frame:

$$\text{Bar Spacing}_{\text{Outer}} \equiv S_o = W_{b_o} - W_c - 2 \cdot T_i = \underline{0.086 \text{ in}}$$

Although the azimuthal distance between the bars increases as the radial distance is increased because of a gain in circumferential space, the bar separation in the bar's frame is affected by the augmentation of the pitch angle.

The space in between the bars in the straight section can also be determined in this section. The inter-bar distance at the end of the armature is the same as the azimuthal separation since the bars are no longer skewed with regard to the axial direction. Recalling that  $C_b$  is the maximum azimuthal space available to the bar and knowing the actual width of the uninsulated bar ( $W_c$ ) we write:

$$\text{Straight Section Bar Separation} \equiv S_{\text{str}} = C_b - (W_c + 2 \cdot T_i) = \underline{0.161 \text{ in}}$$

for the innermost layer. Since this "gap" is shared between two adjacent armature bars, it follows that the maximum thickness of an end connector is half of this length. Thus:

$$\text{Max. End Connector Thickness} \equiv Et_1 = Et_2 = S_{str} / 2 = 0.080 \text{ in thick.}$$

Despite the extra azimuthal space available in the second layer, only one type of end connector will be used in this armature in order to keep the current density uniform and to simplify manufacturing.

### 10) Bar Compression Ratios and Conductor Area

In this section, we shall determine the bar's compression ratios by comparing the dimensions of a manufactured bar to the size of a stack of unwoven basic conductors. The diameter of an uninsulated strand of AWG#21 wire is  $d_c=0.0285$ " but by adding a heavy film coating, the effective diameter becomes  $d_w=0.0306$  inches<sup>45</sup>.

By winding  $C_s=19$  basic conductors around each other, as shown in Figure 2.4-d, we obtain a bundle with a diameter roughly equal to  $C_y=5$  times that of the insulated basic conductor. In turn, these 19 bundles are woven into a bar whose cross section appears as  $N_w=2$  bundles wide by  $N_h=10$ . An unwoven collection of basic strands would, therefore, have the following dimensions:

$$\text{Uncompressed height} \equiv H_u = C_y * d_w * N_h = \underline{1.530"} \quad \text{and}$$

$$\text{Uncompressed width} \equiv W_u = C_y * d_w * N_w = \underline{0.306"} \quad \text{and}$$

The bar's compression factor is the ratio of the manufactured size to the uncompressed dimensions. Thus:

$$\text{Height compression factor} \equiv H_{comp} = H_b/H_u = 96.8\%$$

$$\text{Width compression factor} \equiv W_{comp} = W_c/W_u = 96.4\%$$

The bar, as a whole, is composed of a total of  $19 \times 19 = 361$  conductor strands which give the litz a consolidated copper area of .2303 square inches. Hence, the bar is roughly the electrical equivalent of an AWG #1 conductor.

The equations and results discussed in this section have both been tabulated and summarized in **Table 2.5** for easy reference.



Armature Shape Calculation			
Object	Symbol	Formula	
Outer Radius	Ro	=26.744/2	
Inner Radius	Ri	=18.442/2	
Cooling Height: Inner	Hc	0.125	
Cooling Height: Mid	Hcm	0.25	
Cooling Height: Outer	Hco	0.125	
Insulation Thickness	Ti	0.06	
Finish Tube Thickness	Tf	0.45	
Bar Height	Hb	=(Ro-Ri-Hc-Hcm-Hco-4*Ti-Tf)/2	
Length to Ends	L	34.12	
End Bend Radius	Re	2	
Number of Turns	Nt	34	
Number of Bars	Nb	=3*Nt	
		<b>Layer 1</b>	<b>Layer 2</b>
Winding Radius	Rt	=Ri+Hc	=C18+Hcm+2*Ti+Hb
Circumference	Ct	=PI()*Rt	=PI()*Rt
Circumference To Bends	Ca	=Ct-2*Re*(1-COS(Th))	=Ct-2*Re*(1-COS(Th))
Length To Bends	La	=L-2*Re*(SIN(Th))	=L-2*Re*(SIN(Th))
Helix Angle	Th	=ATAN(Ca/La)	=ATAN(Ca/La)
Helix Length	Lh	=SQRT(Ca^2+La^2)	=SQRT(Ca^2+La^2)
Bend Length	Lb	=Re*Th	=Re*Th
Straight Length	Lst	0.75	0.75
Total Bar Length	Ltot	=Lh+2*(Lb+Lst)	=Lh+2*(Lb+Lst)
Circ. Per Bar	Cb	=2*Ct/Nb	=2*Ct/Nb
Total Bar Width	Wb	=Cb*COS(Th)	=Cb*COS(Th)
Max. conductor bar width	Wcmax	=Wb-2*Ti	=+C29
Conductor Bar Width	Wc	0.295	=C30
Bar Spacing: Inner	Si	=(Wb-Wc-2*Ti)	=(Wb-Wc-2*Ti)
Bar Spacing: Outer	So	=(Wbo-Wc-2*Ti)	=(Wbo-Wc-2*Ti)
Outer Layer Radius	Rlo	=Rt+Hb+2*Ti	=Rt+Hb+2*Ti
Outer Layer Circumference	Clo	=PI()*Rlo	=PI()*Rlo
Outer Circ Per Bar	Cbo	=2*Clo/Nb	=2*Clo/Nb
Outer Width Per Bar	Wbo	=Cbo*COS(Th)	=Cbo*COS(Th)
Bar Spacing: Straight Sect.	Sstr	=+Cb-(Wc+(2*Ti))	=+Cb-(Wc+(2*Ti))
Max. End Tab Thickness	Et	=+Sstr/2	=+C38
Conductor Diameter insl/bare	dw	=+D40+0.0021	0.0285
Conductor Layer Order	Cy	5	
Strands/Conductor	Cs	19	
Groups High	Nh	10	
Groups Wide	Nw	2	
Uncomp height	Hu	=Cy*dw*Nh	
Uncomp Width	Wu	=Cy*Nw*dw	
Compression Height	Hcomp	=Hb/Hu	
Compression Width	Wcomp	=Wc/Wu	
Number of Strands		=Cs*(Nw*Nh-1)	
Conductor Area		=C49*(PI()/4)*((D40)^2)	

Table 2.5A: Design Calculation Equations

Helical Armature Shape Calculation				
Object	Explanation	Symbol	Numerical Value	
Outer Radius	Maximum outer radius of armature	Ro	13.372	
Inner Radius	Radius of stator bore tube	Ri	9.221	
Cooling Height: Inner	Radial thickness of innermost channel	Hc	0.125	
Cooling Height: Mid	Thickness of the double sized middle channel	Hcm	0.250	
Cooling Height: Outer	Radial thickness of the outermost channel	Hco	0.125	
Insulation Thickness	Thickness of the line to ground bar insulation	Ti	0.060	
Finish Tube Thickness	Thickness of the outer torque tube	Tf	0.450	
Bar Height	Calculated maximum height of conductor bar	Hb	1.481	
Length to Ends	Axial distance between the ends of the end turns	L	34.120	
End Bend Radius	Radius of curvature of the end turns	Re	2.000	
Number of Turns	Number of turns per phase	Nt	34	
Number of Bars	Number of bars per layer	Nb	102	
			Layer 1	Layer 2
Winding Radius	Distance between bar layer and armature long axi	Rt	9.346	11.197
Circumference	Azimuthal projection of the total bar length	Ct	29.361	35.175
Circumference To Bends	Projection of the helical section onto the azimuthal	Ca	28.333	33.883
Length To Bends	Projection of the helical portion onto the axial axis	La	31.442	31.176
Helix Angle	Angle between helical section and axial direction	Th	0.733	0.827
Helix Length	Total Length of the helical section of the bar	Lh	42.325	46.044
Bend Length	Length of the transition region of the bar	Lb	1.467	1.654
Straight Length	Length of the straight sections at the ends of bar	Lst	0.750	0.750
Total Bar Length	Length of the entire armature bar	Ltot	46.758	50.852
Circ. Per Bar	Maximum allowable azimuthal space for insul. bar	Cb	0.576	0.690
Total Bar Width	Maximum width of insulated bar	Wb	0.428	0.467
Max. conductor bar width	Maximum width of the conductor bar	Wcmax	0.308	0.308
Conductor Bar Width	Actual width of the conductor bar used	Wc	0.295	0.295
Bar Spacing: Inner	Space between inner part of bars in helical portio	Si	0.013	0.052
Bar Spacing: Outer	Space between outer part of bars in helical portio	So	0.086	0.119
Outer Layer Radius	Distance between outer edge of bar and long axis	Rlo	10.947	12.797
Outer Layer Circumference	Circumferential length traveled by bar's outer edg	Clo	34.389	40.203
Outer Circ Per Bar	Max. allowable azimuthal space for top of insl. bar	Cbo	0.674	0.788
Outer Width Per Bar	Max. width of insulated bar at outer layer radius	Wbo	0.501	0.534
Bar Spacing: Straight Sect.	Space in between bars in straight section	Sstr	0.161	0.275
Max. End Tab Thickness	Maximum thickness of end tab	Et	0.080	0.080
Conductor Diameter insl/bar	Diameter of basic conductor with and without film	dw	0.0306	0.0285
Conductor Layer Order	Number of basic conductors across each bundle	Cy	5	
Strands/Conductor	Number of basic conductor in each bundle	Cs	19	
Groups High	Number of bundles stacked vertically (aspect)	Nh	10	
Groups Wide	Number of bundles stacked side by side (aspect)	Nw	2	
Uncomp height	Height of an unwoven stack of basic conductors	Hu	1.530	
Uncomp Width	Width of an unwoven stack of basic conductors	Wu	0.306	
Compression Height	Height compression factor (Rel. to unwoven stack)	Hcomp	0.968	
Compression Width	Width compression factor (Rel. to unwoven stack)	Wcomp	0.964	
Number of Strands	Total number of basic conductors in each bar		361	
Conductor Area	Total copper area of bar		0.2303	

Table 2.5B: Results of Design Calculation Spreadsheet

## CHAPTER 3 COMPONENT DESIGN

### 3.1 Selection of the Conductor Bar

The conductor bar is, without question, the most important and one of the most basic components of the armature. When this conductor is properly insulated and suitably shaped, it becomes an armature bar. As explained in detail in the previous section, armature bars of two different layers are connected in series in order to form a complete loop capable of linking magnetic flux. Hence, phase belts, which are the workhorse of the winding, are comprised of a set of conductor bars each connected in series.

The word "conductor bar" is, strictly speaking, a misnomer since it denotes a component which is monolithic and uniformly conducting throughout. In reality, our so called "bar" is a cable comprised of a number of insulated conductors that have been wound together and compacted into a flat rectangular cross-section litz. This stranded magnetic conductor cable provides a convenient shape, high turn densities and less than 15% of void space within the cable<sup>46</sup>. By dividing the bar into smaller conductors, eddy currents are greatly reduced at the expense of the total conductor space. In this section we shall quantitatively specify the attributes of the conductor bar based upon experimental tests and our mathematical modeling.

#### 1) Conductor Material

The first decision involves the selection of the core of the cable. The ideal material will be ohmic in nature, have a low resistivity, offer a large number of conduction (free) electrons per unit volume and be readily available at an economical price. Based upon these requirements, the electric industry has traditionally used four metals (silver, gold, copper and

aluminum) more than any other substance. Because of the prohibitively high costs of the first two materials and because of the mediocre characteristics of the last, the litz will be composed exclusively of copper wires. **Table 3.1**, below, compares the properties of the four metals<sup>47</sup>. A useful set of quantum mechanical properties for copper has been calculated in **Appendix C** for completeness.

**Table 3.1:** Comparison of Widely Used Conductor Materials

Property	Gold	Silver	Copper	Aluminum
Atomic Number	79	47	29	13
Atomic Weight	196.97	107.87	63.55	26.98
Electron shell configuration	5p <sup>6</sup> 5d <sup>10</sup> 6s <sup>1</sup>	4p <sup>6</sup> 4d <sup>10</sup> 5s <sup>1</sup>	3p <sup>6</sup> 3d <sup>10</sup> 4s <sup>1</sup>	3s <sup>2</sup> 3p <sup>1</sup>
Density (g/cm <sup>3</sup> )	19.30	10.50	8.96	2.70
Melting Temperature (C)	1064.4	961.9	1084.8	660.4
Specific Heat (J/g K)	0.129	0.235	0.385	0.897
Thermal Conductivity (W/cm K)	3.17	4.29	4.01	2.37
Linear Expansion Coef. (10 <sup>6</sup> /K)	14.2	18.9	16.5	23.1
Resistivity (10 <sup>-8</sup> Ω-m)	2.27	1.63	1.725	2.73

## 2) Film Insulation

The next step in the bar selection process involves choosing a conductor insulation. The basic copper wires that were selected above must be shielded from one another in order to reduce circulating current losses. Since the objective is to separate quasi-equipotential conductors, the coat of insulation will only have to withstand electrical gradients of the order of a volt. Film insulations, which are commonly used in industry, are an elegant solution to this design requirement as they offer a combination of a good space factor and an appropriate electrical insulation.

The ideal film should be certified to withstand high temperatures (over 145 °C) while offering good mechanical properties such as high film flexibility and abrasion resistance. In addition, the film insulation should offer good

electrical properties and, if possible, some dielectric strength. In addition, the material will bond firmly with the copper core but, for ease in manufacturing, will either be removable with standard solvents or be solderable.

Six film insulation materials are most commonly used in wire manufacturing. These are: Polyvinyl Formal, Polyurethane (with and without a nylon overcoat), Polyester (imide and amide-imide) and Polyimide (ML). These chemical films are often sold under their respective trade names: Formvar, Sodereze, Nyleze, Thermaleze T (PTZ), Armored polythermaleze 2000 (APTZ) and ML. The first five are registered trademarks of the Phelps Dodge Corporation, the second largest producer of copper and other minerals. **Table 3.2**, below, offers a summary of the advantages and limitations of each of these materials.

**Table 3.2:** Comparison of Film Insulation Materials

Material	Temperature rating	Advantages	Limitations
Polyvinyl Formal	105 °C	Very good resistance to abrasion and solvents. Good electrical properties.	Must be stripped before soldering.
Polyurethane	155 °C	Solderable, good film flexibility Excellent electrical properties.	Lower abrasion resistance than above.
Polyurethane with Nylon overcoat	155 °C	as above but with excellent film flexibility and abrasion resistance.	Low performance in hot transformer oil.
Polyester imide	180 °C	Solderable at high temperatures, good electrical properties and compatible with most solvents.	As above but lower abrasion resistance than all the above.
Polyester -imide-amide	200 °C	Good film flexibility and abrasion resistance, high solvent resistance, superior dielectric strength and excellent electrical properties and moisture resistance.	Incompatible with hot oils and cellulosic materials. must be stripped prior to use.
Polyimide (ML)	220 °C	Excellent flexibility, high dielectric strength, adequate abrasion resistance.	Will solvent craze but must be stripped before soldering.

Since armature bars must withstand high temperatures, only the last five film insulation materials were retained for testing. Samples of polyester and ML insulated AWG #20 wires, which were provided by New England Electric and the Israel Electric Wire Company, were tested in order to determine the ease of removal of the insulation by using chemical stripping agents and direct soldering. The four chemical strippers which were used in the experiment were: Insulstrip jell, Insulstrip liquid, Insulstrip 220 and Insulstrip 220 (rev 3053). Samples of these film removers were purchased from the manufacturer, Ambion Corporation. The following results were obtained.

Insulstrip jell is a high speed non-corroding stripper for removing enamel, lacquer and resinous insulation from magnet wires. Wire samples are dipped into the jell, which contains dichloromethane, formic acid, phenol and toluene, and then placed aside. When the blistering of the film insulation is complete, the samples are rinsed with 1,1,1 trichloroethane and water. This product worked best with polyurethane based films and marginally with the polyamide-imide insulation. It was, however, not reactive with high temperature films such as ML. Although this stripper is easy to apply, it typically requires a long time to work and is ineffective at stripping stranded cables. Due to the inability to strip high temperature insulations, this product is unsuitable for our application.

Although much less viscous, the second product, Insulstrip liquid, is chemically similar to Insulstrip jell. Both products work by breaking the bond between the wire and the insulation and cause the film to blister. Wire samples were submerged in a test tube containing Insulstrip liquid until the insulation began to blister or peel away from the copper. Subsequently, the wire samples were rinsed with a solution containing 1,1,1 trichloroethane

and water. The liquid Insulstrip was found to be much more corrosive and quicker in removing film insulation, however it too lacked the ability to strip high temperature insulation materials such as ML. The product nearly dissolved polyurethane based films and performed admirably with stranded cables. Despite the excellent performance with low temperature films, Insulstrip liquid is ineffective with high temperature films and, therefore, will not be used in the manufacture of the armature bars.

The last two strippers, Insulstrip 220 and Insulstrip 220-Revision 3053 are high temperature, high speed dissolving type film removers. Both products are based on sodium hydroxide and are thus highly alkaline. Though environmentally safer than the first two strippers, their use is more complex. A test tube containing Insulstrip 220 was immersed into a beaker containing boiling water in order to maintain the stripper at nearly 212 F. Wire samples were then inserted into the test tube containing the hot stripping fluid and remained submerged until the insulation had dissolved. Wires were then rinsed clean with water. It was determined experimentally that Insulstrip 220 was effective only on polyester (amide and amide-imide) based insulation. The film was swiftly dissolved leaving a clean copper conductor. On the other hand, revision 3053 was very effective at dissolving ML insulation but was incompatible with all other materials. Both of these strippers are ideally suited for litz-wires composed of high temperature film insulation as they could strip stranded cables. However, since the armature bars will be designed with ML insulation, Insulstrip 220-Revision 3053 is the only effective, and thus recommended, stripper.

The ability for a coated wire to be soldered was also gauged. Samples were submerged in a .5 cm pool of a molten eutectic composed of tin and lead (60/40) and the resistance between both ends of the wire was measured with

a Fluke ohm-meter. Only the low temperature polyurethane based films were found to be easily solderable. Hence there is a need for a chemical stripper prior to soldering the end tabs when using high temperature insulations.

Another series of tests was conducted to qualitatively determine the film flexibility and abrasion resistance in order to ascertain windability. The first series of tests involved finding the scratch resistance of the various films. Wire samples were lightly and then more heavily rubbed against a fine sheet of emery board paper and then observed under a magnifying glass. It was determined that polyurethane-nylon, polyester-amide-imide and ML were the most scratch resistant.

The second mechanical test ascertained the flexibility of the coated conductor. Wire samples were put through a hand operated lab bench rolling mill, shown in **Figure 3.1**, and flattened until the insulation gave way or peeled off. The AWG #20 samples were compressed in increments of 8.8 mils, or 13% of the original size of the insulated diameter and observed under the magnifying glass. It was found that ML and Polyester polyamide-imide were, by far, the most flexible films.

The results of the experiments described above have been summarized in **Table 3.3**, for reference. From these tests, it is clear that the Polyimide (ML) insulation is uniquely suited for use in the litzwire forming the armature bars. This film combines excellent mechanical properties, such as flexibility and scratch resistance, good electrical properties and the ability to be completely dissolved chemically. Moreover, this material offers the highest temperature rating of any film insulation (220 °C) as measured according to the NEMA standards at a price significantly below that of Nyleze or APTZ. Hence, it has been experimentally proven that the magnet wires forming the litzwire should be insulated with a heavy coat of polyimide (ML) insulation.



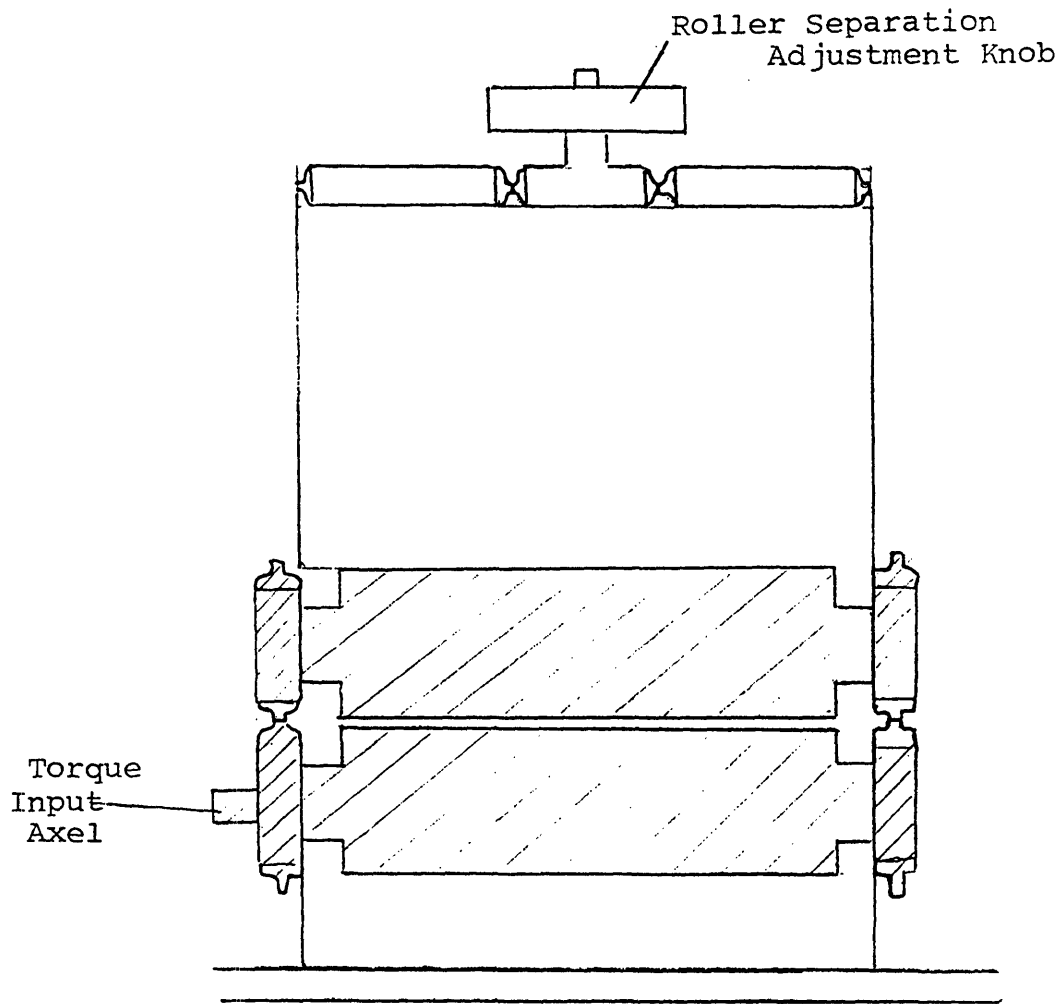


Figure 3.1: Hand Operated Lab-Bench Rolling Mill

T a b 1 e 3.3	Mechanical Test Conductor Insulation	Solder Test	Qualitative Scratch Resistance Test	Qualitative Flexibility Test
	Polyimide (ML) CLASS 220 C	Non solderable. The molten eutectic sticks to the film but does not cause it to burn off	Light friction causes scratches of the film. Heavy friction causes deep blistering of the insulation. Overall scratch resistance: average	Shows some bands at 48% compression. At 35% the bands are more pronounced but there is no cracking of the insulation. Overall performance: excellent
	Polyester Polyamide-imide (also called Armored Poly Thermaleze T) CLASS 200 C	Non solderable. The molten eutectic sticks to the film. After 10 min the insulation blackens and the solder does not bond to the conductor.	LF: causes deep scratches of the film. HF: causes the film to weaken in spots. Overall resistance: above average	Bands appear early (74%) The insulation fails at 48% with the appearance of heavy bands and cracks. Overall performance: good
	Polyester-imide (also called Thermaleze T) CLASS 180 C	Non solderable. The insulation blackens but the molten solder does not bond well with the copper conductor.	LF: causes deep blisters HF: the insulation completely disappears. Overall performance: below average	Stretch bands and tiny cracks appear at 0.74 compaction. The insulation fails at a 61% compression ratio. Overall performance: above average
	Polyurethane with Nylon Overcoat (also called Nylizee) CLASS 155 C	Easily solderable. In 2 min the insulation "boils away" and the eutectic bonds very well with the metal. Results in a low resistance connection. Does not form any thick globs of molten metal.	LF: slight scratches on the insulation. HF: causes deep chaffing of the film. Overall rating: good	At just an 89% compression, deep bands and cracks are clearly visible. Overall performance: below average
	Polyurethane (also called Sodereze) CLASS 155 C	Solderable. In 2 min the film boils away and the eutectic forms a good connection.	LF: the insulation is completely removed. HF: --- Overall performance: below average	Film begins to crack and peel off at a 74% compression ratio. Overall performance: average

Chemical Test  
Conductor Insulation

Insulstrip Jell

Insulstrip Liquid

Insulstrip 220

Rev. 3053

<p>Polyimide (ML) CLASS 220 C</p>	<p>No reaction at all. No reaction to repeated exposure.</p>	<p>No reaction to prolonged exposure</p>	<p>No reaction. With prolonged exposure (15 min) some of the film erodes but the base coat which bonds the film to the metal remains.</p>	<p>Relatively quick reaction. In 6 min most of the insulation is gone After 9 min the film is completely dissolved and the metal is left clean. Works well for stranded wires.</p>
<p>Polyester Polyamide-Imide (also called Armored Poly Thermaleze) CLASS 200 C</p>	<p>Takes a long time to work (15 min). Does not cause a "blistering" of the film only a mild "cracking" of the insulation. Still leaves spots of film on wire. Requires strong rubbing action to be marginally effective.</p>	<p>Fair amount of time to work (5 min). Discrete cracks and spots appear but no blistering. Leaves the sheath of insulation almost intact as it is only capable of separating the insulation from the metal. Can't be rinsed away. Requires strong wiping action.</p>	<p>Rapid reaction (5 min). The insulation is completely dissolved leaving the copper clean. The metal seems free from copper oxides</p>	<p>Ineffective even after 20 min. The film becomes brittle and may be peeled off. Does not dissolve insulation.</p>
<p>Polyester-Imide (also called Thermaleze T) CLASS 180 C</p>	<p>No reaction.</p>	<p>No discernible reaction.</p>	<p>Very rapid on of reaction (2 min). In 3 min the film is spotty. After 5 min the insulation is completely dissolved and the wire is left clean.</p>	<p>No reaction.</p>
<p>Polyurethane with Nylon Overcoat (also called Nylze) CLASS 155 C</p>	<p>Blistering is slightly delayed (2-3 min). Quick reaction (3 min) Insulation is almost completely liquefied. Insulation can be rinsed clear.</p>	<p>Fairly rapid reaction (2 min) The insulation is almost completely separated and "floats away". Insulation may be rinsed off.</p>	<p>No reaction. With prolonged exposure (20 min), a slight discoloration occurs.</p>	<p>No reaction.</p>
<p>Polyurethane (also called Sodereze) CLASS 155 C</p>	<p>Blistering is almost immediate (1 min). The reaction is quickly over (3 min later). The insulation is well broken up into a soft powdery residue. The stripper causes a loosening of the film. A light wipe is needed. Ineffective in between wires.</p>	<p>Works on contact (1 min) Almost dissolves insulation. (very soft) May be rinsed off without wiping. Commendable performance in penetrating between conductors.</p>	<p>No reaction.</p>	<p>No reaction.</p>

### 3) Basic Conductor Diameter

An important consequence of Faraday's law of electromagnetic induction, stated in chapter 1, is the generation of eddy currents. These currents, which flow in closed loops in planes that are normal to the direction of magnetic induction, arise in a conductor through which the magnetic flux is changing.

When the current within the wire alters in direction electromotive forces (emfs) are created because of a change in magnetic flux per unit time ( $\frac{d\Phi}{dt}$ ). Within the conductor, the emfs will induce a type of current defined in **Appendix D** and commonly known as eddy currents. Obeying Lenz's law, these circulating currents act in turn to decrease the magnitude of  $\frac{d\Phi}{dt}$  within the conductor. However,  $\frac{d\Phi}{dt}$  will be reduced if  $\Phi$  within the metal is reduced.

This is accomplished when the concentration of current flows at the surface of the wire and the inside of the conductor is free of a magnetic field. Thus, with wires thicker than the skin depth, there is a tendency for the eddy currents to be limited to the outer skin of the conductor and for the field deep within the metal to be zero, as shown in **Figure 3.2**. Furthermore, since the emfs which produce these effects are proportional to  $\frac{d\Phi}{dt}$ , the magnitude of the circulating surface current increases with the ac frequency.<sup>48</sup> As shown in **Figure 3.2**, the magnetic field outside the conductor is, of course, unaffected by the internal current distribution.

Two conclusions may be drawn from this qualitative explanation of the skin effect. The first is that if a conducting sheet is to be used as an electromagnetic shield, it must be thicker than the skin depth. The second and more important consequence of the rapid attenuation of high frequency fields as they penetrate a conductor is that high-frequency currents are

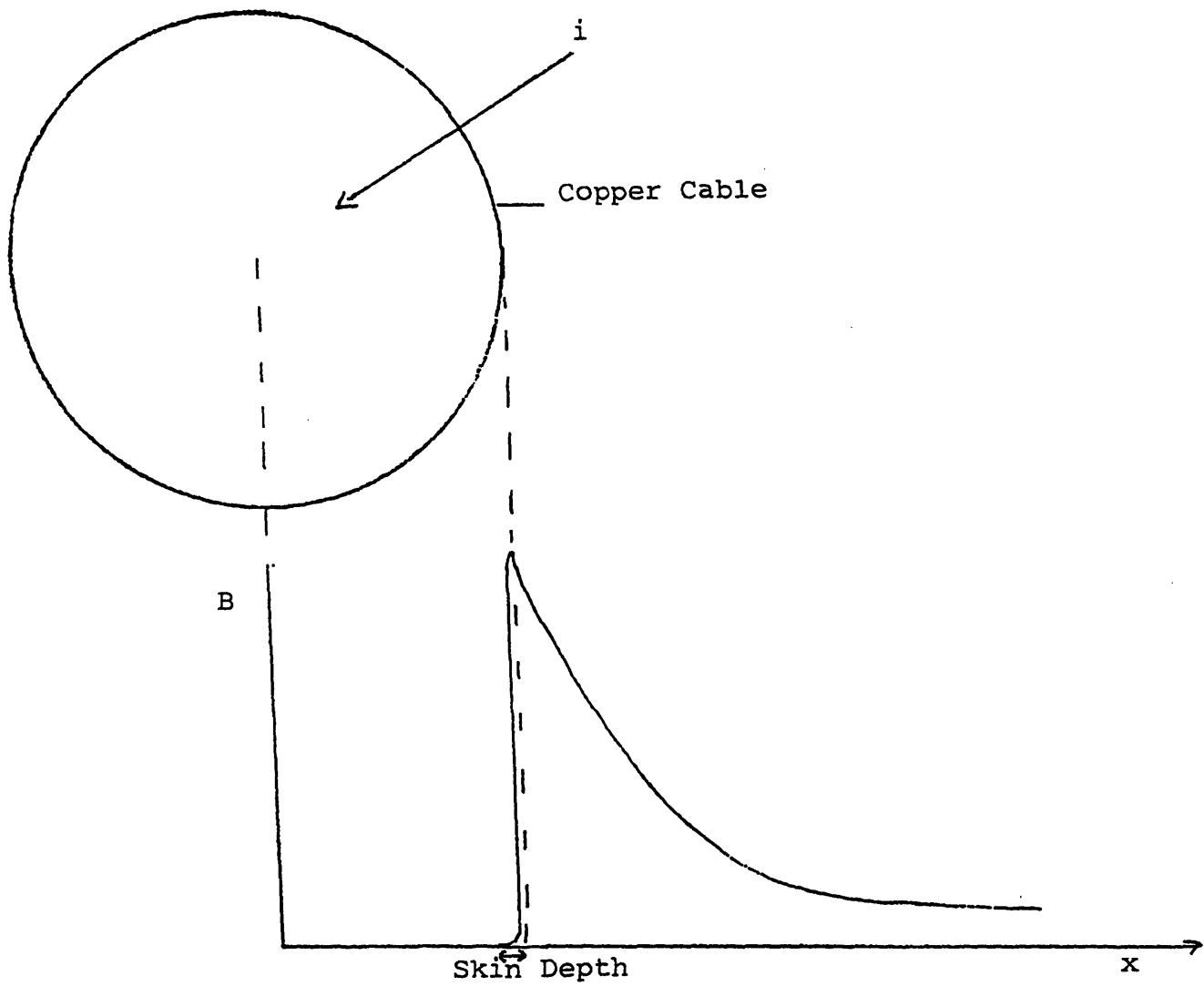


Figure 3.2: Magnetic Field Outside and Just Inside the Conductor

Note: When the diameter is larger than the skin depth the current is limited to the outer skin of the conductor and the magnetic field within the body is 0.

concentrated in a narrow surface shell. This effect, which becomes more pronounced as frequency increases, has the result that the effective resistance of a wire increases with frequency since the effective cross-sectional area of the conductor is decreasing. Thus, for high frequency applications it is preferable to use a wire composed of many fine strands rather than a single large diameter conductor.

Consequently, we must now determine the maximum allowable size for the basic conductors which are to be used in the armature. By modeling a long cylindrical copper wire as an infinite sheet of metal whose thickness corresponds to the diameter of the wire, we find the average power dissipated by the eddy currents in **Calculation 3.1**. We note that the power loss depends on the conduction of the metal, the maximum field, the square of the operating frequency and, most importantly, the fourth power of the wire diameter.

The design tradeoff in the selection of the basic conductor involves balancing the desire for maximum copper space with the necessity to decrease the eddy current loss factor. Thus we must determine the power loss factor per unit volume, which depends only on the square of the diameter, and multiply it by the volume of the active region of the armature. In order to incur less than a .1% eddy current loss, relative to the rated power of the machine, the basic conductor should be no larger than 0.0269 inches. Thus we select AWG #21 as a primary conductor. The 10 kW Joule heating, caused by the eddy currents, will have to be removed by the armature cooling system.

Although the model used in Calculation 3.1 is valid for our generator which operates at a relatively low frequency (60 Hz), the exact solution has

## CALCULATION 3.1

In this calculation we shall derive the power dissipated by eddy current losses for a long cylindrical copper wire by modeling it as an infinite sheet of metal of equivalent thickness equal to the diameter of the wire. Furthermore we shall assume that the diameter of the wire is much less than the skin depth. Since eddy currents arise in a conductor through which the magnetic flux is changing, we shall model the time varying magnetic field created by the rotor by:

$$B = B_o \sin(\omega t)$$

where  $B_o$  is the peak value of the magnetic field at the armature's inner radius and  $\omega$  is the angular frequency. Since the MIT Generator is designed to operate at a frequency of  $f = 60$  Hz,  $\omega = 2\pi f = 377 \text{ rad/s}$ .

The magnetic flux flowing through the wire is found by taking the magnetic field vector and dotting it with the area vector. Since the cross sectional area of the cylinder is a circle, we have:

$$\Phi = B \cdot A = B(\pi r^2) \text{ where } r \text{ is the radius of the wire.}$$

Lenz's law of electromagnetic induction states that an emf is set up in order to oppose the time rate of change of the magnetic flux. Thus:

$$V = -\frac{d\Phi}{dt} = -\pi r^2 \frac{dB}{dt} = -\pi r^2 B_o \omega \cos(\omega t)$$

The power dissipated by the joules effect losses is proportional to the voltage for a material obeying Ohm's law. Therefore:

$$P = I^2 R = \frac{V^2}{R} \text{ where } R \text{ is the resistance of the conductor.}$$

But, by cutting the long wire into a series of concentric "donuts" of radial thickness  $dr$  and of unit axial thickness, as drawn in **Figure 3.3** we may write the resistance as:

$$R = \rho \frac{l}{A} = \rho \left( \frac{2\pi r}{dr} \right)$$

where the length  $l$  corresponds to the perimeter of the donut and  $1 \cdot dr$  is the cross sectional area. We can now write the inverse of the above relation and replace the resistivity of the material by the conductivity. Hence:

$$\frac{1}{R} = \sigma \left( \frac{dr}{2\pi r} \right)$$

Substituting these expressions into the equation for power we obtain:

$$dP = \sigma \left( \frac{dr}{2\pi r} \right) [\pi^2 r^4 B_o^2 \omega^2 \cos^2(\omega t)]$$

By integrating both sides we get:

$$P = \frac{1}{2} \sigma \pi B_o^2 \omega^2 \cos^2(\omega t) \int_r r^3 dr = \sigma \pi B_o^2 \omega^2 \cos^2(\omega t) \frac{r^4}{4}$$

In order to find the average power dissipated during a period, we must take the time average value of the time dependent term. We note that:

$$\langle \cos^2(\omega t) \rangle = \frac{\omega}{2\pi} \int_{-\pi/\omega}^{+\pi/\omega} \cos^2(\omega t) dt = \frac{1}{2}$$

Thus the average power dissipated, over an entire period for a long wire of total length  $l$  is simply:

$$\langle P \rangle = \frac{1}{8} \sigma \pi B_o^2 \omega^2 r^4 = \frac{\sigma \pi B_o^2 \omega^2 d^4}{128} l \text{ where } d \text{ is the diameter of the wire.}$$

It may be shown that for constant space factor, the number of wires is inversely proportional to the square of the diameter. The number of basic conductors,  $n$ , of diameter  $d$  which may be fitted inside a rectangular bar of cross-sectional area  $A_r$ , is:

$$n = \frac{4A_r}{\lambda \pi d^2} \text{ where } \lambda \text{ is the space factor}$$

Thus the total eddy current loss for the entire winding is given by:

$$\langle P \rangle = \frac{\sigma B_o^2 \omega^2 d^2 A_r}{32\lambda}$$

or alternatively by:

$$\langle P \rangle = \frac{3}{32} \theta_{\text{vac}} R_{\text{ao}}^2 (1-x^2) \omega^2 \sigma \lambda B_{\text{av}}^2 l_{\text{ed}} d^2 \text{ (Basic Field Analysis, Rating Laws, Summer}$$

Program, J. L. Kirtley, Jr., 1974)

where  $\theta_{\text{vac}} = \text{Pole pairs} * \text{armature winding angle}$ ,  $R_{\text{ao}}$  is the outer radius of the "A" phase,  $x$  is the ratio of the inner to the outer radii of phase "A",  $\lambda$  is the space factor and  $B_{\text{av}}$  is the mean-squared magnetic field seen by the conductor. As explained above, we note that the power loss is now proportional to the square of the wire diameter

\* \* \*

We shall now use the formula for the power dissipated by eddy currents for a single round wire. Recalling that the machine is composed of three phases which are, in turn, composed of 34 turns each and that each turn is composed of a combination of an inner layer bar (of total length 46.758 inches) and an outer layer bar (of length 50.852 inches) we can determine the total conductor length:

$$l = 3 * 34 * (46.758 + 50.852) = 9,956.22 \text{ inches} = 252.880 \text{ m.}$$

The conductivity of copper, the conducting material, is:

$$\sigma = 1/\rho = 5.882 \times 10^{-9} \Omega^{-1} m^{-1}$$

Since it was determined in the previous section that the bars would measure 1.481 by 0.295 inches,  $A_r = 0.4369 \text{ square in} = 2.8187 \times 10^{-4} m^2$

Allowing for a realistic space factor of 125% and recalling that the peak magnetic field at the inside of the stator is  $B_o = 1.2 \text{ T}$ , we may solve for the maximum allowable diameter as a function of allowable losses. Tolerating a maximum of .1% eddy current loss relative to the rated power of the machine, we find:

$$d = 6.8272 \times 10^{-4} m = \underline{0.0269 \text{ in}} \text{ which is closer to } \underline{\text{AWG \#21}} \text{ than to AWG \#22.}$$

Thus we have selected the diameter of our basic conductor.

We should note that the exact solution to the cylindrical wire is much more complicated. The electric field within the wire must satisfy  $\nabla^2 E = 0$  and be a solution to the Dirichlet problem. The radial symmetric form of the Laplace equation for the electric field in cylindrical coordinates is:

$$\frac{d^2 E}{dr^2} + \frac{1}{r} \frac{dE}{dr} - \gamma^2 E = 0 \text{ where } \gamma = \sqrt{j\omega\mu\mu_o\sigma} \text{ is the propagation velocity.}$$

The solution of this equation, which involves Bessel functions, is:

$$E = C_1 I_o(\gamma r) + C_2 K_o(\gamma r) \text{ where } I_o \text{ and } K_o \text{ are Bessel's and Hankel's functions of imaginary}$$

argument.

Since  $E$  must be finite at  $r=0$   $C_2$  must be zero and the solution is just the first term.



It can be shown that the current density within the conductor is given by:

$$I = \frac{I^2}{\pi r^2} \frac{\gamma r I_0(\gamma r)}{2 I_1(\gamma r)}$$

This function has been plotted in **Figure 3.4** for wires of increasing diameter. It can be seen from the graph that, as explained above, the current density acquires its lowest value along the mid-line of the wire and increases towards the surface. We note that the skin effect increases with the radius, conductivity, permeability of the metal and operating frequency.

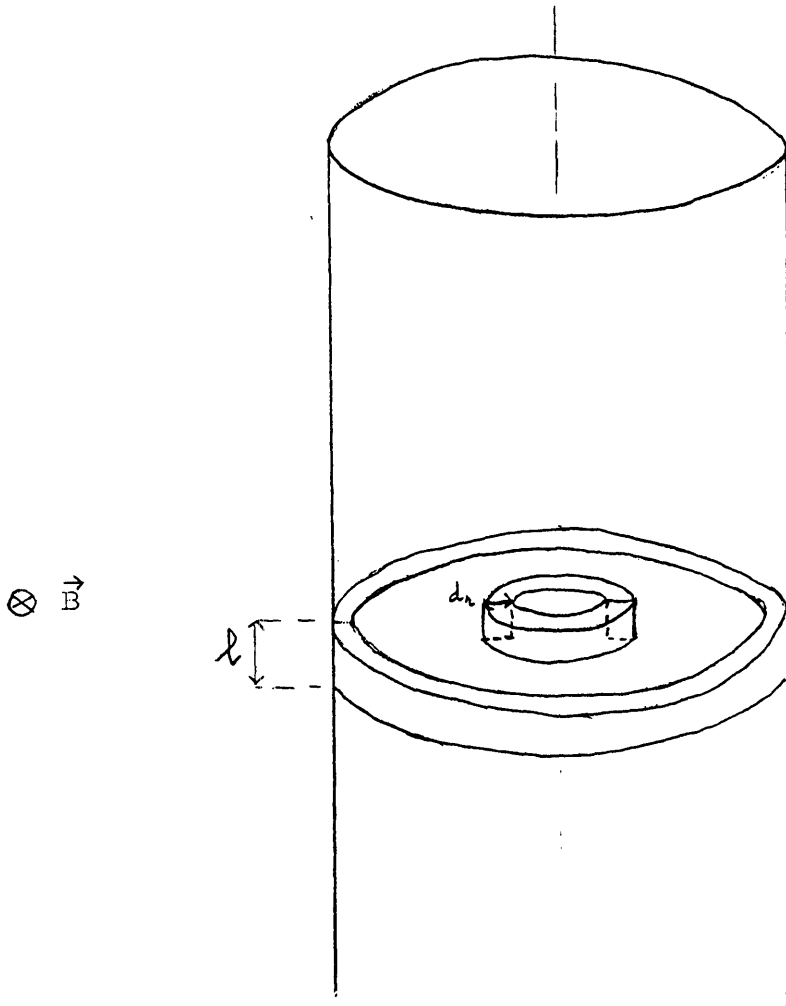


Figure 3.3: Cut of a Conducting Wire into Thin Concentric Shells

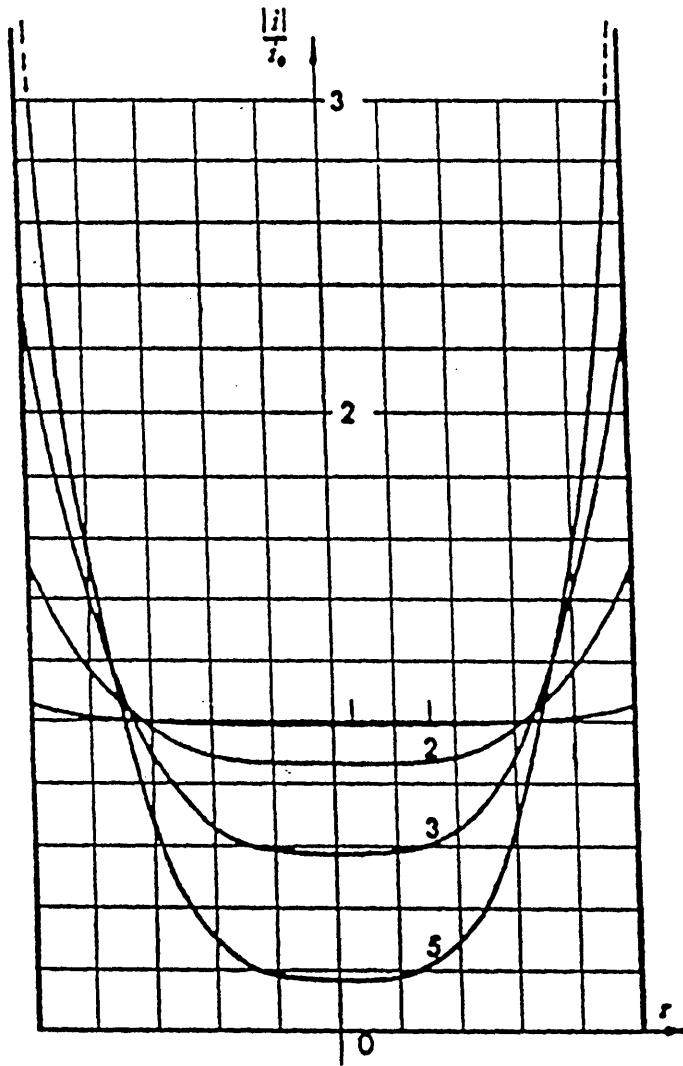


Figure 3.4: Distribution of the Induced Current Within  
a Copper Wire at Increasing Operating Frequencies

been included for completeness<sup>49</sup>. The results obtained by the infinite sheet approximation fall within 1% of those predicted by the Dirichlet model<sup>50</sup>.

We should point out that although we have selected the diameter of the wires in the armature bars to be much less than the skin depth, there are times where it is useful to design components which are thicker than the skin depth. For instance, in order to protect the rotor from the large first harmonic ac fields generated in the stator core, a shield with a thickness greater than the skin depth is required. At the 60 Hz operating frequency the circulating currents are less than 1% of their value at the surface at a depth of about 1.8 inches. The currents which flow in this thick shield are dampened by a resistor located in the rotor assembly. A second shield which is made of a rolled sheet of copper is placed inside the outer shield and serves as a barrier to 3rd and 5th harmonic losses. Although it would be possible to design the entire shielding system with just the second shield, it would not be practical since the rate at which the helium would boil off (as a result of large Joules effect heating) would be too high. Since both shields spin with the rotor assembly, they do not see a change in the rotor's magnetic flux and hence do not have any effect on the field created by the rotor.

#### 4) Design of Conducting Bar

In choosing a design for the conductor bar we must consider three factors. First we need a cable in which the conductors undergo a full transposition pattern. In other words, in order for each of the basic conductors to be at the same potential at the end of the armature, all of the strands should take all possible positions in the cross section of the bar. Hence our need for a Litz wire. Our second requirement involves maximizing the armature space factor. Thus, armature bars with a rectangular cross section are to be used in order to fill the space available in the armature as

much as possible. Third, the actual length of the conductors within the litz must be as short as possible in order to reduce Joules losses. Thus we find that the Roebel transposed rectangular compacted litz (type 8) pioneered by New England Electric Wire Corporation is ideally suited for our application.

Having selected a litz cable design we must now determine its construction. In chapter 2 we calculated the dimensions of the conductor bar based on the design requirements. It was determined in the engineering design spreadsheet that the conductor bars would be 1.481 inches high by 0.295 inches wide. Since the litz cable will be composed of heavily insulated 21 gage wires, in order to increase the film's windability, we must take the insulation thickness into account. The New England Electric Catalogue states that at AWG #21, the heavy insulation thickness measures 0.0021 inches over the bare wire diameter of 0.0285 inches. Thus we are to design a cable composed of magnet wire of effective diameter of  $d = 0.0306$  inches.

The easiest solution would be to build the litz out of 19 bundles of wires, which are in turn composed of 19 basic conductors. The bundles of wires would be constructed of two concentric layers of wires of alternate winding direction wrapped around a central wire. This closed packed form would have one wire at the center, six wires in the first layer and twelve in the outermost layer. The bundles themselves will be woven into two "columns" of bundles and then be put through a Turk's head press to form the bar. The compaction and the back twist on the bundles and wires prevent the bar from unwinding and coming apart easily.

The cross sectional dimensions of the rectangular compacted litz that was selected depends on the effective diameter of the insulated basic conductor. As it can be seen from **Figure 3.5**, the dimensions of the conducting bar is slightly discounted by the disposition of the outermost

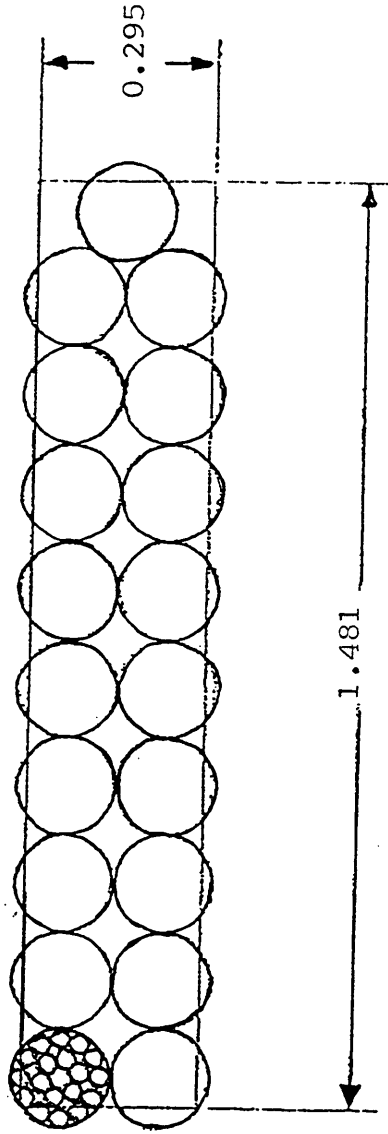


Figure 3.5: Relationship Between the Basic Conductor Diameter and the Overall Dimensions of the Litz Wire

wires. Since the diameter of a bundle of wires is five times that of a wire, it can be shown that the relationship between the diameter of the wire and the size of the litz are:

$$H = \text{Height} = \left[ (10 * 5) - \frac{2}{\cos \alpha} \right] * d \text{ and}$$

$$W = \text{Width} = [(2 * 5) - 1 * \cos \alpha] * d$$

where  $d$  is the insulated wire diameter and  $\alpha$  is the winding angle which, for this type of cable, is usually around  $15^\circ$ . We find that: Height = 1.4667 and Width = 0.2764 inches and thus we are close to our required dimensions. In reality, the size of the wire can be adjusted by varying the winding angle. At these dimensions, however, the bar's packing factor is:

$$\lambda = \frac{361 * \pi * d^2}{4 * H * W} = 65.5\%$$

The next, but related, item which must be specified to the wire manufacturing plant is the *twist pitch*. The twist pitch is the "wavelength" of the winding of the litz cable. As shown in **Figure 3.6**, it is the length required for a bundle to travel back to the same position. The twist pitch,  $l$ , is related to the winding angle by:

$$l = \frac{2H}{\tan \alpha}$$

Since we want all of the conductors to link the same amount of magnetic flux, we must select our litz so that the length of the active portion of the bar corresponds to a multiple of one and a half (1.5) of the twist pitch. Furthermore, since we strive to reduce Joule effect losses, we shall select the lowest possible multiple that can be accommodated without compromising the integrity of the cable. The design specification data contained in Table 2.5 indicates that the average active length of the conductor bar is about 47.30

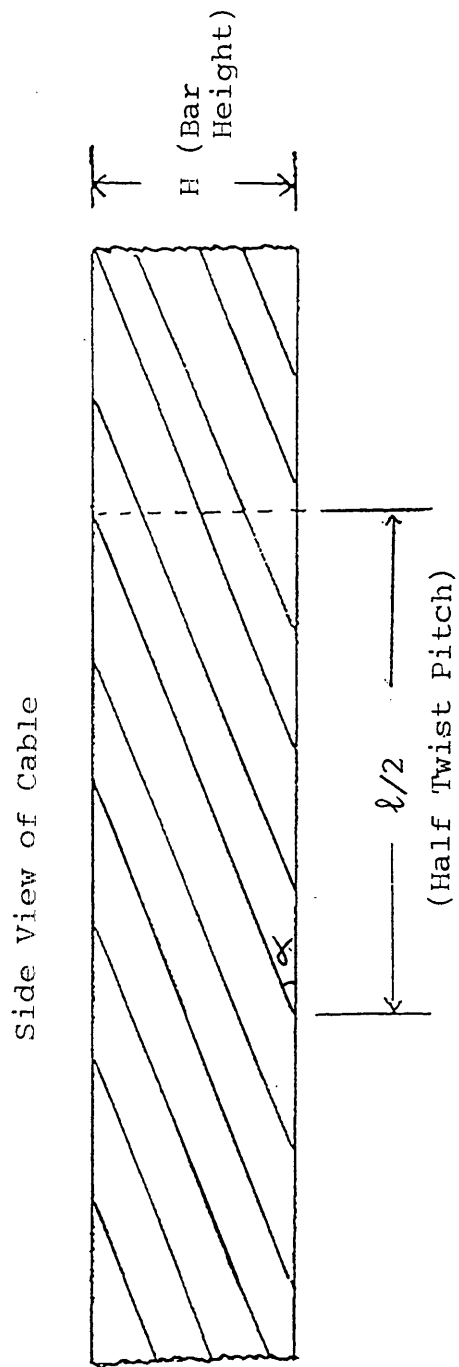


Figure 3.6: Definition of the Twist Pitch



inches, thus if we make the pitch angle  $15.5^\circ$  the bar length would measure nearly 4.5 times the twist pitch.

The bar design requirements listed above have been accepted by New England Electric and a copy of the quote has been placed at the end of this thesis.

### **3.2 Selection of the Bar Insulation**

The bar insulation is an important component of the bar subassembly. When properly prepared, this insulation individually sheathes each of the conductor bars selected above, and together they form an armature bar. The bar insulation serves two purposes. First it electrically shields the armature bars from each other so that they may be closely packed. Second, with the removal of the thick major insulation layer that was used in the delta machine, the bar insulation should also offer a mechanical resistance to shear stresses occurring during electrical transients. Thus, the two overlying design requirements for the bar insulation are: high steady-state dielectric strength and high mechanical shear strength.

#### **1) Electrical Requirements**

To achieve a high steady-state dielectric strength, a material should have three characteristics<sup>51</sup>. First, the insulation should be composed of a material with a high intrinsic dielectric strength. In conventional generators the insulation, which was designed to insulate bars in iron slots, was composed of a woven cotton cloth impregnated with asphalt. Often large flakes of mica were stuck to the asphalt since this mineral is an excellent electrical insulator and resists corona. Although this type of insulation is often used for low power generators, it is inadequate for our unit since the bitumen impregnation may migrate out of the bars and leave voids.

The second characteristic is that the material must have a homogeneous structure in order to avoid electrical stress concentrations. *Voids*, or spaces of vacuum or air, perturb the consistency of the bar and can cause high electrical stress concentrations which may, in turn, lead to dielectric breakdown and tracking. The voids themselves may cause a surface breakdown of the insulation, called corona, and lead to a failure of the insulator. Thus, because of the non uniform nature of the aforementioned insulation schemes it is impractical, if not impossible, to obtain a uniform bar. An elegant solution to this problem is to use a mica paper, whose electromechanical properties are consistent since it contains very small flakes, and impregnate it with an epoxy resin whose dielectric properties are similar to those of the insulating material.<sup>52</sup> Other solutions to the problem would involve liquid impregnants such as oil and cellulose, or extruded plastics such as polyethylene.<sup>53</sup> However, research indicates that cellulose breaks down at high temperatures and that thermoplastics are subject to tracking.<sup>54</sup> Thus, we will investigate the use of impregnated cloth and impregnated synthetic paper, such as fiberglass and Nomex respectively.

The third characteristic of the insulating material is that it should have good resistance to corona. As explained before, mica offers a good corona resistance while being an excellent insulator. Since voids may become locations for corona inception, and thus cause the insulation to eventually fail, the bar manufacturing process must ensure their absence. Since voids are usually composed of air or of empty space, their removal may be accomplished by one of two ways. The first method involves using a vacuum and subsequently replacing the spaces by an epoxy delivered under pressure. This process, known as *vacuum/pressure* impregnation, typically uses a 100-1000  $\mu\text{m}$  of mercury vacuum and an epoxy delivery pressure of about 100

psig.<sup>55</sup> Another, more practical, method involves the hot press or shrinkable film molding of resin-rich tapes.

Under steady-state operating conditions, the *nominal insulation stress* must typically be between 30 and 40 V/mil. In the present generator, the maximum difference in potentials between the bars occurs at the center of the armature, where radially separated bars have a potential difference equal to the line voltage. Thus, for a 33.3 V/mil nominal stress, the two bars should be separated by:  $4000(\text{V}) / 33.3(\text{V}/\text{mil}) = 120$  mils of insulation. Disregarding the center cooling channel and the cooling fluid, each of the bars requires an insulation thickness of about 60 mils for full line-to-line shielding.

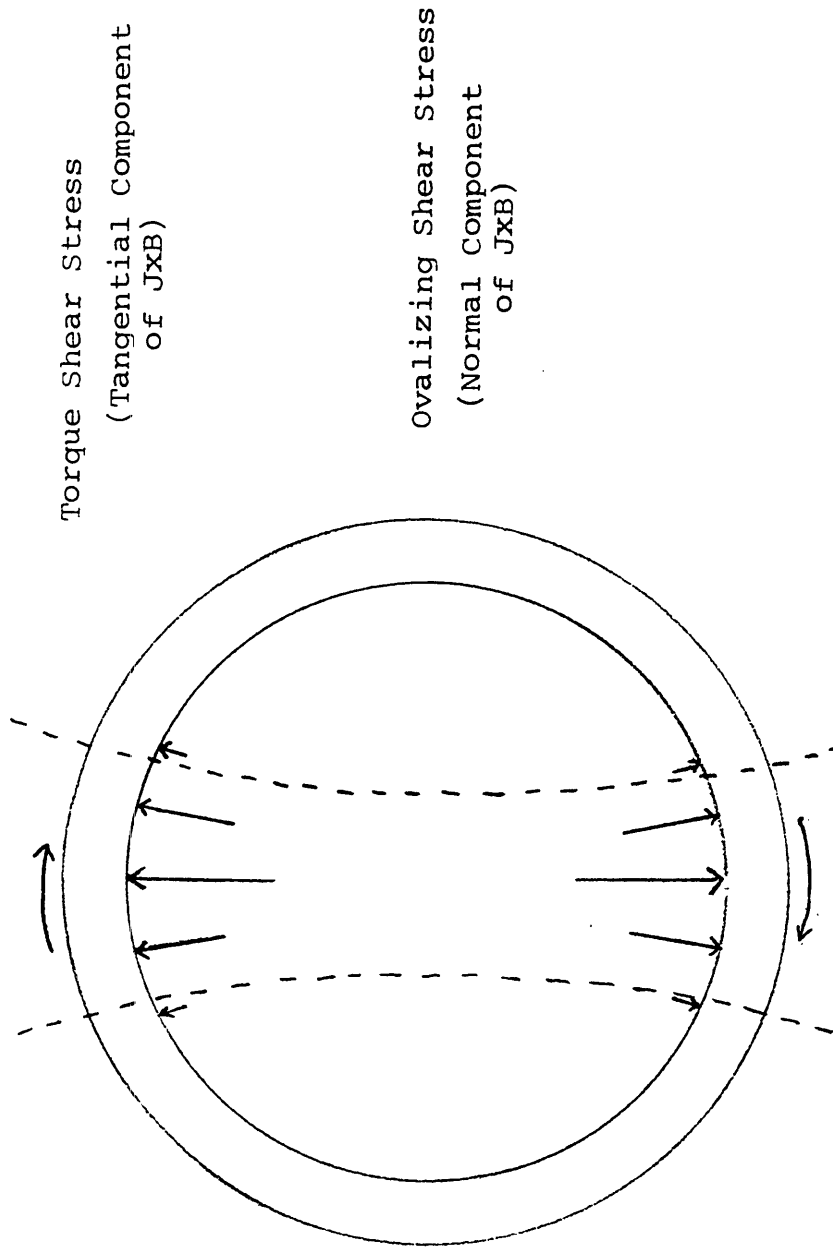
In order to be certified, the generator must meet certain ANSI standards (C50-15) pertaining to its basic insulation limit (BIL). Two tests are usually performed for certification. The first test, also known as the *proof test* or the acceptance test, consists of exposing the generator to twice the rated voltage plus 1 kV for one minute to a 60 Hz wave form. In our case, the peak voltage is:  $V_{\text{proof}} = 9$  kV. Although the significance of this test is controversial, it contends that if the generator can survive at the *surge voltage* for an interval of one minute, that it can operate at the rated voltage for a period of about 20 years.

The second test, called the *impulse test*, involves exposing the generator with the surge arrestors to large high frequency voltage spikes. It should be pointed out that this high frequency test, which is often used for transformers, is almost meaningless for an air-gap machine. These two tests reassure us that the value of the machine's *short term voltage breakdown* is in excess of the proof voltage and that tracking will not occur during switching surges that occur during normal operation.

## 2) Mechanical Requirements

With the major insulation system no longer present in the new design, as explained above, the mechanical duties of the bar insulation are much greater than in the old delta machine. During a sudden terminal fault, the voltage in one or more phases is nearly zero and the magnetic flux is trapped within that phase. The currents which flow in the armature winding to maintain the trapped flux produces image currents on the rotor's surface and the interaction between these currents produces a stress distribution. The two principal mechanical stresses that occur within the armature during transients are the shear stress, due to the ovalizing forces on the armature, and the torque shear stress. Although the ovalizing shear stress is much greater than the torque shear stress, the fluid between the monolithic armature and the magnetic shield serves as a support and prevents large deformations of the stator. Thus this ovalizing shear stress becomes more of a compressive stress on the bars. The torque shear stress, therefore, becomes the dominant shear in the armature and must be taken into account in the stator design. Both of these shear stresses are due to the  $\mathbf{J} \times \mathbf{B}$  cross product. However, the ovalizing stress is due to the normal component and the torque shear stress is due to the tangential component. Hence, the two values are out of phase with each other but they both have the same periodicity. **Figure 3.7** illustrates the distribution of the two components of  $\mathbf{J} \times \mathbf{B}$  that cause the two fault stresses.

Two possible solutions for the bar insulation suggest themselves. Although the possibility of a compliant insulation was investigated, the nature of commercially available products and the machine geometry favor the choice of a rigid insulation system. To achieve a high mechanical shear



Torque Shear Stress

(Tangential Component  
of  $J \times B$ )

Ovalizing Shear Stress

(Normal Component  
of  $J \times B$ )

Figure 3.7: Fault Stresses on the Armature Winding

strength, a material must have both an intrinsically high shear strength and a homogeneous structure.

The need for materials having an intrinsically high shear stress has been of paramount importance throughout the evolution of new insulating materials. For example, the original material used in the cotton/asphalt insulation was replaced by a woven fiberglass cloth which offered a much higher tensile strength as well as significantly better thermal properties (105 vs. 260 °C). Synthetic papers, such as DuPont Nomex, offer significant mechanical advantages over natural pulp-based paper but have a lower tensile strength than fiberglass cloth. As explained previously, mica is an ideal electrical insulator, but has a poor electrical shear strength since its structure is planar. Mica paper must be wrapped in half lap layers (an analogous disposition is that of a brick wall) and cured with epoxy in order to prevent the interfaces between each layer from degrading the shear strength. Furthermore, the regular winding of the insulation and the monolithic nature of the bar give rise to a homogeneous structure and thus reduce local mechanical stress concentrations.

The mechanical stress analysis for a helically wound air-gap armature winding was performed by Peter Conley and Patrick Bolger in 1980. Since a full stress analysis is beyond the scope of this paper, only a first order analysis is presented in **Calculation 3.2**. Although our crude determination of the shear stress, due to the ovalizing forces on the armature, concurs with Conley's result of about 2,100 psi<sup>56</sup>, the more precise calculations undertaken by Bolger<sup>57</sup> show that the maximum shear stress in the machine is about 725 psi. The maximum mechanical shear stress occurring in between the two layers of bars is calculated to be of the order of 385 psi, in accordance with the results reported by General Electric Corporation<sup>58</sup>.

## CALCULATION 3.2

### Mechanical Shear Stresses in the Armature

In this calculation we shall determine the shear stress due to ovalizing forces on the armature and the mechanical shear stress expected in between the two layers of bars. Although these calculations are imprecise at best, they serve to gain some insight as to the mechanical and structural requirements.

#### I. Torque Shear Stress for a Thin Circular Section

According to the sixth edition of Roark's Formulas for Stress and Strain, the torsional stiffness for a concentric circular section of inner radius  $r_i$  and outer radius  $r_o$  is:

$$K = \frac{1}{2}\pi(r_o^4 - r_i^4)$$

Thus, the maximum torque shear stress, at the outer boundary, is given by:

$$\tau_{\max} = \frac{2Tr_o}{\pi(r_o^4 - r_i^4)} \text{ where } T \text{ is the applied torque.}$$

However when the annulus is thin, the inner and outer radii are almost identical and the aforementioned formula can be simplified considerably. Thus when  $r_o \ll t$  we may write:

$$\tau_{\max} = \frac{T}{2\pi r_o^2 t} \text{ where } t \text{ is the thickness of the section.}$$

#### II. Shear Stress due to Ovalizing Forces

The ovalizing shear stresses, which are the largest stresses in the machine, depend on the three phase fault torques. During the normal operation of a generator, the rated torque which is supplied by the prime mover does work in order to generate electric power. When the MIT superconducting generator, which is rated at 10 MVA and runs at an angular frequency of 377 rad/s, is in steady-state operation the LM-1500 gas turbine must supply a torque of:

$$T_r = \frac{P}{\omega} = 2.65 \times 10^4 \text{ N.m}$$

The three phase fault torque, which has been explained in this chapter, is related to the rated torque by:

$$T_f = \frac{1.3}{\text{Subtransient Reactance}} \times T_r$$

The sub-transient reactance of our generator is nearly 13% and thus the fault torque is roughly ten times the rated torque. Hence:

$$T_f = 2.65 \times 10^5 \text{ N.m}$$

The net torque which is transmitted out of each end of the machine is about one half of this value, or  $T_t = 1.3 \times 10^5 \text{ N.m}$ .

The maximum torque shear stress present at the outer bore tube of radius  $r_o=13.372$  inches and thickness 0.450 inches may be found by using the formula derived above. Thus we determine that:  $\tau_{\max} = 15.6 \text{ Mpa}=2270 \text{ psi}$  which is similar to Conley's value of about

2100 psi. However, Bolger's detailed analysis proved that the actual value for the shear stress is closer to 750 psi.

### III. Mechanical Shear Stress in between bar layers

The torque shear stress which occurs in the region in between the two layers of bars is due to the tangential component of  $J \times B$ . We will now concentrate on a thin axial cut taken at the center of the machine. Working in a 60 degree wedge of the armature (see **Figure 3.8**), which is the space occupied by one of the six phase belts, we notice that the 17 upper bars and the 17 lower bars carry the current in the same direction. Having determined that the bar current is about 1,445 A, the basic current flowing through the wedge is:

$$I_b = 1,445 \times 34 = 49,130 \text{ Amp turns.}$$

The surface current may be found by dividing the basic current by the length of the arc subtended by the wedge's cross section. The surface current is therefore largest at the inner radius ( $r_i=9.221$  inches) of the 60 degree wedge. Hence:

$$I_{sMax} = \frac{I_b}{r_i\theta} = 200,312 \text{ A/m}$$

The maximum value for the space fundamental, which corresponds to the first order coefficient of the Taylor approximation of the total current, is given by:

$$S_{Max} = \frac{3}{2} I_{sMax} \sin(\theta) = 260.2 \times 10^3 \text{ A/m}$$

Knowing that the total magnetic field in the center of the armature is about 1.2 T peak (=0.8485 T rms), we determine that the shear stress occurring in the wedge is:

$$\tau_{Max/wedge} = S_{Max} \times B_{tot} = 220.8 \text{ kPa} = 32.02 \text{ psi}$$

Since the torques due to the electromagnetic force acting on each of the six wedges are additive, the total torque shear stress in the center of the armature is:

$$\tau_{Max} = 6 \times \tau_{Max/wedge} = 192.14 \text{ psi}$$

Now we must find the total shear stress for the entire armature, not just in the center. Knowing that both the current and the magnetic field have a sinusoidal distribution in the axial direction and that they are both maximum in the middle of the stator, we may write:

$$\tau_{Total} = 2 \times \tau_{Max} = \underline{384.3 \text{ psi}} \quad \text{since } \langle \sin^2(\frac{z}{l}) \rangle = 1/2$$

Our final result falls well within the values of 200-400 psi predicted by General Electric. We note that this shear stress is well within the capabilities of certain bar insulation materials.



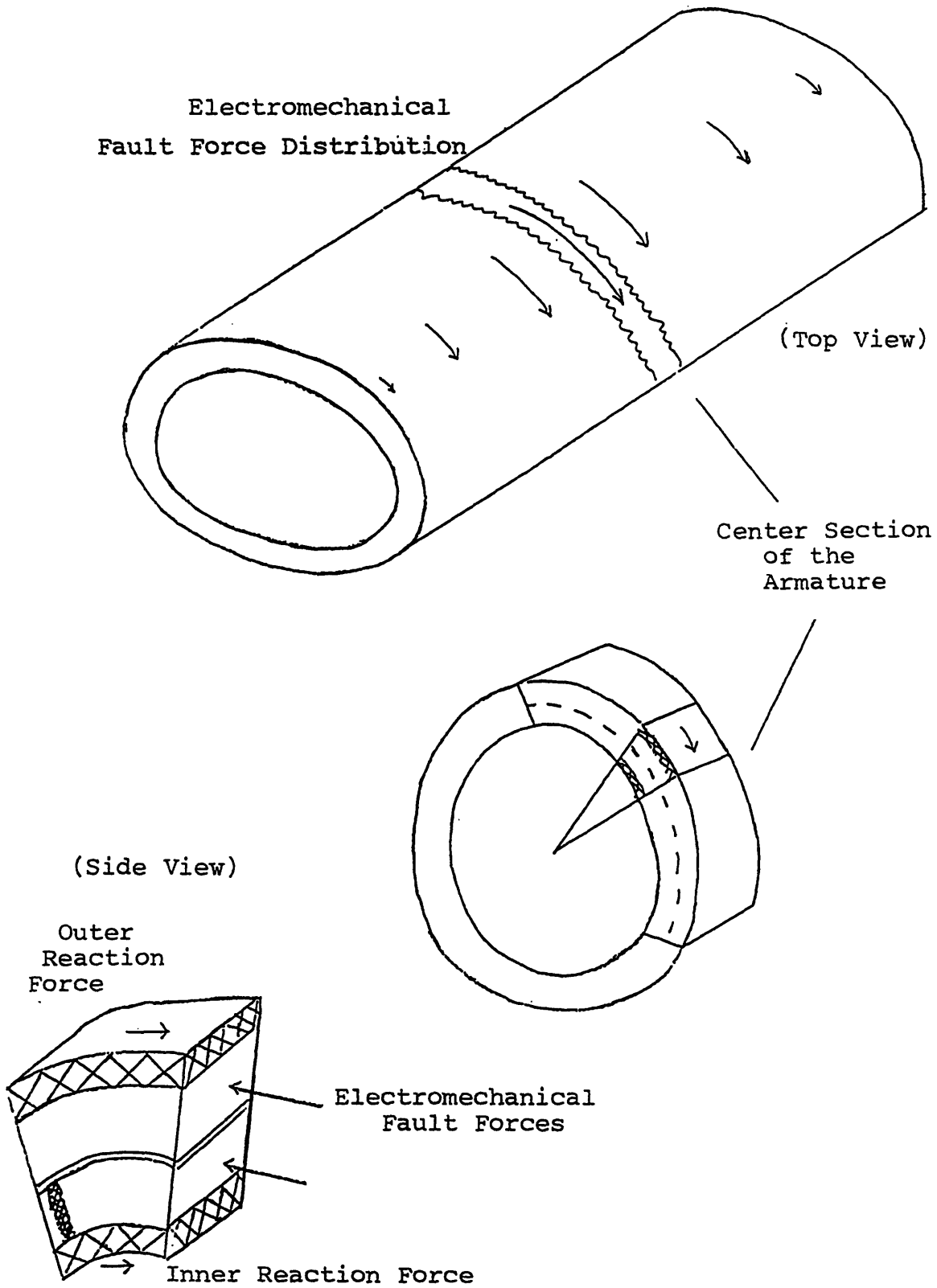


Figure 3.8: Torque Shear Stress on a Center Section  
Of the Armature

### 3) Selection Criteria

Although there is no single material that possesses all of the desired characteristics described above, a composite material could be selected so that the two materials may complement each other's abilities. Research was therefore concentrated on the selection of resin impregnated solid insulation systems.

The selection criteria for the solid insulation demanded that the material have a high dielectric strength, a good corona resistance, is suitable for impregnation and has a high mechanical strength and temperature resistance. The resin must also have good electrical properties and mechanical strength as well as a low viscosity, a long pot life and a high heat distortion temperature. The resin and the solid insulation must be compatible with each other, have reasonably similar properties and be commercially available.

We investigated three separate materials which meet our selection criteria described above. The first material, Owens Corning type E glass was selected for its intrinsically high shear stress despite its lackluster electrical performance. According to the vacuum/pressure impregnation (VPI) tests performed by Wayne Hagman, the best resin to impregnate type E fiberglass is GE Arnox 3120, despite its relatively short pot life of about 8 hours. Resins which are to be used in VPI systems must be solventless in order to allow for vacuum degassing. After curing the sample at 80 °C for one hour and at 175 °C for half an hour, Miller Stevenson MS-122 is injected as a mold release agent. This process was reported to yield samples that were rigid and fully cured, but which had indentations along the top surface.

The second material, DuPont Nomex M Type 418 is an aramid and mica paper with outstanding electrical properties but with mediocre shear

strength. The VPI tests performed in 1981 indicated that the optimal products to use were a Shell Epon 826, 100 pts solventless resin with NADIC Methyl Anhydride (89 pts) and Benzyl-dimethylamine (1 pt) as an accelerator. Using Dow-Corning DC-7 as a mold release, a homogeneous and fully impregnated sample could be easily manufactured and released from the mold. With a pot life of nearly a week and a cure schedule of only an hour at 120 °C, this process is more efficient and also yields better samples than the previous one. Although this material was used in the major insulation layer of the 10 MVA Delta machine, a better insulation material for the bars of the new generator was indicated.

It was clear from the aforementioned results that a fiberglass and mica tape would combine the electrical advantages of the mica with the superior mechanical characteristics of fiberglass. Furthermore, it was determined that a vacuum pressure impregnation treatment was not necessary in our 4 kV design and that a more practical high voltage insulation technology was called for.

An extensive search revealed that a resin-rich treatment (RRT) would offer a number of benefits which were ideally suited for our application. The RRT allows for denser structures with higher mica content for maximum voltage life, mechanical strength, space factor and thermal conductivity. In addition, the technology permits a better control of the size and shape of the bars and minimizes corona discharge through the use of corona suppressants.

MicaMat, manufactured by Insulating Materials Incorporated, a General Electric spin-off, is a family of B-staged epoxy resin-rich tapes compatible with RRT processing. The tape, which consists of a fiberglass cloth reinforced by a polyester mat and contains thin mica flakes, is placed in a form for hot molding. Since MicaMat is solventless, vacuum processing is

no longer required to remove volatiles. Furthermore, by using pre-impregnated tapes the need for large quantities of resin and impregnation tanks are eliminated and manufacturing is greatly simplified. Mr. George Cotzas of General Electric in Schenectady reported that this process had been used by the Power Generation Unit and that satisfactory results were obtained. Unfortunately, samples were not released to us by the time of writing.

Using the IMI Material Insulation Handbook, we realize that MicaMat 77984 is recommended for both ground insulation of high voltage ac stator windings and for shop winding using RRT. In addition this product has a relatively high temperature rating of 185 °C. A summary of the properties of Nomex M 418, Dow Corning E type glass and GE MicaMat 77984 have been reported in **Table 3.4**, below.

**Table 3.4:** Comparison of Bar Insulation Materials

	Nomex 418	Corning E	MicaMat
Max. Temperature (°C)	250	260	185
Nom. Fin Thickness(mils)	14	10	8.5
Density (g/cc)	1.12	1.42	1.3
Tensile Strength (psi)	85	500	450
Elongation (%)	3.0	4.8	3.2
Max Tear Resistance	8.5	51	46
Tear Strength (elm.)	7.8	8	8.1
Thermal Conduct(W/mK)	0.097	0.155	0.142
Dielectric Constant(kV/mm)	36	6.33	30
Max. Electrical Stress (v/mil)	50	10	65

Thus, it is clear that the resin-rich treatment of IMI MicaMat 77984 will yield the ideal bar insulation system while simplifying manufacturing. A finished thickness of 60 mills is expected after the epoxy is cured for one hour at 150 °C.

### **3.3 Design of the End Connector**

The end connectors, which are located at both ends of each armature bar, have been of a particular interest in this research. In the old Delta connected 10 MVA machine, the end connectors were essentially copper tabs which were brazed onto each layer of the armature bar. Experience has shown that this process was tedious and far too labor intensive for efficient manufacturing. Furthermore, since the armature bars used in the present design are composed of a single monolithic litz, the old end-tab design is, of course, unsuitable. Thus, a new solution for the end connectors must be found based on our three main design requirements.

The ideal end-connector must allow the current of a bar in one layer to flow to a bar in the opposite layer with the minimum amount of resistance. Thus, end connectors must be manufactured of a material with a coefficient of conductivity similar to, or better than, that of copper. Since a silver connector is economically unjustifiable, the end connectors will be made out of copper. However, in order to secure the end connector to the conductor bar and insure a good electrical connection, a silver or eutectic solder is recommended. In addition, the end connector's cross section will be designed to be twice that of the bar so as to significantly reduce the current density.

The end connector, which will have to be insulated, must also be designed to conform to the tight space available in the straight end-section of the armature. It was determined in the last chapter that the maximum size for the uninsulated end connectors is about 80 mils. Although the radial and azimuthal space are limited, the axial space does offer a leeway of about two inches per side. By staggering the locations of the end tabs and by stretching the tabs in the axial direction, it is possible to take advantage of this extra

space. It is also possible to gain additional azimuthal space for the end connector by using a tapered design.

The third and final design requirement involve manufacturing. The process of installing the end connectors must be efficient and integrated. Connecting the appropriate bars in the armature must be made simple, despite the limited space available, without sacrificing reliability.

An optimal design quickly emerged from our standard product development method and our design requirements. The end connector will consist of a close die forged tapered copper sleeve, designed to fit over a tapered bar, with a machined L shaped tab, as shown in **Figure 3.9**. It was experimentally determined, by using a test press, that litz cables could be compressed to one half of their standard thickness over a run equal to the height of the bar without incurring any conductor breakage. Therefore, the specifications for the die that will be used in a press to deform the cable into the shape depicted in **Figure 3.10** are straightforward to determine. On one side the die must be .295 inches deep while on the opposite end, 1.5 inches away, the die should measure .147 inches in depth. The constant slope angle is determined to be:

$$\beta = \tan^{-1} (t/4h) = 2.85^\circ \text{ where } t \text{ is the thickness and } h \text{ is the height of the bar.}$$

Thus, the dimensions of the end-connector vary from a sleeve of about 20 mils in thickness over an opening of about 1.485 inches long by 0.298 inches wide at the thinnest part to a sleeve of about 93 mils thick in the width direction and 20 mils thick in the length direction over an opening of about 1.485 by 0.151 inches in the mid section. By using such a design, see **Figure 3.11**, the conductor surface area of the end cap is about 1.2 times larger (.437 vs. .511 sq. in) than that of the original sized bar and the current density is therefore reduced.

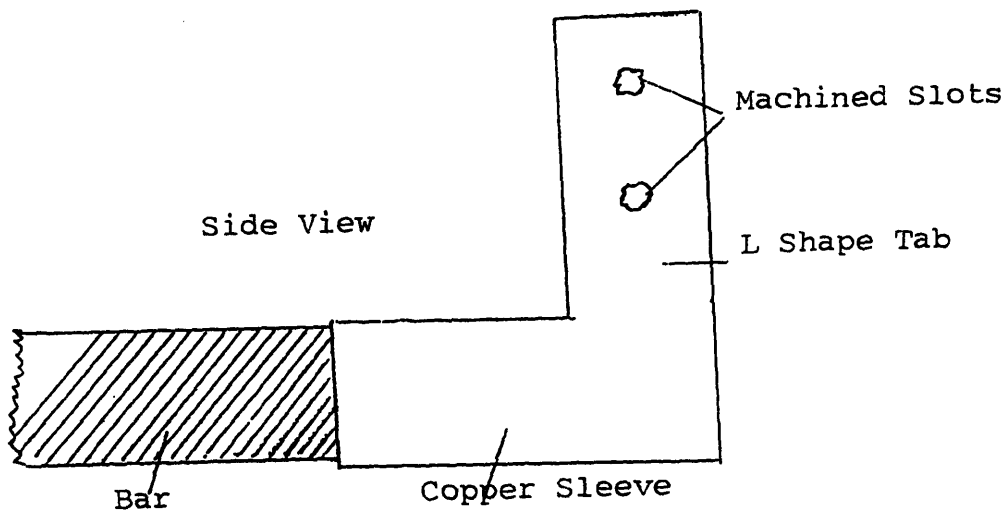
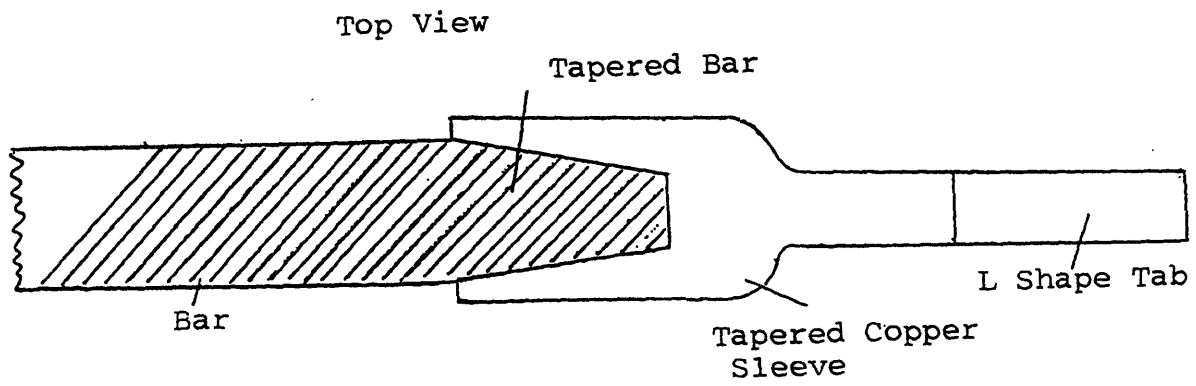
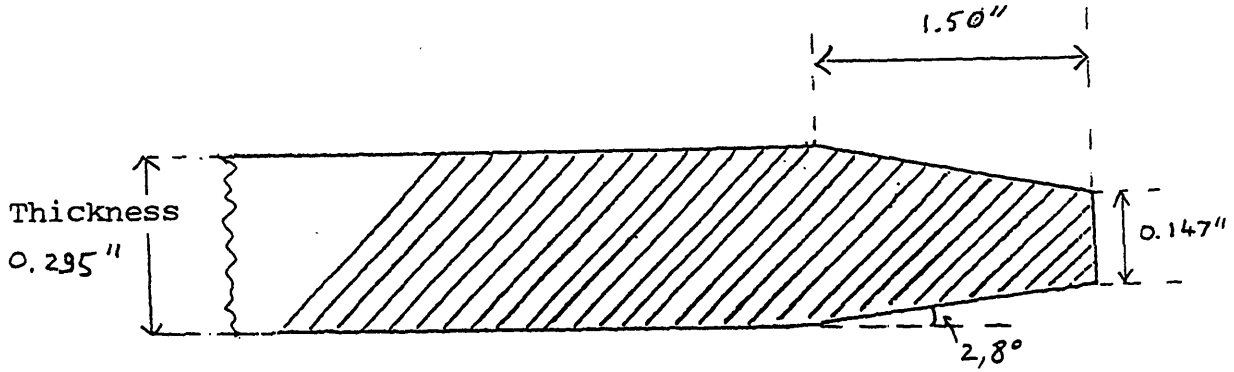


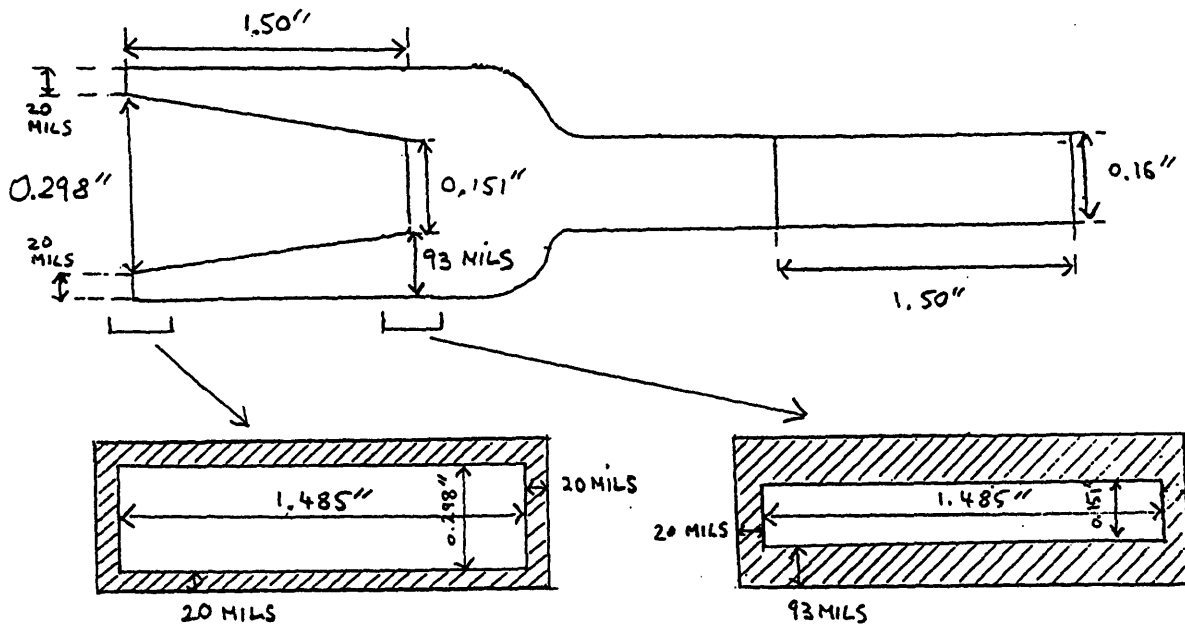
Figure 3.9: Sketch of the End Connector

Figure 3.10: Top View of Compressed Bar



Note: Side view remains unchanged

Figure 3.11: Design of the End Connector



Cross-Sectional Diagrams



The L shaped tabs, which run in the radial direction, serve to connect two radially separated bars. Made out of copper, the tabs are machined to a size of 1.5 inches in the axial direction by .16 inches in the azimuthal direction. In the tab, the current density is reduced even further, and measures about 1.5 times less than in the bars.

The end connectors and the end tabs are to be insulated with MicaMat 77956, a polyester film reinforced non woven glass tape offering an increased mica content and maximum conformability. This thin tape, which uses a polyester rather than an epoxy binder, combines a high short term dielectric strength of 1200 v/mil with excellent mechanical properties. A 36 mil total built-up thickness has been chosen as a compromise between the electrical insulation requirements and the lack of space. We note, however the 55 V/mil nominal electrical stress represents about half of the limit offered by this mica tape.

The connection between the copper end tabs is secured by using two screws. The screws which pass through slits machined onto the tab provide a tight fit between the two copper tabs, prevent relative rotation, and allow for conduction through the screw. A high voltage test of this type of connection proved that the contact resistance was at par with that obtained by soft soldering the end tabs together.

### **3.4 Design of the Cooling Spacer**

The power rating of the generator is limited, among other factors, by the current that the armature bars can carry. When the value of the rms current increases, the armature bars generate more heat due to the larger joules effect losses. This heat must be removed from the bars at the same rate that it is being produced if the temperature within the armature is to remain

constant and below the rated operating temperature. Thus an armature cooling system must be designed and integrated into the stator system.

The design requirements for the cooling spacers are fairly similar to those of the bar insulation. Mechanically, the cooling channel component should be capable of withstanding the fault torque as well as the compressive shear stresses described earlier while its cavities are sufficiently large for the cooling medium to flow efficiently. The channels should be made of a material that offers good electrical properties and which resists high temperatures but which may still be molded, extruded or shaped.

The simplest cooling channel design involves using a rolled sheet of an extruded non-conducting inorganic material. This material, which is based on mica, is capable of withstanding large compressive loads and voltage gradients when cured and resists attack by organic oils and solvents. The sheet is composed of two integral parts, as shown in **Figure 3.12**. The "base" of the cooling spacer, which is 60 mils thick, supports the cooling dividers that measure 65 mils in height. For efficient cooling the path of the cooling fluid must be minimized. Therefore, the channels are designed to run in the axial direction rather than follow the path of the helical bars. The cooling spacer is designed with only one base so that the fluid may be in actual contact with the armature bars and so that it may fill the inter-bar spaces. By submerging the sides of the bars, the ability to remove heat rises due to the increase in the total wetted area. Furthermore, the dielectric nature of the cooling fluid may reduce the nominal electric stress of the bar insulation.

The width of the cooling dividers and the fluid carrying channels are dictated by the width of the insulated armature bar and by mechanical stress considerations. As shown in **Figure 3.12**, armature bars are supported by twice the width of a cooling divider and are therefore exposed to two separate

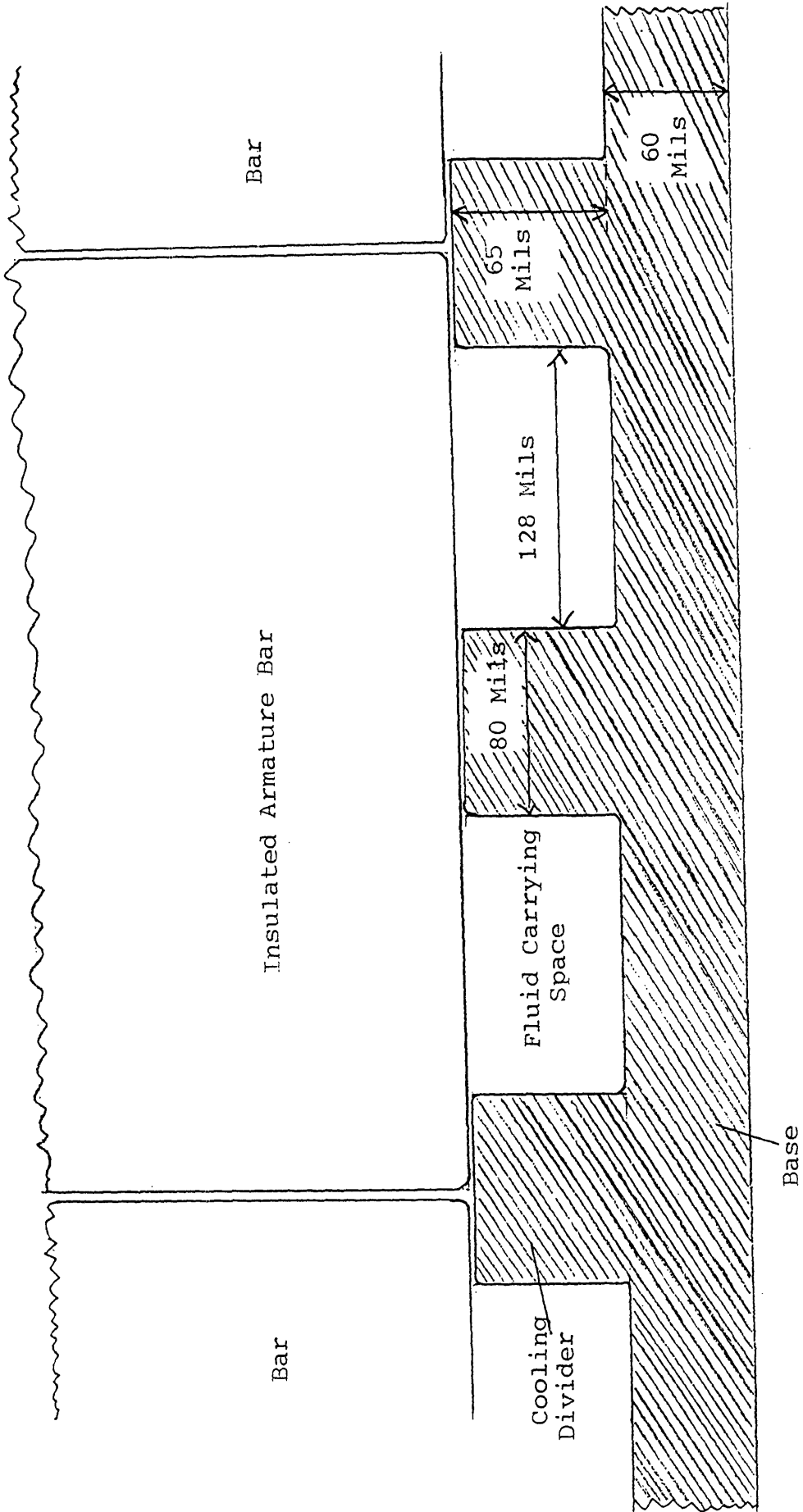


Figure 3.12: Cooling Channel Design

fluid streams. It was determined that the ideal solution to the compromise between structural requirements and cooling requirements consists of using 80 mil wide cooling dividers. The fluid carrying space thus becomes 128 mils wide and covers nearly 62% of the top and bottom surfaces of the bar.

Since all of the innermost and outermost cooling channels may be created from one extrusion die and the central channel from another, the cost of manufacture of this component is not anticipated to be high. It is recommended that when the sheet of cooling channels is installed onto the cylindrical stator that the edges be ultrasonically welded together in order to prevent deformations.

### **3.5 Torque Tube Selection**

The stator torque tubes offer a rigid support for the armature bars. These tubes are manufactured from fiberglass rovings strengthened with epoxy resin. The fiberglass rovings were wound with a mixture of helical and circumferential paths for optimal mechanical properties.<sup>59</sup> With a modulus of rigidity,  $G$ , of approximately  $.5 \cdot 10^6$  psi, the cylindrical shell may withstand an inter laminar shear stress of nearly 20,000 psi while being under an inch thick.

On the basis of our shear stress requirement of 8960 psi and upon the experience of the delta connected machine, we decide to leave the thickness of the outer torque tube unchanged at  $T_f = 0.450$  inches. In order to prevent large deformations, the monolithic armature's outer torque tube will be exposed to a 20 mil thick fluid support. The nature of the fluid will be circulating oil.

## CHAPTER 4 MANUFACTURING and TESTING

### 4.1 Production Sequence

The MIT armature winding is a complex structure requiring a carefully planned out production sequence. Having a highly modular approach permits the use of concurrent manufacturing techniques while the top shape design reduces the number of different parts to a minimum. The benefits offered by incorporating these two techniques are significant in industrial scale manufacturing.<sup>60</sup>

First, by using under eight different parts, the inventory management is considerably simplified, logistics problems are eliminated and factory supply costs are kept to a minimum. A list of required parts is given in **Table 4.1**, below. Second, by requiring less than ten processes in the production of the generator, few workers are needed and labor costs are kept low.<sup>61</sup> Furthermore, since the tasks are relatively simple to perform, the training costs may be minimized through task specialization. Third, due to the selection of materials, the construction of the armature does not require expensive equipment thereby reducing the factory's capital costs. The final advantage resides in the ability to rapidly produce this armature through efficient assembly line manufacturing. Thus, the present armature design is quite amenable for low cost high quality production and should appeal to public utilities.

Table 4.1: Part Requirement List

Inner bore tube	1
Sheets of cooling spacers	3
Conductor Bars	204
Bar Insulation Material and paint	
End Connectors	408
End Tabs	204
Finish tube	1

The production sequence for the 10 MVA armature winding requires several streamlined procedures. The inner tube is received, tested and prepared before installing the cooling channel system and the armature bars. These components will be manufactured and tested in a secondary assembly line and assembled into the armature device. The outer bore tube is then built-up and the end flanges are installed. After a thorough testing procedure, the monolithic armature will be secured into the stator core and the rotor will be installed.

An assembly process flowchart, shown in **Figure 4.1**, summarizes the aforementioned manufacturing steps. In the next two parts we shall explain in greater detail the manufacturing and testing of the bars and of the entire armature.

## **4.2 Manufacturing and Testing of the Bars**

The most important component of the armature winding is the bar. It is this component which is responsible for linking magnetic flux, in order to produce a voltage, and through which the electric current flows. All of the other components, such as the torque tubes and the cooling channels, are there to support the role of the bars. The rigorous manufacturing and testing processes for this significant unit will be described below.

### **1) Manufacturing of Bars**

The first phase of the bar manufacturing process takes place at a wire shop, such as New England Electric Wire Corporation. In the factory, AWG #21 wires are extruded and dipped into a bath in order to coat the basic conductor with the ML film insulation. Since our application requires a scratch resistant and highly durable film, the basic conductors will be dipped twice so as to form a "heavy" film coating.

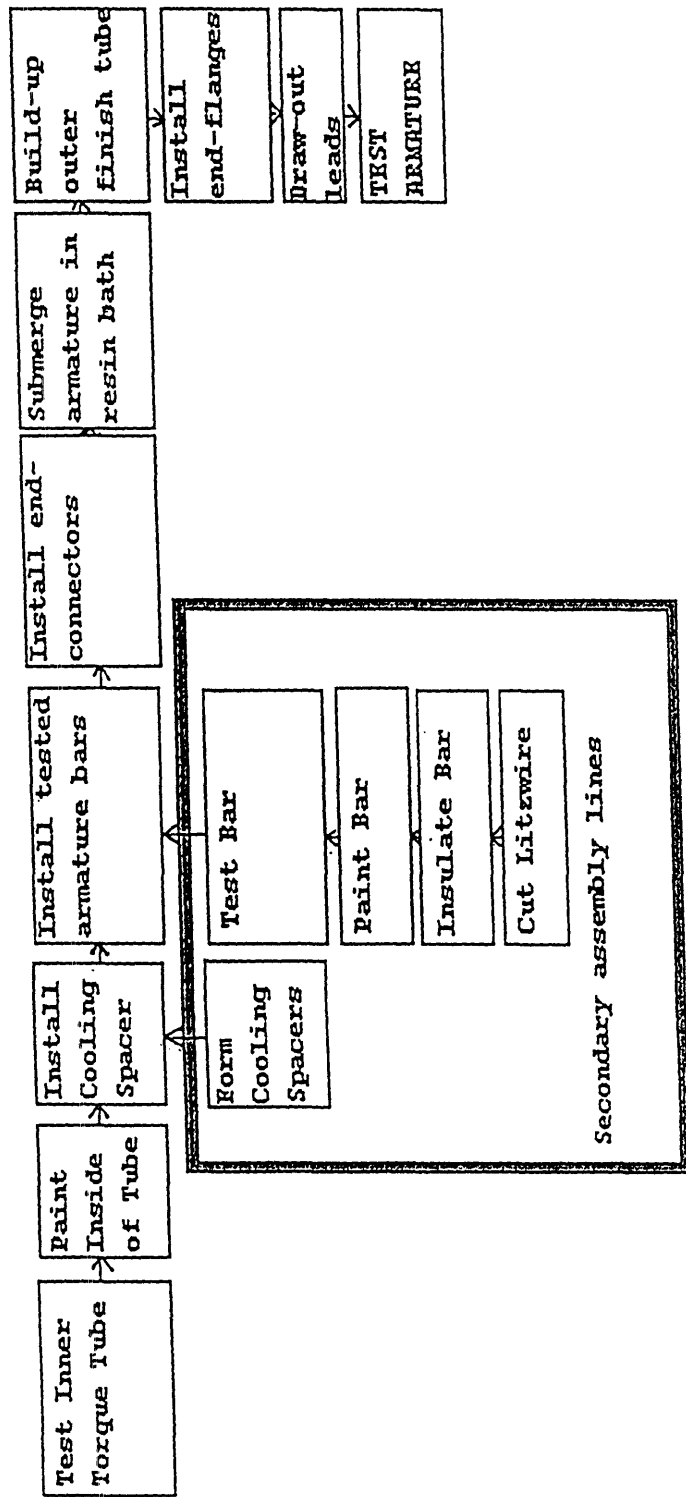


Figure 4.1: Assembly Process Flow Chart

The insulated conductors are then woven into a nineteen strand cable by a geared winding machine. The resultant cable has one wire at the center, six wires closely packed around it and wound in one direction and twelve wires wrapped in turn around the group of seven and wound in the opposite direction. The winding machine imposes a "back twist" on the basic conductors so that the wires will not untwist and come apart.

The 19 conductor bundles are, in turn, woven into a rectangular litz cable by a proprietary machine which forces the wires into parallel slots while imposing a slight back twist. The litz is then inspected and compacted by a Turk's head press. This machine, which is essentially composed of two orthogonal pairs of tapered edge rollers, is highly effective in controlling the compression ratios and thus the final dimensions of the bar.<sup>62</sup> Furthermore, the woven bundles have less of a tendency to unwind when compressed. After a final test for quality, the litz is wound on a large spool and shipped to the armature construction facility.

At the armature construction site, the litz is received and is carefully cut to size in order to form a conductor bar. The section of cable which is to be cut is taped off from the spool and then tightly clamped in between a pair of 30 mil thick plates of cold rolled steel. A small tooth band saw, placed on its slowest speed, cuts through the sacrificial plates and thus cuts the cable. By using this method, the litz suffers very little deformation at the ends and damage is kept to a minimum.

The extremities of the conductor bar are then submerged to a depth of about 1.5 inches into a beaker containing a solution of Insulstrip 220-revision 3053 for about twelve to fifteen minutes in order to dissolve the ML insulating film. It is recommended that the beaker containing the stripper be immersed into boiling water so as to keep its temperature constant and that



the stripping be conducted under a well-ventilated hood. Trichloroethane and water may be used subsequently to wash off any undissolved residue and to rinse the wires.<sup>63,64</sup>

The leads of the bars, stripped of insulation, are then compressed to one half of the original thickness of the conductor bar in order to increase the space factor and accommodate the end connectors. This is accomplished by placing the last 1.5 inches of the litz, sandwiched in between a carbon steel die, into a 20 ton press. This process, which has similar characteristics to drop forging, will steadily deform the ends of the litz into a dense structure capable of supporting large current densities.

The copper end connectors, which have a tapered cross-section designed to complement the profile of the compressed ends, is crimped onto the conductor bar to prevent it from moving. A 60/40 lead/tin eutectic soft solder is melted into the end connector while the bar is water cooled in order to reduce the damage associated with thermal penetration. Without cooling, the bar would behave as if it were a long fin and the temperature profile explained in **Appendix E** would be observed. Soft solder is used because it serves two critical purposes: much higher mechanical strength and improved electrical conduction.

In order to transform the conductor bar into an armature bar, a thick bar insulation must be applied. This insulation must not only shield the bar for the full line-to-ground voltage (2300 V rms) but must also be able to resist the transient shear stresses and the compressive loads. The first step in the bar insulation process consists of wrapping the entire length of the bar, with the exception of the end tabs, with 3 layers of half-lapped MicaMat 77984 solventless epoxy tape. This tape is often used as ground insulation on ac stator windings of up to 13.8 kV. The half lap winding technique insures that

the surface of the bar is uniformly covered and, similar to a brick wall, the staggered disposition reinforces the mechanical strength of the insulation. Thus, due to the overlap, the three layers of MicaMat will have a thickness of six times that of a single layer.

A single layer of Fusa-Flex sealable armor tape is wrapped over the MicaMat. This tape is a B-staged epoxy coated polyester-glass tape that shrinks and fuses during cure to provide a tough moisture and chemical seal. Fusa-Flex, when cured, will provide a low dissipation factor, a high dielectric strength and good insulation resistance to the bar. A single layer of half-lapped IMI 76856 shrinkable release film is applied over the MicaMat and the Fusa-Flex layers. When heated over a curable insulation, this polyester-polyvinyl fluoride film laminate exerts a pressure sufficient to compact the system and, thus, aids in the formation of a smooth and void free structure. At about 120 °C, this film produces a shrink tension of about 3500 psi and shrinks about 10% by volume. In addition, this particular film laminate offers improved release properties when used with epoxy resins.

The insulated bar is then inserted into an aluminum mold and placed into a 150 °C oven for one hour so that the B-staged epoxy may flow and cure. When the bar reaches room temperature it is ejected from the mold and the shrinkable release film can be removed and discarded. The thick bar insulation may then be painted on all four sides with a thin coating of Glyptal 9921 semiconducting paint. This conductive paint serves to eliminate any voltage discontinuities on the surface of the bar, to prevent the buildup of static charges and to establish a ground potential outside the armature bar.<sup>65</sup>

An armature bar, with a 59.5 mil thick insulation layer is the final result of the bar manufacturing process. This procedure is repeated for each of the 204 bars of the armature. With the exception of the total length and of

the slightly different mold, the upper and lower bars undergo the same manufacturing process. Before inserting the insulated bars into the armature, they must be properly tested and certified.

## 2) Bar Testing Procedures

The goal of the bar testing phase is twofold. One set of tests concerns the conducting litz while the other pertains to the bar insulation. The first test, called the *resistance test*, seeks to ensure that nearly all of the basic conductors are in contact with both of the end-connectors located at the leads of the bar. In this test, the end tabs of the armature bar are connected to a high dc current source of about 2,500 A while being oil cooled. Using a millivoltmeter to measure the small difference in potential across the bar, the overall resistance of the conductor may be determined. When compared to the theoretical resistance of the bar, given by:

$$R = \frac{\rho L}{A} + C$$

(where  $\rho$  is the resistivity of copper,  $L$  is the bar length,  $A$  is the total conductive area and  $C$  is the

effective contact resistance.)

it is possible to determine if the bar was properly manufactured. Through experience, the limits for the resistance test will become firmly established and the discrimination between acceptable and defective bars will become systematic.

The next electrical test, known as the *short test*, consists of proving that the middle of the bar is free from wire to wire contacts. These shorts, which may result from either an error in fabrication or from mishandling of the litz, would result in unacceptably large eddy current losses in an operating generator. Unfortunately, the only test that has been devised to prove that the bars are relatively free from shorts involves placing the armature bar in a large time varying magnetic field and measuring the ac

resistance. Thus, the only way to perform this test is by installing the bars into the armature and testing the machine as a whole. Since there is no practical test for inspecting individual bars, this experiment is rendered moot.

The second and final test that will be performed prior to bar certification is the *mega test*. This test seeks to demonstrate that the bar insulation is homogenous and that insulation leakage will not occur during the lifetime of the generator. In this test, a large dc difference in potential of about 5 kV is applied between the conductor bar and the thick bar insulation and a micro-amp meter is used to measure the leak current which may flow through the MicaMat insulation. If a current is measured on the micro-amp meter it would mean that a non-zero potential is driving the current and thus demonstrate the inadequacy of the bar insulation.

Bars which pass both tests are then visually examined for cracks in the semiconducting coating and then are used in the assembly of the armature winding. This process will be described in detail in the next section, below. It is recommended that bars which fail one of the above tests be discarded since the repair of a cured bar is too labor intensive as compared to the cost of manufacture.

### **4.3 Assembly and Testing of the Armature**

The armature winding forms the heart of the superconducting generator. This component, whose central role is to link the rotor's flux in order to produce usable electric power, must be manufactured to survive the rigors incurred by electrical and mechanical transients. We shall now detail the manufacturing and testing process for this component.

### 1) Armature Assembly

The first step in the principal assembly line is to prepare and pre-test the inner torque tube for manufacturing. This fiber reinforced epoxy tube will be purchased from Permal Corporation rather than be constructed at MIT. A provision should be made at both ends of the torque tube for a bolt circle, capable of accommodating 60 3/8 inch bolts, by drilling blind holes of thread depth of about 2 inches. In addition, the ends should also be prepared for an O-ring seal between the torque tube and the end plate. The inner surface of the tube must be coated with a semiconductive paint so as to ensure that the entire tube is at ground potential and to eliminate voltage gradients. General Electric Glyptal 9921, which has a surface resistivity of 10 kΩ per square centimeter, is recommended for coating epoxy/fiber materials.

In order to certify that the tube is free from structural defects, it will be subjected to a series of tests prior to assembling the armature bars. In the first test, the tube must demonstrate its capability in withstanding a single torsional load of  $2 \times 10^5$  N.m in both the clockwise and counterclockwise direction. For the second test, the tube is sealed using the O-ring surface and bolt circles so that a vacuum test can be made. Under high vacuum, the air leak through the inner torque tube should not exceed  $2 \times 10^{-7}$  cubic centimeters per second. Finally, a test of the dielectric strength of the cylinder will be conducted prior to assembling the armature bars. In accordance with ANSI standards C57.12.90, the test voltage shall be 5 kV.

The second step of the production sequence is the assembly of the cooling spacers onto the bore tube. The extruded sheet, which was manufactured in a secondary production line, is rolled and glued to the inner tube and the ends are ultrasonically welded together. The bonding agent must be strong, have a low cure temperature to prevent distortion of the bore

tube and be compatible with the cooling oil. Aquanel 513, Fusa-Flex and Fabri-Therm are currently being evaluated for this process.

The third step involves the installation of the insulated bars that were manufactured and pre-tested in the secondary production sequence detailed in the previous section. A bar molded for the inner layer will be glued onto the cooling channel shell and a Teflon coated plastic manufacturing spacer will be used to ensure that a proper bar spacing is maintained. The manufacturing spacers, which have a wedge shaped cross-section in order to fit between the bars, are pulled out after the bars have cured onto the armature and may be used again. Although a coating of a semiconducting paint may be applied over the cooling spacers, it is not necessary to do so because the bar insulator is already coated and is rated for full line-to-ground insulation.

The last two steps are repeated, in reverse order, for the outer bar layers. It is important to note that the outer layer manufacturing spacers will be larger than the inner layer spacers due to the increase in available azimuthal space.

The end connections must be made and insulated in the fourth step of the manufacturing process. The L shaped end-connectors, located at the extremities of the bars, include a copper tab that extends in the radial direction in order to connect bars of one layer to those of the alternate layer. As explained in the last chapter, the end tabs will be secured by screws that pass through slits before being insulated for full line-to-ground voltage. The end tabs will be wrapped with 3 layers of half-lapped IMI 77956, a polyester film and non-woven glass combination offering increased mica content and maximum conformity.

Subsequently, the phase belt connections are made and then insulated with the same material. These connections, which are described in Chapter 2, are made so as to arrive at a single circuit Wye connected armature winding. The four leads, one from each of the three phases and one from the ground, are brought out and protected. Much later, when the generator is assembled, they will be brought out through a bushing box.

In the fifth step, the cooling channels are sealed and the entire armature is dipped in IMI 74030 solventless epoxy resin and then baked for four hours at 150 °C. After the part has reached room temperature, the cooling channels are cleared and the wound stator is visually inspected.

The sixth step consists of building up the outer torque tube to a thickness of 450 mils. Since this tube serves as a mechanical support for the monolithic winding and since it interfaces with the aluminum end flanges, it will be made out of a filament wound fiber reinforced plastic. This material offers both excellent mechanical strength and good electrical insulation. To further strengthen the end joints, steel dowel pins will also be used.

## 2) Testing the Armature

The final step in the armature manufacturing process consists in testing the armature component as a whole. The prototype armature will undergo five separate tests in order to prove the validity of the design while production armatures must pass only the first three tests.

The first test, known as the *armature resistance test*, is very similar to the bar resistance test that was performed on each bar prior to installation into the stator. This test seeks to ensure that all of the end-connectors, which link the upper bars to the lower ones, and the inter phase-belt connections are well made. In this experiment, a large dc current of the order of 2,500 A is allowed to flow through a phase belt while a voltmeter is used to measure

the drop in potential between the leads of the phase belt. The phase belt's effective resistance, determined by Ohm's Law, is then compared to the maximum acceptable value. Should the resistance of a phase belt exceed the theoretical value, it would indicate that an end-connector is poorly installed since the bars have already been certified.

The second test, which has been explained earlier, is called the proof test. Pursuant to ANSI standards (C50-15), the armature must be exposed to a 9 kV 60 Hz waveform for one minute. This test, which pertains to the basic insulation limit (BIL), seeks to prove the overall integrity and adequacy of the insulation used in the armature. The mega test is, therefore, superseded by the much tougher proof test and need not be conducted at the factory.

The *phase impulse test* constitutes the third inspection of the machine. In this test, a full wave impulse is applied between the ground and each of the three phase terminals. According to ANSI standards C57.12.90 and C57.12.98, this high frequency impulse should have a rise time of about 250 microseconds and a fall time to half of the peak voltage of about 2500 microseconds. The peak voltage of this impulse must be no less than 32 kV for our machine. This experiment seeks to simulate the effects of sudden large voltage spikes which may occur, for example, during a lightning storm. It must be noted, however, that surge arrestors typically protect the generator from such events.

The prototype armature, which will be built in part at MIT, will need to undergo two additional tests after the generator is completely assembled. The fourth experiment is an *open circuit test* which is used to verify that the behavior of the generator conforms to that predicted by the field analysis and flux linkage calculations. This test is usually performed at a fraction of the maximum excitation current. The fifth test, performed at about 30% of the



rated excitation current, is the *short circuit heat removal test*. In this test, the rated current flows through the armature circuit in order to produce Joule heating and the oil cooling system is tested. By measuring the inlet and outlet oil temperature, the amount of heat removal and the temperature of the hot spot may be determined and compared to theoretical estimates. By using less than the full excitation current to perform these two tests, the induced voltage in the armature is kept low thus limiting potential catastrophic damage to the generator.

In addition to the electrical tests, the prototype armature, as well as the production units, must pass two mechanical and structural tests. The first mechanical test is the *outer torque tube shear stress test*. In this experiment, both of the ends of the inner torque tube are left free and one of the end flanges is kept fixed. A torque of  $2 \cdot 10^5$  N.m is applied at the other end flange in both the clockwise and the counterclockwise direction. The second test, called the Inner torque tube shear stress test, is similar in concept to the previous test. Holding one end of the outer torque tube fixed, a torque of  $1.5 \cdot 10^5$  N.m is applied, in both directions, at the opposite end on the inner torque tube. Production armatures must be able to support these torques if they are to survive the three-phase fault torque of about  $2.65 \cdot 10^5$  N.m. This value, which was derived in calculation 3.2 was excessive for a non-destructive test.

Other tests, such as one measuring the real power output, may take place only after the seven aforementioned tests are successfully passed.

## **CHAPTER 5**

### **THERMODYNAMIC PROPERTIES**

#### **5.1 Cooling System Layout**

The 10 MVA armature winding is composed of 208 insulated armature bars, which travel helically around the cylindrical stator. Since the conductors within each of the bars are composed of copper, they will generate Joules heating when a current flows through them. This heating, which is due to the inherent resistivity of the conductor, must be removed from the armature in order to prevent overheating and physical damage. The simplest method for removing this large quantity of heat is through the use of oil filled cooling channels. These channels, which measure 65 mils high by 128 mils wide and are separated from each other by 80 mils, run in the axial direction in order to shorten their path and reduce the necessary pumping pressure.

The working fluid which was selected for the armature cooling fluid is Dow Corning 561 transformer fluid. This dimethyl siloxane polymer is a dielectric coolant exclusively designed for electrical machinery<sup>66</sup>. The fluid, which will be contained in a large sump, is pumped and then strained before being inserted into a shell-and-tube type heat exchanger. After cooling the silicone oil with cold water, it is inserted into the lead end of the armature. Under the pump's pressure, the oil is forced into the cooling channels and is collected at the opposite end of the armature so that it may be returned to the sump. **Figure 5.1** graphically illustrates this closed-loop cooling system.

In the next two sections, a thermodynamical analysis of the armature cooling system will be presented in order to determine the minimum oil flow required to keep the insulation from degrading. Subsequently, the temperature profile within the insulated bars will be determined and plotted.

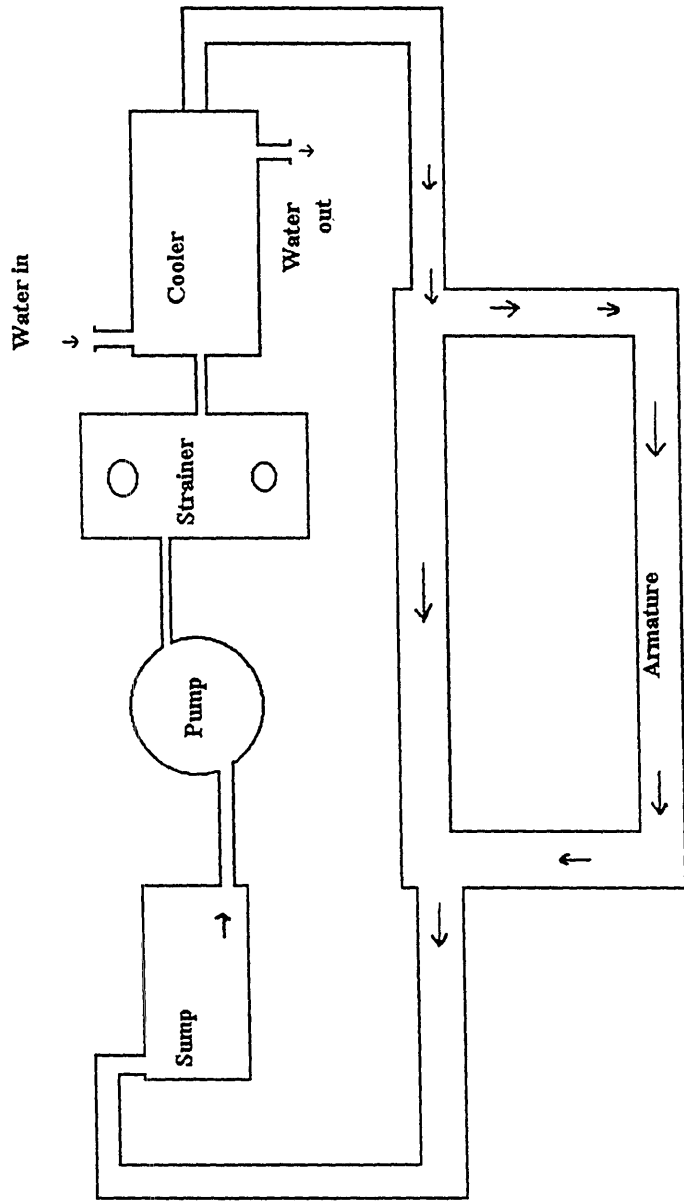


Figure 5.1: Armature Cooling System

## 5.2 Thermodynamic Analysis

The first steps in our thermodynamic modeling of the armature winding is to draw the helical portion of the bar in the axial-azimuthal plane and to overlay the cooling channels which run axially. Figure 5.2 portrays a control volume, defined by the intersection between a single armature and a cooling channel. Table 5.1, below, summarizes the properties of the materials used in the MIT armature winding.

**Table 5.1:** Physical Properties of Armature Materials

	Avoir du pois	Systeme International
<b>Armature</b>		
Axial Length	35.620"	$9.047 \cdot 10^{-1}$ m
<b>Cooling Channel</b>		
Width	0.128"	$3.251 \cdot 10^{-3}$ m
Height	0.065"	$1.651 \cdot 10^{-3}$ m
Separation	0.080"	$2.032 \cdot 10^{-3}$ m
Total number	1128	
<b>Armature Bar</b>		
Height	1.601"	$4.067 \cdot 10^{-2}$ m
Width	0.415"	$1.054 \cdot 10^{-2}$ m
Insulation thickness	0.060"	$1.524 \cdot 10^{-3}$ m
Separation	0.013"	$3.302 \cdot 10^{-4}$ m
Insulation rated temperature	185°C	
Thermal conductivity (k)		$6.301 \cdot 10^{-1}$ j/m K
<b>Conductor Bar</b>		
Height	1.481"	$3.762 \cdot 10^{-2}$ m
Width	0.295"	$7.493 \cdot 10^{-3}$ m
Number of conductors	361	
Density of copper		$1.70 \cdot 10^{-8}$ Ω.m
Radius of conductor	0.01425"	$3.620 \cdot 10^{-4}$ m
Film insulation rated temperature	220°C	
<b>Cooling fluid</b>		
Density ( $\rho$ )		$9.572 \cdot 10^2$ kg/m <sup>3</sup>
Heat capacity ( $c_p$ )		$1.507 \cdot 10^3$ j/kg K
Thermal conductivity (k)		$1.507 \cdot 10^{-1}$ j/m K
Kinematic viscosity ( $\nu$ )	32.5 saybolts	$1.345 \cdot 10^{-6}$ m <sup>2</sup> /s

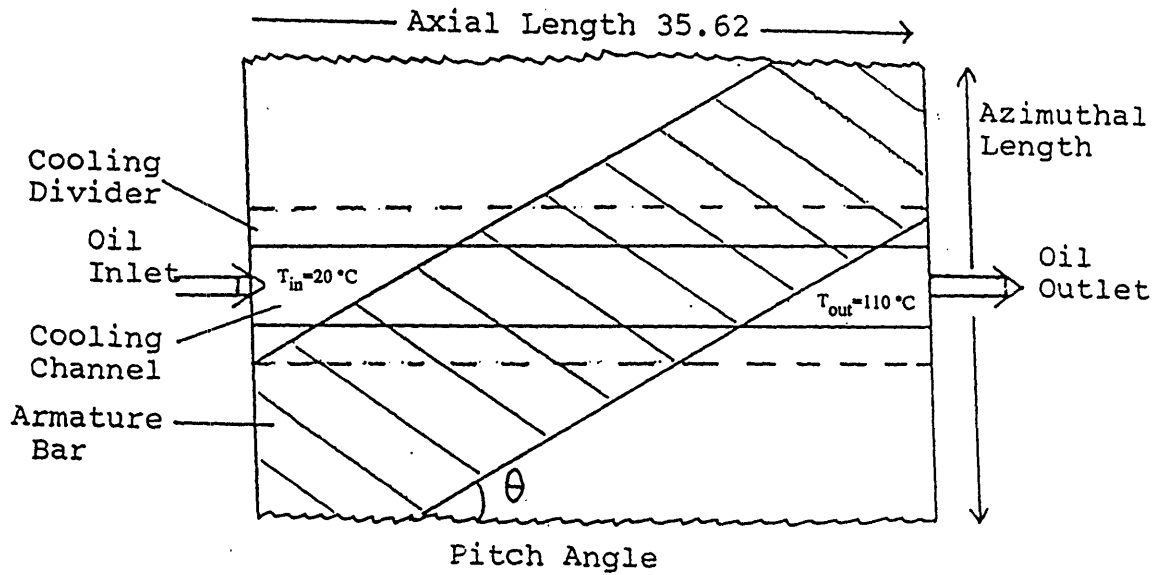


Figure 5.2A: Path of a Cooling Channel under a Helical Armature Bar

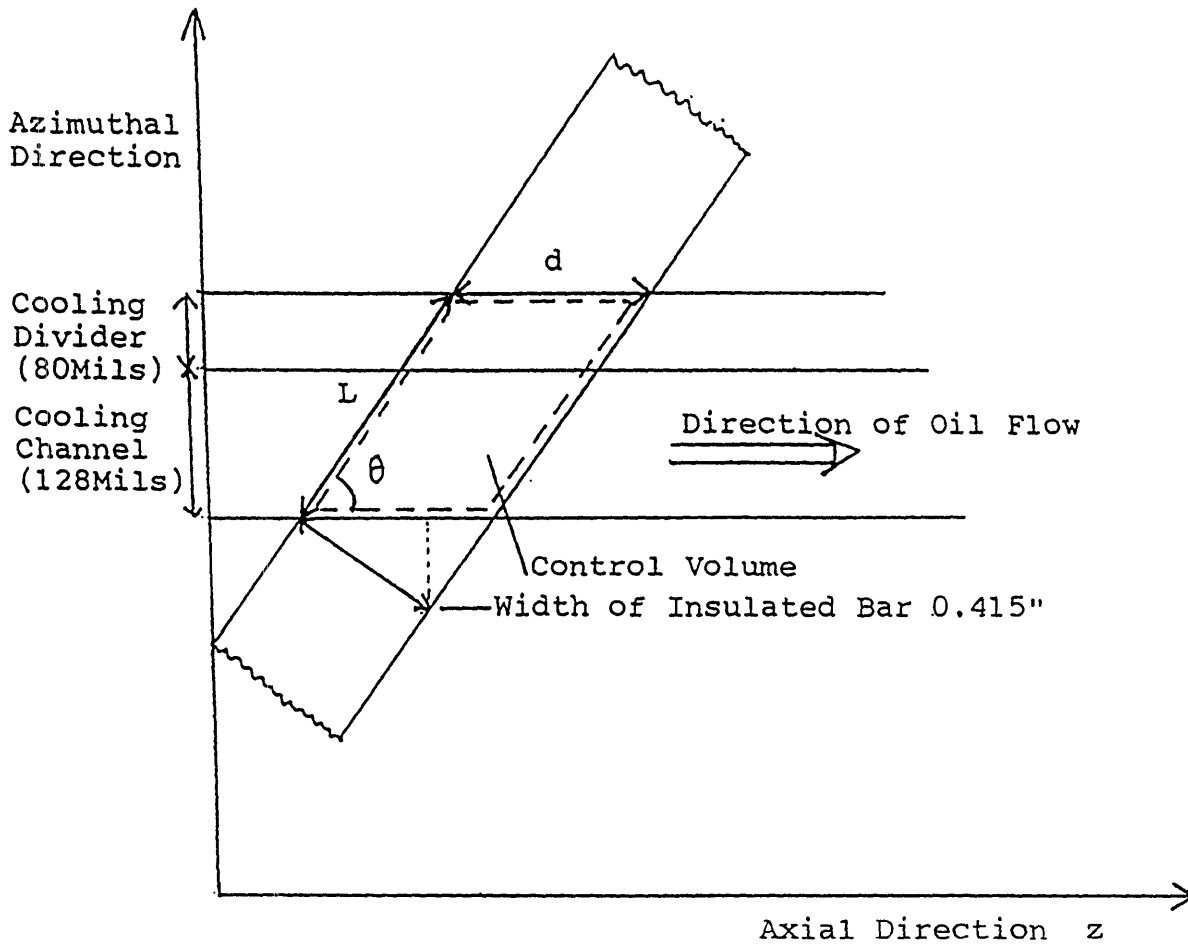


Figure 5.2B: Geometric Definition of the Control Volume

### 1) Heat generated in control volume

In order to determine the heat generated in the control volume, we must first determine the resistance of a single AWG #21 conductor traveling along the length of the plotted volume. Knowing that the area of the basic conductor is  $A = \pi r^2 = 4.116 \cdot 10^{-7} \text{ m}^2$  and that its length is given by:

$$L = \frac{(i + c)}{\sin(\theta)} = 7.8956 \cdot 10^{-3} \text{ m}$$
 where  $\theta$  is the pitch angle and  $i$  is the separation between

cooling channels, each of width  $c$ .

The resistance of the individual wire is proportional to the conductivity of copper ( $\rho$ ) times the ratio of the length to the cross sectional area, thus:

$$R = \rho \frac{L}{A} = 3.261 \cdot 10^{-4} \Omega$$

The Joules effect loss for a conductor is proportional to the square of the current flowing through the wire times its resistance. An armature bar, composed of 361 conductors, carries a current of 1,445 A during steady state operation. Each wire, therefore, carries a current of about  $I_w = 1,445/361 = 4 \text{ A}$ . The heat generation per conductor is given by:

$$P = I_w^2 \cdot R = 5.225 \cdot 10^{-3} \text{ W}$$

Thus, the total heat generated in the control volume is 361 times larger, so

$$Q_{c.v.} = 1.886 \text{ W}$$

### 2) Minimum fluid velocity

In this section we shall first compute the total heat which a single cooling channel must remove during steady state conditions. Knowing that a cooling channel will encounter 102 armature bars during its passage through the armature and remembering that each layer of bars is cooled by two layers of cooling channels, we write:

$$Q_{c.c.} = (1/2) \cdot 102 \cdot Q_{c.v.} = 96.19 \text{ Watts}$$

Specifying that the inlet temperature of the silicone oil is smaller than  $T_{in}=20\text{ }^{\circ}\text{C}$  and that the maximum outlet temperature is  $T_{out}=110\text{ }^{\circ}\text{C}$ , we may calculate the minimum fluid velocity by modeling the cooling channel as a simple heat exchanger. Recalling that  $Q = m' c_p \Delta T$  and that the mass flow rate  $m' = \rho A V$ , we may write<sup>67</sup>:

$$V_{oil} = \frac{Q_{cc}}{\rho \cdot A \cdot C_p \cdot \Delta T} \text{ where } A \text{ is the cross sectional area of the cooling channel}$$

( $=5.368 \cdot 10^{-6} \text{ m}^2$ ) and where  $\rho$  and  $C_p$  are the oil's density and heat capacity, respectively.

By numeric substitution we find that the minimum velocity for the oil traveling through the channel is about  $V_{oil}=0.138 \text{ m/s}$ . This corresponds to a mass flow rate of about  $7.09 \cdot 10^{-4} \text{ kg/s}$  or a volume flow rate of about  $7.407 \cdot 10^{-4} \text{ liters per second}$ .

Thus the total flow rate through the armature is roughly 1128 times greater, or about 0.8355 liters per second.

### 3) Describing the flow

We shall now turn our attention to a quantitative description of the flow in a single channel. The first step in our analysis consists of determining the Reynolds number, which characterizes the relative influences of inertial and viscous forces in a fluid. This dimensionless number is proportional to the velocity of the fluid stream and the hydraulic diameter but inversely proportional to the kinematic viscosity. Thus:

$$Re = \frac{V \cdot D}{\nu} = 225 \text{ where } D = (4 \cdot \text{Area cooling channel}) / \text{Perimeter of channel}$$

Since the value of the Reynolds number is below 2300, it is indicative of a laminar flow instead of a turbulent one.

The second dimensionless constant, called the Prandtl number, seeks to compare the fluid's ability to transfer momentum to its ability to diffuse heat. The Prandtl number is proportional to the heat capacity, the viscosity

and the density of the oil but inversely proportional to its thermal conductivity. Thus:

$$Pr = \frac{C_p \cdot \nu \cdot \rho}{k} = 13 \text{ in our case.}$$

#### 4) The heat transfer coefficient

The thermal entry length, which marks the transition into a fully developed flow, is of great importance in laminar flow since the thermal undeveloped region may become very long for large Prandl numbers. In our situation, which involves a laminar flow with a constant heat flux, the thermal entry length is given by<sup>68</sup>:

$x = 0.05 D Re Pr = 0.32 \text{ m}$  and thus this transition occurs about a third of the way through the armature.

It should be noted that in a non-fully-developed flow the heat transfer is superior to that of a fully developed flow, since the heat need not pass through thermally resistive layers of oil in order to get to the faster moving fluid at the center. Instead, the fluid traveling near the walls is cold enough to allow a relatively large heat flux. To illustrate this point we shall compare the Nusselt number in both cases. This dimensionless number is proportional to the heat transfer coefficient,  $h$ , or in other words it is inversely proportional to the thickness of the thermal boundary layer.

The Nusselt number for a fully developed laminar flow in a rectangular pipe with constant heat flux is  $Nu = 4.1$ .<sup>69</sup> For a non-fully-developed laminar flow the boundary layer must be taken into account. Thus:

$$Nu = 0.453 Pr^{1/3} Re^{1/2} = 15.8 \text{ which is significantly higher.}$$

Basing our thermodynamical model on the average Nusselt number of  $Nu = 8.50$ , we shall calculate the average heat transfer coefficient. From the definition of the Nusselt number, we have:



$$h = \frac{Nu \cdot k}{D} = \underline{584.9 \text{ W/m}^2 \text{ K}}$$

where k is the thermal conductivity of the oil and D is

again the hydraulic diameter of the channel.

### 5) Minimum pumping pressure

The oil pressure necessary for forcing the cooling fluid through the armature cooling channels may be determined next. For a pipe with a rectangular cross section and a laminar flow, the pressure drop is given by<sup>70</sup>:

$$\Delta P = 4.4(f) \frac{L}{D} \left( \frac{1}{2} \rho V^2 \right)$$

where f is the friction factor, L is the total length of the

cooling channel and  $\rho$  and V are the density and velocity of the oil, respectively.

In our situation the friction factor is related to the Reynolds number by the following correlation<sup>71</sup>:

$$f = \frac{62}{Re} = 0.2756.$$

Thus, it is apparent that the pressure drop across the

armature is linearly related to the velocity of the fluid stream and that  $\Delta P = 0.67 \text{ psi}$ . Although the value of this pressure drop might seem slightly low, we must recall that the cooling channels run straight through the machine. By taking into account the complexities of the armature cooling system, as well as the pressure drop across the strainer and the oil cooler, we find that the pumping pressure must be roughly three times larger, or of about 2 psi.

### 6) Bulk Temperature

In this brief section we shall assume that the heat absorbed by the oil stream is constant throughout the length of the cooling channel. This assumption will allow us to relate the oil temperature at any given point to its axial position, as shown in **Figure 5.3**. Since a constant heat absorption results in a linear temperature rise, and having previously specified the inlet and outlet temperature, we have:

$$T_b(z) = \frac{T_{out} - T_{in}}{L} z + T_{in} = (99.48) z + 20$$

where z is the axial coordinate.

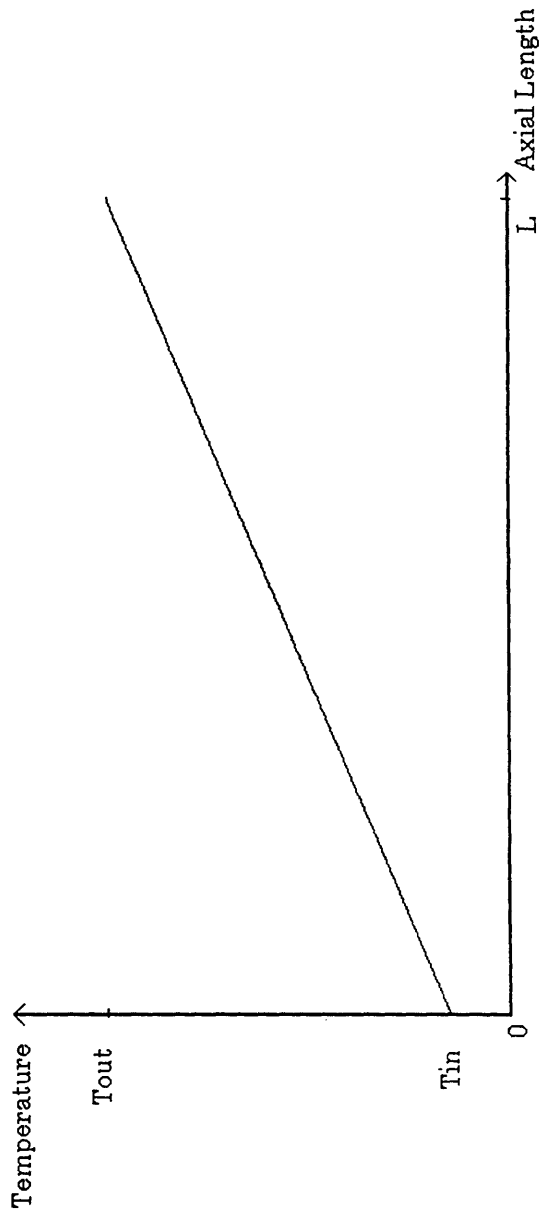
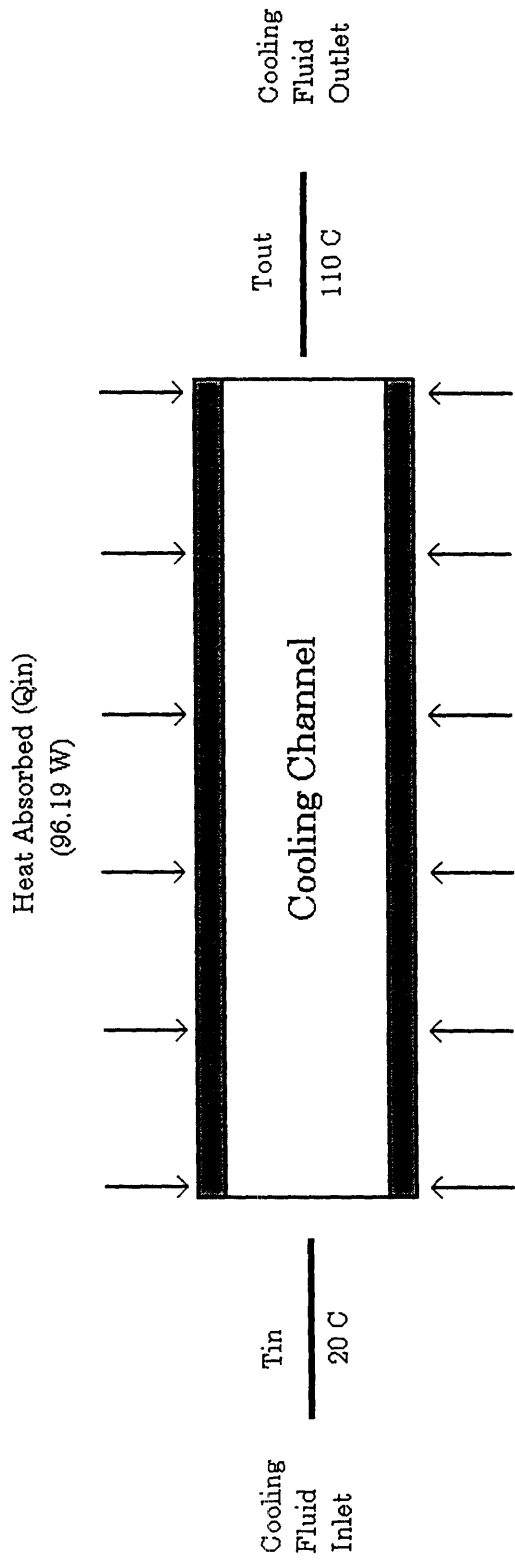


Figure 5.3: Temperature Rise in the Cooling Channel

### 5.3 Temperature Profile

In this section we shall determine the temperature within the armature bars based on the data derived in the thermodynamical analysis. Expressing the temperature in the bar as a function of a coordinate collinear to the radial direction will require the use of a technique taught in the graduate level course in heat transfer at MIT. This method simplifies the problem by separating it into three discrete sections and subsequently matching them together. We shall now implement this technique for the conductor bar, the insulation layer and the cooling channel regions of the armature.

#### 1) Conduction and Generation in the conductor bar region

In the rectangular compacted litz, which will be treated as a uniform copper bar, two physical phenomena are simultaneously taking place. The heat, which is generated by Joulian losses, is diffused throughout the copper and conducted to the thick bar insulation. Writing the general energy conservation equation which states that the heat conduction plus the heat generation is equal to the energy increase term plus the convection, we have<sup>72</sup>:

$$\nabla^2 T + \frac{q'}{k} = \frac{1}{\alpha} \left( \frac{\partial T}{\partial t} + u \cdot \nabla T \right) \text{ where } q' \text{ is the heat generation per unit volume and}$$

$\alpha = k/\rho c$  is the thermal diffusivity.

In our steady-state analysis we will assume that the Biot number, which is defined as the ratio of the conduction resistance to that of convection, is sufficiently large so as to make the effect of convection negligible. Thus the energy conservation equation reduces to:

$$\nabla^2 T = -\frac{q'}{k} \text{ where } k \text{ is the thermal conductivity of copper.}$$

The one dimensional solution to this differential equation is given by:  
 $T(x) = (-q'/2k)x^2 + cx + d$  where the x coordinate is measured from the center of the bar. From symmetry principles, we obtain the two boundary conditions:

$$T(0) = T_{\max} \quad \text{and} \quad T'(0) = 0, \text{ we get:}$$

$T(x) = (-q'/2k)x^2 + T_{\max}$  where the constant term corresponds to the high temperature spot located at the center of the bar and, as such, must never exceed the film insulation rated temperature.

We must now determine the heat generation per unit volume. In order to find q', we must divide the heat generated in the control volume by its volume. Recalling that:

$V_{c.v.} = A_{c.v.} * h = (w * L) * h = 2.226 * 10^{-6} \text{ m}^3$  where  $A_{c.v.}$  and L are the surface area and the length of the control volume and w and h are the width and height of the litzwire.

Therefore the heat generation per unit volume is  $q' = 8.474 * 10^5 \text{ W/m}^3$  and thus the temperature inside the copper bar is given by:

$$T(x) = (-1.089 * 10^3)x^2 + 200$$

Using this equation to predict the temperature drop between the center of the bar and the edge of the copper region, located at  $x = 1.881 * 10^{-2} \text{ m}$ , we find that  $\Delta T = T_m - T_s = \underline{.385^\circ \text{C}}$ . Since the temperature drop is of the order of a third of a degree, we shall model the entire copper space as a material having a uniform temperature by assuming that  $T_m = T_s$ .

## 2) Convection in the Fluid Stream

The second region which we will analyze is the interface between the bar insulation and the fluid stream. Recalling that the heat transfer coefficient (h) times the temperature gradient between the wall and the bulk

temperature ( $T_{\text{wall}} - T_{\text{bulk}}$ ) is equal to the surface heat flux ( $Q'/A$ ) out of the insulation and into the cooling channel, we may write:

$$\Delta T = (T_{\text{wall}} - T_{\text{bulk}}) = \frac{Q'}{hA}$$

The contact area,  $A$ , between the fluid and the bar corresponds to the axial projection of the bar's width times the width of the cooling channel.

Thus,  $A = (w/\sin\theta) * c = 5.122 * 10^{-5} \text{ m}^2$ . Recalling that the heat generated in the control volume is removed by two fluid streams, we find that:

$$Q' = Q/2 = 1.886/2 = 0.943 \text{ Watts.}$$

Numerical substitution yields that:  $\Delta T = 31.5 \text{ }^\circ\text{C}$  indicating that the wall temperature is moderately higher than the bulk temperature. We note, with satisfaction, that the highest wall temperature, located near the oil outlet, will be of about  $142 \text{ }^\circ\text{C}$ ; comfortably lower than the insulation's rated temperature.

### 3) Conduction Through the Bar Insulation

We will now turn our attention to the temperature profile within the thick bar insulation. Once again, we will begin with the general energy conservation equation and simplify it by treating the steady-state, convection-free problem. Since there is no heat generation within the insulation, the energy conservation equation becomes:

$$\nabla^2 T = 0$$

The one dimensional solution to this differential equation is, of course, a linear function. Thus:

$$T(x) = \frac{-q}{k_{\text{ins}}}x + T_o \text{ where } k \text{ is the thermal conductivity of the MicaMat insulation.}$$

The surface heat flux,  $q$ , corresponds to the ratio of the heat, which travels through the insulation, to the area through which it passes. Since the width of the armature bar varies linearly as a function of  $x$ , we shall use an

average width in our determination of the active area. This average width is simply:  $w=0.295+0.060= 0.355"= 9.017*10^{-3}$  m.

Thus the average area A is:

$$A= W * L = 7.119*10^{-5} \text{ m}^2 \text{ where L is the length of the control volume.}$$

Recalling that the heat which passes from the conductor, through the insulation, to a cooling channel is  $Q' = Q/2=1.886/2 = 0.943$  Watts, we now have:

$$T(x) = (- 2.102*10^4 ) x + T_0$$

By moving the origin of the x axis to the position of the wall-channel interface and by reversing the direction of this axis so that it points into the bar, this equation becomes simpler to use. After the change of frame, the temperature distribution within the insulation becomes:

$$T(y) = (2.102*10^4) y + T_b(z) \quad \text{where } T_b \text{ is the bulk temperature.}$$

Or, alternatively:

$$T(y,z) = (2.102*10^4) y + (99.48) z + 20$$

and we note that the temperature gradient in the bar insulation is of the order of  $\Delta T = T_s - T_m = \underline{32 \text{ degrees Celsius}}$ .

#### 4) Summation

In this section, we shall use the results derived above in order to obtain a complete understanding of the heat transfer processes occurring within the armature. Since the temperature distribution is a continuous function, the profiles, which were derived separately, must match each other at the interfaces. However, since the heat conductivity varies from material to material, kinks are to be expected in the curve.

The temperature profile within the armature bar and the adjoining cooling channel has been plotted, at a given axial location, in **Figure 5.4**. Since the bulk temperature was determined to be linearly dependent on the

axial position, the curve represented in Figure 5.3 is expected to scale accordingly. We note that the parabolic temperature distribution within the conductor is greatly exaggerated in this figure.

Ignoring the effects of contact resistances, the temperature in the metal, which is the hottest body in the machine, may be approximated by:

$$T_m(z) = (99.48) z + 52$$

Thus, the temperature at the hot spot, which is located at the center of the bar and near the outlet of the cooling channel, is of the order of 145°C.

Therefore, even the hottest point of the armature is well within the capabilities of the materials selected. Since the thermal equilibrium relaxation times are much greater than the electrical relaxation times, a thermal analysis during short-term electrical transients would be unwarranted and, thus, beyond the scope of this design thesis.

#### **5.4 Generator Control**

The MIT Superconducting generator's power output is controlled by three separate, but related, factors, as shown in Figure 5.5. The first control input is the shaft torque produced by the gas turbine engine. By augmenting the torque supplied to the rotor, a higher real power is available for conversion into electric power. The General Electric 7LM-1500-PE101, which will be used as a prime mover, is capable of outputting a torque significantly higher than that required by the generator. When the gas turbine engine is operating at 5500 RPM and producing about 16,000 HP (89% power), the power turbine can spin at 3600 RPM and produce 14,500 HP of continuous power to 15,750 HP of intermittent power. At rated power, the specific fuel consumption is about 0.65 pounds of diesel per hour per horsepower. We also

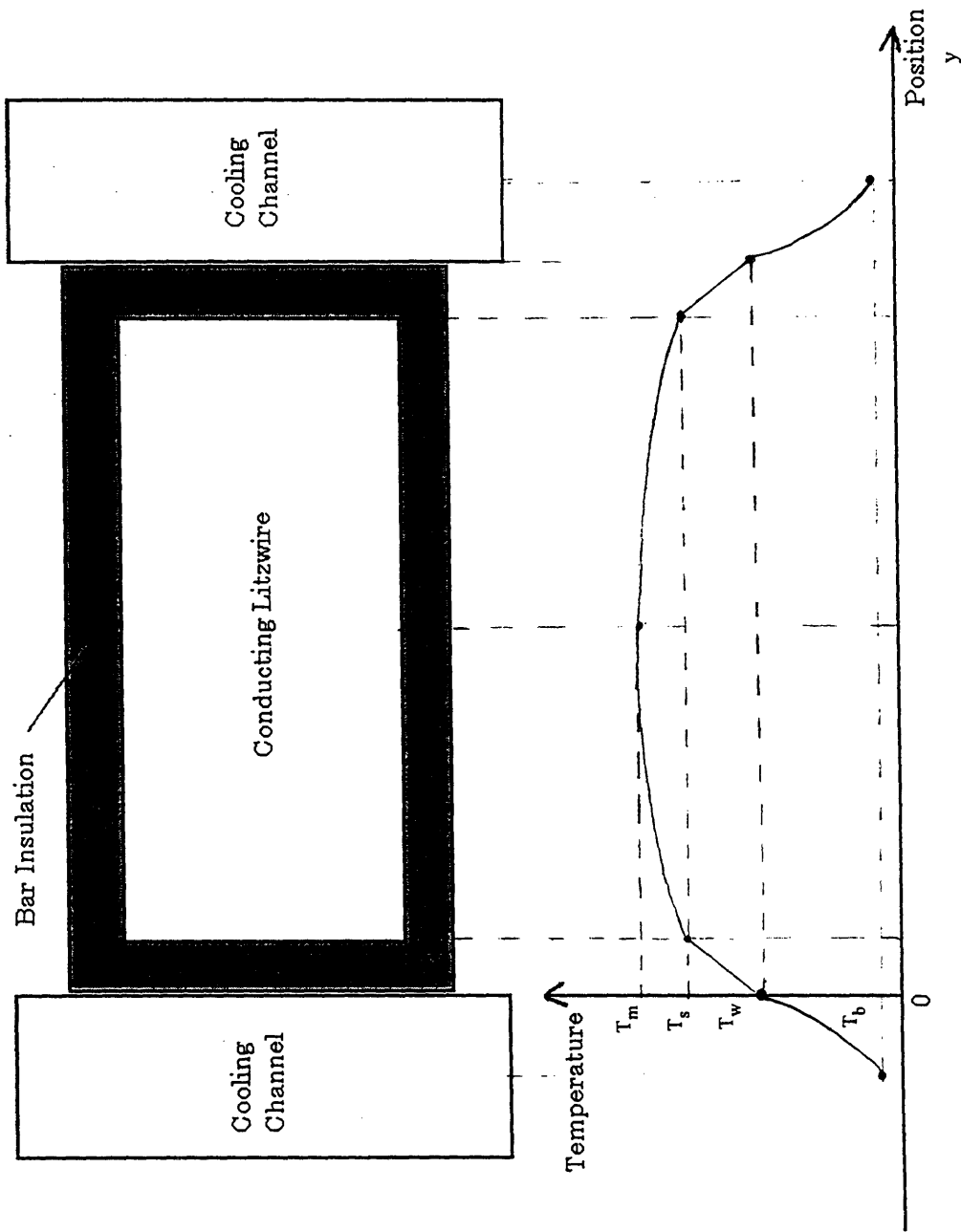


Figure 5.4: Temperature Profile in Armature Bar



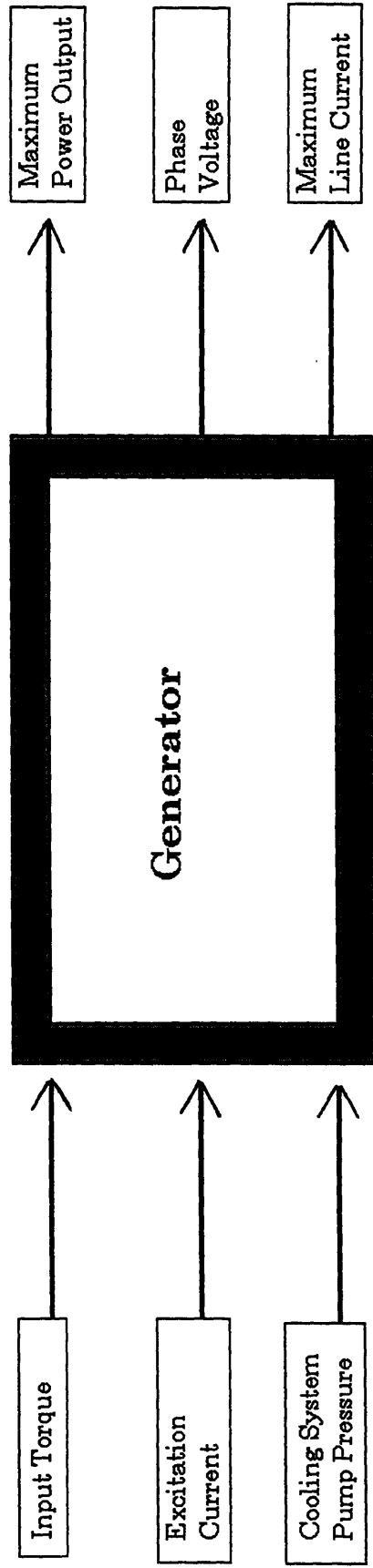


Figure 5.5: Generator Control Diagram

note that, at this setting, the power turbine's inlet temperature should be 1070 °F and that the gas generator must have a speed of 7500 RPM.<sup>73</sup>

The second control input is the excitation current supplied to the superconducting field coil located within the rotor assembly. Augmenting the excitation current results in a linear increase in the magnitude of the magnetic field and thus causes the induced voltage in the armature to increase proportionally. It must be noted that the internal voltage of the armature is limited by the design of the machine and by the selection of the insulation. The bus into which the generator will be connected is usually selected so as to accept the highest voltage which the machine is capable of. Under steady state conditions, the field current is of the order of 939 amperes and generates a peak field of about 4.8 Tesla.<sup>74</sup>

The third input parameter, which limits the current flowing through the armature, is the pumping pressure of the liquid coolant supplied to the armature. As explained earlier, an increase in the coolant's pumping pressure causes a proportional increase in the velocity of the fluid stream and thus allows higher amounts of Joulian heat to be removed from the machine.

A generator's power, which is delivered by a combination of the voltage drop across the terminals and current flowing through the conductor, should always be limited by the machine's design rather than by the torque supplied to it. When using a gas turbine as a prime mover, the selection of the turbine becomes critical since these units operate efficiently only when at full power. Therefore, the recommended prime mover for the MIT 10 MVA generator should be a Pratt & Whitney PW306A or a Textron-Lycoming FJ44-P turbine. These slightly smaller turbines, which are significantly more economical, are adaptations of those used on mid-sized business jets.

Since most generators in operation today are connected to a bus, which is designed to accept only a well determined voltage, the line current is the only variable used for controlling the machine's power output. Thus, the output power of our generator will be bounded by the performance of the cooling system rather than by any of the aforementioned factors.

## CHAPTER 6

### ELECTRICAL PROPERTIES

#### 6.1 Circuit Modeling

Most of the electric power used throughout the world is generated by *synchronous machines* driven by turbines. These generators, which can efficiently and steadily convert mechanical energy into electrical energy, use a complex spinning rotor in order to produce an alternating magnetic field. Since most rotors differ in field and damper winding design, they will exhibit different electrical properties<sup>75</sup>. In this chapter, we shall start with a simplified picture of the synchronous machine and model the dynamic behavior of the generator.

The author of this thesis wishes to acknowledge the substantial contributions of Professor James L. Kirtley in his guidance, his time and the numerous works he produced on the subject.

#### 1) Flux-Current Relationship

We will begin by modeling the circuit by assuming that a synchronous machine may be fairly represented by six *equivalent windings*. Four of these windings, the three armature windings and the phase winding, are actual windings. The remaining two, which represent the effects of distributed currents on the rotor's surface, are called "damper" windings. Thus, the phase and rotor fluxes ( $\lambda_{ph}$  and  $\lambda_R$ ) may be related to the phase and rotor currents

( $I_{ph}$  and  $I_R$ ) by a compound induction matrix (L). Thus:<sup>76</sup>

$$\begin{vmatrix} \lambda_{ph} \\ \lambda_R \end{vmatrix} = \begin{vmatrix} L_{ph} & M \\ M^T & L_R \end{vmatrix} \begin{vmatrix} I_{ph} \\ I_R \end{vmatrix} \quad \text{where } L_{ph} \text{ and } L_R \text{ are the inductance sub-matrix}$$

describing the armature winding and the rotor inductances, respectively; and M is the stator-to-rotor *mutual inductance* sub-matrix.

We note that:

$$\lambda_{ph} = \begin{bmatrix} \lambda_a \\ \lambda_b \\ \lambda_c \end{bmatrix} \quad \text{and} \quad \lambda_R = \begin{bmatrix} \lambda_f \\ \lambda_{sd} \\ \lambda_{sq} \end{bmatrix}$$

Expanding the sub-matrices and assuming that all rotor to armature mutual inductances vary sinusoidally with the rotor's position, we obtain the machine's flux-current relationships shown in **Equation 6.1**.

## 2) The Park Transform

The first step in the development of a dynamic model is to transform the stator's variables ( $U_{ph} = [U_a \ U_b \ U_c]^T$ ) into a reference frame fixed in the rotor by using the Park's Transformation. The axes of this new coordinate system will be called *direct*, *quadrature*, and *zero sequence* ( $U_{dq} = [U_d \ U_q \ U_0]^T$ ). The direct axis armature winding is the equivalent of one of the phase windings which is aligned with the field, while the quadrature winding is situated 90 electrical degrees ahead of the field winding. The zero sequence axis corresponds to quantities which vary, in all three phases, at the rate of rotation of the armature. The Park Transformation ( $T$ ), such that

$$U_{dq} = [T] U_{ph}, \text{ and its inverse, are given by } \mathbf{Equation 6.2.}^{77}$$

Applying the transformation equation to the flux-current relationship given in Equation 6.1 results in three separate sets of apparently independent flux/current relationships shown in **Equation 6.3**.

## 3) Voltage-Current Relationship

Assuming that the machine rotates at a constant angular frequency,  $\omega$ , such that  $\phi = \omega t$  and using  $p$  to denote the time differentiation,  $p = d/dt$ , we

$$\begin{bmatrix} \lambda_a \\ \lambda_b \\ \lambda_c \\ \lambda_f \\ \lambda_{sd} \\ \lambda_{sq} \end{bmatrix} = \begin{bmatrix} L_a & L_{ab} & L_{ab} & M \cos \phi & M_S \sin \phi & i_a \\ L_{ab} & L_a & L_{ab} & M \cos(\phi - \frac{2\pi}{3}) & M_S \sin(\phi - \frac{2\pi}{3}) & i_b \\ L_{ab} & L_{ab} & L_a & M \cos(\phi + \frac{2\pi}{3}) & M_S \sin(\phi + \frac{2\pi}{3}) & i_c \\ M \cos \phi & M \cos(\phi - \frac{2\pi}{3}) & M \cos(\phi + \frac{2\pi}{3}) & L_f & 0 & i_f \\ M_S \cos \phi & M_S \cos(\phi - \frac{2\pi}{3}) & M_S \cos(\phi + \frac{2\pi}{3}) & L_{fd} & L_d & i_{sd} \\ M_S \sin \phi & M_S \sin(\phi - \frac{2\pi}{3}) & M_S \sin(\phi + \frac{2\pi}{3}) & 0 & 0 & i_{sq} \end{bmatrix}$$

Equation 6.1

$$\begin{bmatrix} u_d \\ u_q \\ u_o \end{bmatrix} = \sqrt{\frac{2}{3}} \begin{bmatrix} \cos \phi & \cos(\phi - 2\pi/3) & \cos(\phi + 2\pi/3) & u_a \\ -\sin \phi & -\sin(\phi - 2\pi/3) & -\sin(\phi + 2\pi/3) & u_b \\ 1/2 & 1/2 & 1/2 & u_c \end{bmatrix}$$

$$U_{dq} = [T] U_{ph}$$

$$\begin{bmatrix} u_a \\ u_b \\ u_c \end{bmatrix} = \sqrt{\frac{2}{3}} \begin{bmatrix} \cos \phi & -\sin \phi & 1 & u_d \\ \cos(\phi - 2\pi/3) & -\sin(\phi - 2\pi/3) & 1 & u_q \\ \cos(\phi + 2\pi/3) & -\sin(\phi + 2\pi/3) & 1 & u_o \end{bmatrix}$$

Equation 6.2

$$\begin{array}{l}
 \lambda_d \\
 \lambda_q \\
 \lambda_o \\
 \lambda_f \\
 \lambda_{sd} \\
 \lambda_{sq}
 \end{array}
 =
 \begin{bmatrix}
 (L_a - L_{ab}) & 0 & 0 & \frac{\sqrt{3}}{2} M & -\frac{\sqrt{3}}{2} M_s & 0 \\
 0 & (L_a - L_{ab}) & 0 & 0 & 0 & -\frac{\sqrt{3}}{2} M_s \\
 0 & 0 & (L_a + 2L_{ab}) & 0 & 0 & 0 \\
 \frac{\sqrt{3}}{2} M & 0 & 0 & L_f & L_{fd} & 0 \\
 \frac{\sqrt{3}}{2} M_s & 0 & 0 & L_{fd} & L_d & 0 \\
 0 & -\frac{\sqrt{3}}{2} M_s & 0 & 0 & 0 & L_d
 \end{bmatrix}
 \begin{array}{l}
 i_d \\
 i_q \\
 i_o \\
 i_f \\
 i_{sd} \\
 i_{sq}
 \end{array}$$

Equation 6.3

$$\begin{array}{l}
 d \\
 q \\
 o \\
 f \\
 sd \\
 sq
 \end{array}
 =
 \begin{bmatrix}
 (L_a - L_{ab})p - (L_a - L_{ab})\omega & 0 & \frac{\sqrt{3}}{2} M_p \frac{\sqrt{3}}{2} M_{sp} & \frac{\sqrt{3}}{2} M_s \omega \\
 (L_a - L_{ab})\omega & (L_a - L_{ab})p & \frac{\sqrt{3}}{2} M \omega \frac{\sqrt{3}}{2} M_s \omega & -\frac{\sqrt{3}}{2} M_{sp} \\
 0 & 0 & (L_a + 2L_{ab})p & 0 & 0 & 0 \\
 \frac{\sqrt{3}}{2} M_p & 0 & 0 & L_{fp} & L_{fdp} & 0 \\
 \frac{\sqrt{3}}{2} M_{sp} & 0 & 0 & L_{fdp} & L_{dp} & 0 \\
 0 & -\frac{\sqrt{3}}{2} M_{sp} & 0 & 0 & 0 & L_{dp}
 \end{bmatrix}
 \begin{array}{l}
 i_s \\
 i_q \\
 i_o \\
 i_f \\
 i_{sd} \\
 i_{sq}
 \end{array}$$

Equation 6.4

obtain the voltage-current relationship displayed in **Equation 6.4** by taking the time derivative of Equation 6.3.

By comparing the two aforementioned relationships we note that<sup>78</sup>:

$$V_d = \frac{d}{dt} \lambda_d - \omega \lambda_q \text{ and that}$$

$$V_q = \frac{d}{dt} \lambda_q + \omega \lambda_d$$

#### 4) Power and Torque

Recalling from chapter 2 that the instantaneous power is given by:

$$P = V_a I_a + V_b I_b + V_c I_c,$$

we can use the Park Transform on the above equation to obtain:

$$P = 3/2 V_d I_d + 3/2 V_q I_q + 3 V_o I_o$$

and by substituting the voltage-current equations derived in the last section,

we find that:

$$P = \omega \frac{3}{2} (\lambda_d I_q - \lambda_q I_d) + \frac{3}{2} \left( \frac{d\lambda_d}{dt} I_d + \frac{d\lambda_q}{dt} I_q \right) + 3 \frac{d\lambda_o}{dt} I_o$$

Calling  $p$  the number of pole pairs and noting that the above equation

describes the electrical output power as the sum of the shaft power and the

rate of change of the stored energy, we can infer that the torque is given by<sup>79</sup>:

$$T = \frac{3}{2} p (\lambda_d I_q - \lambda_q I_d)$$

#### 5) The Synchronous Reactance

The per-unit synchronous reactance ( $x_d$ ) must be normalized to the internal voltage of the machine ( $E_f$ ). Since the internal voltage is given by:

$$E_f = \frac{\omega M I_f}{\sqrt{2}}, \text{ we have}^{80}:$$

$$x_a = X_a \frac{I_a}{E_f} = \frac{\omega (l_a - L_{ab}) I_a}{E_f}$$



Using the fact that the internal voltage is related to the terminal voltage ( $V_t$ ) as shown in Figure 6.1. We have<sup>81</sup>:

$$\frac{V_t}{E_f} = \sqrt{1 - x_a^2 \cos^2 \Psi} - x_a \sin \Psi$$

Hence, the per-unit synchronous reactance is then:

$$x_d = \frac{I_a X_a}{V_t} = x_a \left( \frac{E_f}{V_t} \right)$$

### 6) The Transient Inductance

The transient inductance relates the flux to the current during the time where the field winding is linking a constant flux and the damper currents have become negligible. Thus, we set:

$$I_{sd} = I_{sq} = 0 \quad \text{and} \quad V_f = \sqrt{\frac{3}{2}} p M I_d + L_f I_f = 0$$

Therefore, we obtain the expression for direct axis flux<sup>82</sup>:

$$\lambda_d = (L_a - L_{ab}) I_d + \sqrt{\frac{3}{2}} M I_f = \left[ (L_a - L_{ab}) - \frac{3}{2} \frac{M^2}{L_f} \right] I_d$$

Since the quadrature axis flux does not depend on the field current, it has a similar, but simplified, expression as the synchronous flux:

$$\lambda_q = (L_a - L_{ab}) I_q$$

### 7) The Transient Reactance

Based on the data contained in the preceding section, we find that the transient reactances are<sup>83</sup>:

$$x_d' = x_d \left[ 1 - \frac{3}{2} \frac{M^2}{(L_a - L_{ab}) L_f} \right] \quad \text{and}$$

$$x_q' = x_d$$

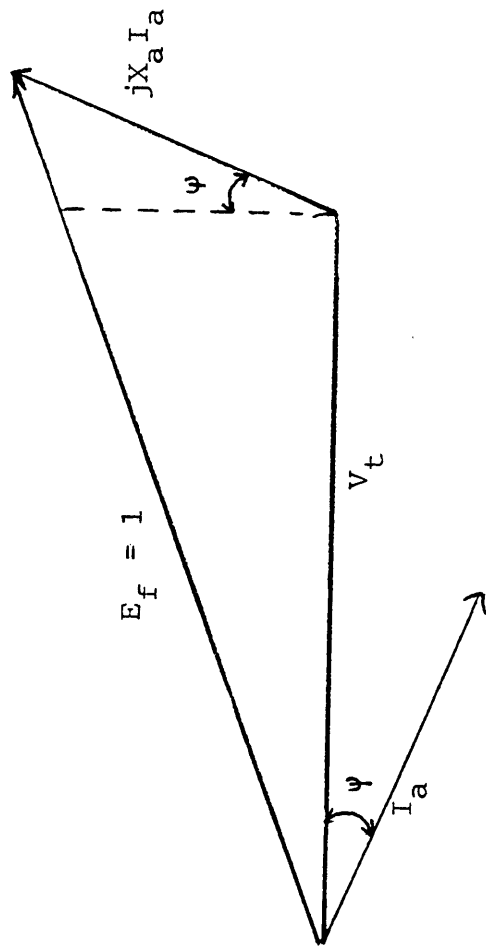


Figure 6.1: Voltage-Current Phasors

## 8) The Subtransient Reactance

The subtransient reactance is calculated by assuming that the flux linked by the damper shield is constant and that each of the three rotor windings trap flux. Thus  $V_{sd}=V_{sq}=V_f=0$ <sup>84</sup>. In evaluating the subtransient reactance, we note that the damper shell is symmetric, causing the direct and quadrature axis reactances to be equal. Thus, since there is no subtransient saliency, we find that<sup>85</sup>:

$$X_q'' = X_d'' = X_d \left[ 1 - \frac{3}{2} \frac{M_s^2}{(L_a - L_{ab})L_{d1}} \right] \text{ and the damper shell time constant is}$$

given by:

$$T_{do}'' = \frac{\mu_0 \sigma_f d R_f}{2p} \left[ 1 \pm \left( \frac{R_f}{R_s} \right)^{2p} \right]$$

Since the *synchronous reactance* is the reactive impedance between the internal voltage and the armature's terminals<sup>86</sup>, it is clear that too high a value will result in inferior dynamic performance, low transient stability limits, as well as more frequent adjustments of the excitation current for maintaining proper terminal voltage under varying loads. The open circuit field time constant depends on the excitor circuit's equivalent resistance. Since the field winding is superconducting, its resistance is zero and thus the open circuit field time constant is going to be very long. Thus, rapid field flux changes must be accomplished by applying a voltage to the field winding or by inserting a resistance in the field circuit.

## 9) Results

Using the expressions for  $L_a$  and  $L_{ab}$ , given in **Equations 6.5**, we may numerically compute the values of some of the aforementioned quantities by using MathCad 4.0. The results have been tabulated and are presented in **Table 6.1**, below<sup>87</sup>.

When  $np \neq 2$

$$L_a = \sum_{n \text{ odd}} \frac{16 I_a \mu_a N_a^2 \sin^2 \left( \frac{n\theta}{2} \right) \text{wae}}{3 n^3 \pi \theta^2 \text{wae} (n^2 p^2 - 4) (1-x^2)^2} \left[ (np-2) + 4x^{np+2} - (np+2)x^4 + 2 \left( \frac{np-2}{np+2} \right) (1-x^{np+2})^2 \left( \frac{R_{ao}}{R_s} \right) 2np \right]$$

If  $p=2$ ,  $n=1$  component:

$$L_a = \frac{8 I_a \mu_a N_a^2 \sin^2 \left( \frac{\theta}{2} \right) \text{wae}}{\pi \theta^2 (1-x^2)^2} \left( x^4 \ln x + \frac{1-x^4}{4} + \left( \frac{1-x^4}{8} \right)^2 \left( \frac{R_{ao}}{R_s} \right)^4 \right)$$

When  $np \neq 2$

$$L_{ab} = \sum_{n \text{ odd}} \frac{16 I_{ab} \mu_{ab} N_{ab}^2 \sin^2 \left( \frac{n\theta}{2} \right) \text{wae} \cos \left( \frac{2n\pi}{3} \right)}{3 n^3 \pi \theta^2 \text{wae} (n^2 p^2 - 4) (1-x^2)^2} \left( (np-2) + 4x^{np+2} - (np+2)^4 + 2 \left( \frac{np-2}{np+2} \right) (1-x^{np+2})^2 \left( \frac{R_{ao}}{R_s} \right) 2np \right)$$

If  $p=2$ ,  $n=1$  component:

$$L_{ab} = \frac{4 I_{ab} \mu_{ab} N_{ab}^2 \sin^2 \left( \frac{\theta}{2} \right) \text{wae}}{\pi \theta^2 (1-x^2)^2} \left( x^4 \ln x + \frac{1-x^4}{4} + \left( \frac{1-x^4}{8} \right)^2 \left( \frac{R_{ao}}{R_s} \right)^4 \right)$$

Equation 6.5

**Table 6.1:** Electrical Characteristics of 10 MVA Generator

Power Factor	.85
No load field current ( $I_{fnl}$ )	803 A
Armature current at short circuit ( $I_{fsi}$ )	216 A
Field current ( $I_f$ )	935 A
Synchronous reactance ( $x_d$ )	.27
Transient reactance ( $x_d'$ )	.20
Subtransient reactance ( $x_d''$ )	.13
Open circuit subtransient time constant ( $T_d''$ )	.1
Open circuit transient time constant ( $T_d'$ )	10

## **6.2 Transient Behavior**

Based on the parameters which were derived in the above section, we shall use a simulation model in state-space form to qualify the transient behavior of the machine. This model<sup>88</sup>, which assumes that the damper winding shell surrounds the field winding shell, and that the armature winding, in turn, surrounds both shells, offers significant benefits. These advantage include: an ease in studying machine and system transients as well as a more qualitative understanding of the qualifiers such as "transient" and "subtransient". In this model, flux changes in the armature must diffuse through the damper before affecting the rotor's winding.

The model for the synchronous machine, which was derived by Professor Kirltey at MIT<sup>89</sup>, may be summarized by a set of seven coupled first-order differential equations. These relations, which are given in **Equation 6.6**, may be simplified for use in an HP-48SX programmable scientific calculator. The restated equations, which were used in the analysis, are given in **Equation 6.7**.

$$\begin{aligned}
\frac{d\psi_d}{dt} &= -\frac{\psi_d}{T_{ad}} + \frac{e''_q}{T_{ad}} + \omega\psi_q + \omega_0 V \sin \delta \\
\frac{d\psi_q}{dt} &= -\omega\psi_d - \frac{\psi_q}{T_{aq}} - \frac{e''_d}{T_{aq}} + \omega_0 V \cos \delta \\
\frac{de''_q}{dt} &= -\frac{x'_d e''_q}{x''_d T''_{do}} + \frac{e'_q}{T''_{do}} + \left( \frac{x'_d - x''_d}{x''_d} \right) \frac{\psi_d}{T''_{do}} \\
\frac{de''_d}{dt} &= -\frac{x_q e''_d}{x''_q T''_{qo}} - \left( \frac{x_q - x''_q}{x''_q} \right) \frac{\psi_q}{T''_{qo}} \\
\frac{de'_q}{dt} &= -\alpha \frac{e'_q}{T'_{do}} + (\alpha - 1) \frac{e''_q}{T'_{do}} + \frac{e_{af}}{T'_{do}} \\
\frac{d\delta}{dt} &= \omega - \omega_0 \\
\frac{d\omega}{dt} &= \frac{\omega_0}{2H} \left[ T_m + \frac{\psi_d e''_d}{x''_q} + \frac{\psi_q e''_q}{x''_d} + \psi_d \psi_q \left( \frac{1}{x''_q} - \frac{1}{x''_d} \right) \right]
\end{aligned}$$

Equation 6.6

$$\begin{aligned}
\frac{de''_q}{dt} &= -\frac{e''_q}{T''_{do}} + \frac{e'_q}{T''_{do}} + \frac{x'_d - x''_d}{T''_{do}} i_d \\
\frac{de''_d}{dt} &= -\frac{e''_d}{T''_{qo}} - \frac{x_q - x''_q}{T''_{qo}} i_q \\
\frac{de'_q}{dt} &= -\alpha \frac{e'_q}{T'_{do}} + (\alpha - 1) \frac{e''_q}{T'_{do}} + \frac{e_{af}}{T'_{do}} \\
\frac{d\delta}{dt} &= \omega - \omega_0 \\
\frac{d\omega}{dt} &= \frac{\omega_0}{2H} (T_m + e''_q i_q + e''_d i_d)
\end{aligned}$$

Equation 6.7

$$i_a \approx \frac{1}{x''_d} e^{-\frac{t}{T''_d}} - \left\{ \frac{1}{x_d} + \left( \frac{1}{x'_d} - \frac{1}{x_d} \right) e^{-\frac{t}{T'_d}} + \left( \frac{1}{x''_d} - \frac{1}{x'_d} \right) e^{-\frac{t}{T''_d}} \right\} \cos(\omega t)$$

Equation 6.8

Using the aforementioned equations, we shall model the behavior of the generator when it is subjected to a sudden symmetrical fault. During the short circuit, the terminal voltages are set to zero and, consequentially, the machine draws currents which, in turn, produce torques. Assuming that there is no subtransient saliency and that the speed does not vary during the fault ( $\omega = \omega_0$ ), the following conditions must hold<sup>90</sup>:

$$\psi_{d0} = e_{q0}'' = e_{q0}' = e_{af} = 1$$

$$\psi_{q0} = e_{d0}'' = 0.$$

Thus, it can be shown that the current during the fault is given by **Equation 6.8**. A plot of the current versus time, during a sudden short circuit fault, has been plotted in **Figure 6.2**. This plot, which was obtained by setting the speed of the machine to about 1500 RPM and the field current to about 25 A, depicts a transient similar to that exhibited by conventional synchronous machines<sup>91</sup>. It is important, however, to note that the superconducting machine has a much longer time constant than conventional generators.

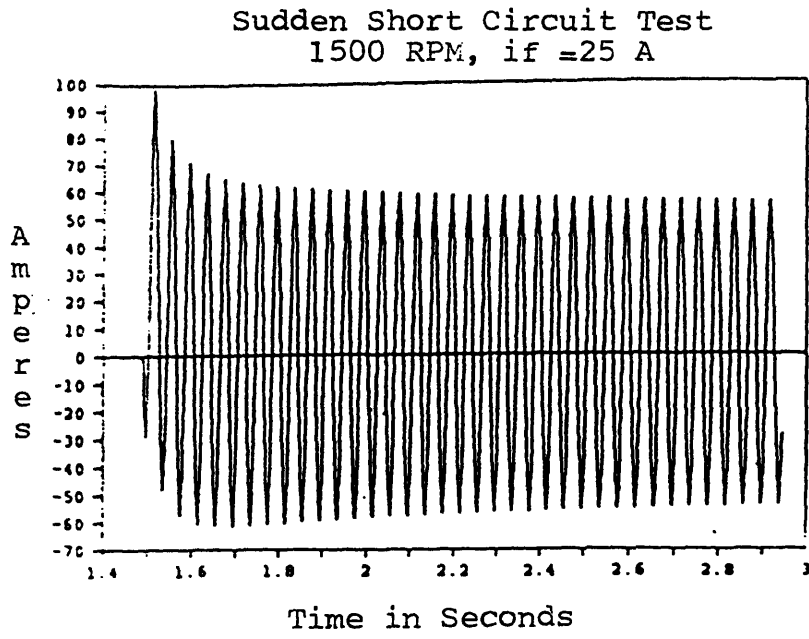


Figure 6.2: Current During Sudden Short Circuit



## **APPENDICES**

# SPECIFICATION

**Massachusetts  
Institute of  
Technology**

CRYOGENIC ENGINEERING LABORATORY  
ELECTRIC POWER SYSTEMS ENGINEERING LABORATORY

## APPENDIX A MIT 10 MVA HELICAL ARMATURE SPECIFICATIONS

### 1- Armature Specifications

#### 1.1 Electrical Specifications

Rating	10 MVA
Phase voltage	2,300 V
Phase voltage per turn	67.65 V rms
Rated voltage	4 kV
Phase current	1,445 A
Number of phases	3
Circuits per phase	2
Arrangement of circuits	Serial
Turns per phase	34
Turns per circuits	17
Number of bars per circuit	34
Total number of armature bars	204
Connection	Wye
Winding scheme	Helical
Operating frequency	60 Hz

#### 1.2 Mechanical Specifications

Inner radius	9.221 in
Outer radius	13.372 in
Tolerance	±0.005 in
Roundness	0.005 in
Taper	0.005 in
Overall length	53.1 in
Active length	43.12 in
Total axial length of bars	35.62 in
Length to ends	34.12 in
Support tube thickness	0.450 in
Maximum operating temperature	145 °C

			ISSUED			TITLE	
			CK'D			182	
			APP'D			<b>SP</b>	
			REL				
REV	BY	DATE		BY	DATE	REF DWG	SHEET OF

# SPECIFICATION

**Massachusetts  
Institute of  
Technology**

CRYOGENIC ENGINEERING LABORATORY  
ELECTRIC POWER SYSTEMS ENGINEERING LABORATORY

## 1.3 Electrical Parameters

Power Factor	0.85
$I_{fni}$	800 A
$I_{fsi}$	233 A
$I_f$ (rated)	943 A
Reactances	
Synchronous $x_d$	.29
Transient $x'_d$	.20
Subtransient $x''_d$	.14
Open-Circuit Time Constant	
Transient $T'_d$	10
Subtransient time $T''_d$	.1

			ISSUED			TITLE
			CK'D			183
			APP'D			<b>SP</b>
			REL			
REV	BY	DATE		BY	DATE	REF DWG
						SHEET OF

# SPECIFICATION

**Massachusetts  
Institute of  
Technology**

CRYOGENIC ENGINEERING LABORATORY  
ELECTRIC POWER SYSTEMS ENGINEERING LABORATORY

## 2- Structural Components

### 2.10 Inner Torque Tube

Material	Fiber reinforced epoxy
Thickness	0.394 in

### 2.11 Preparation

- 1) The ends of the tube must be prepared for the drilling of the bolt circles which will be described below.
- 2) The end surfaces must also be prepared for an O-ring seal between the torque tube and the end plate.
- 3) The inner surface of the torque tube will be coated with Glyptal 9921 semiconducting paint.

### 2.12 Inner End Flange Specifications

Number of inner circle bolts	60
Size	3/8 in
Inner bolt circle radius	9.438 in
Inner bolt circle blind holes, thread depth	2 in
Tolerance	±0.005 in

### 2.13 Testing

- 1) Torque Test: Tube must withstand a tortional load of  $2 \cdot 10^5$  n.m in both the clockwise and the counterclockwise direction.
- 2) Vacuum Test: The air leak through the inner torque tube, while under a high vacuum, must not exceed  $2 \cdot 10^{-7}$  cm<sup>3</sup>/sec.
- 3) Electrical Test: Test of the dielectric strength of the coated cylinder.

			ISSUED			TITLE	
			CK'D				184
			APP'D			<b>SP</b>	
			REL				
REV	BY	DATE		BY	DATE	REF DWG	SHEET OF

# SPECIFICATION

**Massachusetts  
Institute of  
Technology**

CRYOGENIC ENGINEERING LABORATORY  
ELECTRIC POWER SYSTEMS ENGINEERING LABORATORY

## 2.20 Outer Torque Tube

Material	Filament wound fiber reinforced epoxy
Pattern	Helical and circumferential
Nominal thickness	0.450 in

## 2.21 Construction Notes

- 1) The outer torque tube ends should be built-up and formed so as to mesh with the end flanges.
- 2) Steel dowel pins should be used to strengthen the end joints.

## 2.22 Outer Torque Tube Flanges

Material	Aluminum 6061
Number of outer circle bolts	40
Size	3/8 in
Outer bolt circle radius	11.210 in
Outer bolt circle blind holes, thread depth	1/4 in
Tolerance	±0.005 in

			ISSUED			TITLE	
			CK'D				185
			APP'D			<b>SP</b>	
			REL				
REV	BY	DATE		BY	DATE	REF DWG	SHEET OF

# SPECIFICATION

**Massachusetts  
Institute of  
Technology**

**CRYOGENIC ENGINEERING LABORATORY  
ELECTRIC POWER SYSTEMS ENGINEERING LABORATORY**

## 3- Armature Bar Specifications

### 3.1 The Conductor Bar

Specification	New England Electric Type 8 Litzwire
Description	Rectangular compacted litz
Winding pattern	Full Roebel Transposition
Finished height	1.481 in
Finished thickness	0.295 in
Pitch angle	15.5 degrees
Twist pitch	10.681 in
Number of bundles	19
Basic conductors per bundle	19 (concentric)
Total number of conductors	361
Aspect	10 group high x 2 groups wide
Basic conductor	AWG #21 copper magnet wire.
Diameter	0.0285 in
Film insulation	Heavy ML (Class 220 °C)
Film thickness	2.1 mils
Compression factor	about 96%
Packing factor	65.5 %

### For a bar in the 1st layer

Pitch angle	42 degrees
Helical length	42.325 in
Bend radius	2.00 in
Bend length	1.467 in
Cut conductor to	46.75 in
Length to bends	31.43 in

### For a bar in the 2nd layer

Pitch angle	47.4 degrees
Helical length	46.044 in
Bend radius	2.00 in
Bend length	1.654 in
Cut conductor to	50.85 in
Length to bends	31.18 in

			ISSUED			TITLE	
			CK'D			186	
			APP'D			<b>SP</b>	
			REL				
REV	BY	DATE		BY	DATE	REF DWG	
						SHEET	OF

# SPECIFICATION

**Massachusetts  
Institute of  
Technology**

CRYOGENIC ENGINEERING LABORATORY  
ELECTRIC POWER SYSTEMS ENGINEERING LABORATORY

## 3.2 Bar Insulation

Insulation requirement	Line-to-ground (2,300 V)
Material	MicaMat 77984
Description	Solventless B-staged epoxy tape Mica flake, glass cloth reinforced by a polyester mat
Application	3 layers (half-lapped)
Temperature rating	185 °C
Thermal conductivity	0.6301 j/m K
Finish thickness	0.051
Armored tape	Fusa-Flex (IMI #76593)
Description	Sealable epoxy armor tape
Application	1 layer
Temperature rating	185 °C
Finish thickness	0.0075 in
Shrinkable film	IMI 76856
Description	Polyester and polyvinyl fluoride film
Application	1 layer (half-lapped)
Thickness	0.002 in (removed after use)
Operating temperature	120 °C
Epoxy resin	IMI 74030 solventless epoxy resin
Semiconducting paint	Glyptal 9921
Application	Painted over entire outer bar surface
Thickness	1.5 mils
Total insulation thickness	60 mils
Nominal electrical stress	38.3 V/mil
Stiffness	500 MG

			ISSUED			TITLE			
			CK'D						187
			APP'D			<b>SP</b>			
			REL						
REV	BY	DATE		BY	DATE	REF DWG	SHEET	OF	

# SPECIFICATION

**Massachusetts  
Institute of  
Technology**

**CRYOGENIC ENGINEERING LABORATORY  
ELECTRIC POWER SYSTEMS ENGINEERING LABORATORY**

### 3.3 End Tab Assembly

Description	Close die forged tapered copper sleeve with a machined L shaped end-tab.
Minimum thickness	20 mils
End tab dimensions	1.5" axial x 0.16" azimuthal
 Application	 Slipped at end of stripped and tapered leads of bar and soft soldered with a 60/40 eutectic.
 Film insulation stripper Description	 Ambion Insulstrip 220 rev. 3053 High temperature film insulation dissolving agent.
Procedure	Dip last 1.5 inches of bar into a beaker containing stripper maintained at 99°.
Rinsing agent	1,1,1 Trichloroethane
 Bar taper	 Thickness gradually compressed by 50% over the last 1.5 inches of the bar
Taper angle	2.8 degrees
 End-connector insulation End-tab insulation Description	 MicaMat 77956 MicaMat 77956 (same) Polyester film backed non-woven glass
Application	3 layers (half-lapped)
Temperature rating	185 °C
 Finished thickness	 40 mils
Stiffness	600 MG
Nominal electric stress	50 V/mil
Max. dielectric strength	1200 V/mil

			ISSUED			TITLE	
			CK'D				188
			APP'D			<b>SP</b>	
			REL				
REV	BY	DATE		BY	DATE	REF DWG	SHEET OF



# SPECIFICATION

**Massachusetts  
Institute of  
Technology**

CRYOGENIC ENGINEERING LABORATORY  
ELECTRIC POWER SYSTEMS ENGINEERING LABORATORY

### 3.4 Bar Manufacture

- 1) Cut bar to appropriate length.
- 2) Strip leads.
- 3) Compress leads using a 20 ton press.
- 4) Install and solder end-connectors.
- 5) Wrap insulation over bar leads.
- 6) Wrap insulation over length of bar.
- 7) Insert into aluminum mold.
- 8) Bake for 60 minutes at 150 °C under a pressure of 80 psi.
- 9) Coat with semiconductive paint after cure.
- 10) Test bars.

### 3.5 Bar Testing Process

1) Resistance Test: A dc current of 2,500 A will flow, at low voltage, across an armature bar and the bar's resistance will be measured. If too high a resistance is found, the bar will be discarded.

2) Mega Test: A 5 kV dc voltage is applied between the bar and the insulation and the potential leak current is measured on a micro-ampere meter. This test confirms the integrity of the insulation.

			ISSUED			TITLE	
			CK'D				189
			APP'D			<b>SP</b>	
			REL				
REV	BY	DATE		BY	DATE	REF DWG	SHEET OF

# SPECIFICATION

Massachusetts  
Institute of  
Technology

CRYOGENIC ENGINEERING LABORATORY  
ELECTRIC POWER SYSTEMS ENGINEERING LABORATORY

## 4- Cooling Spacers

### 4.1 Description

The cooling spacers, located above and below each layer of bars, remove the heat generated by Joules effect heating taking place within the bar. They are extruded and rolled onto the stator assembly.

### 4.2 Specifications

Material	Aquanel or Fusa-Flex or Fabri-Therm
Number of channels	4 channels per bar (two above and two below the bar)
Total number	1128
Base thickness	60 mils
Height of cooling divider	65 mils
Width of cooling divider	80 mils
Length of channel	0.9047 m
Height of channel	65 mils
Width of channel	128 mils
Cross sectional area of channel	$5.37 * 10^{-6} \text{ m}^2$

Note: Cooling spacers must be free from any obstructions.

### 4.3 Cooling Fluid Properties

Specification	Dow Corning type 561
Description	Silicone transformer liquid.
Density	957 kg/m <sup>3</sup>
Heat capacity	1507 j/kg K
Thermal conductivity	0.1507 k/m K
Kinematic viscosity	$1.345 * 10^{-6} \text{ m}^2/\text{s}$

			ISSUED			TITLE	
			CK'D				190
			APP'D			<b>SP</b>	
			REL				
REV	BY	DATE		BY	DATE	REF DWG	SHEET OF



# SPECIFICATION

**Massachusetts  
Institute of  
Technology**

**CRYOGENIC ENGINEERING LABORATORY  
ELECTRIC POWER SYSTEMS ENGINEERING LABORATORY**

## 5- Armature Manufacture and Tests

### 5.1 Armature Manufacture

- 1) Prepare inner torque tube.
- 2) Coat inner surface of torque tube with semiconductive paint.
- 3) Test inner torque tube.
  
- 4) Install cooling channels.
- 5) Install molded bars using manufacturing spacers.
- 6) Repeat process for outer layer of bars.
  
- 7) Make end-connections and phase belt interconnections.
- 8) Insulate all connectors with MicaMat 77956
- 9) Seal cooling channels
- 10) Dip entire armature into a bath of IMI 74030 solventless epoxy resin.
- 11) Bake for four hours at 150 °C
- 12) Clear cooling channels and visually inspect stator winding
  
- 13) Build up outer torque tube and install end flanges

### 5.2 Mechanical Stresses in Armature

Steady state torque	2.65*10 <sup>4</sup> nm
Fault torque	2.65*10 <sup>5</sup> nm
Max. shear stress due to ovalizing forces	2270 psi
Max. torque shear stress between bar layers	385 psi

Glue joints must be designed to withstand large fault stresses, compressive loads and fatigue stresses throughout the life of the generator. An adaptation from Conley's and Hagman's thesis is given below.

Shear fault stress	2000 psi
Compressive load fault stress	6000 psi
Shear fatigue stress	55 psi
Compressive fatigue load	28 psi

			ISSUED			TITLE	
			CK'D			192	
			APP'D			<b>SP</b>	
			REL				
REV	BY	DATE		BY	DATE	REF DWG	SHEET OF

# SPECIFICATION

Massachusetts  
Institute of  
Technology

CRYOGENIC ENGINEERING LABORATORY  
ELECTRIC POWER SYSTEMS ENGINEERING LABORATORY

## 5.3 Armature Tests

1) Armature Resistance Test: Similar to the bar resistance test, a large dc current of about 2,500 A is allowed to flow through each of the phase belts and the small drop in potential across the winding is measured. The effective resistance of the coil is obtained and compared to the established limits.

2) Proof Test: The armature is subjected to a 9 kV 60 Hz waveform for one minute in order to prove the integrity of the insulation.

3) Phase Impulse Test: A full high frequency wave impulse of peak voltage of over 32 kV is applied between the ground and each of the three phase terminals. This test is used to simulate the effects of sudden large voltage spikes which may occur, for example, during thunderstorms.

4) Open Circuit Test: Undergone by the prototype armature, this test is performed at a fraction of the maximum excitation current. This experiment seeks to validate the results obtained by our theoretical modeling of the armature.

5) Short Circuit Heat Removal Test: This test, also undergone by the prototype armature and performed at a fraction of the maximum excitation current, seeks to demonstrate the capabilities of the cooling channels.

In addition to the electrical tests, the prototype armature as well as the production units must undergo two mechanical and structural tests.

6) Outer torque tube shear test: Leaving both ends of the inner torque tube free, the armature must support a torque of  $2 \times 10^5$  nm applied in both directions at one end flange while the other flange is kept fixed.

7) Inner torque tube shear test: Holding one end of the outer torque tube fixed, the opposite end of the inner torque tube will be subjected to a torque of  $1.5 \times 10^5$  nm in both directions.

			ISSUED			TITLE	
			CK'D				193
			APP'D			<b>SP</b>	
			REL				
REV	BY	DATE		BY	DATE	REF DWG	SHEET OF

## NEW ENGLAND ELECTRIC WIRE



FAX: (603) 838-6160

FAX: (603) 838-2805

## CORPORATION

365 MAIN STREET, LISBON, NEW HAMPSHIRE 03685

TEL: (603) 838-6624

TELEX #323602

## QUOTATION

To: MIT  
Morris Reconti

DATE: 07/27/93  
NEEWC QUOTE # 8269  
CUSTOMER RFQ#  
REPRESENTATIVE: Factory

In response to your recent inquiry, we are pleased to submit the following quotation:

ITEM	DESCRIPTION	QUANTITY	PRICE
#1	19(19/21 AWG H. nyleze) type 8 litz finished dim. 0.295" thick x 1.481" wide	1,000'	\$4.81/ft. (firm)

Terms: Net 30 days.

Min. Order: 1,000'

FOB: Lisbon, NH

Lead Time: 6 wks. A.R.O.

Salesperson: Cliff Boivin

All orders are subject to a +/- 10% quantity variance.

This Quotation is valid for 30 days.

FAX (603) 838-2805 OR (603) 838-6160

## APPENDIX B

### Designing Bars with Smooth Transition Sections

#### I. Introduction

In this section we shall explain another option available in the design of the armature bars. Instead of using circular arcs in the transition regions, a parabolic section can be used as a bridge between the helical and the straight portions of the bar. A smooth transition region, which would start out with zero curvature at the end and increase the curvature at a constant rate until the helix angle is reached, would offer several benefits. The two major advantages inherent in this method are the fact that all of the bars lie exactly on top of each other and that it can easily be programmed in a milling machine operating in the axial-azimuthal plane exclusively. It is for these reasons, among others, that a smooth transition region was incorporated into the 10 MVA delta connected armature<sup>1</sup>. In the remaining part of this section, we will describe how the present armature could have been designed with smooth transition regions.

#### II. The Curvature in the Helical Region

**Figure B1** represents an armature bar having a length to ends of 34.14 and a length to ends of 31.54. Except for the fact that the transition region is a smooth curve rather than a circular section, the bar is almost identical to the one described in chapter 2. It is also evident, since the geometry of the bar has changed, that the helix angle is no longer the same.

The trick in determining the helix angle lies in recognizing the fact that the entire bar must travel 180 degrees. By plotting curvature, or  $\frac{d\theta}{dz}$ , versus axial distance (Z) in **Figure B2**, the trick now involves realizing that the area under the curve must be 180 degrees. Making the unknown, C, the curvature of the armature bar, and by breaking down the curve into a rectangular region and a pair of triangular surfaces, we may write:

$$(31.52 * C) + 2 * (\frac{1}{2} * 1.3 * C) = 180$$

Solving this equation we find that  $C=5.48446$  degrees per inch or  $C=0.09572$  rad/inch. This tells us that, in the helical region, for every inch traveled along the axial direction, the bar turns by 5.5 degrees. Having determined the curvature in the helical region, we shall write the equation of the path of the bar.

---

<sup>1</sup> Private conversation with D. Otten, MIT Electric Power Systems Engineering Laboratory, Cambridge MA.

### III. Parametric Equations of the Bar

Working in cylindrical coordinates in the  $(r, \theta, Z)$  frame, we will determine the parametric equation describing the path of the bar. We will start by the helical region first, as it is simpler than the transition section.

#### a) The Helical Region

In the helical section, the bar has a constant helical angle and thus the curvature is constant. Since this curvature,  $C$ , has just been determined above, we have:

$$\frac{d\theta}{dZ} = C = 0.09572$$

After integrating both sides with respect to  $Z$ , we find that the parametric equation for theta is:

$$\theta(Z) = 0.09572 * Z \quad (\text{helical region})$$

#### b) The Transition Region

In the transition region, things are a bit more complicated. It can be seen, from inspection of Figure B2, that the linear relationship between curvature and axial distance is:

$$\text{Curvature} = \frac{d\theta}{dZ} = \left( \frac{\Delta \text{Curvature}}{\Delta Z} \right) \cdot Z = 0.07363 Z$$

After integrating both sides with respect to  $Z$ , we find that the parametric equation for theta is:

$$\theta(Z) = 0.03681 Z^2 \quad (\text{transition region})$$

### IV. Bar Length

The total length of the bar will be determined by separately calculating the lengths of the helical and the transition sections. We recall from basic calculus that the formula for arc length for a parametrically defined function is given by<sup>2</sup>:

$$L(A, B) = \int_A^B \sqrt{\left(\frac{dx}{dt}\right)^2 + \left(\frac{dy}{dt}\right)^2 + \left(\frac{dZ}{dt}\right)^2} dt$$

In our case, since  $Z$  is the independent parameter, we have  $t=Z$  and thus  $\frac{dZ}{dt} = \frac{dZ}{dZ} = 1$ . Furthermore, we recognize that:

$$\left(\frac{dx}{dZ}\right)^2 = r^2 \sin^2(\theta) \left(\frac{d\theta}{dZ}\right)^2 \quad \text{and} \quad \left(\frac{dy}{dZ}\right)^2 = r^2 \cos^2(\theta) \left(\frac{d\theta}{dZ}\right)^2 \quad \text{using the law of cosines, we}$$

immediately notice that:

$$\left(\frac{dx}{dZ}\right)^2 + \left(\frac{dy}{dZ}\right)^2 = r^2 \left(\frac{d\theta}{dZ}\right)^2 \quad \text{where } r \text{ is the radial distance between the middle of the insulated}$$

bar and the  $Z$  axis of the cylindrical armature. For the first layer,

$$r = R_i + H_c + \frac{1}{2}(H_b + 2 * T_i) = 9.221 + 0.125 + \frac{1}{2}(1.481 + 2 * 0.060) = 10.1465 \text{ inches.}$$

<sup>2</sup> William E. Boyce, R. DiPrima, Calculus, J. Wiley, 1988, pp. 763-771



Substituting these results into the arc length equation, we are left with:

$$L(Z_1, Z_2) = \int_{Z_1}^{Z_2} \sqrt{r^2 \left( \frac{d\theta}{dZ} \right)^2 + 1} dZ$$

We will now determine the total length of a bar located in the innermost layer by separately evaluating the above integral for the helical section and for the transition region.

#### a) The Helical Region

As depicted in Figure B2, the helical region, which begins at  $Z_1=1.3$  and extends to  $Z_2=32.82$ , has a constant curvature. It was determined in the previous section that, in this region, the relationship between curvature and the axial distance ( $Z$ ), is:

$\frac{d\theta}{dZ} = 0.09572$ . Substituting this result into the final expression of arc length, we find that, for the first layer:

$$L_{helix}(1.3, 32.82) = \int_{1.3}^{32.82} \sqrt{(10.1465)^2 \cdot (0.09572)^2 + 1} dZ = 1.39401 * (32.82 - 1.3) = 43.939 \text{ in.}$$

#### b) The Transition Region

Since both transition regions are identical, we shall concentrate exclusively on the one located on the left of the helical section. We recall from Figure B2 that the left transition region begins at  $Z_1=0$  and ends at  $Z_2=1.3$ . Substituting the expression for curvature:  $\frac{d\theta}{dZ} = 0.07363 \cdot Z$ , determined above, into the arc length formula, we write:

$$L_{Transition}(0, 1.3) = \int_0^{1.3} \sqrt{(10.1465)^2 \cdot (0.07363 \cdot Z)^2 + 1} dZ$$

This integral was numerically evaluated by using MathCad 4.0 on a Windows system. The length of the transition region for bars located in the inner layer is:

$$L_{Transition}(0, 1.3) = 1.482 \text{ inches.}$$

#### c) The Total Length

The total length of the bar can now be determined by adding together the lengths of the individual parts. Thus:

$$L_1 = L_{Helix} + 2*(L_{Transition}) + 2*(L_{Straight})$$

$$L_1 = 43.939 + 2*(1.482) + 2*(.750) = 48.403 \text{ inches}$$

If this method were used, the first layer of armature bars would be cut to about 48.40 inches instead of the 46.76 inches determined by using circular transition regions. As explained in the text, both methods have their own advantages and shortcomings.

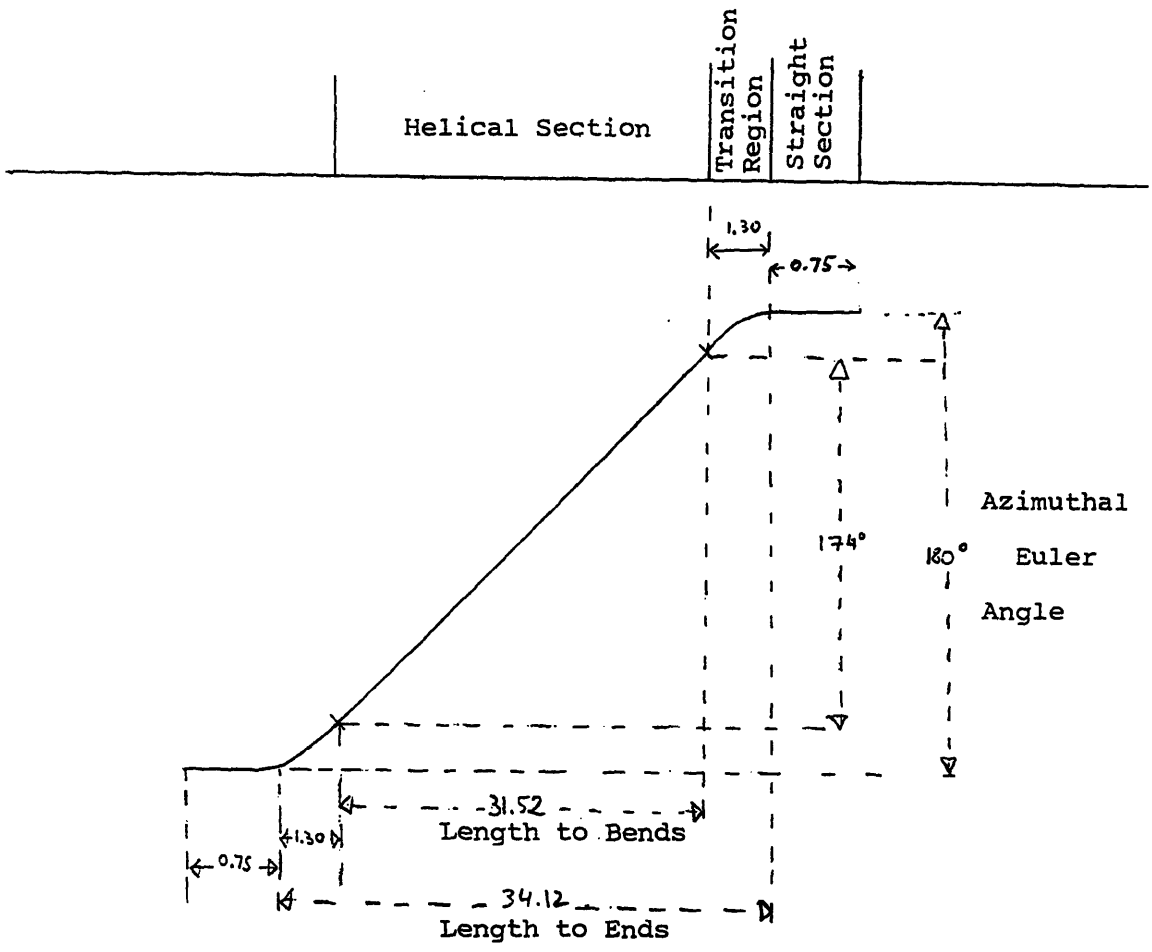


Figure B1: Representation of Armature Bar with Smooth Transition Regions in the Axial-Azimuthal Plane

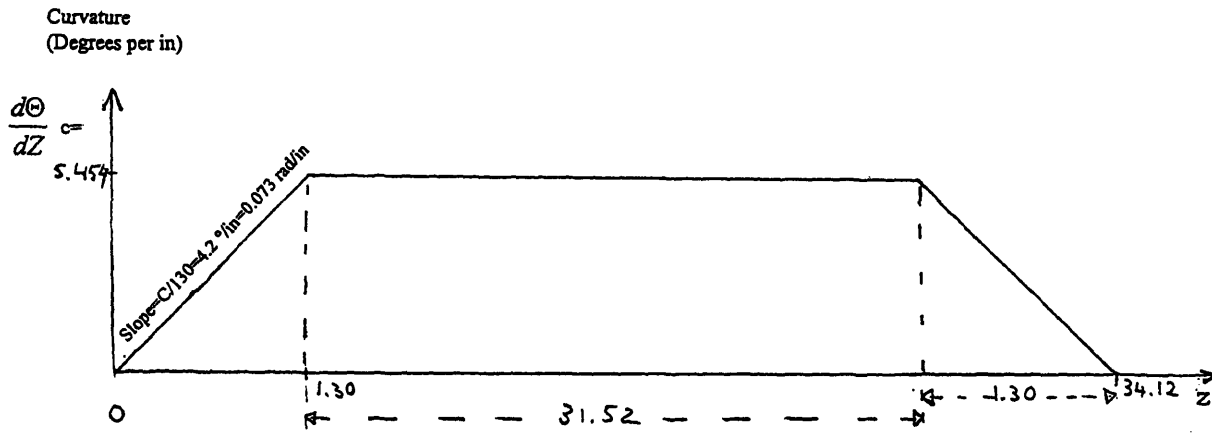


Figure B2: Curvature as a Function of Axial Distance for a Smooth Transition Helical Bar

## APPENDIX C

### Quantum Mechanical Properties of Copper

#### I. The Free Electron Theory of Metals

The great physicist Niels Bohr said that in order to fully understand a complex system, one must intimately understand its basic components. In this section we shall explore the ability of metals in conducting heat and electricity through the use of the free electron theory. The concept of "free electrons" in metals was first suggested by Thomson, the discoverer of the particle, at the end of the 19th century. Sommerfeld later modified an electron-gas model to account for the degeneracy of this fermion in 1928. This work allowed transport coefficients, such as thermal and electrical conductivity, to be related to basic quantum mechanical properties.

#### II. States of Particles in Momentum Space

The transport properties of electrons can be explained by considering the states of the particles in momentum space. Hence, we will describe this space and understand how it is filled by a set of degenerate free particles. We know from basic quantum mechanics that the states of a Fermi system at T=0 K are filled up to the Fermi energy,  $\epsilon_F$ , and that states above this energy are empty. Based on the Schrodinger equation, the energies of traveling wave states in a cubical box of volume  $V=L^3$  are:

$\epsilon_{1,2,3} = \frac{h^2}{2mL^2}(l_1^2 + l_2^2 + l_3^2)$  where  $h$  is the Plank constant,  $m$  the mass of the particle and  $\epsilon$  is the energy.

but since momentum,  $p$ , is related to the kinetic energy by:  $\epsilon = \frac{p^2}{2m}$ , we may write, by substitution:

$$p_i = \frac{h \cdot l_i}{L} \text{ where } l_i = 0, \pm 1, \pm 2, \dots \text{ where } i \text{ denotes the coordinate } (x, y, z)$$

We note that both positive and negative momentum values are allowed, corresponding to particles traveling in opposite directions. Due to the Pauli exclusion principle, each of these momentum states may be occupied by one electron of each spin type. At T=0 K the occupied states in momentum space form a *Fermi sphere* whose radius,  $p_F$ , corresponds to the *Fermi momentum*. The Fermi momentum, is intimately related to the *Fermi energy*, an intrinsic property of the material in question, by the following expression:

$$p_F = \sqrt{2m\epsilon_F} \text{ where } \epsilon_F \text{ is the Fermi energy.}$$

The Fermi velocity is, of course, simply:  $V_F = \frac{p_F}{m}$

We note that only the states within the Fermi sphere represented in Figure C1 are occupied.

The Fermi energy for copper, our core material, is  $\epsilon_F = 7$  eV therefore the Fermi momentum of the metal is:  $p_F = 1.42 \times 10^{-24}$  kg m/s and the Fermi velocity is about  $V_F = 1.6 \times 10^6$  m/s.

### III. Electrical Conductivity

We will now consider electrical conductivity and relate the macroscopic transport properties to quantum mechanical phenomena. We recall from elementary electrostatics that there is no electric field in a metal at equilibrium. However, in a steady-state non-equilibrium situation, charge flows in an attempt to cancel out the electric field within the metal. The electrical transport law:

$$J_E = K_E \cdot E$$

relates the charge per second per unit area ( $J_E$ ) moving in the material to the electric field ( $E$ ) established in the metal through a constant of proportionality known as the *electrical conductivity*  $K_E$ .

An electron in such a non-equilibrium situation feels a force  $F = -qE$ , as a result of the electric field and its own charge  $-e$ . This particle would accelerate freely if it did not lose energy to resistive interactions within the metal. In this simplified model, we shall assume that the interactions with impurities, ion cores and other electrons are proportional to the electron's velocity. Taking this drag force into account, we write the equation of motion of the particle:

$$m \frac{dV}{dt} = -\alpha V - eE \text{ where } \alpha \text{ is a constant determined by the nature of the frictional forces.}$$

In the absence of an electric field, the last term drops out and the solution to the differential equation gives:

$$V = V_0 \cdot e^{-\frac{\alpha}{m}t} \text{ where } V_0 \text{ is the particle's initial velocity.}$$

This expression states that the velocity decays to zero and the time constant of this decay is called the relaxation time,  $\tau = \frac{m}{\alpha}$ .

When an electric field is present, the system relaxes until  $\frac{dV}{dt} = 0$  and we have a steady-state non-equilibrium situation. The solution to the aforementioned differential equation becomes:

$$V = -\frac{eE}{\alpha} = -\frac{e\tau}{m}E$$

In the presence of an electric field, every particle cannot have the same small velocity determined above since this would violate the Pauli exclusion principle. What happens instead is that the velocity of every particle in the Fermi sphere is shifted in velocity by the small amount  $\delta V = V = -\frac{e\tau}{m}E$ . Thus, the entire Fermi sphere is shifted by an amount:

$$\delta k = \frac{\delta p}{\hbar} = \frac{m\delta V}{\hbar} = -\frac{e\tau E}{\hbar} \text{ (where } \hbar = \frac{h}{2\pi}\text{)}$$

as shown in **Figure C2**.

We note that since this shift of origin is quite small, most of the states which were occupied initially remain unchanged. Because of the electric field, a thin crescent of states has been vacated at one edge of the figure in favor of another one located at the opposite end. As is characteristic of degenerate Fermi systems, only electrons which were near the Fermi surface have undergone a change of quantum state.

The electric current density is the charge density times the particle velocity. Thus:  $J_E = -e\delta\rho V_F$  where  $\delta\rho$  is the density of current carriers.

The density of the current carriers may be determined by using the familiar equation for the density of states. The number of energy levels per unit energy between  $\epsilon$  and  $\epsilon + \delta\epsilon$  is:

$$D(\epsilon) = \frac{m^{3/2}}{\sqrt{2} \pi^2 \hbar^3} V \epsilon^{1/2} = \frac{3\rho V \epsilon^{1/2}}{4\epsilon_F^{3/2}} \text{ in terms of the Fermi energy.}$$

Since for fermions there are two particles per energy level, the density of *particles* per unit energy  $R(\epsilon)$  is obtained by multiplying the expression above by  $2/V$ . Thus:

$$R(\epsilon) = \frac{3\rho \epsilon^{1/2}}{2\epsilon_F^{3/2}}$$

The density of current carriers is just the density of particles per unit energy, evaluated at the Fermi energy, times the energy width of the crescent. Hence:

$$\delta\rho = R(\epsilon_F) \cdot \delta\epsilon = \frac{3\rho}{2\epsilon_F} \delta\epsilon$$

The energy width of this crescent is related to the shift in velocity, determined above, by the following equation:  $\delta\epsilon = mV_F\delta V$ . Combining these results, we can write an approximate relationship for the current density:

$J_E \sim \frac{e^2 \tau \rho}{m} E$  and recognize that the coefficient of electric conductivity is:

$$K_E \equiv \frac{e^2 \tau \rho}{m}$$

Thus we have related a macroscopic quantity,  $K_E$ , to quantum properties.

Now, let's return to copper. The resistivity of copper at room temperature is:  $r = 1/K_E = 1.7 \times 10^{-8} \Omega \cdot m$ . Knowing that the average separation of copper atoms is about 0.2 nm and that each atom contributes only one conduction electron, we find a density on the order of:  $\rho \approx \frac{1}{(2 \times 10^{-10} m)^3}$ . Thus, the relaxation time of the electrons within the copper core is:  $\tau = \frac{m}{e^2 \rho r} \approx 2 \times 10^{-14}$  seconds.

Since at room temperature the average time between collisions is about the same as the relaxation time,  $\tau$ , we can determine the average distance that the electron travels in between such events. This distance, known as the *mean free path* is given by:  $d = V_F \tau$  and is represented in **Figure C3**. For copper, the mean free path of electrons within the metal is about 32 nm, more than two orders of magnitude larger than the mean atomic separation. Aluminum, on the other hand, has a significantly lower mean free path than copper and therefore a higher resistivity. Although it is a lighter and cheaper material, it will not be used in the armature of the MIT generator.

#### IV. The Drift Velocity

When a potential difference is applied across the conductor, an electric field is created in the metal. This field, in turn, creates an electric force on the electrons and hence, a current. As we have explained in detail above, the electrons do not simply move in straight lines along the conductor but undergo repeated collisions with the ion cores, impurities and other electrons. These interactions result in the roughly random zig-zag motions which were drawn in **Figure C3**. However, despite the collisions, the electrons move slowly along the conductor, in a direction opposite

to the electric field, at an average velocity called the *drift velocity* ( $V_d$ ). This drift velocity is much smaller than the average speed between collisions,  $V_F$ , determined in the preceding section. Figure C4 illustrates the motion of a mobile charged carrier in a conductor in the presence of an electric field. It is apparent that the random motion of the particle is modified by the field and that the electron has a drift velocity.

Since the work done by the electric field on the moving electron is greater than the average energy lost in the collisions, a net current ( $I$ ) flows. From elementary physics we recall that a current is just the rate at which charge flows through the cross sectional area ( $A$ ) of the conductor. Thus:

$$I = \lim_{\Delta t \rightarrow 0} \left( \frac{\Delta Q}{\Delta t} \right) \text{ where } Q \text{ is the total charge flowing through the surface during time } \Delta t.$$

The charge  $\Delta Q$  contained in a thin slice of thickness  $\Delta x$  of the conductor is:  $\Delta Q = \text{number of charges within the slice} \times \text{charge per particle} = (nA\Delta x)e$ . Since the charge carriers move with speed  $V_d$ , they travel a distance  $\Delta x = V_d\Delta t$  in time  $\Delta t$ . Substituting these last two relations into the definition of current, we get:

$$V_d = \frac{I}{neA} \text{ where } n \text{ is the number of conduction electrons per unit volume and } e \text{ is the electron charge } (-1.6 \times 10^{-19} \text{ C}).$$

We will now determine the drift velocity for electrons traveling through a phase belt of the MIT generator armature, as it operates at rated power and voltage. The conductor bar is composed of 361 individual wires each of area  $A = 4.12 \times 10^{-7} \text{ m}^2$ . Knowing that the bar current is 1,445 A, each individual conductor carries a current of  $I=4$  Amperes.

To determine the number of conduction electrons per unit volume for copper, we must divide Avogadro's number ( $N$ ) by the volume occupied by a mole of copper atoms. We have:

$$n = \frac{N\rho}{W} = \frac{6.02 \times 10^{23} \times 8.95 \times 10^6 \text{ g/m}^3}{63.5 \text{ g}} = 8.48 \times 10^{28} \text{ electrons/m}^3 \text{ where } \rho \text{ is the density and } W \text{ is the atomic weight of copper.}$$

Thus, we find that the drift velocity in a basic conductor is:  $V_d = 7.16 \times 10^{-4} \text{ m/s}$ . As explained above, this drift velocity is much smaller than the average speed between collisions  $V_F \approx 1.6 \times 10^6 \text{ m/s}$ . We remark that when an electrical switch is closed, light appears instantly since it is the electric field itself which carries the signal at a velocity on the order of that of light ( $3 \times 10^8 \text{ m/s}$ ).

## V. Thermal Conductivity

Having explained in great detail the quantum mechanical nature of electrical conductivity, we shall now concentrate on a similar treatment of thermal conductivity. We recall Fourier's law of heat conduction, for a temperature gradient in the  $z$  direction:

$$J_T = -K_T \frac{dT}{dz} \text{ where } J_T \text{ is the heat current density, or in other words the heat flow per unit cross sectional area per second and } K_T \text{ is the coefficient of thermal conductivity.}$$

Once again it is the electrons near the Fermi surface which are responsible for conduction since for every particle within the sphere going in the +z direction, there is one traveling in the opposite direction. This phenomenon is sometimes called *momentum pairing*. The heat current density is therefore:

$$J_T = (\text{number of heat carriers per unit volume}) * (\text{velocity of a carrier}) * (\text{heat carried per particle})$$

The first of these terms is just the density of conduction electrons ( $\rho$ ) times the fraction of particles that are thermally excited since they are exclusively responsible for the heat conduction. Thus:

$$\text{number of heat carriers per unit volume} = \rho \frac{k_B T}{\epsilon_F} \text{ where } k_B \text{ is Boltzmann's Constant.}$$

As explained at length above, the velocity of the carrier is the Fermi velocity so the second term is just:  $V_F$ . The third term is the net heat carried by the particle. In between each collision, the net heat transferred along the z axis is given by Boltzmann's law:  $\delta E = k_B \delta T$ .

Since we can assume that a temperature change of order  $\delta T$  occurs every time the particle travels a mean free path,  $d$ , we can state that the gradient in temperature is:  $\frac{dT}{dz} = -\frac{\delta T}{d}$  where the minus sign indicates that heat flows from high to low temperatures, in the direction opposite to the gradient.

Thus,  $\delta T = -\tau V_F \frac{dT}{dz}$ . Substituting this expression into Boltzmann's law, above, we determine that the net energy carried per particle is:

$$\delta E \sim -k_B \tau V_F \frac{dT}{dz}$$

Combining these results finally gives the heat current density:

$$J_T \sim -\frac{\rho}{\epsilon_F} k_B^2 T \tau V_F^2 \frac{dT}{dz}$$

Recognizing that  $\epsilon_F = \frac{1}{2} m V_F^2$ , we may use the definition of kinetic energy to simplify the final expression written above. Comparing this equation to Fourier's law of heat conduction, we recognize the coefficient of thermal conductivity to be:

$$K_T \equiv \frac{2\rho}{m} k_B^2 T \tau$$

As expected, the thermal conductivity of copper (4.0 j.cm.K/s) is superior to that of aluminum by about a factor of two. It is clear that the heat developed within the copper bars will be smaller than that of aluminum (because of the lower resistivity of copper) and that heat will flow more readily out of copper (because of the higher thermal conductivity of copper). By using copper cores in the armature bars, we reduce our Joules effect losses and gain cooler bars. The advantages of copper over aluminum have been well demonstrated.

As an aside, if we take the ratio of  $K_T$  to  $K_E$  we "discover" an interesting rule named the Weidemann-Franz Law:

$$\frac{K_T}{K_E} = \frac{k_B^2 T}{e^2}$$

Because the processes which govern the relax of electrons in electrical conductivity are not identical to those that are involved in thermal conductivity, the Weidemann-Franz law often breaks down. However, the relationship, which assumes that both relaxation times are comparable, does explain why materials which are good electrical conductors are also good conductors of heat.

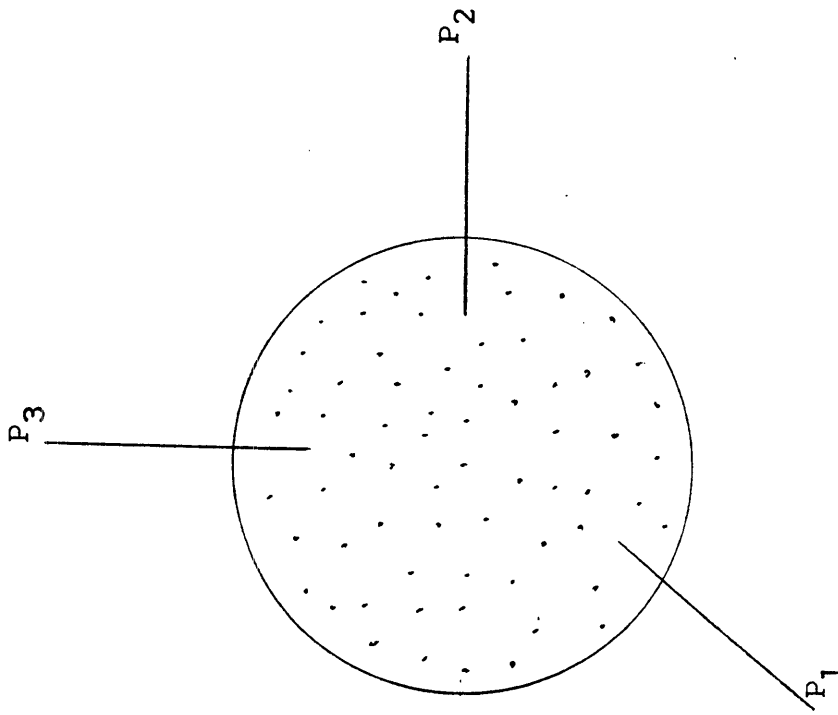


Figure C1: Fermi Sphere in Momentum Space

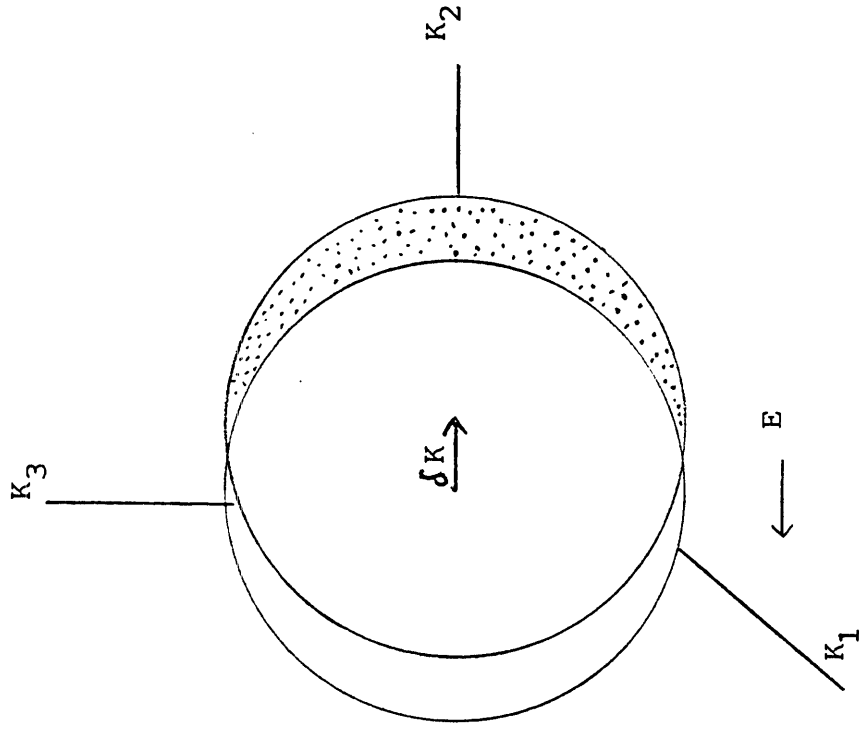


Figure C2: Shift of Fermi Sphere by an Electric Field



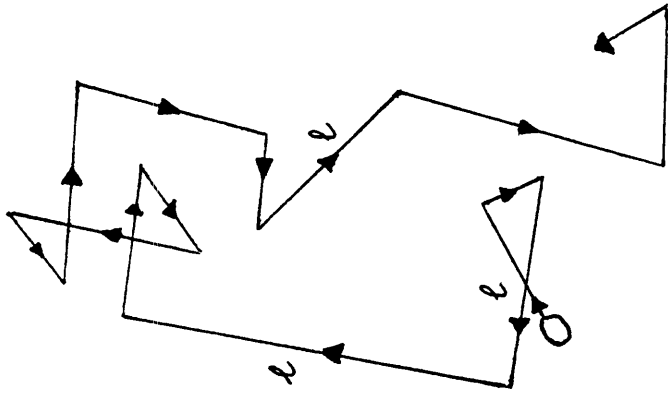


Figure C3: Random Motion of a Charged Carrier in an Insulated Conductor

Note: The average distance in between collisions is the mean free path  $d$ .

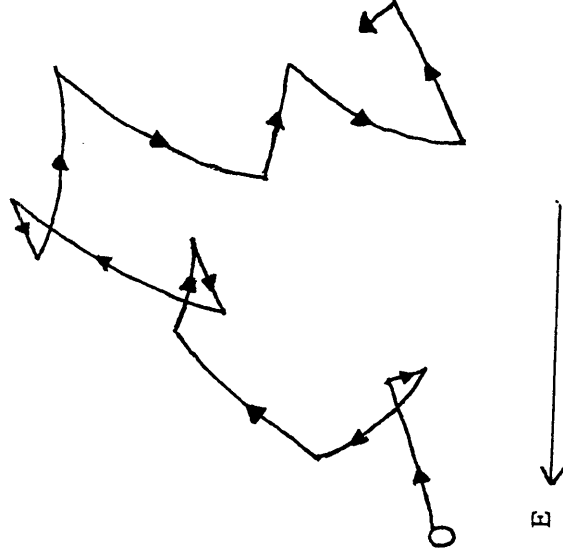


Figure C4: Motion of a Charged Carrier in a Conductor in the Presence of an Electric Field

Note: The particle has a drift velocity in a direction opposing the field.

## Bibliography of Appendix C

The author acknowledges the help from the following sources:

Eisberg, R., and Resnick, R., *Quantum Physics of Atoms, Molecules, Solids, Nuclei and Particles*. New York: Wiley, 1985.

Tipler, Paul A., *Modern Physics*. New York: Worth, 1978

Brehm, J., and Mullin, W., *Introduction to the Structure of Matter*. New York, Wiley, 1989.

Feynman, R., Leighton R., and Sands M, *The Feynman Lectures on Physics, Vols 1-3*, Reading MA: Addison Wesley, 1963-1965.

Serway, R. A., *Physics for Scientists and Engineers*, Saunders 1985.

Recanati, M. A., *Electron Conduction and Tunneling through Nanometer Size Gaps*, 1989

Recanati, M. A., Quantum Mechanics I, II and III Class Notes.

and, of course, the help of John Winhold, Professor Emeritus, Rensselaer Polytechnic Institute.

## APPENDIX D

### Electromagnetic Waves in Conducting Media

In this section we shall investigate the transmission of a electromagnetic wave into a volume of material having a non-negligible resistivity. We shall discover that there is a significant penetration of the wave into the metal but that the strength of the ac field decays exponentially. Furthermore, we will find that the depth of penetration depends on the resistivity of the metal and the operating frequency.

We begin by writing Lenz's law and note that it is true for an arbitrary closed path.

$$\oint E \cdot dl = -\frac{\partial \Phi}{\partial t}$$

The magnetic flux,  $\Phi$ , is defined as:

$$\Phi = \int B \cdot ds$$

where the surface over which B is summed is any surface bounded by the arbitrary path selected in the first integral. Thus, by Stokes's theorem we write:

$$\oint E \cdot dl = \int (\nabla \times E) \cdot ds = -\frac{\partial}{\partial t} \int B \cdot ds$$

But if we shrink the surface of integration to an infinitesimal one, we have:

$$\nabla \times E = -\frac{\partial B}{\partial t}$$

This equation, which relates the electric field to the magnetic induction at any point, is crucial in understanding the induction of currents in metals. Multiplying both sides of the equation by  $\sigma$ , the conductivity, and taking the curl we obtain:

$$\nabla \times [\nabla \times (\sigma E)] = -\sigma \frac{\partial}{\partial t} (\nabla \times B)$$

We assume the situation in which the metal is ohmic and thus obeys the microscopic form of Ohm's law:

$$I = \sigma E$$

Substituting this relation into the left side of the previous equation and making use of a well known vector identity, we find:

$$\nabla \times (\nabla \times I) = \nabla(\nabla \cdot I) - \nabla^2 I = -\sigma \frac{\partial}{\partial t} (\nabla \times B)$$

Since there is no accumulation of charge, the divergence of the current field is zero and the second term drops out ( $\nabla \cdot I = 0$ ). For a material without a permanent magnetization M, we may write B in terms of a more useful field quantity, H, usually called the magnetic field intensity. The circulation of this new vector field quantity depends only on the free macroscopic current.

$$H = \frac{1}{\mu_0} B - M = \frac{1}{\mu_0} B \text{ in this case.}$$

Thus,

$$\nabla^2 I = \sigma \mu_0 \frac{\partial}{\partial t} (\nabla \times H) = \sigma \mu_0 \frac{\partial I}{\partial t} \text{ since } \nabla \times H = I$$

Induced currents satisfying the above equation are known as eddy currents. Two comments can be made on this equation. First we note that the induction B satisfies the same differential equation as the current I. Second, we immediately recognize that this differential equation is the same as the heat equation. Thus the quantity  $\frac{1}{\sigma \mu_0}$  is a measure of the rate at which the currents diffuse into the conductor.

In order to obtain a description of the induced currents we must find a solution to this differential equation. Since the equation is linear, the current will vary linearly with time and we may separate I into a space part and a time part:

$$I = I' e^{j\omega t} \text{ (where } j \text{ is the imaginary number and } I' \text{ is the space part of the solution)}$$

If the z axis is pointed into the metal, along the propagation of the wave, the induced current will depend only on z. Thus the problem has been reduced to solving the time independent differential equation:

$$\frac{d^2 I'}{dz^2} = j\omega\mu_o\sigma I'$$

This equation has a familiar solution, namely:

$$I' = I_o e^{\alpha z} \text{ where } \alpha^2 = j\omega\mu_o\sigma$$

or  $\alpha = \pm \sqrt{j\omega\mu_o\sigma} \frac{(1+j)}{\sqrt{2}}$  however since we know that the current must decay with increasing z (deeper penetration within the metal) we must choose the negative sign.

The final solution for I is then:

$$I = I_o e^{-\sqrt{\frac{j\omega\mu_o\sigma}{2}} z} e^{j(\omega t - \sqrt{\frac{j\omega\mu_o\sigma}{2}} z)} \text{ where } I_o \text{ is the current just inside the boundary}$$

The second exponential represents a traveling wave moving into the metal, but it is multiplied by the first exponential which represents a dampening factor. This equation shows that

$$\delta = \sqrt{\frac{2}{\mu_o\sigma\omega}} \text{ measures the exponential dampening of the current (or the wave)}$$

as it travels into the metal. This quantity, which has the units of length, is called the skin depth.

In the case of our generator, which operates at 60 cycles per second, the currents are less than 1% of their value at the surface when at a depth of 5 cm (1.97 inches). In order to protect the rotor from the ac fields of the armature, the outer shield was designed to have a thickness greater than the skin depth. Since the shield is optimized for first harmonic waves, a second inner shield was also designed. Since both shields spin with the rotor assembly they do not have any effect on the rotor's magnetic field.

## Bibliography

Harnwell, G., *Principles of Electricity and Magnetism*, McGraw Hill, 1938

Kip, A., *Fundamentals of Electricity and Magnetism*, McGraw Hill, 1962

Recanati, M., *Lecture Notes from Electricity and Magnetism*, Fall 1991

and the help of Professor Emeritus Paul Yergin of Rensselaer Polytechnic Institute.

## APPENDIX E

### Thermal Conduction and Convection in a Fin

In this section we will model the conducting litzwire as a fin, in order to determine how far the heat penetrates into the litzwire when the end connectors are being soldered. This distance, known as the *thermal penetration depth*, is of importance for the manufacturing of the bars since it predicts the spread of the damage to the film insulation used throughout the litz cable. Although the results of this analysis will be overly pessimistic, due to the assumption that the base of the cable is in thermal equilibrium with the surrounding solder, it will yield an intuitive understanding of natural convection cooling.

This section will be subdivided into two parts. The first part will derive the temperature distribution equation from basic principles while the second part applies this relation in order to get numerical results.

### I. The Fin Equation

Let us consider the cable drawn in **Figure E1** and model it as a fin whose base temperature is nearly that of the molten 60/40 lead-tin eutectic. The cable's rectangular cross-sectional area is  $A = w * t$  and the perimeter is  $P = 2 * (w+t)$ , where  $w$  and  $t$  are the width and the thickness of the cable, respectively. Since the conductor employed in the armature bars is a uniform rectangular compacted litz, the area and perimeter of the wire are constant throughout its length.

Using the energy conservation principle on a slice of cable located between  $x$  and  $x + \Delta x$ , and realizing that heat is entering the slice through conduction and leaving through a combination of conduction and convection, as shown in **Figure E2**, we write:

$qA|_x = qA|_{x+\Delta x} + hP\Delta x(T - T_e)$  where  $h$  is the heat transfer coefficient and  $T_e$  is the air temperature.

By taking the limit of this equation when the thickness of the slice becomes infinitesimally small, we obtain:

$$\frac{d}{dx}(qA) = -hP(T - T_e)$$

Using Fourier's law ( $q = -k \frac{dT}{dx}$ , where  $k$  is the thermal conductivity ) we obtain the fin differential equation:

$$kA \frac{d^2 T}{dx^2} - hP(T - T_e) = 0$$

Since we desire to study the fin itself, we shall specify the base temperature and we will disregard the negligible effects of tip convection at the end of the wire. Thus, the two boundary conditions become:

$$T|_{x=0} = T_o \text{ and } \frac{dT}{dx}|_{x=L} = 0$$

By grouping the parameters into a more convenient form, we may significantly simplify the the fin differential equation by recasting it into the following form:

$$\frac{d^2\theta}{dx^2} - \beta^2\theta = 0 \quad \text{where } \theta = T - T_e \text{ and } \beta^2 = \frac{hP}{kA}$$

The solution to this differential equation is given by:

$$\frac{T-T_e}{T_o-T_e} = \frac{\cosh[\beta(L-x)]}{\cosh(\beta L)}$$

This equation is of paramount importance in understanding the temperature distribution within a body which acts like a fin. It has been plotted in **Figure E3**.

\*\*\*

The heat dissipated from the fin may be determined at present by applying Fourier's law at the base of the fin. Thus, using the temperature distribution equation derived above, we find:

$$\dot{Q} = -kA \left. \frac{dT}{dx} \right|_{x=0} = kA\beta(T_o - T_e)\tanh(\beta L)$$

The rate at which heat is being removed from the molten solder, located within the end connector, is important since it governs the eutectic's solidification time.

## II. Application of Theory

The first step in determining the temperature profile within the conductor bar when the end connectors are being installed is to determine the physical parameters for the system. Knowing that the bar measures  $w=1.481''=3.762 \cdot 10^{-2}$  m wide by  $t=0.295''=7.493 \cdot 10^{-3}$  m thick, we find that the perimeter and cross sectional area are:  $P=9.022 \cdot 10^{-2}$  m and  $A=2.819 \cdot 10^{-4}$  m<sup>2</sup>, respectively.

The heat transfer coefficient,  $h$ , is correlated to the ratio of the temperature difference to the hydraulic diameter of the fin,  $D$ . Thus,

$$h = 1.3 \left( \frac{\Delta T}{D} \right) \quad \text{where } D = (4A)/P = 1.250 \cdot 10^{-2} \text{ m}$$

Allowing  $\Delta T$ , the temperature gradient between the fin and the air temperature, to be of the order of 30 degrees Celsius, we determine that:

$$h \approx 3,100 \text{ W/m}^2 \text{ K.}$$

Since the heat conductivity of copper is  $k=389$  J/m K, we find that

$$\beta = \left( \frac{hP}{kA} \right)^{1/2} = 50.5$$

Thus, if the eutectic melts at  $T_e=225$  C, the bar will cool to 75 C at a distance of 3/4 of an inch away. In conclusion, we find that water-cooling the armature bars when soft soldering the end-connectors is not really required, but desirable. This conclusion is based on the fact that ML insulation is rated to 220 C and on the understanding that the analysis performed in this section is based on a steady-state base temperature rather than on a transient condition.

As an aside, we note that the energy carried out from the eutectic by the bar is of the order of  $\dot{Q}=170$  W/m<sup>2</sup>. At least this much heat must be supplied to the end-connector during manufacture in order to keep the eutectic from solidifying.

We also note that, based on the fin efficiency calculation, the armature bar is a highly inefficient fin:

$$\eta = \frac{\tanh(\beta L)}{\beta L} \approx 1.6\%$$

This is principally due to its excess length which serves little purpose, if any, in transporting heat.

## Bibliography

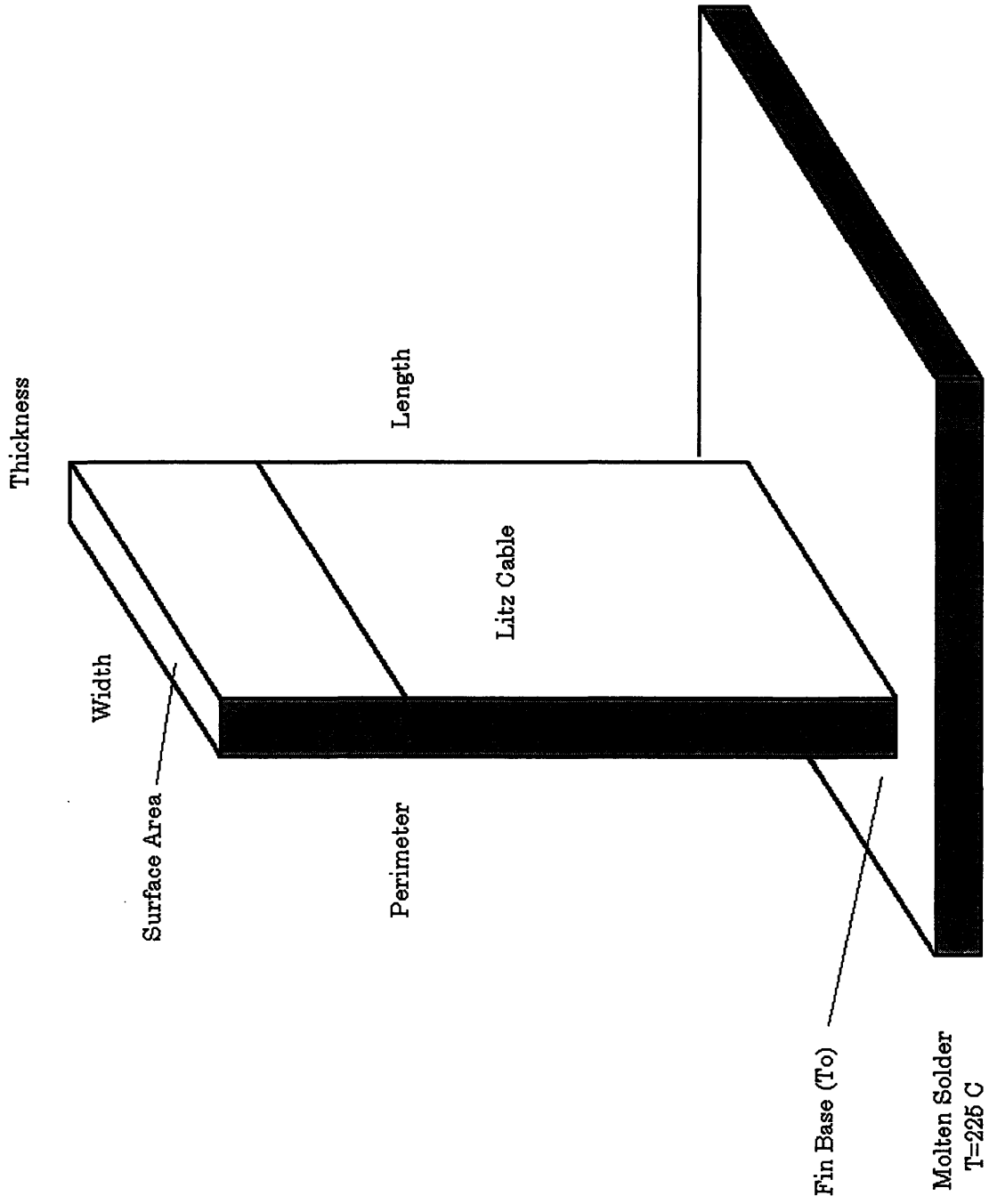
The author acknowledges the help from the following sources:

Incropera F., DeWitt D., Fundamentals of Heat and Mass Transfer, Wiley, New York, NY, 1985.

Mills, A., Heat Transfer, Irwin, Homewood, Il, 1992.

Lienhard, J., A Heat Transfer Textbook, Prentice-Hall, Englewood Cliffs, NJ, 1987.

and the help of Edward Ognibene, graduate student in Mechanical Engineering, Massachusetts Institute of Technology.



**Figure E1: Litz Cable Modeled as a Fin**



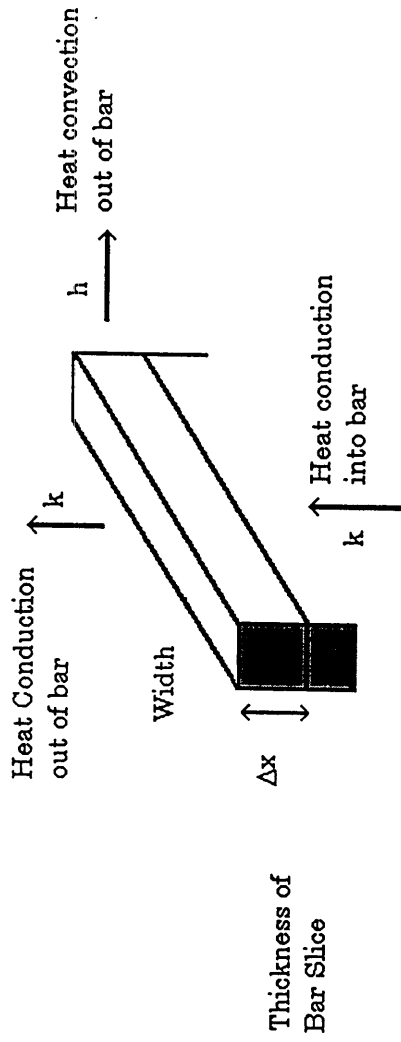


Figure E2: Heat Flow in Fin

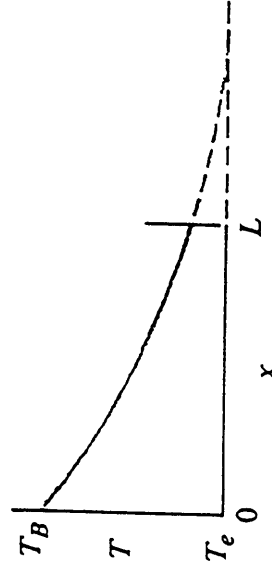


Figure E3: Temperature Distribution in Fin

## FOOTNOTES

- 
- <sup>1</sup> Westinghouse Corporation, Annual Report 1991, pp 19.
- <sup>2</sup> M. A. Recanati, "Sollicitation to a Large Holding Corporation", June 1993.
- <sup>3</sup> M. A. Recanati, "Proposal for Funding for the MIT Superconducting Generator", April 1993.
- <sup>4</sup> James L. Kirtley, Jr., "Application of Superconductors-High Tc and Otherwise-to electric Power Generators", Electric Machines and Power Systems, pp. 121-134, 1988.
- <sup>5</sup> Superconducting Generators: Impact of High Tc Superconductors, Report to the Electric Power Research Institute, Massachusetts Institute of Technology, March 1988.
- <sup>6</sup> J. L. Smith Jr. and A. G. Liepert, "Construction of MIT-DOE 10 MVA Superconducting Generator", 1985, pp. 791-794.
- <sup>7</sup> J. A. Schwoerer and J. L. Smith Jr., Transient Cooling of a Fault-Worthy Superconducting Electric Generator", Advances in Cryogenic Engineering, Vol. 25, pp. 266-274, 1980.
- <sup>8</sup> A. G. Liepert, "A Helium Conditioning System External to a 10 MVA Superconducting Generator", S. M. Thesis Mech. Eng., MIT, August 1982.
- <sup>9</sup> J. L. Kirtley Jr., J. L. Smith Jr. and Stephen D. Umans, "Ten MVA Superconducting Generator Development Status at the End of 1989", IEEE 1990.
- <sup>10</sup> A. E. Fitzgerald, C. Kingsley Jr., S. D. Umans, Electric Machinery, McGraw-Hill Book Company, New York, 1971.
- <sup>11</sup> Raymond A. Serway, Physics for Scientists and Engineers, 2nd Ed., 1986, pp. 708-717.
- <sup>12</sup> S. D. Umans, P. Roemer, J. A. Mallick, G. L. Wilson, "Three Dimensional Transient Analysis of Superconducting Generators", IEEE Transactions on Power Apparatus and Systems, Vol. 98 No. 6, Nov/Dec 1979, pp. 2055-2064.
- <sup>13</sup> J. L. Smith et al, "MIT-DOE Program to Demonstrate an Advanced Superconducting Generator", IEEE Trans. Magn., Vol. MAG-15, pp. 727-730, January 1979.
- <sup>14</sup> General Electric Turbine Generator Marketing Operation, For Power Generation Leadership, Generators 150,000 kVA and Larger, Publication No. GEA-8710, General Electric Corporation, Schenectady, New York, 1980.
- <sup>15</sup> J. L. Kirtley, MIT course 6.061 Supplementary Notes 2: "AC Power Flow in Linear Networks", and Notes 3: "Polyphase Networks", June 1991.

- 
- 16 James L. Kirtley, Jr., "Application of Superconductors-High Tc and Otherwise-to electric Power Generators", Electric Machines and Power Systems 1988, pp 121-134.
- 17 Demonstration of an Advanced Superconducting Generator, Interim Report 8, December 1978 to May 1979, Chapter 5.
- 18 Private communication with J. L. Kirtley Jr., MIT Electric Power Systems Engineering Laboratory, August 1993.
- 19 A. Still and C. S. Siskind, Elements of Electrical Machine Design, pp. 168-184, McGraw-Hill Book Company, New York, 1954.
- 20 Private communication with J. L. Kirtley Jr., MIT Electric Power Systems Engineering Laboratory, August 1993.
- 21 W. H. Hagman, "A High Voltage Armature Insulation System", S. M. Thesis Electrical Engineering, MIT, February 1981.
- 22 T. Bratoljic, "Delta Connected, Two Layer , Three Phase Winding for an Electrical Machine", United States Patent No. 4,200,817, April 29, 1980.
- 23 W. C. Brenner, D. W. Deis, R. F. Edwards, H. E. Haller III, C. J. Mole, C. C. Sterrett, M. S. Walker, L. N. Wedman, "Development of a 5 MVA Superconducting Generator-Electrical Design and Performance", Paper C73 245-8 Presented at 1973 IEEE Winter Power Meeting, New York, January 1973.
- 24 T. J. Fagan Jr., D. C. Litz et all, "Development of a 5 MVA Superconducting Generator - Mechanical and Cryogenic Design", Paper C73 255-7 Presented at 1973 IEEE Winter Power Meeting, New York, 1973.
- 25 J. L. Kirtley Jr., "Armature of the MIT-EPRI Superconducting Generator", Paper F76 385-5 Presented at 1976 IEEE Summer Power Meeting, Portland, Or., July 1976.
- 26 Private communication with W. H. Hagman, MIT Electric Power Systems Laboratory, September 1993.
- 27 A. Still and C. S. Siskind, Elements of Electrical Machine Design, pp. 20-29, McGraw-Hill Book Company, New York, 1954.
- 28 J. S. H. Ross, A. F. Anderson, R. B. Macnab, "Alternating Current Dynamo-Electric Machine Windings", British Patent Specification No. 1,395,152, May 21, 1975.
- 29 J. L. Kirtley Jr., J. L. Smith Jr., "Rotating Machine Having a Toroidal- Winding Armature", United States Patent No. 4,087,711, May 2, 1978.

- 
- 30 M. M. Steeves, J. L. Kirtley Jr., "Toroidal Winding Geometry for High Voltage Superconducting Alternators", IEEE Transactions on Power Apparatus and Systems, Vol. PAS-93, No. 6, November/December, 1974, pp. 1902-1908.
- 31 C. G. Prohazka, "The Design and Construction of a Modified Gramme-Ring Armature for a Generator With a Superconducting Field Winding", M.S. Thesis in Electrical Engineering, MIT, May 1977.
- 32 G. Aicholzer, "New Ways of Building Turbogenerators Up to 2 GVA, 60 kV", Elektrotec. u. Maschinenbau, Vol. 89, January, 1972, pp. 1-11.
- 33 C. Flick, "New Armature Winding Concepts for EHV and High CFCT Applications of Superconducting Turbine Generators", Paper A78 313-9 Presented at 1978 IEEE Winter Power Meeting, New York, January, 1978.
- 34 Private communication with W. H. Hagman, MIT Electric Power Systems Laboratory, September 1993.
- 35 G. Aicholzer, M. Manowarda, "Approach to Development of a 230 kV - Airgap winding", Paper LG3/5, International Conference on Electric Machines, Proceedings, Part 3, Athens, Greece, September 15-17, 1980, pp. 1444-1451.
- 36 P. L. Conley, J. L. Kirtley, Jr., W. H. Hagman, A. Ula, "Demonstration of a Helical Armature Winding for a superconducting Generator", IEEE PES Summer Meeting, Vancouver B. C. April 25, 1979.
- 37 New England Electric Wire Corporation, Specialty Wire Catalogue, 1993, pp. 8-15.
- 38 Private conversation with Steve Umans, MIT Electric Power Systems Laboratory, December 1993.
- 39 Private communication with W. H. Hagman, MIT Electric Power Systems Laboratory, September 1993.
- 40 S. D. Umans, P. B. Roemer, J. Mallick, G. Wilson, "Three Dimensional Transient Analysis of Superconducting Generators", IEEE Rotating Machinery Committee, November 1979.
- 41 General Electric, General Engineers Electrical Products Catalogue 1991.
- 42 Telephone conversation with Sharon Mort, Senior Electrical Engineer, Dow-Corning Corporation, November 1991.
- 43 Private communication with Dave Otten, MIT Electric Power Systems Laboratory, December 1993.
- 44 Based on quoted dimensions of New England Electric Wire Corporation, (Quote #8269), July 1993.

- 
- 45 Handbook of Electrical Engineering, 1985.
- 46 U.S. Patent 4,439,256, Method of Producing Flat Stranded Magnetic Conductor Cable, R. Miserve, 1984
- 47 D. Lide, CRC Handbook of Chemistry and Physics, 72nd ed., CRC Press, Boston, MA. 1989.
- 48 Duckworth H., Electricity and Magnetism, Holt-Dryden Books, 1960.
- 49 Hallen, E., Electromagnetic Theory, pp. 360-365, John Wiley, 1962.
- 50 Andrews L., Introduction to Differential Equations with Boundary Value Problems, pp. 501-517, Harper, 1990.
- 51 W. H. Hagman, "A High Voltage Armature Insulation System", M. S. Electrical Engineering, MIT, February 1981.
- 52 D. Erdman, H. Lauroesch, "Mica Paper for High Voltage Motor and Generator Stator Windings", IEEE Proceedings of the Ninth Electrical Insulation Conference, Boston, MA, 1969, pp. 159-165.
- 53 F. Clark, Insulating Materials for Design and Engineering Practice, John Wiley, New York, 1962.
- 54 Z. Iwata, H. Shii et all, "New Modified Polyethylene Paper Proposed for UHV cable insulation", IEEE Transactions on Power Apparatus and Systems, Vol. PAS-96, No. 5, September/October 1977, pp. 1573-1582.
- 55 Private Communication with Jim Kirtley, Jr., MIT, Summer 1993.
- 56 P. L. Conley, "Electromechanical Stresses and Mechanical Support for a Helically Wound Armature", M.S. Mechanical Engineering, MIT, May 1979.
- 57 P.M. Bolger, "Fluid Support for the Armature of a Superconducting Generator", M.S. Mechanical Engineering, August 1980.
- 58 Letter from T. A. Keim, General Electric Corporation, Schenectady, NY, to A. H. Ula, MIT Electrical Power Systems Engineering Laboratory, Cambridge, MA, March 17, 1980.
- 59 Demonstration of an Advanced Superconducting Generator, Interim Report, MIT August 1981.
- 60 Suh, Cook et al., Manufacturing Engineering, Mc Graw-Hill, New York, 1992.
- 61 S. Eppinger, K. Ulrich, T. Eagar, W. Flowers, Class Notes of 15.783 Product Development in the Manufacturing Firm, spring 1993.
- 62 Private Communication with Mike Bovin, Chief Engineer, New England Electric Wire Corp., Spring 1993.

- 
- 63 Operating Instructions and MSDS, Insulstrip 220 revision 3053.
- 64 Private Communication with Peter Schuyler, Ambion Corp., Winter 1993.
- 65 Insulating Materials Inc., AC Insulation Systems and Insulating Materials Handbooks, 1991
- 66 Dow-Corning 561 Silicone Transformer Liquid Technical Data Guide, Intended for internal use only, 1992.
- 67 Cravalho, E. and Smith, J., Engineering Thermodynamics, pp. 426-440, Massachusetts Institute of Technology, Cambridge, MA, 1981.
- 68 Lienhard, J., A Heat Transfer Textbook, pp. 336, Prentice-Hall, Englewood Cliffs, NJ, 1987.
- 69 Mills, A., Heat Transfer, pp. 270-278, Irwin, Homewood, IL, 1992.
- 70 Recanati, M. A., "Class notes of Heat Transfer (2.55)", MIT, Summer 1993.
- 71 Incropera, F. and DeWitt, D., Fundamentals of Heat and Mass Transfer, 2nd edition, pp. 370-375, Wiley, New York, 1985.
- 72 Lienhard, J., A Heat Transfer Textbook, pp. 296-307, Prentice-Hall, Englewood Cliffs, NJ, 1987.
- 73 General Electric Technical Manual for the GE Model 7LM-1500-PE101 Gas Turbine, pp. 3-40 to 3-56, Volume I, NAVPERS 0941-032-4010.
- 74 Smith, J. L., Jr. and Liepert A., Construction of MIT-DOE 10-MVA Superconducting Generator, IEEE Transactions on Magnetics, Vol. Mag-21, No. 2, March 1985.
- 75 Krause, P., Analysis of Electric Machinery, pp. 211-231, McGraw-Hill, NY, 1986.
- 76 Kirtley, J., "Synchronous Machine Dynamics Models-6.685 Lecture Notes #5", 1993.
- 77 Park, R., "Two Reaction Theory of Synchronous Machines-Generalized Method of Analysis-Part I", AIEE Trans., Vol. 48, July 1929, pp. 716-727.
- 78 Kirtley, J., "Design and Construction of an Armature for an Alternator with a Superconducting Field Winding", PhD. Electrical Engineering, MIT, August 1971.
- 79 Kirtley, J., "Synchronous Machine Dynamics Models-6.685 Lecture Notes #5", 1993.
- 80 Tolikas, M., "6.685 Electric Machines Class Notes", MIT, Spring 1991.

- 
- 81 Kirtley, J. , Edeskuty, F., "Application of Superconductors in Motors, Generators , and Transmission Lines", pp. 1143-1154, Proceedings of the IEEE, Vol 77, No. 8, August 1989.
- 82 Kirtley, J., "Design and Construction of an Armature for an Alternator with a Superconducting Field Winding", PhD. Electrical Engineering, MIT, August 1971.
- 83 Kirtley J., "Basic Formulas for Air-Core Synchronous Machines", IEEE Power Engineering Society, Paper No. 71 CP 155-PWR, New York, 1970.
- 84 Fitzgerald, A., Kingsley, C., Kusko, A., Electric Machinery, 3rd ed., pp. 480-495, McGraw-Hill, NY, 1971.
- 85 Kirtley, J., "Design and Construction of an Armature for an Alternator with a Superconducting Field Winding", PhD. Electrical Engineering, MIT, August 1971.
- 86 Chalmers, B., Williamson, A., AC Machines Electromagnetics and Design, pp. 65-77, John Wiley, England, 1991.
- 87 Some data from Kirtley, J., Smith, J., Umans, D., "Ten MVA Superconducting Generator Development: Status at the End of 1989", pp.7, IEEE Power Engineering Society, Paper No. 90 JPGC 622-1 EC, September 1990.
- 88 Luck, D., "Electromechanical and Thermal Effects of Faults Upon Superconducting Alternators for Electric Utility Power Generation", Sc.D. Thesis, Mechanical Engineering, MIT, January 1971.
- 89 Kirtley, J., "Synchronous Machine Dynamics Models-6.685 Lecture Notes #5", 1993.
- 90 Kirtley, J., "Synchronous Machine Dynamics Models-6.685 Lecture Notes #5", 1993.
- 91 Kirtley, J., Smith, J., Umans, D., "Ten MVA Superconducting Generator Development: Status at the End of 1989", pp.7, IEEE Power Engineering Society, Paper No. 90 JPGC 622-1 EC, September 1990.